Fracture network formation in mechanical layers: field and numerical studies in the South Wales coalfield

A thesis submitted for the degree of Doctor of Philosophy
at the University of London

Tetsuzo Fukunari

Supervised by Professor Agust Gudmundsson

Rock fractures and fluid flow research group
Department of Earth Sciences
Royal Holloway, University of London

Original version submitted in January, 2016
Revised version submitted in November, 2017

Declaration

I, Tetsuzo Fukunari, hereby declare that this thesis and the work presented in it is entirely my own, unless otherwise stated. The main body of thesis, Chapters 4-6, forms a collection of co-authored papers which are in preparation for publication. I am responsible for the data collection and mathematical calculations throughout this thesis, and for primary authorship of all three of the included papers.

Sign 福成徹三 Date 11th January, 2018

Tetsuzo Fukunari
Department of Earth Sciences
Royal Holloway University of London

Abstract

Layer-scale extension fractures developed in stiff sandstones in mechanical layers were studied in the South Wales coalfield. Field structural data of extension fractures and bedding planes associated with compressive folds which developed at the latest stage of sedimentation in the basin were measured from the southern end to northern end of the basin. The geometrical relationship between the fractures and fold suggests the fractures developed before the folding and during basin burial. Numerical modelling conducted to assess the effect of stress rotation after the folding supports the hypothesis that extension fractures initiated during the basin burial. Fluid overpressure at the time of development of extension fractures which are now filled with mineral was examined with aspect (length/thickness) ratios of the veins. The results show the average fluid overpressure was about 35 MPa as maximum values. Mineral assembly of the mineral veins recognised under microscope suggests the driving mechanism for the fluid overpressure was mainly derived from local stresses that concentrated in the sandstones. Based on the results of the field studies and analytical calculations of fluid overpressure, an appropriate model is required to address extension fracture formation in stiff sandstone layers during basin burial. An analytical model which is simplified version of Bourne model with combination of fluid pressure was built. The analytical solutions indicate extension fractures could develop in stiff layers surrounded by soft material during basin burial. The important factors for the extension fracture formation is only not regional stress field. They can be formed in mechanical layers even in compressive stress field with three compressive regional principal stresses, depending on volume ratio of stiff and soft material, contrast of Young's modulus, regional stress field and fluid pressure.

Contents

List of figures & Table

Chapter 6: Analytical calculation for mode I fracture formation in mechanical layers: Effects of mechanical properties, stress fields, pore-pressure and layer thickness

Chapter 1: Introduction

Fracture network has significant impact on, and sometimes likely control, permeability and fluid transport in subsurface geological formation. For instance, open fractures can be main fluid path for tight rock reservoirs which have low-permeability in the matrix on one hand, and on the other hand fractures filled with impermeable materials can be barrier of fluid transportation in conventional reservoirs which commonly have high-permeability in the matrix. It is, thus, of great importance in understanding characteristics of fracture systems regardless of whether the fractures are open or filled, and in recognizing when and where those fractures developed in the geological history to estimate fluid transportation in subsurface reservoirs. However, development mechanisms of several fractures are not fully understood, making estimation of subsurface fracture systems hard.

An example is extension fracture network system formed in sedimentary rocks. In general, analogies of fracture pattern and characteristics at surface exposures of extension fractures are referred to build subsurface fractured rock model of oil and gas reservoir (e.g. Belayneh et al., 2006; Wennberg et al., 2007; Zhao et al., 2014). However, extension fracture formation in sedimentary rocks are controlled by several factors since sedimentary rocks change their deformation style and mechanical properties depending on geological conditions such as including consolidation/diagenesis of the sediments, temperature and confining-pressure conditions, fluid effect and strain-rate of deformation. In addition, heterogeneity and anisotropy of the rocks at the time of fracture formation also affect the local stress field for the fracture formation. Relationship between those many factors and the extension fracture formation is extremely complex and is not clearly explained or revealed in many cases in the industry. This increases uncertainty of oil and gas projects targeting fractured reservoirs, and still heightens the risk of investment to such projects even in recent years.

In order to contribute on the above matter, this thesis focuses on mechanism of extension fracture formation in association with geological history, and attempts to address the possible geological conditions for such kind of fractures. Layer-controlled extension fractures in mechanical layers are especially focused on in the current thesis.

This is because one of the major targets of hydrocarbon reservoirs in recent years is low-resistivity low-contrast pay zones which are electrically conductive hydrocarbon-bearing formations (e.g. Allen, 1984; Berger, 1989). The low-resistivity low-contrast conditions of hydrocarbon reservoirs are commonly caused by thinly bedded/laminated alternating high- and low-resistive layers, such as combination of hydrocarbon-bearing thin sandstone and water-bearing thin shale. In the case thickness of those layers is thinner than resolution of wire-line logging data, the layered rock is detected as one low-resistive zone since electric current can easily and selectively flow in low-resistive layers. In theory, combination of 50 percent volume of 100 ohm*m hydrocarbon-bearing thin sandstones and 50 percent volume of 1 ohm*m water-bearing thin shales is detected as 1.98 ohm*m zone in typical resistivity log. Because of this phenomenon, many of thinly bedded/laminated hydrocarbon-bearing layers were not targeted for drill stem test (fluid flow test) and were overlooked in many drilling wells. However, new analytical approaches and new wire-line logging tools were introduced and applied to detect these undetectable thin hydrocarbon-bearing zones in recent years (e.g. Clavaud et al., 2005; Cao Minh et. al., 2007; Belevich and Bal, 2017). This implies that it will become more vital in the oil and gas industry to understand fluid transportation within thinly bedded/laminated reservoirs. Layer-controlled extension fracture system within those thinly bedded reservoirs must have significant impact on fluid transportation if such kind of fracture system exists in deep, subsurface reservoirs.

In theory, both vertical and lateral principal stresses are commonly compressive in deep depth (Gudmundsson, 2011; Fossen, 2016). Because of this theoretical background, many researches imply tension/extension fractures were mainly formed during crustal uplift/exhumation in relation with pressure/stress release (e.g. Simon et al., 1988; Caputo, 1995; Bai et al., 2002), suggesting the possibility that extension fracture system does not occur in deep, subsurface reservoirs. Therefore, the main hypothesis that this thesis intends to test is existence of another reasonable mechanism for extension fracture formation in mechanical layers, unrelated to crustal uplift/exhumation. This is in order to examine whether layer-controlled fractures are important or not to consider fluid transportation in thinly bedded subsurface hydrocarbon-bearing reservoirs. This thesis focuses on local stress field variation in

mechanical layers, and investigates whether the local stress field can be tensile or not in the mechanical layers even in the case that horizontal regional stresses are compressive.

There is also another possible mechanism to address extension fracture development in deep depth. Many researchers demonstrated extension fractures can be formed by fluid overpressure in relation with geothermal fluid supply from deeper depth (e.g. Collettini et al., 2006; Philipp, 2012). However, there seems to be a significant limitation of extension fracture formation by this mechanism, in which highly pressured fluid must have been supplied from hundreds of metres or deeper depth through continuous faults. Therefore, the extension fracture formation would be limited only around such kind of huge faults in this case. The second hypothesis that this thesis intends to test is whether the geothermal fluid is necessary in any cases or not to develop extension fractures in deep depth.

South Wales coalfield is selected for this study. Since resolution of typical wire-line logging tools is 2 feet (Passy et al., 2006), layer thickness of the low-resistivity low-contrast pay zones is generally less than 2 feet. Therefore, centimetre- to decimetre-scale alternating sand-shale layers are mainly examined in the field.

In chapter 2, geological setting of the study area and brief review of layer-controlled fracture formation in mechanical layers are summarized. In chapter 3, reasons of the study area selection is stated, and methodology of fracture data collection and numerical calculation are explained. Chapter 4, 5 & 6 are main parts of this thesis. Chapter 4 focuses on structural data collected in the field. Timing of the extension fracture formation in the field is discussed based on the geometrical relationship between the fractures and other deformation structures. Simple numerical calculation is also conducted to check the validity of proposed timing. Chapter 5 focuses on extension fractures filled with minerals and calculates fluid overpressure for the vein formation. Contribution of geothermal fluid supply from deeper depth is discusses in this chapter. Chapter 6 proposes analytical solutions for extension fracture formation in mechanical layers in the study area, which is simplified version of Bourne model (Bourne, 2003). From the analytical calculations, possible geological conditions for extension fracture formation in mechanical layers are discussed in the chapter. Then, discussions and conclusions are summarized in chapter 7.

References

Allen, D.F. 1984. Laminated sand analysis. SPWLA 25th Annual Logging Symposium, New Orleans, Lousiana: 20.

Bai, T., Maerten, L., Gross, M.R., Aydin, A. 2002. Orthogonal cross joints: do they imply a regional stress rotation? Journal of Structural Geology 24, 77-88.

Berger, P. 1989. Detecting hydrocarbons in low resistivity environments, Schlumberger.

Belayneth, M., Geiger, S., Matthai, S.K., 2006. Numerical simulation of water injection into layered fractured carbonate reservoir analogs. AAPG Bulletin 90, 1473-1493.

Belevich, A., Bal, A.A. 2017. The problem with silt in low resistivity low contrast pay reservoirs. SPWLA 58th Annual Logging Symposium, Oklahome City, Oklahoma: 19

Bourne, S.J., 2003. Contrast of elastic properties between rock layers as a mechanism for the initiation and orientation of tensile failure under uniform remote compression, Journal of Geophysical Research, 108 (B8), 2395.

Cao Minh, C., Clavaud, J.B., Sundararaman, P., Froment, S., Caroli, E., Billon, O., Davis, G., Fairbairn, R. 2007. Graphical analysis of laminated sand-shale formations in the presence of anisotropic shales. SPWLA 45th Annual Logging Symposium, Austin, Texas: 10.

Caputo, R. 1995. Evolution of orthogonal sets of coeval extension joints. Terra Nova 7, 479-490.

Collettini, C., Paola, N., Goulty, N.R. 2006 Switches in the minimum compressive stress direction induced by overpressure beneath a low permeability fault zone. Terra Nova 18, 224-231.

Clavaud, J.B., Nelson, R., Guru, U.K., Wang, H. 2005. Field example of enhanced hydrocarbon estimation in thinly laminated formation with a triaxial array induction tool: a laminated sand-shale analysis with anisotropic shale. SPWLA 46th Annual Logging Symposium, New Orleans, Louisiana: 15.

Gudmundsson, A. 2011. Rock Fractures in Geological Processes. Cambridge University Press, New York.

Fossen, H. 2016. Structural Geology 2nd Edition, Cambridge University Press, New York.

Passey, Q.R., Dahlberg, K.E., Sullivan, K.B., Yin, H., Brackett, R.A., Xiao, Y.H., Guzmam-Garcia, A.G. 2006. Petrophysical evaluation of hydrocarbon pore-thickness in thinly bedded clastic reservoirs. Tulsa, Oklahoma, American Association of Petroleum Geologists.

Philipp, S.L., 2012. Fluid overpressure estimated from the aspect ratios of mineral veins. Tectonophysics 581, 35-47.

Simon, J.L., Seron, F.J., Casas, A.M. 1988. Stress deflection and fracture development in a multidirectional extension regime: mathematical and experimental approach with field example. Annales Tectonicae 2, 21-32.

Wennberg, O.P., Azizzadeh, M., Aqrawi, A.A.M., Blanc, E., Brockbank, P., Lyslo, K.B., Pickard, N., Salem, L.D., Svana, T. 2007. The Khaviz Anticline: an outcrop analogue to giant fractured Asmari Formation reservoirs in SW Iran. Geological Society, London, Special Publications 270, 23-42.

Zhao, X., Liu, L., Hu, J., Zhou, X., Li, M. 2014. The tectonic fracture modeling of an ultra-low permeability sandstone reservoir based on an outcrop analogy: A case study in the Wangyao Oilfield of Ordos Basin, China. Petroleum Science 11, 363-375.

Chapter 2: Geological settings of the study area

The South Wales coalfield was one of foreland basins developed in front of the northwardly propagating Variscan Orogenic belt which extended from South Wales in the west to the Urals in the east (e.g. Leveridge & Hartley 2006). The basins related with the Variscan Orogeny were widely filled with coal-bearing terrestrial sediments in Silesian times and caused the formation of major coalfields in Europe, including those of the Ruhr in German, the Kent in southeast England and the South Wales coalfield. The Silesian sediments in South Wales are exposed in a complex of northwardly verging synformal structure which trends WNW-ESE and inwardly plunges (Figure 2.1). The structure is asymmetric; the southern limb dips steeply north and the northern limb dips gently south. Though both northern and southern limbs dip south in the western area (Pembrokeshire subbasin), the beddings dip more steeply and compression structures become much more common at the southern limb. These asymmetric features and the increase of deformation intensity from the north to the south reflect the propagation of the Variscan Orogen from the south during the Silesian age.

In this section, characteristics of the Silesian sediments and deformation structures in South Wales are introduced with reviewing their relation to the Variscan Orogeny. Possible P-T (pressure and temperature) conditions at the time of basin subsidence are also estimated from previous studies of coal volatile matter, vitrinite reflectance and fluid inclusion, which come from results of White (1991), Alderton & Bevins (1996) and Bevins et al. (1996). The estimation is not very precise and includes some assumptions. However, the values help understanding the relationship among subsidence, structure development and thermal history of the basin.

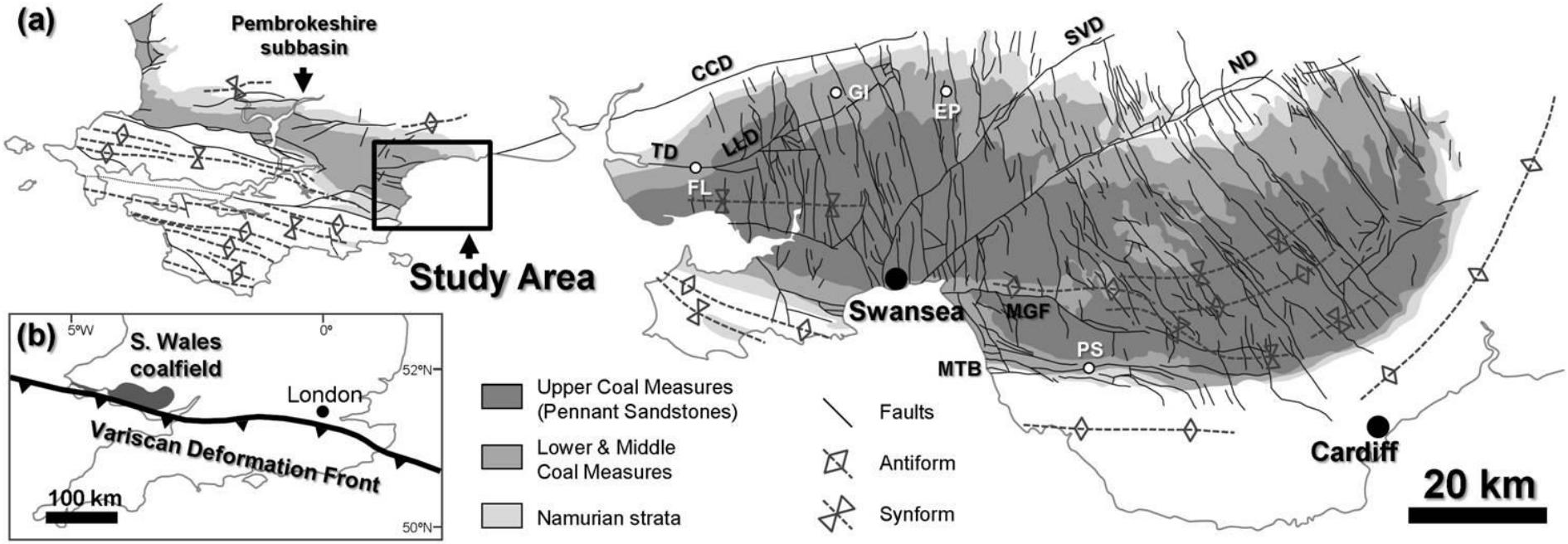

Figure 2.1 **(a)** Geological map of Silesian sediments in South Wales (After Hancock et. al. 1983 and Hartley 1993). The study area is delineated by a box. Opencast coal sites: FL, Ffos Las; GI, Gilfach Iago; EP, East Pit; PS, Park Slip. Key structures: CCD, Carreg Cennen Disturbance; TD, Trimsaran Disturbance; LLD, Llanon Disturbance; SVD, Swansea Valley Disturbance; ND, Neath Disturbance; MGF, Moel Gilau fault; MTB, Margam thrust belt. **(b)** Inset box showing location of the South Wales coalfield and the Variscan Deformation Front.

2.1. Silesian sediments in South Wales

The present-day South Wales coalfield is an erosional remnant in the synformal structure which occupies a region with approximately 90 kilometers in E-W and 30 kilometers in N-S (Figure. 2.1). Central part of this basin is widely filled with Westphalian to early Stephanian Coal Measures and narrow exposures of Namurian sediments surround them.

The Namurian sediments are the oldest siliciclastics of the basin, which rest with regional unconformity on Dinantian carbonates. They only conformably overlie the Dinantian carbonates in the basin centre (e.g. Jones 1974; Leveridge & Hartley 2006). This suggests the possibility that the basin subsidence was initiated in the Dinantian age and that the Namurian sediments continuously filled accommodation space at the relatively subsided basin centre without time gap. However, significant rise of the subsidence rate in the Namurian and the Westphalian age indicates the main period of basin formation was during the Namurian and the Westphalian (Kelling 1988; Burgess & Gayer 2000).

The Namurian strata are mudstone dominated sequences which include decimetre- to a few metre-scale interbedded sandstones. They are interpreted as marine sediments deposited in offshore to shoreface with lesser amount of fluvio-deltaic channels (e.g. George 1970; George & Kelling 1982). The Coal Measures conformably overlie on the Namurian strata. They are subdivided into Upper, Middle and Lower Coal Measures at prominent marine bands (Figure. 2.2). The Lower and Middle Coal Measures (Westphalian A, B and early Westphalian C) are mudstone-dominant sequences deposited in lower to upper coastal plain, where periodic rise of sea-level resulted in the deposition of widely comparable marine bands (e.g. Jones 1989; Hartley 1993). Most of the productive coal seams are involved in these argillaceous units. In contrast, the Upper Coal Measures (Westphalian C and D) are composed of sandstone-dominant facies which contain few productive coal seams and no marine band. The sandy unit is also referred to as Pennant Sandstones. They are interpreted as braided fluvial deposits in alluvial braid plain (e.g. Jones 1989; Hartley 1993). The sedimentation is interpreted to have continued into the Stephanian age though the top of the basin-fill sediments is now eroded.

The Upper Coal Measures of late Westphalian C contain abundant coal clasts as channel lag deposits. They are comparable to coal seams of the Westphalian A (Gayer & Pesek 1992). This indicates the Westphalian A had already been uplifted and exposed in late Westphalian C age. Palaeocurrents of the Westphalian C predominantly show northward transportation (Bluck & Kelling 1963; Kelling 1974; Jones 1989). In addition, no major hiatus or unconformity interrupts the Coal Measure sequences. These sedimentlogical evidences imply migration of the depositional area and orogenic belt toward the north during Westphalian A to C ages: southern side of the basin which had been originally depositional area in Westphalia A age was uplifted in response to northward propagation of the Variscan Orogeny and the exposed Westphalian A sediments were reworked and transported to the current basin area in late Westphalian C age. Migration of basin depocentre toward the north is also recorded by thickness change of the depositional units, supporting the basinward propagation of orogenic belt had continued during the sedimentation (e.g. Kelling 1988; Jones 1989; Leveridge & Hartley 2006).

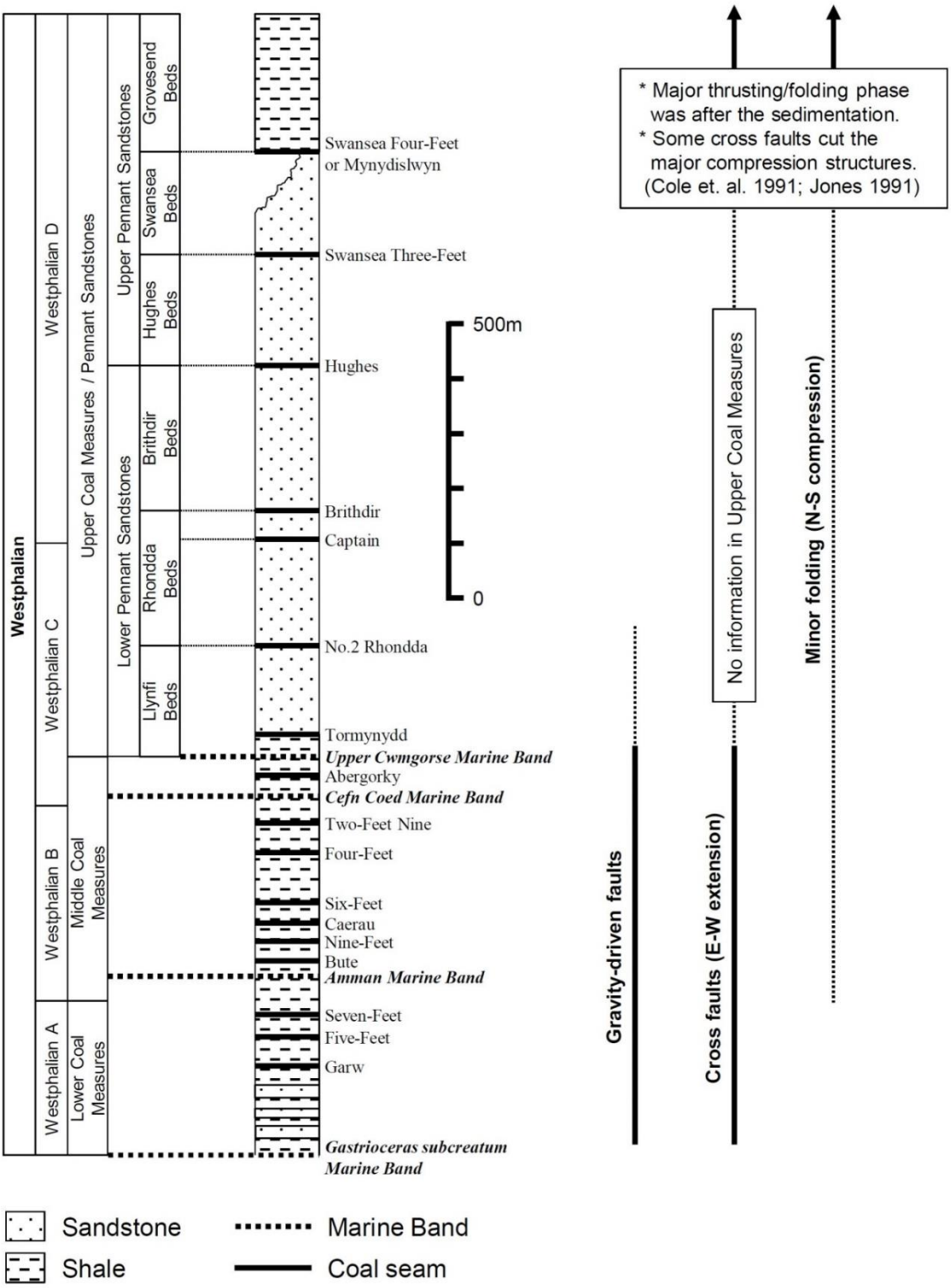

Figure 2.2 Simplified stratigraphy of Silesian sediments in South Wales (after Woodland & Evans 1964 and George 1970). Timing of Silesian structure formation (thrusts, folds, cross faults and gravity slide) is also described.

2.2. Silesian deformation structures in the South Wales

2.2.1. Main deformation structures in the basin

Thrusts and folds are common in the basin. They generally trend E-W which slightly vary from place to place to be sub-parallel to the local basin margin (Figure 2.1). Those compression structures developed in both map-scale and outcrop-scale and produced approximately 30% shortening in the shale-dominant Lower & Middle Coal Measures (Jones 1989; Jones 1991), which rises to 50-60% in the western area of the basin (Frodham & Gayer 1997). The compressive deformation is locally concentrated into narrow zones which are referred to as disturbances (Figure 2.1). They cut across the basin in NE-SW or E-W directions. The highest strain of 70% shortening is recorded at Ffos Las in association with the deformation of Llannon and Trimsaran disturbances (Cole et. al. 1991; Frodsham et. al. 1993). In contrast to the intense shortening within the shale-dominant Lower & Middle Coal Measures, more competent sandstone-dominant sequences of the Upper Coal Measures are much less deformed. They contain only 6% shortening with broad open folds. Thrusts penetrating them are relatively rare (Jones 1989; Jones 1991). This large difference in bulk shortening between Lower & Middle Coal Measures and Upper Coal Measures is interpreted as not timing problem of the deformation but a result of major passive roof thrusts developed at the base of the Upper Coal Measures where the depositional facies and mechanical properties largely change. Jones 1991 reports there is no evidence for syn-depositional thrusting in the Coal Measures. The timing of main compressional deformation is, therefore, interpreted as late Westphalian D at the earliest (Cole et. al. 1991; Jones 1991).

Cross faults which strike sub-perpendicular to the folds and thrusts are also common (Woodland & Evans 1964; Archer 1968). They have downthrows of tens to hundreds metres and generally show strike-slip components together with the normal displacements (Trotter 1947; Owen 1953; Jones 1991). Some of the cross faults have significant thickness changes of sediments across the fault planes, indicating they are syn-depositional structures (Cole et. al. 1991; Jones 1991). Post-depositional displacements are also recorded along the cross faults which cut the E-W trending thrusts of the Variscan Orogeny and vice versa.

Gravity-driven growth faults are also recognised in coal opencasts of the Lower & Middle Coal Measures (Cole et. al. 1991; Jones 1991). Non-tectonic gravity slides can be easily induced under high sedimentation rate because rapid sedimentation over low-permeability shale generates high pore-fluid pressure. The disequilibrium conditions of sediments with high fluid pressure are favoured as gravity slides (e.g. Choudhuri et. al. 2011). High subsidence rate which ranged from 130 to >250 m Ma-1 at South Wales during the Namurian and the Westphalian age (Burgess & Gayer 2000) had high potential to cause the growth faults in the shale-dominant and coal-bearing Lower & Middle Coal Measures.

2.2.2. Summary of relative age relationship of the deformation structures

Syn-sedimentary cross faults and growth faults are the oldest structures in the basin. Most of them are recognised in the Lower & Middle Coal Measures (Westphalian A to early Westphalian C). On the other hand, no evidence is recognised for thrusting during deposition of the Coal Measures and the major phase of compressive deformation is interpreted as late Westphalian D at the earliest (Cole et. al. 1991; Jones 1991). However, Jones 1989 indicates minor deformation of early folding had begun from Westphalian A onwards. The compressional deformation phase, therefore, should be divided into two: local or minor compression from Westphalian A and main compression from Westphalian D. Gayer et al. 1973; Jones 1991 report the cross faults were also active during the main compression deformation because of offset of major fold axes (e.g. Maesteg anticline, Abercynon syncline) along the cross faults and the variation of intensity and style of folding across the faults.

In addition to the Silesian deformation, later reactivation on E-W and NW-SE striking faults were reported by seismic reflection studies in Bristol Channel area (e.g. Brooks & James 1975; Brooks et. al. 1988). The reactivation in extension of the Variscan thrust is interpreted as early Cretaceous (e.g. Brooks & James 1975; Brooks et. al. 1988).

2.3. Pressure and temperature history for the basin subsidence and the relation to the Variscan compression deformation

Physical conditions associated with the basin subsidence are partly constrained by combining results of other researchers. White (1991) and Bevins et al. (1996) provided maximum achieving temperature from volatile matter and vitrinite reflectance. Alderton & Bevins (1996) suggested geothermal gradients of the basin by analysing fluid inclusions. In this section P-T (pressure and temperature) paths during the basin subsidence and the Variscan compression are roughly estimated from their results. This estimation is not very precise but it can help understanding the relationship among sedimentation, deformation and thermal events of the study area.

2.3.1. Maximum achieving temperatures of the basin

White (1991) provided maximum achieving temperature of the basin from volatile matters of major coal seams. Volatile matter is products given off as gas or vapour from a coal specimen and the amount of them can be an indicator of maximum achieving temperature where the specimen experienced. White (1991) collected more than 15,500 data of volatile matter from over 500 sites and estimates vertical and lateral distributions of the maximum achieving temperature of the coal seams in the basin. The coals in South Wales are classified based on the maximum achieving temperature and the coal ranks increase bituminous coal in the South and East crops to anthracite in the North Crop and the Pembrokeshire subbasin (Robinson et. al. 1980; Waters & Davies 2006). Bevins et al. (1996) combined the data of White (1991) with their results of studies of illite crystallinity and vitrinite reflectance and concluded that maximum achieving temperature in anthracite zone is in a range of 200-250 ºC. The range is shown by [X] in Figure 2.3 as the maximum achieving temperature in the study area.

2.3.2. Timing of burial and thermal events and the Variscan compression

With the huge number of data, White (1991) revealed that layers of equal volatile matter (isovols) are folded and that the main compressional deformation was induced after the event of maximum achieving temperature. Bevins et al. (1996) also noted that the isovals broadly intersect with geological strata at angles of 2-3.5 degrees and thus minor folding initiated before the event of maximum achieving temperature. These

observations and implications are concordant with the results of field studies of Cole et al. (1991) and Jones (1991) (section 2.2). They concluded that there was minor folding during sedimentation (before maximum burial) and that major folding took placed after the sedimentation (after maximum burial). This similarity of timing between sedimentation and thermal events compared with the folding suggests these two events of maximum burial and temperature occurred simultaneously and have same meaning in this basin. Both the structural and the thermal studies show minor folding was initiated before the event of maximum burial (or maximum achieving temperature) and that main compression deformation related with the Variscan Orogeny was induced after the sedimentation.

2.3.3. P-T conditions during basin subsidence

Alderton & Bevins (1996) estimated P-T conditions from fluid inclusions trapped in quartz minerals which grew in cavities of siderite nodules in the Lower to Middle Coal Measures. Although the specimens of their study are from not anthracite but low volatile bituminous coal in the Wyndham Colliery which lies near the centre of the coalfield, they provide both pressure and temperature values of the pore-fluid in the basin. Their results show that the pore-fluid was under 130-160 ºC and 40-55 MPa when the quartz formed.

Alderton & Bevins (1996) stated that the cavities in siderite nodules were also filled with carbonates and sulphides. Based on the petrographic characteristics, they interpreted that the carbonates were firstly formed and the quartz were lastly formed. It is generally agreed that carbonate nodules initially form in the top few metres of unconsolidated sediments and possible continue to grow at a depth of several hundred meters as maximum (e.g. Raiswell 1971; Curtis et. al. 1986). It is also known that carbonate minerals are dissolved at shallow depth by pedogenic or meteoric water which is commonly undersaturated with respect to $CaCO_3$ (e.g. Moore & Wade 2013). Since no major unconformity is recognised in the Coal Measures, the siderite nodules and cavities were probably formed at the shallow depth during the earliest stage of their burial. Hence, the minerals within the cavities (carbonates, sulphides and quartz) most likely record the first physical conditions which allowed those minerals to grow and fill the cavities in the burial history. Although it is impossible to estimate precise timing of

the quartz mineralization, Alderton & Bevins (1996) noted that the majority of evidence, such as morphology of the quartz, chemical components of the sulphides and presence of methane-rich fluid as the inclusions, tends to favour a burial-related mineralization of the quartz.

It is, therefore, assumed that the results of Alderton & Bevins (1996) show the first physical conditions for quartz growth during the burial. The range is shown by [Y] in Figure 2.3. It should be noted that the P-T conditions of Alderton & Bevins (1996) represent not rock pressure but pore-fluid pressure and temperature. Pressure exerted on rocks is generally higher than fluid pressure in sedimentary basins although the ratio between the two varies depending on the geological setting.

2.3.4. P-T path for the basin subsidence and the relation to the Variscan compression

By using the results of White (1991), Bevins et al. (1996) and Alderton & Bevins (1996), P-T path of pore-fluid are estimated (Figure 2.3). Most part of the P-T path is a projection from the thermal gradient of [Y]. Clockwise rotation of the P-T path is assumed. This is because pressure directly changes with depth in relation with burial and exhumation while temperature does not change immediately. Temperature change in the ground is controlled by heat conduction, heat convection and decay of radioactive elements. Radioactive decay heat is not related with depth change. Fluid-related heat convection is not very effective in shale-dominant sequences, especially in vertical direction. Heat conduction, hence, should be the main process of heat transfer regarding depth change in the Lower Coal Measures. Heat conduction requires some geological time to achieve steady-state in relation with depth change. High sedimentation rate (130-250 m Ma^{-1}) of this basin (Kelling 1988; Burgess & Gayer 2000) is preferable to encourage the time gap between pressure and temperature changes, supporting the assumption of clockwise rotation of the P-T path in the study area.

[Z] is intersection between the projected P-T path from [Y] and maximum achieving temperature of [X]. The range roughly indicates fluid pressure and temperature at the time of maximum burial of the basin. The conversion point from burial to exhumation also represents the P-T conditions for the initiation of main thrusting and folding caused by Variscan Orogeny in the study area. Note that this

estimation of the P-T conditions includes following assumptions without direct evidence.

- The quartz in siderite nodules was formed during basin burial and the associated fluid inclusions preserved pore-fluid pressure and temperature for basin burial (section 2.2.3.3).
- Pressure/temperature gradient of pore-fluid in anthracite at Pembrokeshire subbasin and low volatile bituminous coal in the Wyndham Colliery was similar to each other during the basin burial (section 2.2.3.3).
- The Silesian South Wales basin experienced clockwise rotation.of the P-T path in their burial and exhumation history (section 2.2.3.4).

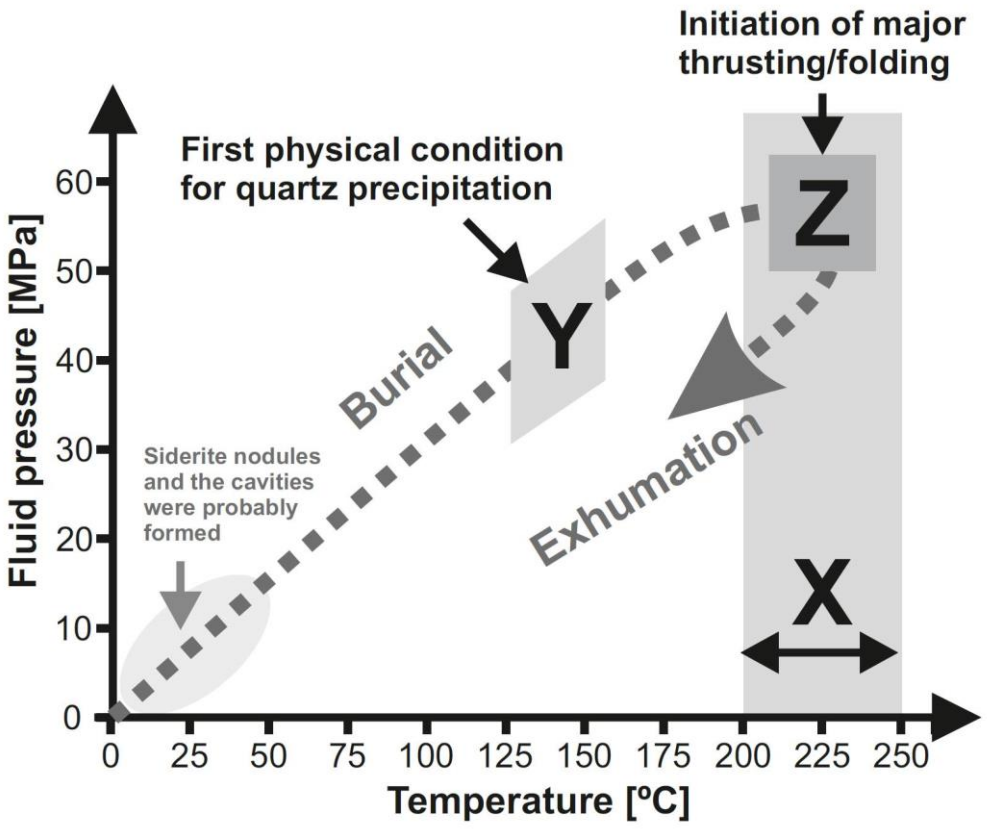

Figure 2.3 Possible P-T path of pore-fluid during the basin subsidence. [X] is maximum achieving temperature in anthracite zone (White 1991; Bevins et al. 1996). [Y] is pressure and temperature conditions at the time of quartz precipitation in siderite nodules (Alderton & Bevins 1996). [Z] is intersection between maximum achieving temperature [X] and projected P-T paths from [Y], which represents P-T conditions for initiation of the main Variscan compression in the study area.

2.4. Brief review of layer-controlled fracturing

Development of extension fractures or open-mode fractures in layered materials have been studied by many researchers. Studies focusing on the relationship between fracture space and layer thickness are the most common. Cox (1952) and Hobbs (1967) offered the first two major studies in the research field to explain fracture space in layered materials and they provided the base of analytical solutions for extension fracture development.

Based on the assumption of friction coupling between adjacent layers and the fractured layer, Kelly and Tyson (1965) and Price (1966) presented concept of "fracture saturation" which controls maximum fracture density in the fractured layer. Wu and Pollard (1995) experimentally confirmed this concept. Bai and Pollard (2000) demonstrated the existence of a critical spacing to layer thickness ratio for fracture development. Bai et al. (2000) also provide results of finite element simulation which shows the local stress distribution within fractured layer and address the relationship between fracture saturation and layer thickness. In contrast to these models based on assumption of frictional coupling or full-slip, Schöpfer et al. (2011) studied impact of interfacial friction coefficients on the relationship between the fracture saturation and layer thickness.

There are huge number of researches related with layer-controlled open-ode fractures. However, all those studies assume remote tensile stress for the open fracture formation. On the other hand, Bourne (2003) is probably the first paper that provides the analytical solutions of fracture opening in the fractured layer under a remote compressive stress field. This thesis follows the concept of Bourne Model in chapter 6 and simplified version of the model was built to analytically examine the possibility of extension fracture formation in relation with the geological history in the study area.

Reference

Archer, A.A. 1968. The Upper Carboniferous and later formations of the Gwendraeth Valley and adjoining areas. Geology of the South Wales coalfield, Special Memoir. Memoirs of the Geological Survey of UK. HMSO, London.

Alderton, D.H.M. & Bevins, R.E. 1996. P-T in the South Wales Coalfield: evidence for coexisting hydrocarbon and aqueous fluid inclusions. Journal of the Geological Society, London, 153, 265-275.

Bai, T., Pollard, D.D. 2000. Fracture spacing in layered rocks: a new explanation based on the stress transition. Journal of Structural Geology, l 22, 43-57

Bai, T., Pollard, D.D., Gao, H. 2000. Explanation for fracture spacing in layered materials. Nature, 403, 753-756

Bevins, R.E., White S.C. & Robinson, D. 1996. The South Wales Coalfield: low grade metamorphism in a foreland basin setting? Geological Magazine, 133, 739-749.

Bluck, B.J. & Kelling, G. 1963. Channels from the Upper Carboniferous Coal Measures of South Wales. Sedimentology, 2, 29-53.

Bourne, S.J., 2003. Contrast of elastic properties between rock layers as a mechanism for the initiation and orientation of tensile failure under uniform remote compression, Journal of Geophysical Research, 108 (B8), 2395.

Brooks, M. & James, D.G. 1975. The geological results of seismic refraction surveys in the Bristol Channel, 1970-73. Journal of the Geological Society, London, 131, 163-182.

Brooks, M., Trayner, P.M. & Trimble, T.J. 1988. Mesozoic reactivation of Variscan thrusting in the Bristol Channel area, UK. Journal of the Geological Society, London, 145, 439-444.

Burgess, P.M. & Gayer, R.A. 2000. Late Carboniferous tectonic subsidence in South Wales: implications for Variscan basin evolution and tectonic history in SW Britain. Journal of the Geological Society, London 157, 93-104.

Choudhuri, M., Guha, D., Dutta, A., Sinha, S. & Sinha, N. 2011. Spatiotemporal variations and kinematics of shale mobility in the Krishna-Godavari Basin, India. In: Wood, L.J. (ed) Shale Tectonics, AAPG Memoir, 93, 91-109

Cole, J.E., Miliorizos, M., Frodsham, K., Gayer, R. A., Gillespie, P.A., Hartley, A.J. & White, S.C. 1991. Variscan structures in the opencast coal sites of the South Wales Coalfield. Proceedings of the Ussher Society, 7, 375-379.

Cox, H. L. 1952. The elasticity and strength of paper and other fiberous materials, British Journal of Applied Physics, 3, 72-79.

Curtis, C.D., Coleman, M.L. & Love, L.G. 1986. Pore water evolution during desiment burial from isotopic and mineral chemistry of calcite, dolomite and siderite concretions, Geochimica et Cosmochimica Acta, 50, 2321-2334

Frodsham, K., Gayer, R.A., James, J.E. & Pryce, R. 1993. Variscan thrust deformation in the South Wales Coalfield: a case study from Ffos Las opencast coal site. In: Gayer, R.A., Greiling, R.O. & Vogel, A.K. (eds) Rhenohercynian and Subvariscan Fold Belts. Earth Evolution Series, Vieweg, Braunschweig, 315-348.

Frodsham, K. & Gayer, R.A. 1997. Variscan compressional structures within the main productive coal-bearing strata of South Wales. Journal of the Geological Society, London, 154, 195-208.

Gayer, R.A., Allen, K.C., Bassett, M.G. & Edwards, D. 1973. The structure of the Taff Gorge area, Glamorgan, and the stratigraphy of the Old Red Sandstone-Carboniferous Limestone transition. Geological Journal, 8, 345-374.

Gayer, R.A. & Pesek, J. 1992. Cannibalisation of Coal Measures in the South Wales Coalfield—significance for foreland basin evolution. Proceedings of the Ussher Society, 8, 44-49.

George, T.N. 1970. British Regional Geology: South Wales (3rd edition), H. M. S. O. London

George, G.T. & Kelling, G. 1982. Stratigraphy and sedimentation of Upper Carboniferous sequences in the coalfield of south-west Dyfed. In: Bassett, M.G. (ed) Geological excursions in Dyfed, south-west Wales. National Museum of Wales, Cardiff, 175-202.

Hancock P.L., Dunne W.M. & Tringham M.E.1983. Variscan deformation in south-west Wales. In: Hancock P.L. (ed) The Variscan Fold Belt in the British isles. Adam Hilger. Bristol. 47-73.

Hartley, A.J. 1993. Silesian sedimentation in South-West Britain: Sedimentary Responses to the Developing Variscan Orogeny. In: Gayer, R.A., Greiling, R.O. & Vogel, A.K. (eds) Rhenohercynian and Subvariscan Fold Belts. Earth Evolution Series, Vieweg, Braunschweig, 159-196.

Hobbs, D. W. 1967. The formation of tension joints in sedimentary rocks: An explanation, Geological Magazine, 104, 550-556.

Jones, J.A. 1989. The influence of contemporaneous tectonic activity on Westphalian sedimentation in the South Wales Coalfield. In: Arthurton, R.S., Gutteridge, P. & Nolan, S.C. (eds) The role of tectonics in Devonian and Carboniferous sedimentation in the British Isles. Occasional Publications of the Yorkshire Geological Society, 6, 243-253.

Jones, J.A. 1991. A mountain front model for the Variscan deformation of the South Wales coalfield. Journal of the Geological Society, London, 148, 881-892.

Kelling, G. 1974. Upper Carboniferous sedimentation in South Wales. In: OWEN, T.R. (ed.) The Upper Palaeozoic and Post-Palaeozoic Rocks of Wales. University of Wales Press, Cardiff, 185-224.

Kelling, G. 1988. Silesian sedimentation and tectonics in the South Wales Basin: a brief review. In: Besly, B. & Kelling, G. (eds) Sedimentation in a synorogenic Basin Complex: The Upper Carboniferous of Northwest Europe. Blackie, Glasgow and London, 38-42.

Kelly, A., Tyson, W.R. 1965. Tensile properties of fiber-reinforced metals: copper/tungsten and copper/molybdenum. Journal of the Mechanics and Physics of Solids, 13, 329-350.

Leveridge, B.E. & Hartley, A.J. 2006. The Variscan Orogeny: the development and deformation of Devonian/Carboniferous basins in SW England and South Wales. In: Brenchley, P.J., Rawson, P.F. (eds) The geology of England and Wales. Geological Society of London, London, 225-255.

Moore, C.H. & Wade, W.J. 2013. Meteoric diagenetic environment. In: van Loon A.J. (ed) Carbonate reservoirs: porosity and diagenesis in a sequence stratigraphic framework, second edition, Elsevier, Oxford, 165-206.

Owen, T.R. 1953. The structure of the Neath disturbance between Bryniau Gleision and Glynneath, South Wales. Quarterly Journal of the Geological Society, London. 109, 333-365.

Price, N.J. 1966. Fault and joint development in brittle and semi-brittle rocks. Pergamon Press, Oxford

Raiswell, R. 1971. The growth of Cambrian and Liassic concretions. Sedimentology, 17, 147-171.

Robinson, D., Nicholls, R.A. & Thomas, L.J. 1980. Clay mineral evidence for low-grade Caledonian and Variscan metamorphism in south-western Dyfed, South Wales. Mineralogical Magazine, 43, 857-863.

Schöpfer, M.P.J., Arslan, A., Walsh, J.J., Childs, C. 2011. Reconciliation of contrasting theories for fracture spacing in layered rocks. Journal of Structural Geology, 33, 551-565.

Trotter, F.M. 1947. The Structure of the Coal Measures in the Pontardawe-Ammanford area. South Wales. Quarterly Journal of the Geological Society, London. 103, 89-133.

Waters, C.N. & Davies, S.J. 2006. Carboniferous: extensional basins, advancing deltas and coal swamps. In: Brenchley, P.J. & Rawson, P.F. (eds) The Geology of England and Wales. Geological Society of London, London, 173-223.

White, S.C. 1991. Palaeo-geothermal profiling across the South Wales Coalfield. Proceedings of the Ussher Society, 7, 368-374.

Woodland, A.W. & Evans, W.B. 1964. The geology of the South Wales coalfield, part IV. The country around Pontypridd and Maesteg (3rd edition). Memoirs of the Geological Survey England and Wales

Wu, H, Pollard, D.D. 1995. An experimental study of the relationship between joint spacing and layer thickness, Journal of Structural Geology, 17, 887-905.

Chapter 3: Methodology

3.1. Selection of the study area

The South Wales coalfield was selected for the study area. Primary reason of the selection is that the area is one of the most well studied onshore sedimentary basins of geological information (e.g. sedimentary history, deformation history, temperature and pressure condition of basin burial, and rock mechanical properties) in UK. It allows us to obtain relatively rigid geological background and physical conditions associated with the layer-scale fracture formation which I focused on this project. The second reason is outcrops are large and continuously exposed along structural dip direction of the basin. Since fieldwork was planned as main methodology to collect structural data in this project, condition of outcrop exposures was an essential factor. The third reason is the layer-scale fractures were well developed in the geological formations of this basin.

The South Wales coalfield is rich in coal deposit, and was originally developed by the coal industry. As of the background, a large number of rock samples including not only outcrop exposures but also subsurface rocks have been available. They were analysed and interpreted from various geological perspectives for both academic research purposes and practical purposes (e.g. Price 1958, Price 1960; Price 1963; White 1991; Bevins et al. 1996; Burgess & Gayer 2000). The results provide relatively detailed geological information throughout the basin. For instance, more than 15,500 volatile matter data and 166 samples for vitrinite reflectance data were analysed in both surface and subsurface formations to constrain thermal history of the basin. The data provide three dimensional distribution of thermal layers which show different level of heating event (e.g. White 1991; Bevins et al. 1996).

The well-studied geology makes it easier to integrate fracture data measured in this project with the associated geological events, and would enable us to examine timing, physical conditions and mechanisms of the fracture formation. In addition, rock mechanical properties (Young's moduli, Poisson's ratios) were measured in the South Wales coalfield and some of them were published (e.g. Price 1958; Price 1960; Price 1963). This also gives more appropriate and reasonable input parameters for analytical and numerical modelling which were tested in the later parts of this project. From those circumstances, the South Wales coalfield is one of the suitable basins to do structural

analyses with newly collected fracture data in outcrops, and to connect the field data with the associated physical conditions and geological event.

Eastern coast of Pembrokeshire was selected for the field data collection. Large cliffs with several meter height are intermittently continued here along the coastal line (NNE-SSW direction), which is sub-parallel to the main dip direction of beddings and deformation structures in the basin (Figure 3.1, Figure 3.2). The rocks are also widely exposed on the ground in a direction perpendicular to the coastal line during low tide as the Bristol Channel has the second highest tidal range in the world (over 10 meters at some locations). Layer-scale fractures are common in alternating sand-shale layers in the Silesian sediments (the Westphalian Lower to Middle Coal Measures and the Namurian sediments).

The layer-scale fractures were mainly measured at sites where upper surfaces of sandstone and/or shale layers are exposed. This is because some structural data (e.g. fracture spacing along two or more scan-lines, vein aspect ratio) focused in the current study required exposures of not only one cross-section surface of the layer but also another cross-section and/or a surface on the layer boundary. The site selection were, therefore, controlled by exposure condition of outcrops in some degree. In general, lateral exposure of layers is relatively limited in the southern area because the formations were strongly deformed by the Variscan compression. It is more difficult to collect fracture data, especially along NNE-SSW direction in the south. On the other hand, outcrops are more suitably preserved for data collection in the northern area where the compression deformation was gently. Although the sites were selected to cover a range from the southern to northern ends of the basin, relatively large number of fractures were measured in the northern area, especially from Saundersfoot to Amroth because of exposure conditions of the rocks.

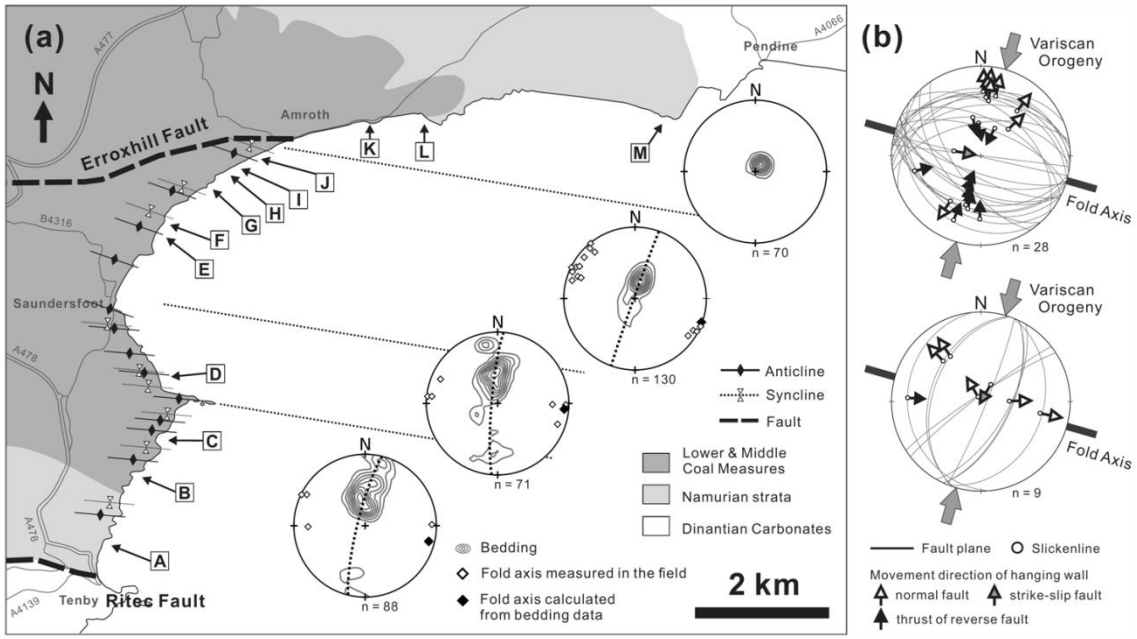

Figure 3.1 **(a)** Geological map of the study area with bedding data. Beddings dominantly dip to south-southwest or north-northeast. Stereonets show contour map of poles to beddings. The number of data is shown at the bottom of the stereonets. Fold axis measured in the field (outcrop-scale fold) and fold axis calculated from the beddings (map-scale fold) are also denoted by white and black markers, respectively. Dashed line indicates best-fit girdle of the beddings. Since the folds are asymmetric, beds dipping to the south are dominant. Capital letters on the map indicate sites where layer-scale fractures were measured. **(b)** Faults measured in the field. Faults dipping to south-southwest or north-northeast are relatively dominant. Faults striking sub-parallel to the fold axis (dipping to NNE or SSW) are plotted on the upper stereonet and faults striking sub-perpendicular to the fold axis (dipping to WNW or ESE) are plotted on the lower. Fault planes are denoted by great circles. Slickenlines are denoted by small white circles. Where the sense of shear could be determined in the field, movement direction of the hanging wall block is indicated by arrows. The shear sense was determined by slickenstep, drag or displacement of surrounding markers (e.g. bedding fabric), and/or geometry of secondary fracture development around the fault. Colour of the arrows is separated based on the shear sense.

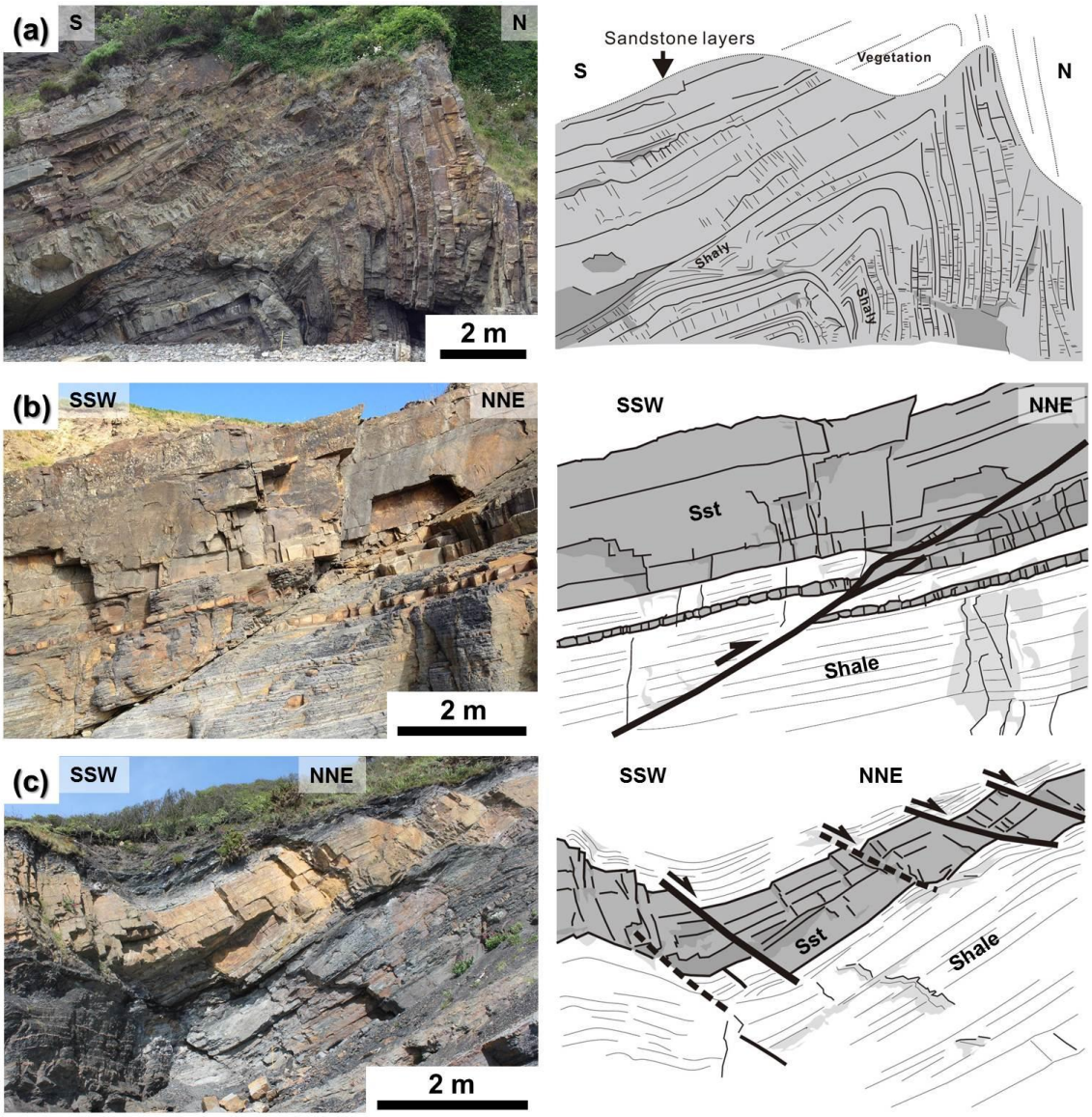

Figure 3.2 Photographs and sketches of deformation structures observed in the study area. **(a)** A chevron fold exposed at around site D. The beds are mostly composed of sandstone with thin shale layers. The compression deformation was locally concentrated in the incompetent shale layers. Layer-scale fractures were formed at both the northern and the southern limbs. **(b)** A thrust dipping to SSW at site I. Offset of sandstone beds indicates approximately one metre displacement along the fault. Extension fractures are relatively well developed in the thinner sandstone layer. **(c)** North-dipping normal faults exposed at site G. They mainly cut sandstone layers and mostly become arrested in shale layers.

3.2. Fracture measurements in the field

3.2.1. Sampling plan

Layer-scale fractures are common in both sandstone and shale layers (Figure 3.3). Majority of the fractures in sandstones become arrested at contact with top and bottom boundaries of the layers. The fractures are generally developed in two or three directions in both the sandstone and shale layers. The patterns vary among the sandstones and shale. The patterns also slightly vary among sites. This is probably due to mechanical properties' variation between rock types (sandstone, limestone and shale) and/or stress field variation in sites. In addition, even in a same rock type and same locality, fracture frequency (fracture density) is different in relation with layer thickness.

In order to investigate those variations, fractures were planned to be measured in 13 different sites to cover the area from the southern end to northern end of the basin (Figure 3.1). In these sites, intensity of the Variscan compression deformation is variable depending on the distance from the Variscan Orogenic Front. Ritec Fault which is the southern boundary fault of the basin can be treated as the Orogenic Front. Effects of rock types and layer thickness on the fracture patterns and fracture intensity were examined at relatively large exposures (e.g. site G & I) where the fractures were measured in 2 or more sandstone layers and shale. Since shale is dominant facies and sandstones with different thickness are commonly observed within the thick shale, sandstones are relatively suitable to examine the relationship between layer thickness and fracture intensity. Consequently, fracture data were measured within 36 layers (25 sandstones; 1 limestone; 10 shales) at 13 sites which are summarized in Table 3.1.

As site name, alphabet "A" was assigned to the southernmost location where the Variscan deformation is the strongest and other alphabets were assigned toward the north in a sequential order (Figure 3.1). 50-200 fractures were measured in each layer. Because fractures are generally less in shale layer, number of measured data is slightly less in shale. As bedding is steeply inclined and folded by the Variscan Orogeny in the southernmost area, measurable fractures are limited, especially in thick sandstone and shale. Number of data is slightly less in the southernmost area. Majority of fracture data was collected at site E-I where beddings are gently inclined and folded (Table 3.1).

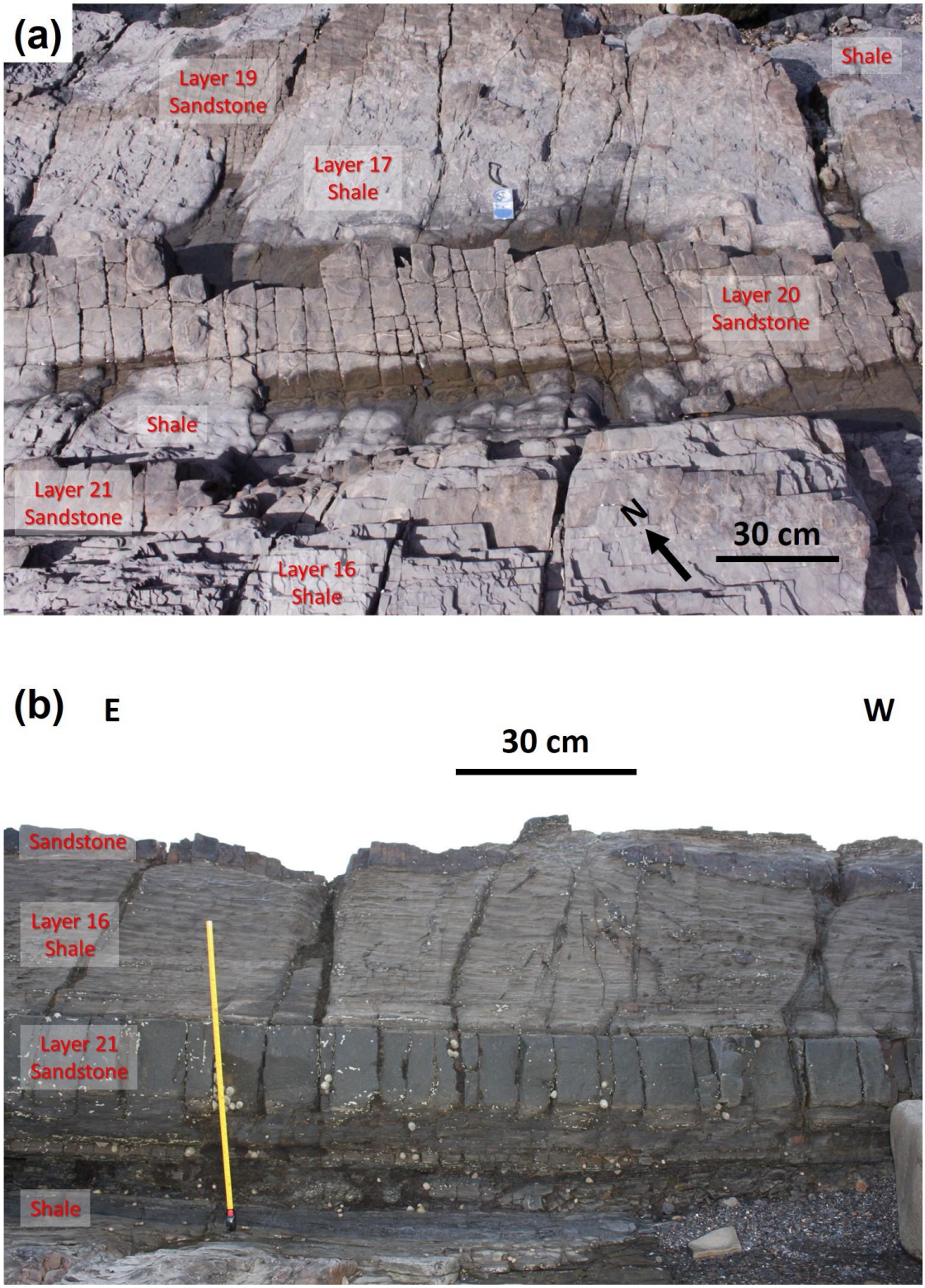

Figure 3.3 Photographs at site G. **(a)** Plane view of layer-scale fractures formed in sandstone and shale layers. Fractures in shale layers strike NE-SW, and ones in sandstones strike NNE- SSW. Layer number is linked to table 3.1. **(b)** Section view. Most fractures in sandstones are arrested at the border with shale.

Table 3.1 Summary of fracture and vein data measured in the field. Each site is shown with distance from the Variscan Orogenic Front which is assumed as Ritec Faults in Figure 3.1. Compression strain by map-scale folds are from Chapter 4. Fractures were measured in several sandstones when outcrops are large enough.

Site	Distance from VOF	Strain by folds	Layer	Lithology	Thick-ness	Bedding plane	Scan line 1				Scan line 2				Scan line 3				Others		Vein aspect ratio
							Direction	Length	Number of data		Direction	Length	Number of data		Direction	Length	Number of data		Number of data		
									Fracture	Vein			Fracture	Vein			Fracture	Vein	Fracture	Vein	
M	8.0km	0%	36	sandstone	37cm	199, 11	115	9.62m	17	25	204	9.42m	0	33							
L	7.4km		35	sandstone	190cm	226, 15	304	19.78m	34	36	204	57.37m	14	28						119	○
			34	shale	520cm	240, 20	303	14.78m	35	0									8		
K	7.2km		33	sandstone	137cm	219,07	295	36.99m	21	57	206	33.15m	23	28							
			32	shale	145cm	233,10	277	16.53m	50	0	212	6.98m	18	0							
J	6.4km	7%	31	limestone	72cm	295,06	021	12.68m	54	0	277	7.60m	63	20							
			30	shale	119cm	359,15	069	23.10m	46	0	082	29.10m	37	0					2		
I	6.2km		29	sandstone	13cm	202,25	116	2.20m	65	0	205	5.29m	61	1							
			28	sandstone	23cm	200,25	118	2.42m	39	19	206	6.21m	49	8							
			27	sandstone		188,13														97	○
			26	shale	91cm	195,23	190	2.40m	22	0	121	4.04m	52	0					4		
H	6.1km		25	sandstone	23cm	209,17	322	5.11m	47	70	035	9.07m	42	0	025	1.39m	0	40		70	○
			24	sandstone	61cm	196,10	152	10.24m	0	72	257	22.17m	46	1						59	○
			23	sandstone	18cm	220,37	302	3.42m	45	0											
			22	shale	295cm	186,20	101	57.99m	69	0											
G	5.9km		21	sandstone	26cm	210,21	295	6.77m	72	0	206	5.17m	43	91							
			20	sandstone	12cm	202,23	113	3.83m	52	24	183	1.82m	23	60	195	3.06m	40	0			
			19	sandstone	4cm	204,23	121	3.21m	79	0	185	3.05m	84	0							
			18	sandstone	6cm	204,26	121	5.34m	69	0	185	4.94m	56	3							
			17	shale	11cm	196,29	123	2.79m	83	0	177	4.90m	77	0							
			16	shale	52cm	204,10	115	6.98m	25	0	205	4.94m	15	0							
F	5.3km		15	sandstone	63cm	048,26	125	15.77m	4	76										116	○
E	5.1km		14	sandstone	19cm	141,13	233	7.51m	62	10	083	11.97m	66	7							
			13	sandstone	17cm	174,16	097	3.35m	81	0	167	0.75m	5	0	063	0.91m	5	0	10		
			12	sandstone	14cm	084,14	126	8.15m	62	13	013	7.48m	24	32						28	○
			11	sandstone	11cm	114,14	063	5.95m	44	20	124	4.07m	44	3	029	1.90m	6	8			
			10	sandstone	11cm	159,15	251	2.94m	40	24	089	1.52m	25	8	210	2.46m	25	10		1	
			9	sandstone	38cm	133,12	123	6.56m	5	26	046	5.89m	9	26	184	4.47m	15	8	10	28	○
			8	shale	65cm	175,11	084	25.05m	63	0											
D	3.1km	21%	7	sandstone	36cm	060,13	115	9.49m	40	11	005	7.60m	32	3						3	○
			6	shale	>1000m	174,23	106	10.47m	31	0	077	17.38m	37	0							
C	2.1km	40%	5	sandstone	27cm	150,21	079	8.59m	34	25										8	○
			4	sandstone	47cm	171,27	094	10.28m	22	32	046	2.99m	5	0					5		
			3	shale	880m	163,45	075	30.04m	29	0									39		
B	1.5km		2	sandstone	27cm	225,11	125	9.38m	29	36	035	11.89m	4	49							
A	0.4km		1	sandstone	11cm	182,06	099	6.20m	40	3	201	3.60m	8	28						5	

3.2.2. Sampling methods

Most fractures were measured along a scan-line to quantify fracture density (Figure 3.4). Fracture orientation (dip direction, dip), fracture spacing, and fracture aperture size were measured. All fractures which traverse the scan-line were measured regardless of the fracture orientation. Tape measure was set along the scan-line to obtain apparent distance (space) from a fracture to the nexte. Some fractures in sandstone and limestone layers are filled with minerals. They were separated from open fractures and grouped as mineral veins (Table 3.1). In contrast to common development of the mineral veins in the stiff layers (sandstones and a limestone), no mineral vein was found in shale.

Apertures size of open fractures and thickness of mineral veins were measured by using a feeler gauge (Figure 3.5). The tool has a number of thin blades with different thicknesses. By inserting a blade or combination of some blades into fracture aperture at cross point between the fracture and the scan-line, aperture size was measured in a range from 0.05 millimetres (thinnest blade size) to centimetre-scale. Vein thickness was also measured by putting the blades on the vein and visually comparing the blade thickness and the vein thickness at the cross point. Because aperture size was generally less than 0.05 millimetres or nil in shale, aperture size was not measured along some fractures in shale.

Since fractures developed in two or more orientations, the data were normally acquired along two or more scan-lines for each layer. If exposure of top surface of the layer is limited, fracture data were collected only limited directions (in this case fractures were measured along only one scan-line). Direction, length, and number of measured fractures for each scan-line are summarized in Table 3.1. Sum of scan-line 1, scan-line 2, scan-line 3, and others in Table 3.1 were total number of measured fractures and veins for each layer. All raw data for each layer are not illustrated in detail in the body text but they are summarized in Appendix (scan-line information, fracture orientation, fracture density, fracture aperture size, and vein aspect ratio).

Vein aspect ratio (length/thickness of a vein on top or bottom surfaces of the layer) was also measured in some sandstone layers to calculate fluid overpressure at the time of vein formation. The data and calculation method are indicated in detail in Chapter 5.

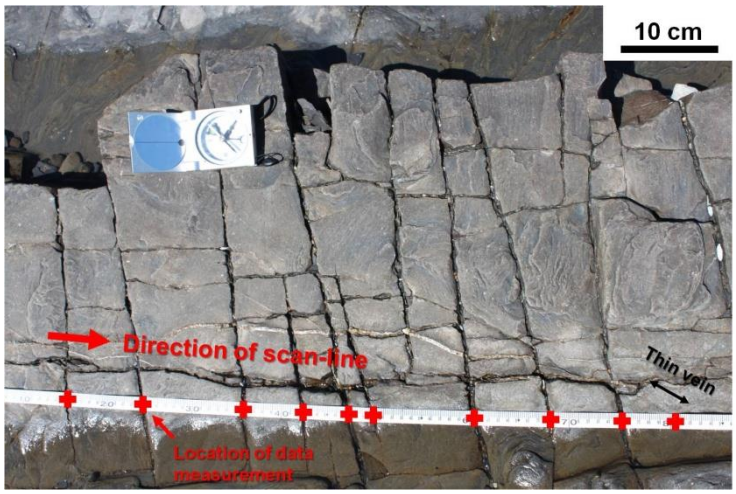

Figure 3.4 Fractures measured along a scan-line. All fractures and veins traversing the tape measure were analysed.

Figure 3.5 Feeler gauge. The blades have different thickness from 0.05 to 1.00 mm.

3.2.3. Fracture plot in stereonet and rose diagram

Fracture orientation (dip direction, dip) is plotted in lower hemisphere of Schmidt net. The reason of selecting the Schmidt net is that projected area is not strained and data concentration are more precisely illustrated. As 50-100 fracture data are generally plotted together in this thesis to investigate fracture patterns, Schmidt net is more appropriate to understand the data distribution. Fracture strike is also plotted in an area-normalized rose diagram to add support information of data concentration. Since normal or length-scaled rose diagram gives rather strong visual impression of data concentration, which easily cause bias (e.g. if twice number of fractures occur in a

direction, the area illustrated in the length-normalized rose diagram becomes 4 times), area-normalized rose diagram is used in this thesis.

All fracture data are plotted as poles to fracture planes in Schmidt net (Figure 3.6). Great circles of individual fractures are generally not shown in this thesis to avoid complicated visualization, except in Appendix (Great circles of individual fractures are illustrated with light grey colour to display all raw data measured in the field in Appendix). Only representative fractures are shown by great circle with black colour. The orientation of representative fractures is calculated by averaging all fractures in a same fracture set. Bedding plane of the layer is also plotted together as great circle with grey colour to check geometrical relationship between the fractures and the bedding.

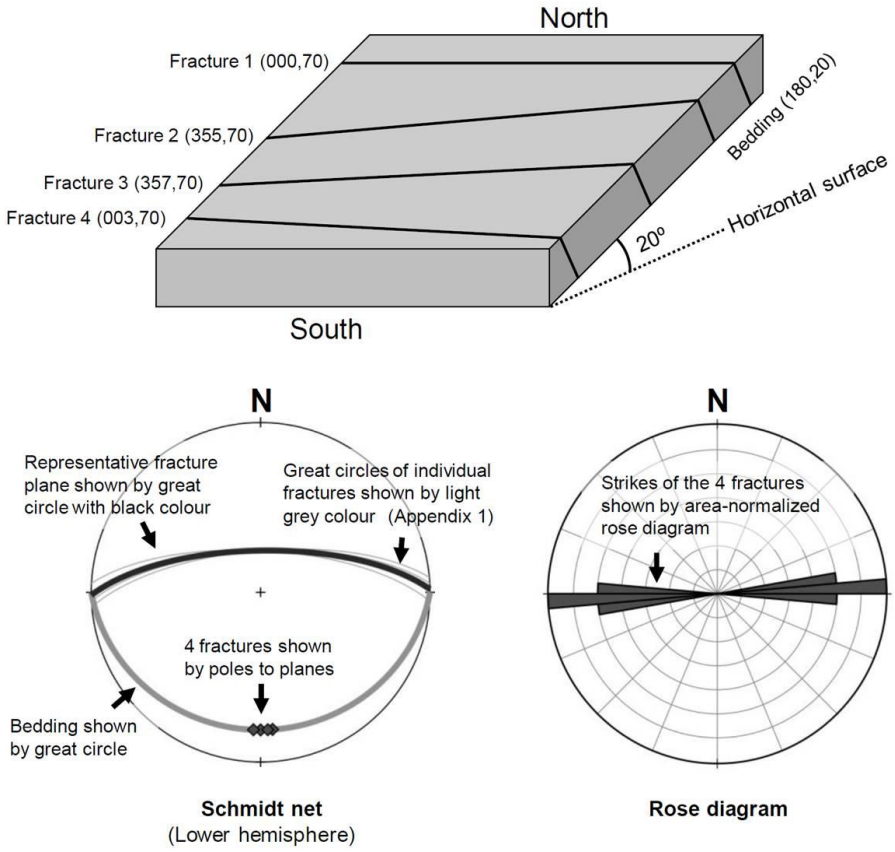

Figure 3.6 An example of fracture plot. 4 fractures in a layer dipping to south at 20 degrees (upper figure) are plotted in Schmidt net (lower left) and area-normalized rose diagram (lower right).

3.2.4. Fracture set identification

Fracture sets are identified based on data concentration of the fracture planes. The fractures are generally separated in two or three orientations based on data plot in stereonet and rose diagram (Figure 3.7). Set number is assigned sequentially from north to clockwise direction. Fractures and veins are separately treated.

In the case of Figure 3.7, set 1 and set 2 would be a conjugate set of shear or hybrid (shear + extension) fractures. However, shear displacement along individual fractures are generally too small to identify in the field. No direct evidence was found in most cases. Therefo

re, fracture set is simply identified in association with data concentration.

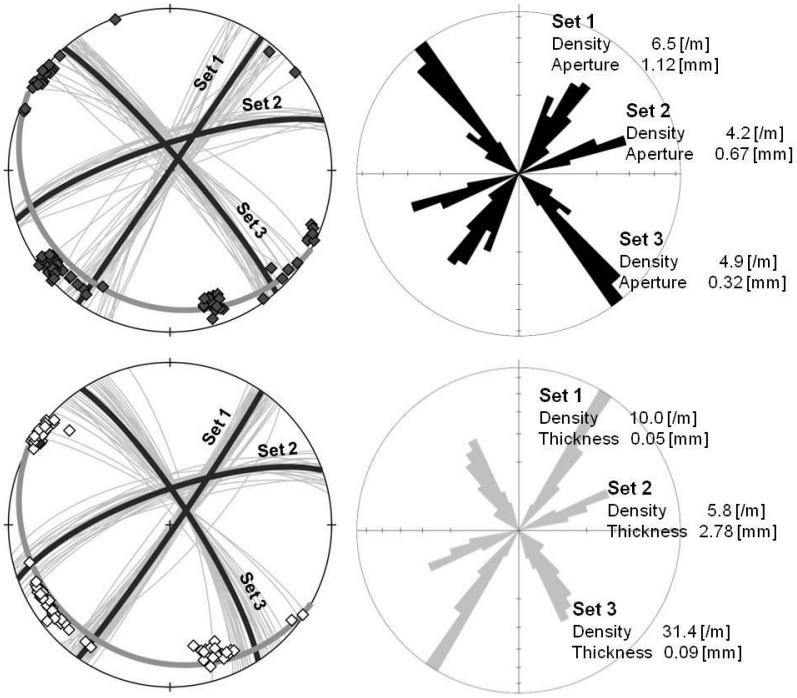

Figure 3.7 Fracture sets and vein sets in layer 25.

3.2.5. Fracture density

Fracture density is calculated for individual fracture set (Appendix). Simple calculation dividing number of fractures by scan-line length is used as raw fracture density.

$$Raw\ density = \frac{number\ of\ fractures\ of\ a\ set}{length\ of\ the\ scanline} \quad (1)$$

A correction factor is also calculated for each fracture to remove the effect of geometrical relationship between the fractures and the scan-line (Tarzaghi 1965). *Q* is defined as angle between a scan-line and pole to a fracture (Figure 3.8), and *cosQ* is defined as the correction factor. Sum of the correction factors of all fractures in a set along the scan-line is used as corrected fracture density.

$$Correction\ factor = \frac{1}{cosQ} \quad (2)$$

$$Corrected\ density = \frac{sum\ of\ correction\ factors\ of\ all\ fractures\ in\ a\ set}{length\ of\ the\ scanline} \quad (3)$$

Calculation of *cosQ*

Geometry of lineations is generally measured as information of three-dimensional polar coordinate system in outcrops: r is constant (no information); φ and θ are trend and plunge of the lineations, respectively. When we calculate *cosQ* from two lineations (scan-line, pole to fracture), inner product of the two lineations simply becomes *cosQ* by assuming r is 1.

$$Inner\ product = \vec{a} \cdot \vec{b} = |\vec{a}|\left|\vec{b}\right| cosQ = \sum a_i b_i \quad (4)$$

$$(|\vec{a}| = \left|\vec{b}\right| = r = 1,\ \vec{a} = (a_1, a_2, a_3),\ \vec{b} = (b_1, b_2, b_3))$$

where $\vec{a}$ and $\vec{b}$ are vectors of scan-line and pole to fracture in stereonet, which can be expressed as (a_1, a_2, a_3) and (b_1, b_2, b_3) in Cartesian coordinate. Therefore, the correction factors for individual fractures can be calculated by converting the lineations (poles to individual fractures and the scan-line) from polar to Cartesian coordinates in stereonet.

In the case that the number of fractures of a set is less than 5 along a scan-line, the raw and corrected fracture density is not calculated. This is because the calculation result becomes less accurate with the small number of data. In the case fracture density can be calculated along two or more scan-lines, scan-line with the largest number of data was used.

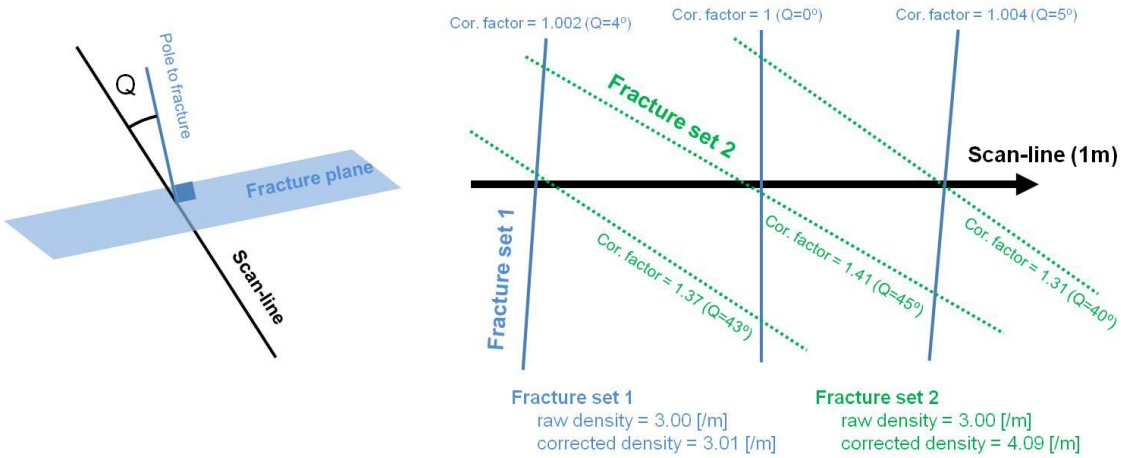

Figure 3.8 Geometrical relationship between fractures plane and a scan-line. Q is angle between individual fractures and the scan-line (left). An example of raw and corrected fracture densities (right).

3.2.6. Fracture aperture size, vein thicknesses, and vein aspect ratio

Fracture aperture sizes and vein thicknesses of individual fracture set and vein set in each layer are summarized in a histogram in Appendix (Figure 3.9). Mean and median of the data are indicated in the histogram. As the data commonly show log-normal distribution or power-law distribution, mean becomes larger than median in most cases. The Mean value is more focused in this thesis since simple multiplication of the mean and correlated fracture density in a same fracture/vein set provides apparent strain caused by the fracture/vein opening associated with the set formation.

Vein aspect ratios of individual vein set in each layer are illustrated in a cross-plot and a histogram in Appendix (Figure 3.9). The cross-plot shows individual vein size (length and thickness) and the histogram indicates distribution of the aspect ratios.

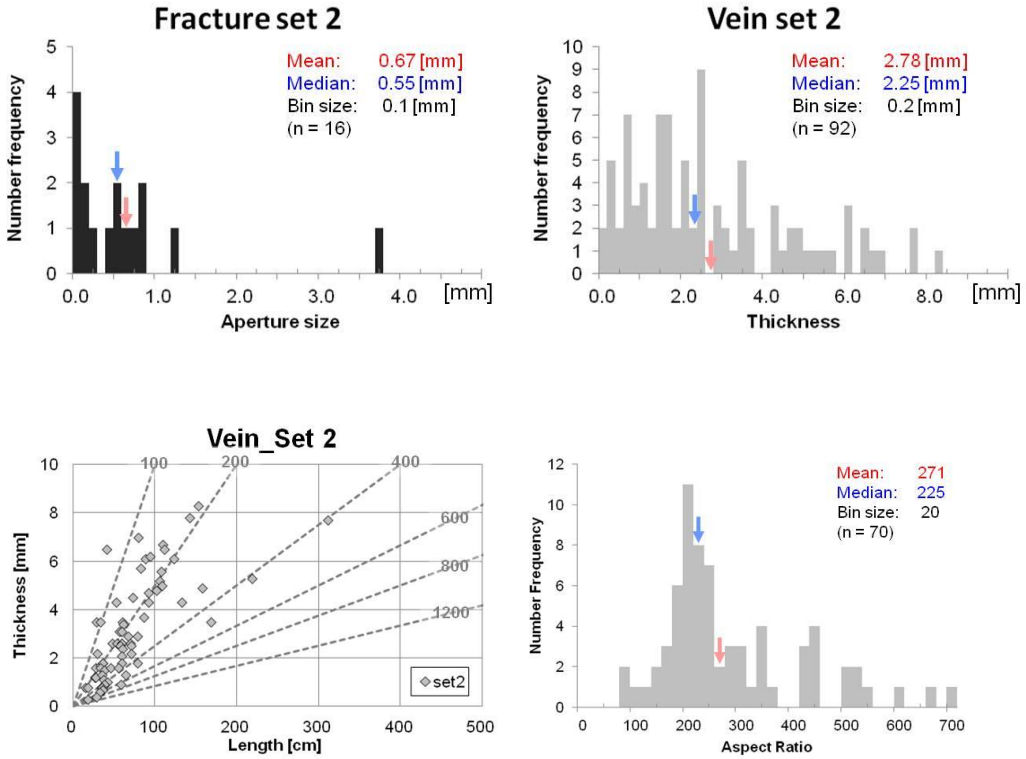

Figure 3.9 An example of data plots of aperture sizes, vein thicknesses, and vein aspect ratios in layer 25. Histograms of fracture set 2 and vein set 2 are shown here: fracture aperture size (upper left), vein thickness (upper right), and vein aspect ratio (lower right). Cross-plot shows the size of vein set 2 (lower left).

3.3. Numerical modelling

Numerical and analytical calculations are applied to examine physical conditions of the layer-scale fracture formation measured in this study. Equations related with the analytical calculations are explained in detail in Chapter 5 and Chapter 6. Here, basic methodology of finite element method (FEM) which is used in Chapter 4 is briefly explained since parts of the logical background are omitted in the chapter.

3.3.1. Basic computation flow of FEM

FEM is one of numerical approaches to solve physical problems in relation with space- and/or time-dependent phenomena. Physical laws for those problems are generally expressed by partial differential equations. However, it is normally difficult or impossible to solve the equations analytically when the analysis object has complex geometry or heterogeneous properties. Analytical solutions can be obtained only in the

case that the object has an appropriate geometry with homogeneous properties in the associated coordinate system. In order to solve physical problems of complex geometry, FEM divides an analysis object into a number of small, simple elements with nodes (Figure 3.10). Physical quantities which will be solved by the computation are assigned at the nodes. Then, the numerical approach builds a matrix equation which satisfies the associated governing equations and boundary conditions at all nodes. Element system matrix which is a matrix equation for an element to satisfy the associated physical laws is firstly built, and the element matrixes are combined to obtain the overall system matrix. The governing equations are generally converted from second-order partial differential equations to first-order equations (weak formulations) with approximations to solve the matrix simultaneously. In different words, the method simply solves huge linear simultaneous equations of approximated governing equations and boundary conditions to obtain physical quantities at all nodes. Physical quantities within the elements are interpolated from the nodes by using a form function (interpolation function). Consequently, the physical quantities are solved for entire analysis domain. Because the numerical approach uses approximations of governing equations, the results contain an error. The error range varies depending on element type, element size and element shape stability, which are discussed later and can be operated to be minimum.

The main advantage of FEM is high applicability for inhomogeneity and complex geometries, and be able to obtain variable physical quantities within the analysis object. In Chapter 4, local stress field caused by stress rotation within linear elastic materials of alternating sand-shale layers is examined. This is because the stress rotation cannot be solved analytically inside and around the arbitrary dipped layers.

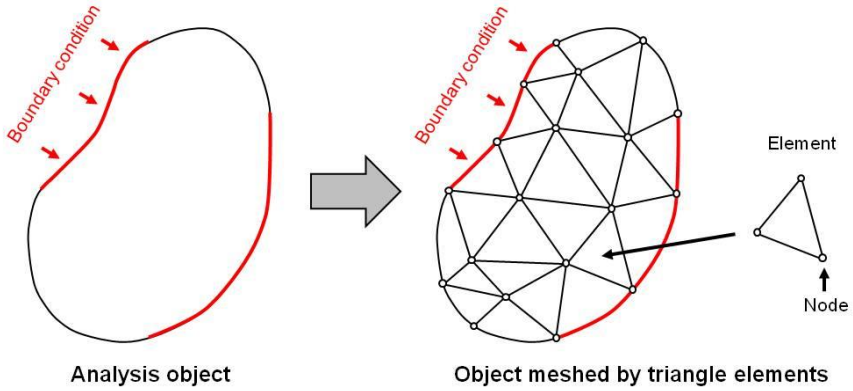

Figure 3.10 Conceptual figure of discretization of FEM

3.3.2. Elements used in Chapter 4

Linear elastic materials of alternating sand-shale layers are assumed in Chapter 4. They are continuous media as their layer boundaries are perfectly bonded. A plane strain condition is assumed (the associated physical problems are solved in 2 dimensional domain, and strain in parallel to σ_2 direction is fixed).

Triangular element is selected in the modelling. As described above, physical quantities are obtained at nodes by the computation, and the other parts are interpolated from the results at the nodes. Therefore, the more nodes are, the more accurate the result is. Common element shape is triangle and rectangle for 2D object (Figure 3.11). In general, rectangular element which has 4 nodes provides more precise computation result. On the other hand, triangular element is more flexibly to mesh complex geometry with stable element shape, which also has impact on accuracy of the computation. Highly strained elements increase error of the computation. Geometry of the analysis objects in Chapter 4 contains a zone with high curvature at the boundary between a sandstone layer and surrounding shale (Figure 3.12), which is better meshed by triangular elements with stable element shape. In addition to element types (triangle or rectangle) and stability of element shape, element size or mesh size are also effective on the simulation results as the number of nodes is changed.

By considering these three factors: element type, stability of element shape and mesh size, triangular element with fine-scale as much as possible would be the best methodology to mesh the analysis object and was applied in the current study.

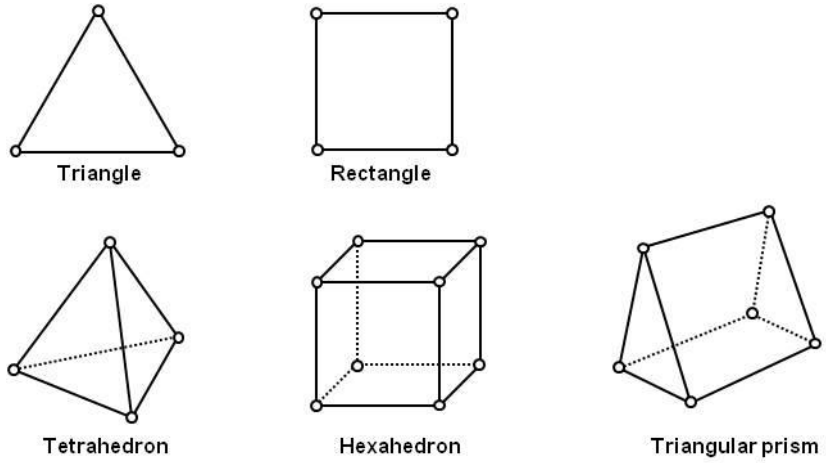

Figure 3.11 Geometry and nodes of linear elements for FEM. Triangle and rectangle are 2D element. Tetrahedron, hexahedron and triangular prism are commonly used 3D element.

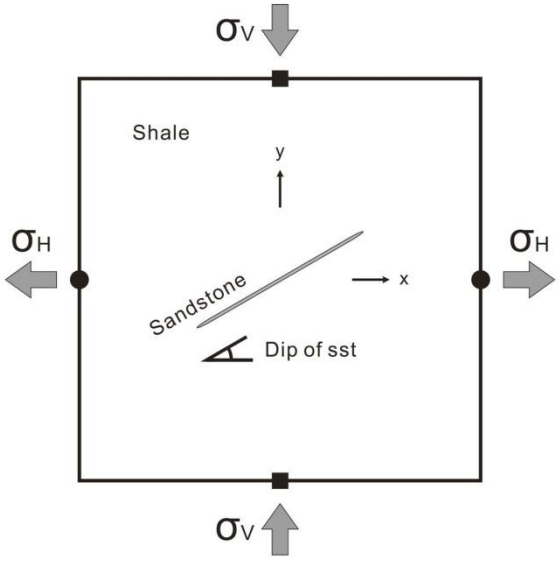

Figure 3.12 Geometry of the analysis object used in Chapter 4. A thin sandstone layer is surrounded by shale. Edges of the sandstone have highly curved zone can make element shape unstable.

3.3.3. Basic formulation of the 2D triangular element

Here, the associated equations for 2D triangular element are explained and an element system matrix is derived from them in order to describe logical background of FEM for elastic mechanics used in Chapter 4. Once an element system matrix is built, the whole matrix equation can be easily obtained from the boundary conditions and combination of the all element system matrix. Because the basic physics behind the computation is same, the matrix equations for both an element and overall domain can be expressed by

following shape (the difference is just number of rows and columns for between an element and overall domain);

$$[\mathbf{K}]\{\mathbf{u}\} = \{\mathbf{F}\} \qquad (5)$$

where $[\mathbf{K}]$ is system matrix (it is referred to as stiffness matrix for elastic mechanics), $\{\mathbf{u}\}$ is vector of displacement and $\{\mathbf{F}\}$ is vector of internal stress.

3.3.3.1. Form function for displacement field

Form function (interpolation function) of displacement field for a triangular element is formulated in this part. Cartesian coordinate is applied for the element (Figure 3.13). u_i and v_i are displacement at node i in x-direction and y-direction, respectively. q_{ix} and q_{iy} are internal stress at node i x-direction and y-direction, respectively. Body force (gravity) is neglected since the analysis object is decimetre to metre scale in Chapter 4 and body force is also neglected in the chapter. The gravity force caused by the object itself is three to four orders of magnitude smaller than the applied boundary conditions for rock mechanical properties in the scale.

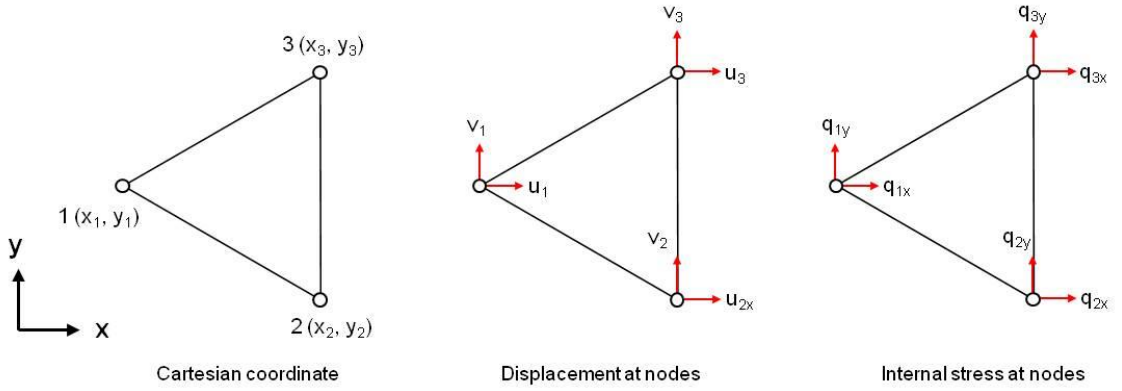

Figure 3.13 Definition of coordinate, displacement and internal stress at 3 nodes of a triangle element.

Displacement field within the element is approximated as the following expressions;

$$u^a(x, y) = A_u + B_u x + C_u y \qquad (6)$$

$$v^a(x,y) = A_v + B_v x + C_v y \qquad (7)$$

where A_u, B_u, C_u, A_v, B_v and C_v are constant values, and an index of "a" is added because the calculation results are not real displacement field but approximated one from the equations. Since the two equations must satisfy displacements at the three nodes in the element, the following formulas become true;

$$\begin{Bmatrix} u_1 \\ u_2 \\ u_3 \end{Bmatrix} = \begin{bmatrix} 1 & x_1 & y_1 \\ 1 & x_2 & y_2 \\ 1 & x_3 & y_3 \end{bmatrix} \begin{Bmatrix} A_u \\ B_u \\ C_u \end{Bmatrix} \qquad (8)$$

$$\begin{Bmatrix} v_1 \\ v_2 \\ v_3 \end{Bmatrix} = \begin{bmatrix} 1 & x_1 & y_1 \\ 1 & x_2 & y_2 \\ 1 & x_3 & y_3 \end{bmatrix} \begin{Bmatrix} A_v \\ B_v \\ C_v \end{Bmatrix} \qquad (9)$$

Therefore, the equation (6) and (7) becomes;

$$u^a(x,y) = \{1 \quad x \quad y\} \begin{Bmatrix} A_u \\ B_u \\ C_u \end{Bmatrix} = \{1 \quad x \quad y\} \begin{bmatrix} 1 & x_1 & y_1 \\ 1 & x_2 & y_2 \\ 1 & x_3 & y_3 \end{bmatrix}^{-1} \begin{Bmatrix} u_1 \\ u_2 \\ u_3 \end{Bmatrix}$$

$$= \frac{1}{2\Delta} \{a_1 + b_1 x + c_1 y \quad a_2 + b_2 x + c_2 y \quad a_3 + b_3 x + c_3 y\} \begin{Bmatrix} u_1 \\ u_2 \\ u_3 \end{Bmatrix} \qquad (10)$$

$$v^a(x,y) = \{1 \quad \mathrm{x} \quad \mathrm{y}\} \begin{Bmatrix} A_v \\ B_v \\ C_v \end{Bmatrix} = \{1 \quad \mathrm{x} \quad \mathrm{y}\} \begin{bmatrix} 1 & x_1 & y_1 \\ 1 & x_2 & y_2 \\ 1 & x_3 & y_3 \end{bmatrix}^{-1} \begin{Bmatrix} v_1 \\ v_2 \\ v_3 \end{Bmatrix}$$

$$= \frac{1}{2\Delta} \{a_1 + b_1 x + c_1 y \quad a_2 + b_2 x + c_2 y \quad a_3 + b_3 x + c_3 y\} \begin{Bmatrix} v_1 \\ v_2 \\ v_3 \end{Bmatrix} \qquad (11)$$

where a_i, b_i, c_i and Δ are as as follows;

$$a_1 = x_2 y_3 - x_3 y_2,\ b_1 = y_2 - y_3,\ c_1 = x_3 - x_2$$
$$a_2 = x_3 y_1 - x_1 y_3,\ b_2 = y_3 - y_1,\ c_2 = x_1 - x_3$$
$$a_3 = x_1 y_2 - x_2 y_1,\ b_3 = y_1 - y_2,\ c_3 = x_2 - x_1$$

$$\Delta = \frac{1}{2}\begin{vmatrix} 1 & x_1 & y_1 \\ 1 & x_2 & y_2 \\ 1 & x_3 & y_3 \end{vmatrix}$$

By combining the equation (10) and (11), the following matrix equation is obtained;

$$\begin{Bmatrix} u^a(x,y) \\ v^a(x,y) \end{Bmatrix} = [\mathbf{N}] \begin{Bmatrix} u_1 \\ v_1 \\ u_2 \\ v_2 \\ u_3 \\ v_3 \end{Bmatrix} \qquad (12)$$

$$[\mathbf{N}] = \frac{1}{2\Delta}\begin{bmatrix} a_1 + b_1x + c_1y & 0 & a_2 + b_2x + c_2y & 0 & a_3 + b_3x + c_3y & 0 \\ 0 & a_1 + b_1x + c_1y & 0 & a_2 + b_2x + c_2y & 0 & a_3 + b_3x + c_3y \end{bmatrix}$$

where 2-by-6 matrix of [**N**] is the form function (interpolation function) of displacement field for the triangular element. The calculated value within the element is not analytical solution but approximation based on equation (6) and (7).

3.3.3.2. Relation of the displacement field to strain field.

The relationship between strain field and displacement field is expressed by the following formula in 2 dimensional problem;

$$\begin{Bmatrix} \varepsilon_x(x,y) \\ \varepsilon_y(x,y) \\ \gamma_{xy}(x,y) \end{Bmatrix} = \begin{Bmatrix} \frac{\partial u}{\partial x} \\ \frac{\partial v}{\partial y} \\ \frac{\partial u}{\partial y} + \frac{\partial v}{\partial x} \end{Bmatrix} = \begin{bmatrix} \frac{\partial}{\partial x} & 0 \\ 0 & \frac{\partial}{\partial y} \\ \frac{\partial}{\partial y} & \frac{\partial}{\partial x} \end{bmatrix} \begin{Bmatrix} u(x,y) \\ v(x,y) \end{Bmatrix} \qquad (13)$$

By substituting equation (12) into (13), approximated strain field is calculated;

$$\begin{Bmatrix} {\varepsilon_x}^a(x,y) \\ {\varepsilon_y}^a(x,y) \\ {\gamma_{xy}}^a(x,y) \end{Bmatrix} = \begin{bmatrix} \frac{\partial}{\partial x} & 0 \\ 0 & \frac{\partial}{\partial y} \\ \frac{\partial}{\partial y} & \frac{\partial}{\partial x} \end{bmatrix} [\mathbf{N}] \begin{Bmatrix} u_1 \\ v_1 \\ u_2 \\ v_2 \\ u_3 \\ v_3 \end{Bmatrix} = [\mathbf{B}] \begin{Bmatrix} u_1 \\ v_1 \\ u_2 \\ v_2 \\ u_3 \\ v_3 \end{Bmatrix} \qquad (14)$$

$$[\mathbf{B}] = \frac{1}{2\Delta}\begin{bmatrix} b_1 & 0 & b_2 & 0 & b_3 & 0 \\ 0 & c_1 & 0 & c_2 & 0 & c_3 \\ c_1 & b_1 & c_2 & b_2 & c_3 & b_3 \end{bmatrix}$$

where 3-by-6 matrix of [**B**] is a function to connect displacement field with strain field. As the equation is also approximation based on equation (6) and (7), index "*a*" is added for the results. As the all parameters are defined from coordinates of the three nodes, [**B**] becomes a constant value in a same element.

3.3.3.3 Stress-strain relation

Stress-strain relation for plane strain problem is as follows;

$$\begin{Bmatrix} \sigma_x \\ \sigma_y \\ \tau_{xy} \end{Bmatrix} = [\mathbf{D}] \begin{Bmatrix} \varepsilon_x \\ \varepsilon_y \\ \gamma_{xy} \end{Bmatrix} \qquad (15)$$

$$[\mathbf{D}] = \frac{E}{(1+\nu)(1-2\nu)}\begin{bmatrix} 1-\nu & \nu & 0 \\ \nu & 1-\nu & 0 \\ 0 & 0 & (1-2\nu)/2 \end{bmatrix}$$

3.3.3.4 Derivation of an element stiffness matrix

In order to derive element stiffness matrix from above equations, virtual work principle is applied. The principle assumes virtual works done by internal stress and external stress become same;

$$W_{INT} = W_{EXT} \qquad (16)$$

Virtual works done by internal stress and external stress are

$$W_{INT} = \iint_S \left({\sigma_x}^a {\varepsilon_x}^{*a} + {\sigma_y}^a {\varepsilon_y}^{*a} + {\tau_{xy}}^a {\gamma_{xy}}^{*a}\right) dxdy \qquad (17)$$

$$W_{EXT} = q_{1x}{u_1}^* + q_{1y}{v_1}^* + q_{2x}{u_2}^* + q_{2y}{v_2}^* + q_{3x}{u_3}^* + q_{3y}{v_3}^* \qquad (18)$$

where u_1^*, u_2^*, u_3^*, v_1^*, v_2^* and v_3^* are virtual displacement. ε_x^*, ε_y^* and γ_{xy}^* are virtual strain. S is an area of the triangle element. By using equation (14) and (15), virtual work done by internal stress becomes as follow;

$$W_{INT} = \iint_S \{\varepsilon_x{}^{*a} \quad \varepsilon_y{}^{*a} \quad \gamma_{xy}{}^{*a}\} \begin{Bmatrix} \sigma_x{}^a \\ \sigma_y{}^a \\ \tau_{xy}{}^a \end{Bmatrix} dxdy$$

$$= \iint_S \{\varepsilon_x{}^{*a} \quad \varepsilon_y{}^{*a} \quad \gamma_{xy}{}^{*a}\} [\mathbf{D}] \begin{Bmatrix} \varepsilon_x{}^a \\ \varepsilon_y{}^a \\ \gamma_{xy}{}^a \end{Bmatrix} dxdy$$

$$= \{u_1{}^* \quad v_1{}^* \quad u_2{}^* \quad v_2{}^* \quad u_3{}^* \quad v_3{}^*\} \iint_S [\mathbf{B}]^T [\mathbf{D}][\mathbf{B}] dxdy \begin{Bmatrix} u_1 \\ v_1 \\ u_2 \\ v_2 \\ u_3 \\ v_3 \end{Bmatrix} \quad (19)$$

where $[\mathbf{B}]^T$ is column-line replacement of matrix [**B**]. Virtual work done by external stress also becomes similar shape of matrix equation;

$$W_{EXT} = \{u_1{}^* \quad v_1{}^* \quad u_2{}^* \quad v_2{}^* \quad u_3{}^* \quad v_3{}^*\} \begin{Bmatrix} q_{1x} \\ q_{1y} \\ q_{2x} \\ q_{2y} \\ q_{3x} \\ q_{3y} \end{Bmatrix} \quad (20)$$

From equation (19) and (20), equation (16) becomes

$$\{u_1{}^* \quad v_1{}^* \quad u_2{}^* \quad v_2{}^* \quad u_3{}^* \quad v_3{}^*\} \left([\mathbf{K}] \begin{Bmatrix} u_1 \\ v_1 \\ u_2 \\ v_2 \\ u_3 \\ v_3 \end{Bmatrix} - \begin{Bmatrix} q_{1x} \\ q_{1y} \\ q_{2x} \\ q_{2y} \\ q_{3x} \\ q_{3y} \end{Bmatrix} \right) = 0 \quad (21)$$

$$[\mathbf{K}] = \iint_S [\mathbf{B}]^T [\mathbf{D}][\mathbf{B}] dxdy$$

In the case that only equation (22) is satisfied, equation (21) becomes true for arbitrary virtual displacement;

$$[\mathbf{K}]\begin{Bmatrix} u_1 \\ v_1 \\ u_2 \\ v_2 \\ u_3 \\ v_3 \end{Bmatrix} = \begin{Bmatrix} q_{1x} \\ q_{1y} \\ q_{2x} \\ q_{2y} \\ q_{3x} \\ q_{3y} \end{Bmatrix} \quad (22)$$

The equation (22) is same shape as equation (5) and 6-by-6 matrix of [**K**] is the element stiffness matrix. As described above, the matrix [**B**] is only defined from coordinates of the three nodes of an element. The matrix [**D**] is constant within an element. [**K**], therefore, becomes constant value within an element.

If we consider second element which shares node 2 and node 3 with 1st element and has one new node (node 4), the overall system matrix $[\mathbf{K}]^*$ becomes 8-by-8 matrix which can be calculated from element matrix equations of 1st and 2nd elements (the asterisk being added for the overall matrix equation). Displacement vector $\{\mathbf{u}\}^*$ and internal stress vector $\{\mathbf{F}\}^*$ become 8 rows in that case.

In the same manner, rise of the number of elements just increases the number of rows and columns of the overall stiffness matrix $[\mathbf{K}]^*$, displacement vector $\{\mathbf{u}\}^*$ and internal stress vector $\{\mathbf{F}\}^*$. By substituting boundary conditions which can be displacement or stress conditions at nodes into the overall matrix equation, the matrix equation (linear algebraic equation) become solvable. The numerical simulation (FEM) computes the matrix equation simultaneously, providing displacement vector $\{\mathbf{u}\}$ and internal stress vector $\{\mathbf{F}\}$ at all nodes, and interpolates the results with equation (12), (14) and (15) to the overall analysis domain.

Reference

Bevins, R.E., White S.C. & Robinson, D. 1996. The South Wales Coalfield: low grade metamorphism in a foreland basin setting? Geological Magazine, 133, 739-749.

Burgess, P.M. & Gayer, R.A. 2000. Late Carboniferous tectonic subsidence in South Wales: implications for Variscan basin evolution and tectonic history in SW Britain. Journal of the Geological Society, London 157, 93-104.

Price, N.J., 1958. A study of rock properties in conditions of triaxial stress. In: Walton, W.H. (Ed.), Proceedings of a Conference on the mechanical properties of non-metallic brittle materials. Butterworth, London, 106-122.

Price, N.J., 1960. The compressive strength of coal measure rocks. Colliery Engineering 37, 283-292.

Price, N.J., 1963. The influence of geological factors on the strength of Coal Measure Rocks. Geological Magazine 100, 428-443.

Tarzaghi, R.D., 1965. Sources of errors in joint survey. Geotechnique, 15, 287-304.

White, S.C. 1991. Palaeo-geothermal profiling across the South Wales Coalfield. Proceedings of the Ussher Society, 7, 368-374.

Chapter 4: Paper 1

Manuscript in preparation

Title: Timing constraint on layer-scale fracture and vein formations in the South Wales coalfield

Authors: Tetsuzo Fukunari and Agust Gudmundsson

Total number of manuscript pages: 32

Statement of my role for the paper 1:

- Collection of structural data
- Numerical modelling
- Writing the manuscript and illustrating the figures

Timing constraint on layer-scale fracture and vein formations in the South Wales coalfield

Tetsuzo Fukunari[1,2*], Agust Gudmundsson[1]

[1]Department of Earth Sciences, Royal Holloway University of London, Egham, Surrey TW20 0EX, UK

[2]Japan Oil, Gas and Metals National Corporation (JOGMEC), Toranomon Twin Building, 2-10-1 Tranomon, Minato-ku, Tokyo 105-0001, JAPN

*email: fukunari-tetsuzo@jogmec.go.jp

Abstract

Fractures and veins increase heterogeneity of permeability in sedimentary rocks (porous media), and have great impact on fluid transportation as they can be fluid pass or barrier. However, development mechanisms of some fracture systems are not well-understood. This is because timings of those fracture formations are not well understood in some cases. Layer-scale orthogonal extension fracture system is one of such fractures. This paper examines layer-scale orthogonal fractures and veins in alternating sand-shale layers in the South Wales coalfields. This paper introduce outcrop-data of the fractures and veins in the area, and discuss timing of their formations in relation with geometrical relationship between the fractures/veins and other deformation structures. The area was developed as a foreland basin associated with northward compression of the Variscan Orogeny. Map-scale folds and thrusts related with the orogeny are common. Field structural data indicate the layer-scale fractures and veins are perpendicular to the folded beds in the sandstones throughout the study area. Local stress field within the stiff sandstones surrounded by soft shale is numerically simulated. The results demonstrate minimum principal stress σ_3 within the sandstone could not be parallel to the bedding after the sandstones were inclined at 45 degrees or more. By taking physical conditions of the vein formation into account, the results of numerical simulation imply at least the layer-scale extension vein system initially formed before the Variscan Folding. Since

the folds formed at the latest stage of sedimentation, the current study results suggest the layer-scale extension veins formed not during crustal uplift/exhumation but during basin burial. Although regionally-developed orthogonal extension fracture systems (they are filled with minerals in the current study area) are occasionally interpreted to have been developed by pressure release during crustal uplift/exhumation, our study results indicate other mechanisms which form orthogonal extension fracture system must exist during basin burial in the study area.

Keywords: finite element method, layer-scale fractures, stress rotation in mechanical layers, South Wales coalfield

1. Introduction

Fractures and veins generally increase heterogeneity of permeability in sedimentary rocks and have significant impact on fluid flow, as open extension fractures can be fluid pass on one hand and mineral veins can be barrier of fluid flow in porous media on the other. It is, therefore, of great importance to understand their characteristics (fracture orientation, fracture density, fracture mode, fracture displacement, filled by solid materials or not, size distribution, and three dimensional distribution), when we estimate fluid transportation in subsurface reservoirs. However, development mechanisms of some fracture systems are not clearly understood, which seems to cause inconsistency between practical approaches of fracture modelling used in the oil and gas industry and theoretical considerations, especially for regionally-developed orthogonal mode I extension fracture system. For instance, surface outcrop analogies of orthogonal extension fracture systems are sometimes used to constrain fracture characteristics in subsurface oil and gas reservoirs which exist in a depth deeper than a few kilometres (e.g. Belayneh et al., 2006; Wennberg et al., 2007). In contrast, some researchers interpret orthogonal extension fractures form during crustal uplift or exhumation, since horizontal principal stresses require being tensile to develop such fracture system (e.g. Simon et al., 1988; Caputo, 1995; Bai et al., 2002). If the latter case is true, orthogonal extension fractures would mostly affect permeability and fluid transportation only in the shallow parts of sedimentary basins which had experienced significant

uplift/exhumation, and outcrop analogies of the orthogonal fractures give little indication of the fracture characteristics in deep, subsurface oil and gas reservoirs.

One of the problems causing this conflict is that timing of the fracture network formation is not well-constrained. In order to contribute on the problem, this paper focuses on outcrop orthogonal extension fractures and veins, and the timings of their formations. We selected the South Wales coalfield for this study (Figure 1). The South Wales coalfield is a foreland basin formed in front of the northwardly propagating Variscan Orogeny (e.g. Gayer and Jones, 1989; Hartley and Warr, 1990; Gayer et al., 1993). Layer-scale extension or hybrid (extension + shear) fractures and veins are common in alternating sand-shale layers in the study area. The fractures and veins generally developed in two (orthogonal) or three directions.

We introduce field structural data of the layer-scale fractures and veins in detail, and discuss relative-age relationships between the fractures, veins and other deformation structures. Folds and thrusts related with the Variscan Orogeny are common in the area. The Variscan compression occurred at approximately same time as the maximum burial of the basin (Cole et al., 1991; Jones, 1991; Bevins et al., 1996). Therefore, investigation of relative-age relationship between the compression structures and the layer-scale fractures and veins has the potential to reveal whether the orthogonal extension fracture and vein systems formed during crustal uplift/exhumation or not. Although some fractures in the basin have previously been documented (e.g. Roberts, 1965; Hancock et al., 1983; Hathaway and Gayer, 1996; Frodsham and Gayer, 1997), timings of the layer-scale orthogonal fracture and vein formations have not been well-constrained. Finite element method is applied to investigate stress field within the folded mechanical layers (alternating sand-shale layers). We also refer to physical conditions of the vein formation estimated by Alderton et al. (2004). The results suggest at least the orthogonal extension vein systems initially formed before the Variscan Folding, though other later stages of fracture formation may exist in the long-lived basin. This implies it is not necessarily the case that orthogonal extension fracture systems formed during crustal uplift/exhumation, and that extension fracture systems observed in outcrops have potential to give essential indications for fractures in subsurface reservoirs although the fracture systems are partly filled with minerals in the current study area.

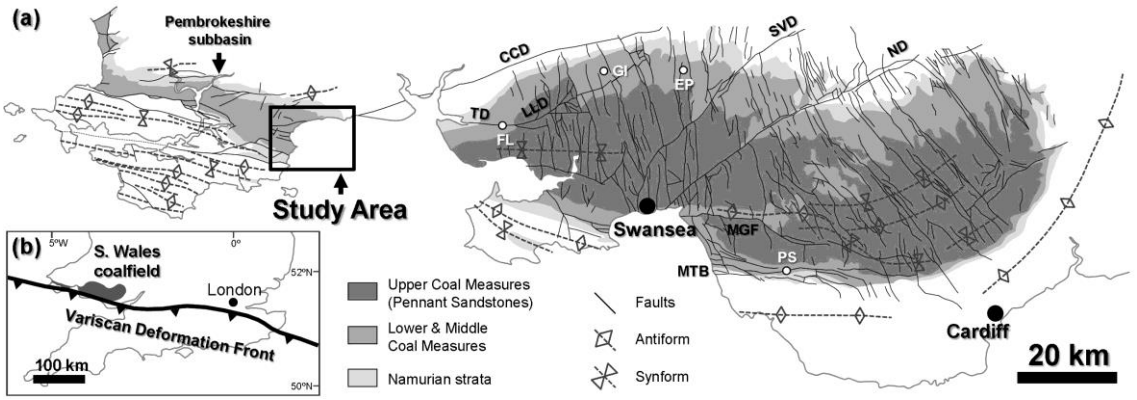

Figure 1 **(a)** Geological map of Silesian sediments in South Wales (Hancock et al., 1983; Hartley, 1993). The study area is delineated by a box. Opencast coal sites: FL, Ffos Las; GI, Gilfach Iago; EP, East Pit; PS, Park Slip. Major structures: CCD, Carreg Cennen Disturbance; TD, Trimsaran Disturbance; LLD, Llanon Disturbance; SVD, Swansea Valley Disturbance; ND, Neath Disturbance; MGF, Moel Gilau fault; MTB, Margam thrust belt. **(b)** Inset box shows the location of the South Wales coalfield and the Variscan Deformation Front.

2. Geological background

2.1. Depositional sediments in the South Wales coalfield

The present-day South Wales coalfield is an erosional remnant in northwardly verging synform which extends for approximately 90 kilometres in the east-west and 30 kilometres in the north-south (Figure. 1). The exposed basin is mainly composed of Westphalian to early Stephanian Coal Measures. The Namurian sediments which surround the Coal Measures in the geological map of Figure 1 are the oldest siliciclastics in the basin. The Namurian regionally rests with unconformity on the Dinantian Carbonates and only conformably overlies the carbonates in the basin centre (e.g. Leveridge and Hartley, 2006).

The Namurian strata are mudstone-dominant sequences interpreted as marine sediments deposited in offshore to shoreface with lesser amount of fluvio-deltaic channels (e.g. George, 1970; George and Kelling, 1982). The Coal Measures conformably overlie on the Namurian strata. Periodic rise of sea-level during the sedimentation of the Coal Measures resulted in flooding and the development of widely comparable marine bands (Calver, 1969). The prominent marine bands subdivide the Coal Measures into Upper, Middle, and Lower Measures. The Lower and Middle Coal

Measures (Westphalian A, B and early Westphalian C) are mudstone-dominant sequences in lower to upper coastal plain (e.g. Jones, 1989; Hartley, 1993). Most of the productive coal seams are involved in these argillaceous units. In contrast, the Upper Coal Measures (Westphalian C and D) are composed of terrestrial sandstone-dominant facies which contain few productive coal seams and no marine bands. The sandy unit is also referred to as Pennant Sandstones. They are interpreted as braided fluvial deposits in alluvial braid plain (e.g. Jones, 1989; Hartley, 1993). Thus, the siliciclastic sediments in the South Wales coalfield record gradual change of depositional environment from offshore-shallow marine in the Namurian to terrestrial braid plain in the Westphalian C and D of the Upper Coal Measures.

2.2. Deformation structures in the South Wales coalfield

Thrusts and folds which formed as a result of basinward propagation of the Variscan orogeny are common in the study area. They generally trend east-west though the trend slightly vary to become sub-parallel to the local basin margin (Figure 1). The compression structures developed in both map-scale and outcrop-scale and produced approximately 30% shortening in the shale-dominant Lower and Middle Coal Measures (Jones, 1989; Jones, 1991), which rises to 50-60% shortening at around Ffos Las (Frodsham and Gayer, 1997). The compressive deformation is locally concentrated into narrow zones which are referred to as disturbances (Figure 1). They cut across the basin in northease-southwest or east-west directions. The highest strain of 70% shortening is recorded at Ffos Las in association with the deformation of Llannon and Trimsaran disturbances (Cole et al., 1991; Frodsham et al., 1993). In contrast to the intense shortening within the Lower and Middle Coal Measures, more competent sandstone-dominant sequences of the Upper Coal Measures are much less deformed. They show only 6% shortening, with broad open folds (Jones, 1991). Thrusts penetrating them are relatively rare (Jones, 1989; Jones, 1991). This large difference in bulk shortening between Lower and Middle Coal Measures and Upper Coal Measures is explained by development of multiple detachments at the base of the Upper Coal Measures (Frodsham and Gayer, 1997).

Cross faults which strike sub-perpendicular to the trend of folds and thrusts are also common (e.g. Woodland and Evans, 1964; Archer, 1968). They generally have

downthrows of tens to hundreds metres together with strike-slip components (Trotter, 1947; Owen, 1953; Jones, 1991). Some of the cross faults have significant thickness changes of sediments across the fault planes, indicating they are syn-depositional structures (Cole et al., 1991; Jones, 1991). Post-depositional displacements are also recorded along the cross faults which cut the east-west striking thrusts of the Variscan orogeny (Cole et al., 1991; Jones, 1991).

2.3. Relative-age relation of the sedimentation and the Variscan deformation

Northward migration of the Variscan orogeny during the basin subsidence is recorded in sedimentological data in the South Wales coalfield. The Upper Coal Measures (late Westphalian C and D) contain abundant coal clasts from the Westphalian A sediments (Gayer and Pesek, 1992). This indicates the Westphalian A sediments had already been uplifted and exposed in the orogenic zone at Westphalian C age and that basinward progression of the orogenic belt during Westphalian A-C period. Northward migration of the basin depocentre is also recorded, which shows continuous progression of the orogenic belt toward the north during the sedimentation (e.g. Kelling, 1988; Jones, 1989; Leveridge and Hartley, 2006).

As a result of basinward progression of the orogen, folds and thrusts were formed in the current basin area. The compression structures mostly developed at the latest stage of the sedimentation as the major phase of Variscan compression is interpreted as late Westphalian D at the earliest (Cole et al., 1991; Jones, 1991). Minor deformation of early folding is also locally reported during the sedimentation (Jones, 1989). Similar evidence is documented by Bevins et al. (1996). They show layers of equal volatile matters (isovols) which preserve thermal history of the sediments are folded and that the main compression was induced just after the event of maximum achieving temperature. They also stated that the isovols broadly intersect with geological strata at angles of 2-4 degrees, suggesting the folding was initiated slightly earlier than the maximum achieving temperature.

As described above, existence of early minor folding suggests that the folding was initiated slightly earlier than maximum burial, and that the main compression of the Variscan Orogeny followed it just after the sedimentation.

3. The Variscan compression structures in the study area

Eastern coast of the Pembrokeshire sub-basin was selected for the fieldwork. This is because the geological formations are continuously exposed along the coastal line over a distance of several kilometres from southern end to northern end of the basin (Figure 2). The Namurian and Lower Coal Measures which are shale-dominant alternating sand-shale layers are main exposures in this area (George and Kelling, 1982; George, 2001). Layer-scale extension fractures are common in both sandstone and shale layers which experienced the Variscan compression.

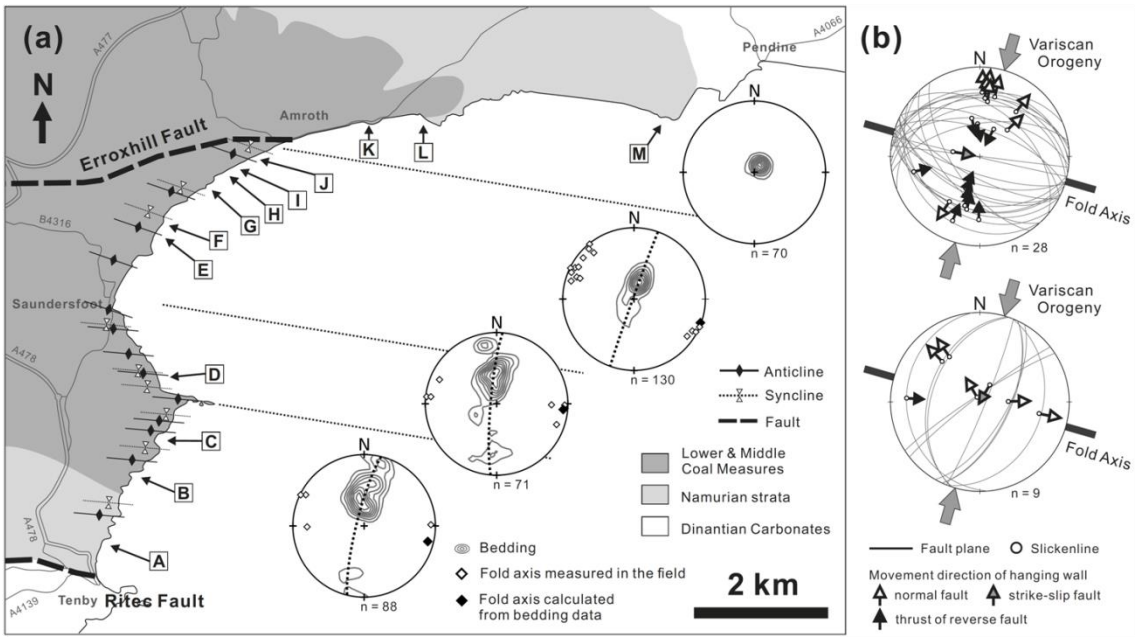

Figure 2 **(a)** Geological map of the study area. Stereonets show contour map of poles to bedding planes. The number of bedding data used to draw the contours is shown below the stereonets. Fold axes measured in the field and a fold axis calculated from the bedding data are denoted by white and black markers with diamond shapes, respectively. Dashed line indicates best-fit girdle of the bedding data. Since the folds are asymmetric, bedding data dipping to the south are dominant. Capital letters on the map indicate sites where layer-scale fractures and veins were measured. **(b)** Fault data in the study area. Faults striking sub-parallel to the fold axis are plotted on the upper stereonet and faults striking sub-perpendicular to the fold axis are plotted on the lower stereonet. Fault planes are shown by great circles. Slickenlines are denoted by small white circles. Where the sense of shear could be determined in the field, movement direction of the hanging wall block is indicated by arrows.

3.1. Map-scale folds

Beddings were measured throughout the study area (Figure 2(a)). The beds gently dip south-southwest as monocline in the northern area (northern side of Erroxhill Fault) while they become folded in the southern area (southern side of Erroxhill Fault). Most of the folds are northward-vergent. The wave-length is hundred metre scale. The shape is mostly a chevron (Figure 3(a)). The dip of folded strata becomes steeper towards the south. Northern limbs of antiform (southern limbs of synform) are sub-vertical in the area closest to the Variscan Orogen and some of them steeply dip south (Figure 2a). Representative fold axes were calculated from the bedding data in the southern side of Erroxhill Fault. The result shows the fold axes trends WNW-ESE and plunges sub-horizontally, which rotates 10-15 dgrees anticlockwise toward the south. Axes of outcrop-scale folds were also measured in the field, which has concordant geometry with the calculated fold axes from the beddings.

By assuming compressive strain is 0% in the northern side of Erroxhill Fault, compression strains in the other areas were calculated (Figure 4). Beds dip south-southwest at 9 degrees at the northern area. Average dips of folded strata at the other areas are 24, 36 and 35 degrees on southern limbs of anticlines and 21, 45 and 86 degrees on the northern limbs, respectively. Since chevron folds are common in the study area (Figure 3a), the folds are assumed to have planar limbs. Based on the above conditions, the shortening strains caused by the map-scale folds become 7%, 21% and 40%, which increases towards the south. As the calculation does not take into account displacement on any thrusts and outcrop-scale folds, the results signify minimum estimates of the shortening.

Although the absolute values of shortening are unclear, a rise of compressive strain towards the Variscan Orogen suggests the map-scale folds in the study area formed in association with the orogenic deformation. The fold axes trending parallel to the Variscan Orogenic Belt also support a close relationship between the two.

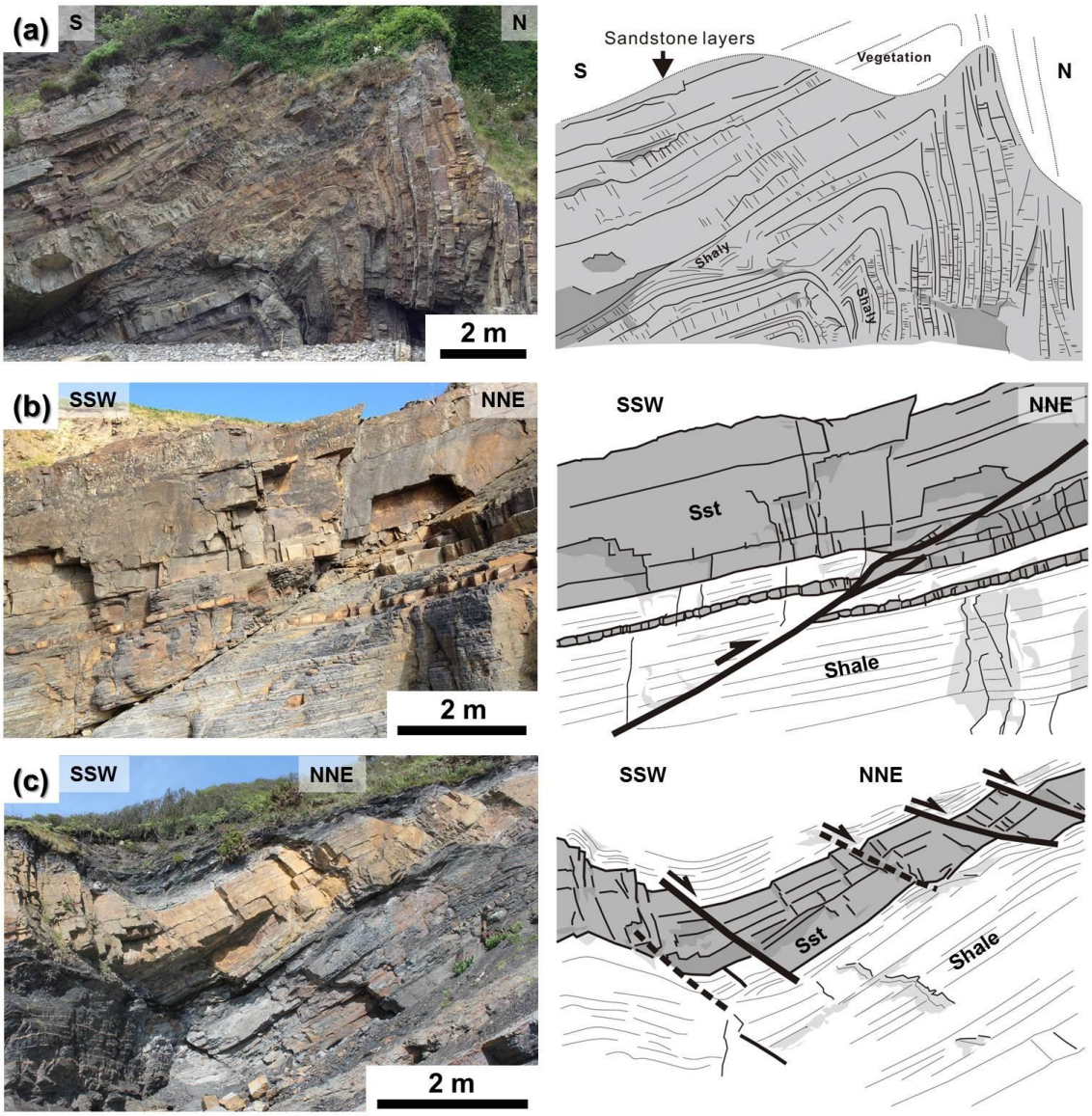

Figure 3 Photographs and sketches of the main structures observed in the study area. **(a)** A chevron fold exposed at around site D in Figure 2(a). The beds are mostly of sandstone. Thin shale layers are interbedded between the sandstones. The compression deformation was locally concentrated at shale dominant part. **(b)** A thrust dipping to south-southwest at site I (Figure 2(a)). Offset of sandstone layers indicates approximately one metre displacement along the fault. Fractures are not very common in upper thick sandstone layer. **(c)** North-dipping normal faults exposed at site G (Figure 2(a)). They mainly cut sandstone layers and become arrested in shale layers.

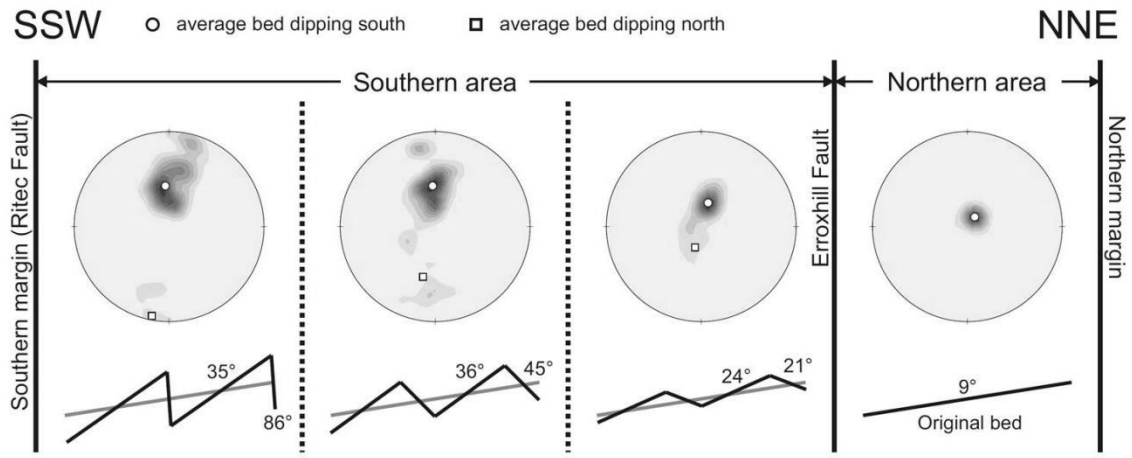

Figure 4 Stereonets showing contours of poles to beddings. Average dips of the northern and the southern limbs of the folds are indicated by squire and circle markers, respectively. Fold shape used for strain calculation is illustrated below the stereonets.

3.2. Thrusts and other faults

Thrusts are commonly observed in the study area (Figure 3(b)). They dip south-southwest and strike parallel to the Variscan Orogenic Belt (upper stereonet in Figure 2(b)). The similar strike direction of thrusts as the Variscan Orogenic Belt suggests that the thrusts were also associated with the Variscan Orogeny. The thrusts are not observed in the northern side of the Erroxhill Faults.

North-dipping normal faults which strike WNW-ESE are locally observed. They are not continuous faults and penetrate only some parts of the sediments (Figure 3(c)). No clear indication was found to categorise them into deformation structures documented by other researchers. However, sediment thickness apparently changes across some of these faults, suggesting they may correspond with syn-sedimentary gravity-driven faults documented by Cole et al. (1991) and Jones (1991).

Normal faults striking sub-perpendicular to the Variscan Orogenic Belt are also observed (lower stereonet in Figure 2(b)). They have metre-scale downthrows. Although displacements along these faults are relatively small, they are likely to be categorised into the cross faults reported in this basin.

4. Layer-controlled fractures and veins

4.1. Characteristics of the fractures and veins in the sandstones, limestone and shale

Layer-scale extension fractures and veins are are widely observed in both sandstones and shale layers in the study area. They developed in two or three directions (Figure 5a & 5b). The majority of the fractures in the sandstones are extension fractures with aperture sizes from a millimetre to a few centimetres (Figure 5c). Hybrid or mixed-mode (extension + shear) fractures were also observed in the sandstones (Figure 5d). They show lateral displacements of less than about one centimetre but have, in addition, clear extension components. Extension fractures are dominant in the outcrops where fractures developed in two orthogonal directions. In contrast, hybrid fractures are relatively common in the sandstones where fractures developed in three directions. This probably reflect the relationship between Mohr's circle and failure envelop: pure extension fracture can develop only perpendicular to minimum compressive stress direction; hybrid or shear fractures develop as two conjugate fractures oblique to the principal stress directions.

Most of the extension and hybrid fractures in the sandstones are arrested at contacts with shale (Figure 5e). The fractures in the sandstones are commonly brittle and flat fracture surface. On the other hand, fractures penetrating shale have geometries that may indicate semi-ductile behaviour of the shale during fracture development, in particular fractures with curved planes. In addition, boudinage structures are locally observed (Figure 5f), also indicating ductile behaviour of shale in the stage of extension fracture formation. Because of the fracture plane is variable in shale, it is comparatively difficult to analyse the fracture patterns in the shale. Although fractures in shale are also summarized in Figure 6, the focus in this paper is on the fractures in the brittle sandstone layers. Fractures in shale commonly oblique to beddings (Figure 5e), which suggests they may be shear or hybrid fractures based on the theoretical relationship between Mohr's circle and failure envelop as described above. However, no clear indication for shear and/or extension displacement was observed in the field.

Only one carbonate layer is recognised in outcrop J in Figure 2(a). This is known as Amroth Freshwater Limestone which contains abundant non-marine bivalve (George and Kelling, 1982). Because the fracture pattern in the limestone is similar to

those in the sandstones, the layer-scale fractures in both types of layers are plotted together in Figure 6. The outcrop photograph is also shown in Figure 3e of chapter 5.

The fractures in the sandstones, limestone and shale were developed in both limb and hinge parts of the map-scale folds, and the fracture density does not change between the limb and hinge parts (e.g. Appendix of chapter 3). This suggests the layer-scale fractures were mostly not associated with the buckling of the folds though parts of them must have been developed or deformed in relation with the folding. The fractures are well developed in thin sandstone layers whose thickness is less than about 1 m but are not common in thicker sandstone layers (Figure 3b). This may imply that fracture formation was associated with local stress fields concentrated in each sandstone layer.

Several fractures are filled with quartz, that is, are mineral veins. They commonly developed in same directions as the layer-scale extension fractures. These veins are never seen penetrating the shale, suggesting that shale was not sufficiently consolidated – was too ductile - during the vein formation. The observations suggest that the shale was ductile at the same time as the sandstone was brittle during extension fracture formation associated with mineral precipitation.

All fractures and veins in the sandstones, limestone (only at outcrop J) and shale are plotted in the stereonet in Figure 6. The structural data are also grouped into three areas depending on distance from the Variscan orogen: strongly folded area (southern area, outcrop A to D), gently folded area (central area, outcrop E to J), and unfolded area (northern area, outcrop K to M). Area-normalised rose diagrams of the three areas are shown in Figure 7 to compare the fracture patterns between folded and unfolded areas. Only fractures and veins in the sandstones and veins are plotted in Figure 7.

Both fractures and veins are most dominant in the direction parallel to the Variscan compression in all three areas. In a large sense, fractures and veins developed in two strike directions with orthogonal pattern are more common in the northern area where the compression of Variscan Orogeny was the weakest (Figure 7). On the other hand, fractures and veins developed in three directions become relatively common toward the south. In particular, fractures and veins sub-perpendicular to the Variscan compression show wider strike orientations (Figure 7).

4.2. A possible control for the fracture development in 2 or 3 directions

The change of fracture and vein patterns toward the south most likely reflects the difference of local stress field within the sandstones at the time of extension fracture/vein formation. In the southern area, compressive stress in NNE-SSW direction must have been larger because of the close distance to the Variscan Orogen if the fractures/veins formed during basin formation. It is required that differential stress is smaller than 4 times tensile strength of the host rock for extension fracture formation (Griffith, 1924; Gudmundsson, 2011). At the time of extension fracture initiation, effective minimum principal stress should be negative and same absolute value as tensile strength of the host rock. Therefore, effective maximum principal stress for extension fracture formation must be less than 3 times tensile strength of the host rock with positive value. Relatively large maximum compressive stress in NNE-SSW direction associated with the Variscan Orogen may have kept the effective maximum principal stress higher than 4 times tensile strength of the sandstones in the southern area and resulted in development of hybrid fractures subperpendicular to the Variscan Orogen.

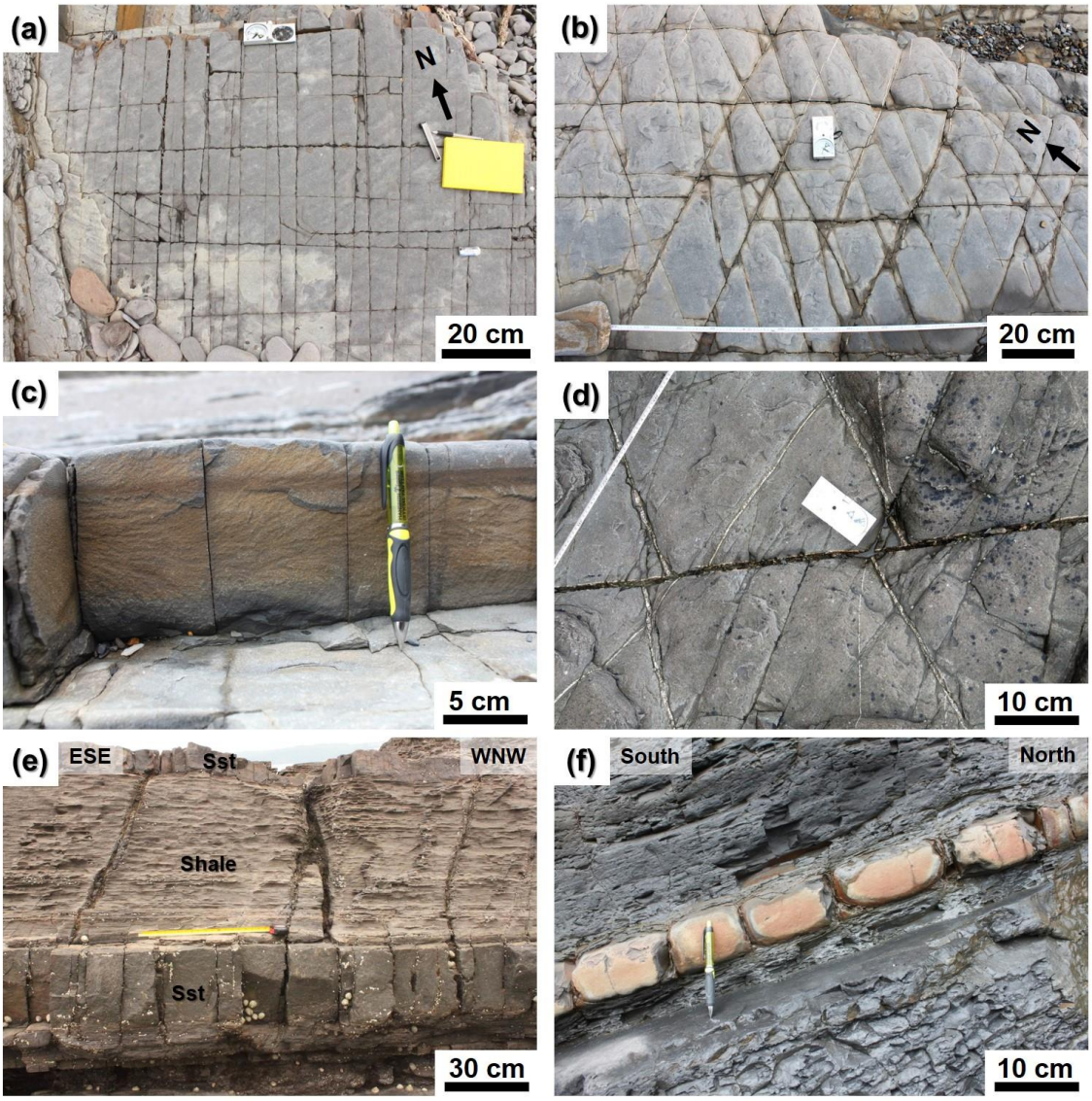

Figure 5 Photographs of layer-scale fractures in the field. The outcrops locations are shown in Figure 2a. **(a)** Orthogonal fractures (two directions) at outcrop I. **(b)** Fractures and mineral veins with three directions at outcrop H. **(c)** Fractures in sandstones and shale at outcrop I. Plumose structures on the fracture surface indicates it is extension fractures. Extension fractures are common where orthogonal fracture developed, which is concordant with relationship between Mohr circle and failure envelope. **(d)** Hybrid (shear + extension) fractures at outcrop H. Hybrid fractures are more common where fractures developed in three directions. **(e)** Fractures in sandstones and shale at outcrop G. Most fractures in the sandstones become arrested at their contacts with the shale. Fractures penetrating shales show semi-ductile nature and their planes are slightly curved or bent while fractures in the sandstones indicate brittle nature. Fractures in shale have different strikes, dips, and fracture modes from those in the sandstones. (**f**) Boudinage at outcrop I. Shale behaved as ductile to semi-ductile material during the extension fracture formation in the sandstone here.

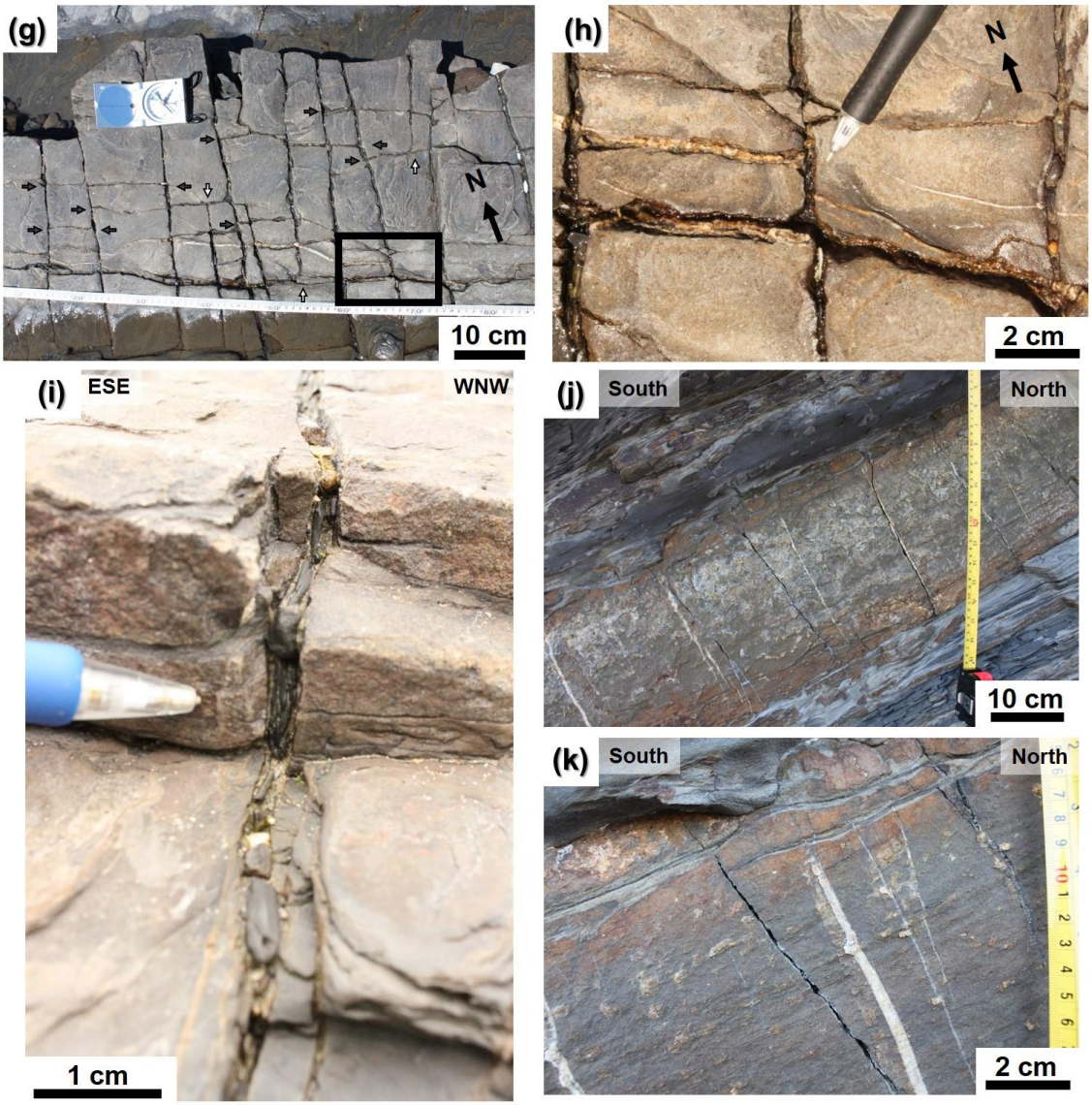

Figure 5 **(g)** Relative-age relationship between fractures at outcrop G. NNE-SSW striking fractures become arrested at white arrows and WNW-ESE striking fractures become arrested at black arrows. (**h**) Close up of the box of (g). Veins striking WNW-ESE also become arrested by fractures striking NNE-SSW in the sandstone layer. (**i**) NNE-SSW striking extension fractures which is filled with shale at the outcrop G. (**j**) Section view of extension fractures and veins at outcrop G. (**k**) Section view of the same sandstone layer as (j). Fiber structure perpendicular to the vein wall can be observed in the vein, which indicates simultaneous development of mineral precipitation and extension fracture opening (e.g. Figure 4 of chapter 5). Extension fracture in this section view probably developed later than the veins since they were not filled during mineral precipitation phase.

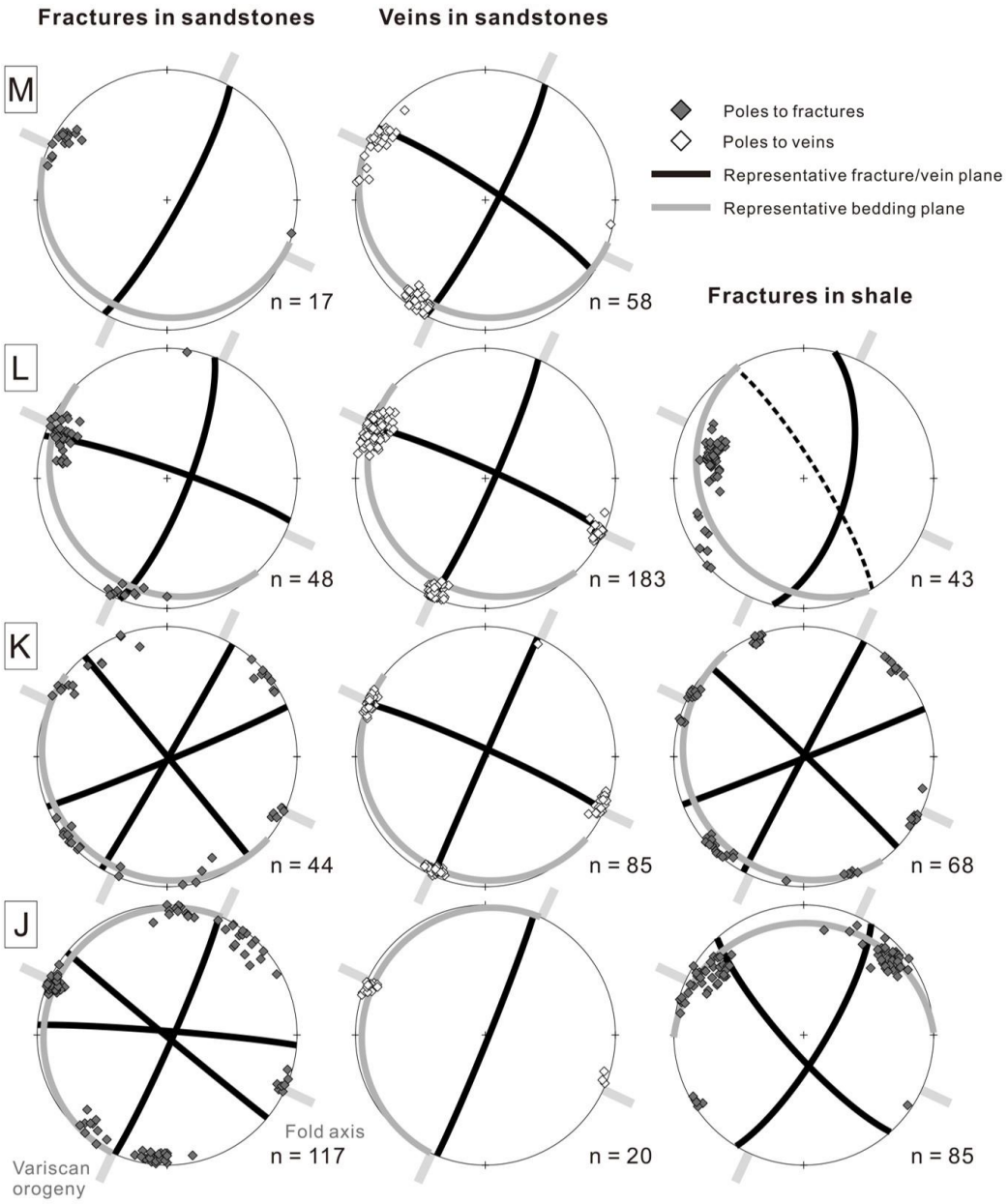

Figure 6 Fracture and vein patterns in the sandstones and shale layers. Capital letters on the upper left of stereonets indicate localities shown in Figure 2a. Fractures and veins were also measured in Amroth Freshwater Limestone in outcrop J. All fractures and veins are plotted as poles to the planes in the stereonets. Representative fracture or vein planes are shown by black great circles. Average bedding planes in the outcrops are also denoted by great circles in grey colour. The total number of fractures and veins is shown on the lower right of stereonet. Direction of fold axis calculated by beddings is shown with the stereonets. The Variscan orogeny is perpendicular to the fold axis.

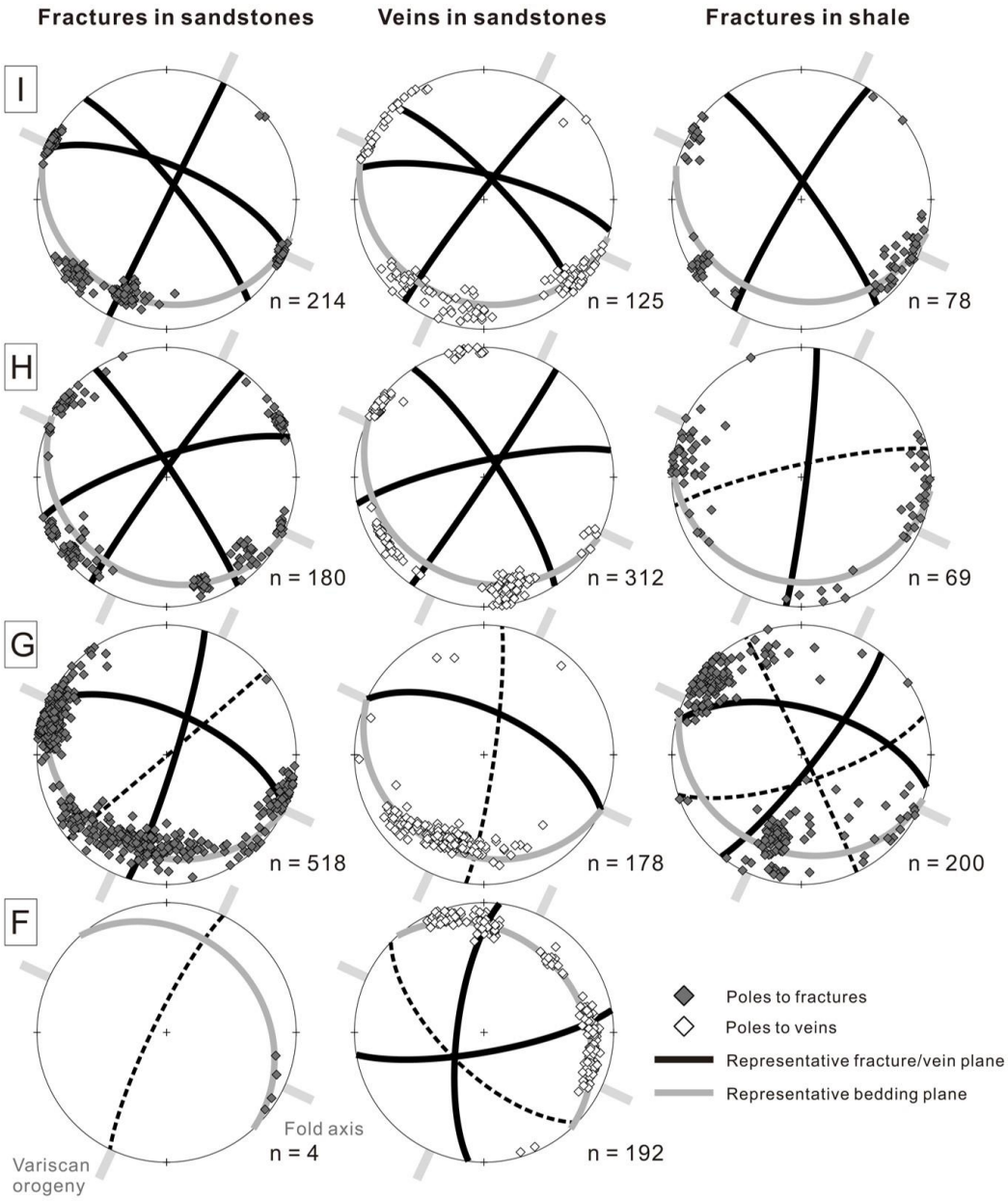
Fractures in sandstones
Veins in sandstones
Fractures in shale
I
H
G
F
n = 214
n = 125
n = 78
n = 180
n = 312
n = 69
n = 518
n = 178
n = 200
Fold axis
n = 4
n = 192
Variscan orogeny
Poles to fractures
Poles to veins
Representative fracture/vein plane
Representative bedding plane

Figure 6

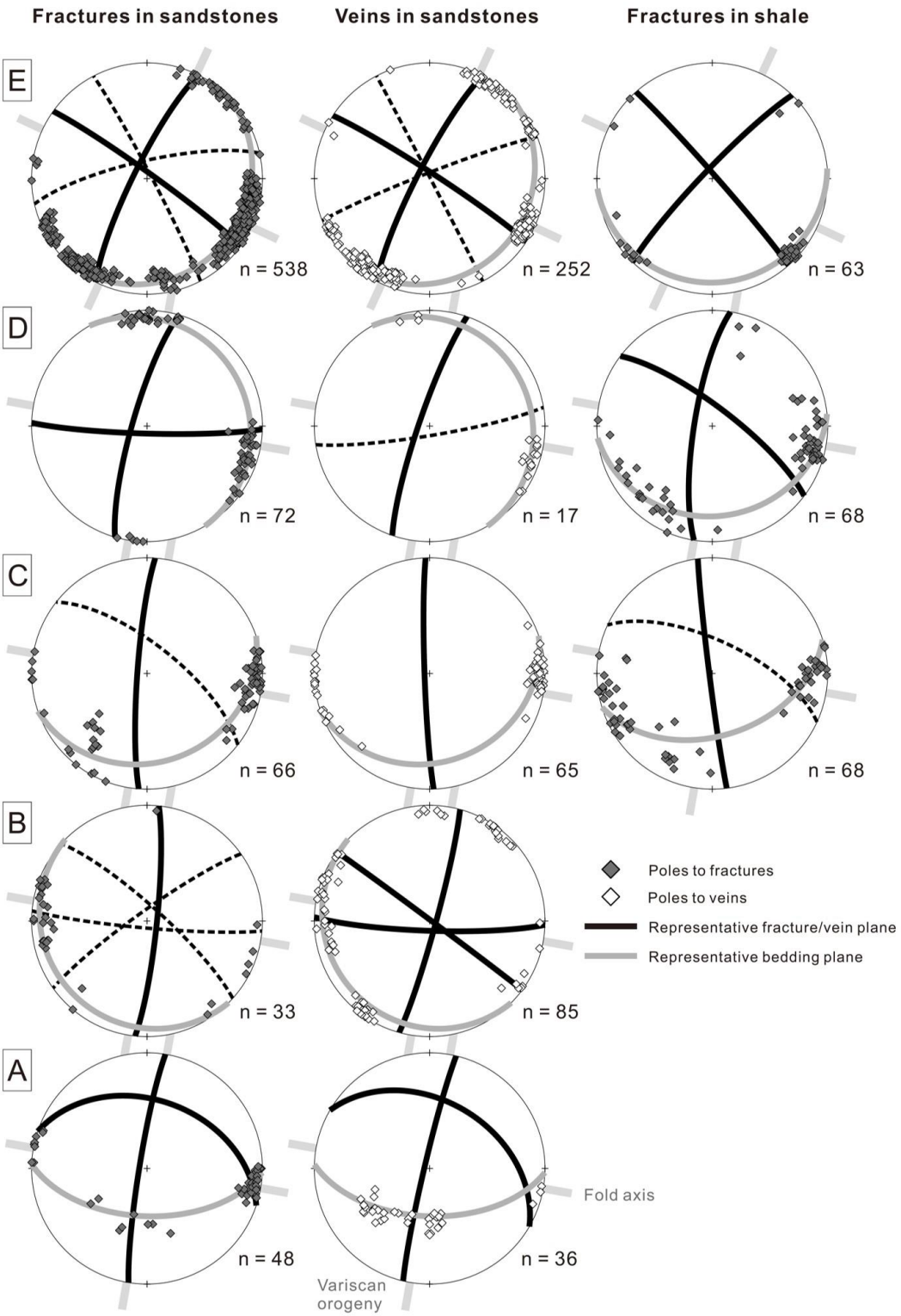
Fractures in sandstones
Veins in sandstones
Fractures in shale
E
n = 538
n = 252
n = 63
D
n = 72
n = 17
n = 68
C
n = 66
n = 65
n = 68
B
n = 33
n = 85
A
n = 48
n = 36
Variscan orogeny
Poles to fractures
Poles to veins
Representative fracture/vein plane
Representative bedding plane
Fold axis

Figure 6

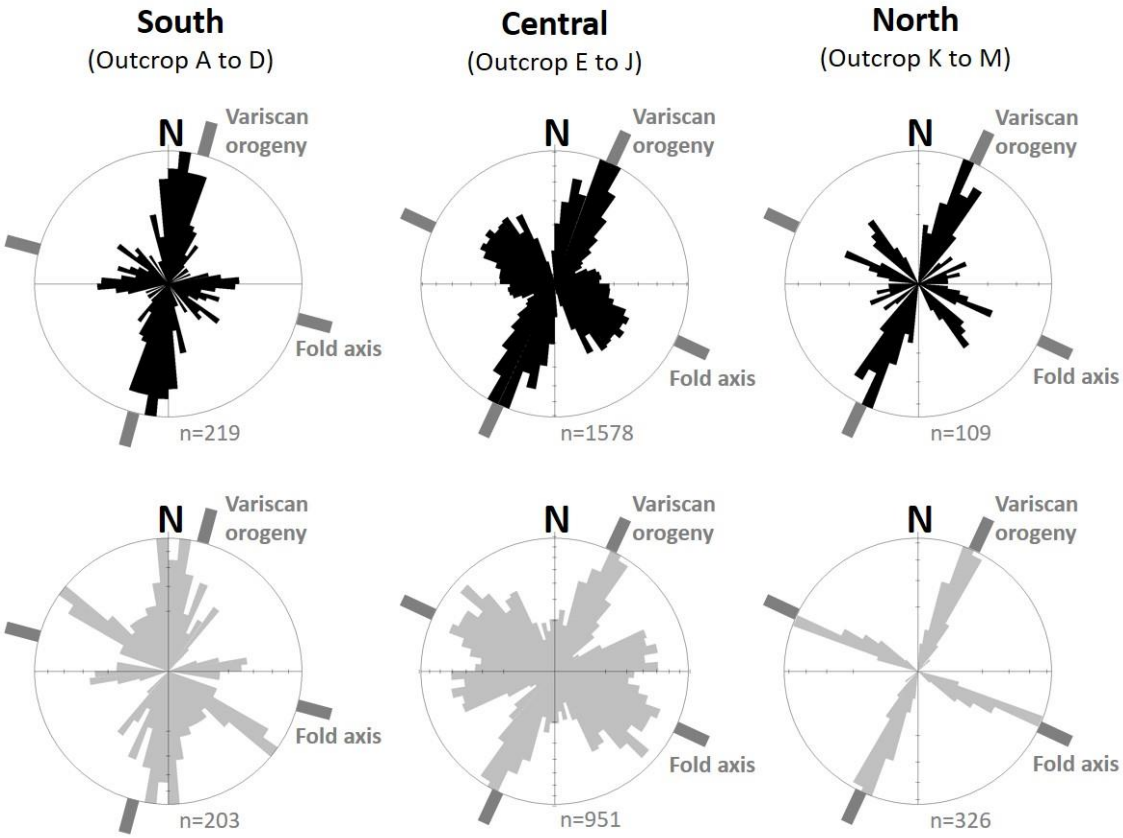

Figure 7 Area-normalised rose diagrams for fractures and veins within sandstones and limestone in three areas: South, central and north. Fractures in shale are not included. Upper rose diagrams are for extension fractures and lower diagrams are for mineral veins.

4.3. Relative-age relationship between the fractures and veins

Figure 5(g) shows relative-age relationships between the fractures developed in the two directions at outcrop G. The fractures show orthogonal pattern: one of the fracture sets is parallel to the compression of Variscan orogeny and the other is perpendicular or sub-perpendicular to the orogeny. In Figure 5(g), it is seen that many fractures striking WNW-ESE become arrested at contact with fractures striking NNE-SSW. This indicates the fracture propagation in the WNW-ESE direction was arrested by pre-existing discontinuities. Thus, fractures parallel to the Variscan compression (NNE-SSW) are older than ones perpendicular to the compression (WNW-ESE). However, some fractures striking NNE-SSW also become arrested on meeting fractures striking WNW-ESE, suggesting they were also formed or propagated after the development of WNW-ESE-striking fractures. This indicates extension fractures striking NNE-SSW

were initiated earlier but the two sets of fractures have formed at approximately same time in geological time scale at this outcrop.

A remarkable observation at the outcrop G is that the extension fractures are partly filled with shale (Figure 5i), suggesting the extension fractures formed before shale consolidation. Veins striking WNW-ESE also become arrested by the fractures with shale intrusion (Figure 5h). As described above, ductile to semi-ductile behaviour of shale is observed in association with extension fracturing at several outcrops (Figure 5f). Extension fractures associated with ductile shale might have been developed at the older stage.

In contrast, extension fractures developed at the stage younger than vein formation must exist in the long history of the basin. Several fractures clearly formed after the mineral precipitation are also observed in the field (Figure 5j, k). They may be formed in relation with crustal uplift/exhumation of the basin.

As a summary, there must be at least two stages for extension fracture formation which are not filled with minerals. Fractures associated with ductile to semi-ductile shale probably developed at the earliest stages. Extension fractures filled with shale formed earlier than veins striking WNW-ESE at least at outcrop G. However, veins (extension fracture formation associated with mineral precipitation) probably formed at the nearly same time as the shale-related extension fracture formation since shale also behaved as ductile material during the vein formation as the veins never penetrate shale in the study area. Younger fractures not filled with any materials also exist although number of development stages of the fractures which are younger than veins is not clear.

4.4. Relation of timing of the fractures and vein formation to basin history

As described above, the shale layers behaved as ductile to semi-ductile material during the fracture formation at several outcrops while the sandstone layers behaved as brittle. The semi-ductile nature indicates that the shale was not fully consolidated at that time. Unconsolidated shale is common in sedimentary basins, especially in cases where the sedimentation rate is high. This is because pore-fluid pressure is kept high in the impermeable shale during sedimentation and the high pore-fluid pressure prevents consolidation. The semi-ductile behaviour of the shale layers suggests that the extension

fractures formed when the sandstone layers were sufficiently consolidated to behave as brittle while shale layers were not.

Poles to the fractures mostly fall on the great circle of the bedding plane at all the outcrops (Figure 6), indicating the beds and fractures are mutually perpendicular throughout the study area. This is despite the fact that the beds are strongly folded as a result of the Variscan orogeny. The perpendicular attitude suggests the possibility that the fracture formation somewhat predates or coincides with that of the regional folding. The folding in this area was initiated slightly earlier than the maximum burial of the basin (Cole et al., 1991; Jones, 1991; Bevins et al., 1996). This further supports our suggestion that the layer-scale fracture networks were not formed during crustal uplift/exhumation but rather during basin subsidence.

However, before this conclusion as to the age of the fracture sets is set forth as clear conclusion, the possibility of the mechanical differences between the sandstones and shale causing stress rotation in which local principal stresses became parallel and perpendicular to the layer boundaries needs to be explored. This phenomenon may have caused the fractures to form perpendicular to the beddings after the folding. The impact of stress rotation after the folding is, therefore, studied by numerical modelling in next section and the relative-age relationship between the folding and fracture formation is examined in more detail.

5. Stress rotation within an inclined stiff sandstone layer surrounded by soft shale

5.1. Geometry and settings of the model

In order to examine the effect of stress rotation in the mechanical layers, we made numerical models with dipping stiff sandstone layer hosted by soft (more compliant) shale (Figure 8a). The shape of sandstone is assumed to be a flat ellipse in the model. The top and bottom boundaries are set to be parallel to each other and only edge parts of the sandstone are rounded. The rounded shape is to avoid local stress concentration caused by the sandstone shape with sharp layer corners.

COMSOL Multiphysics 4.3 (finite element code) was used for this computation. Liner elastic, continuous behaviour of the rocks and plane strain condition are postulated for the entire model. As the sandstone layer and shale are fully bounded as continuous media in the model, no slip is allowed along the layer boundaries. If we

assume layer-parallel slip along the boundaries, minimum principal stress σ_3 in the sandstone cannot be parallel to the layer during the deformation and no extension fracture perpendicular to the layer would form. This is not consistent with observed fact in the field. The case is, therefore, not simulated in this paper. Because scale of the modelling target (mechanical layers) is small enough (centimetre- to metre-scale) compared with stiffness of the rocks, self-weight of the sandstone and surrounding shale is ignored. Constant value of 0.25 is assigned to Poisson's ratio of both the sandstone and shale. This is because difference of Poisson's ratio between the rocks is commonly smaller than that of Young's modulus and has less impact on the computation results. Instead, relatively high Young's modulus ratio sandstone/shale, denoted by E_r, is used as a function ranging from 10 to 1000. This ratio represents the differences in stiffness, partly reflecting diagenesis (and thus compaction) of sandstone and shale.

Middle of top and bottom boundaries of the model are fixed in the *x*-direction and middle of the left and right boundaries are fixed in the *y*-direction (Figure 8a). Tensile stress σ_H is applied on the right and left boundaries as deformation event which formed tensile fractures in the sandstone layer. Compression stress σ_V is applied on the upper and lower boundaries as overburden pressure at the time of fracture formation. Ratio of vertical and horizontal stresses σ_V/σ_H is used as the other function. $\sigma_V/\sigma_H = 0$ represents surface condition while $\sigma_V/\sigma_H < 0$ indicates subsurface condition in the model.

By changing the dip of the sandstone as a consequence of the folding, direction of local principal stress σ_3 (tensile stress) generated by the input stresses σ_H and σ_V in the sandstone is numerically simulated. Subsequently, the angular difference, or 'angle gap' between the local principal stress σ_3 within the sandstone and dip of the sandstone layer is measured (Figure 8b). If the local principal stress σ_3 is parallel to the dip of sandstone (angle gap is approximately zero) as a result of stress rotation, tensile fracture perpendicular to the layer can be formed with the model setting.

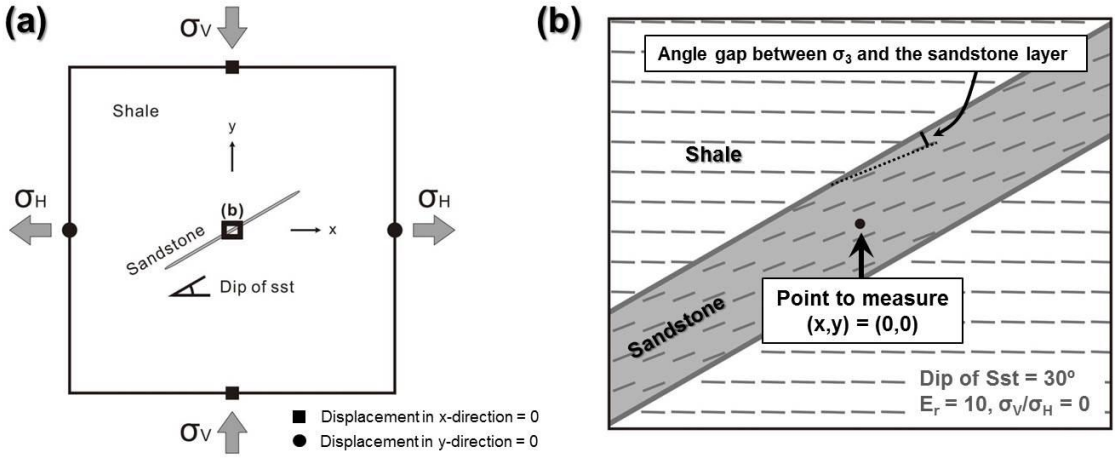

Figure 8 **(a)** Model geometry and boundary conditions. Coordinate origin is at the centre. Thin stiff sandstone is emplaced in the centre of soft shale. Middle of top and bottom boundaries of the model are fixed in *x*-direction and middle of the left and right boundaries are fixed in *y*-direction. Tensile stress σ_H is applied on the right and left boundaries and compression stress (overburden pressure) σ_V is applied on the upper and lower boundaries. **(b)** One of computation results at the model centre. Dip of sandstone, relative Young's modulus E_r and relative boundary stress σ_V/σ_H is set to be 30º, 10 and 0 in the model, respectively. The trajectories of σ_3 are shown. Angle gap between σ_3 and the sandstone layer is measured at the centre of model (x,y) = (0,0).

5.2. Results

Figure 9 shows computation results with six combinations of the above two functions (E_r, σ_V/σ_H). Abscissa axis is dip of sandstone and ordinate axis is angle gap between local stress σ_3 within the sandstone and the layer. The results indicate principal stress σ_3 cannot be parallel to the sandstone when it dips at 60 degrees or larger in surface condition ($\sigma_V/\sigma_H = 0$). This happens regardless of Er. The angle at which σ_3 cannot be parallel to the layer anymore is referred to as "critical angle" in this paper. Critical angle for surface condition ($\sigma_V/\sigma_H = 0$) is, thus, 60 degrees. When dip of the sandstone reaches the critical angle, σ_3 trajectories become horizontal in the entire model according to tensile stress applied as input at the right and left boundaries (Figure 10a). The critical angle is controlled by the function of σ_V/σ_H. It becomes smaller with smaller σ_V/σ_H, meaning the critical angle becomes smaller than 60 degrees in subsurface conditions (Figure 9). The relationship between σ_V/σ_H and critical angle is shown in Figure 10b.

The relative Young's modulus (sandstone/shale) E_r does not affect the critical angle. It is a function of curvature of the curvilinear relationship between the abscissa

and ordinate axes (Figure 9). As increase of E_r, the curvature becomes larger and the principal stress σ_3 within the sandstone becomes nearly parallel to the bedding if the bed's dip is smaller than critical angle. By contrast, as E_r is one (the smallest value, assuming that shale cannot be stiffer than sandstone), the curvature becomes zero and the curvilinear relationship becomes linear with same values in the abscissa and ordinate axes.

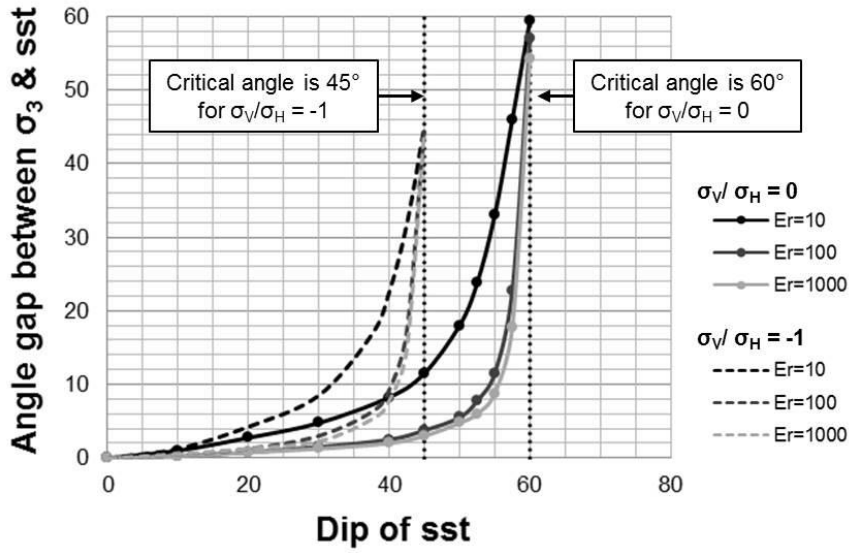

Figure 9 Angle gap (ordinate axis) between principal stress σ_3 within the sandstone and the bed under different geological conditions. If the dip of sandstone (abscissa axis) is 60 degrees (critical angle for surface condition) or larger, σ_3 cannot be parallel to the bedding regardless of Er. The computation results indicate that ratio of vertical and horizontal stresses σ_V/σ_H directly controls the critical angle (Figure 10b). Relative Young's modulus E_r controls curvature of the curvilinear relationship between abscissa and ordinate axes.

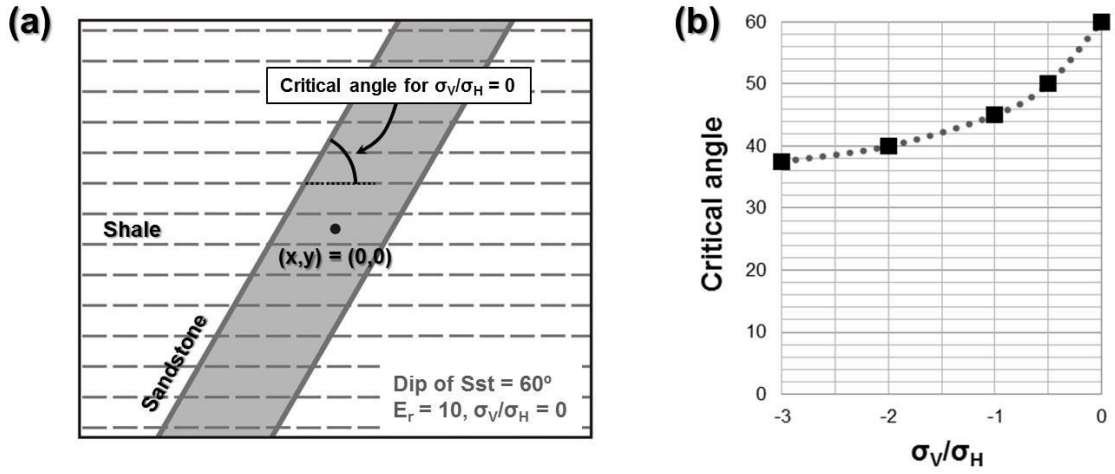

Figure 10 **(a)** A computation result showing σ_3 trajectories when dip of sandstone reaches critical angle. Dip of sandstone, E_r and σ_V/σ_H are 60º, 10 and 0, in the model, respectively. However, Er actually has no influence on critical angle. σ_3 trajectories become horizontal regardless of Er when the dip of sandstone reaches critical angle. **(b)** Relationship between critical angle (ordinate axis) and ratio of vertical to horizontal stresses σ_V/σ_H (abscissa axis).

6. Discussion

6.1. Possibility of extension fracture formation perpendicular to the beddings after the Variscan Folding

Price (1963) reports tensile strength of the Pennant sandstones is 15-19 MPa, based on laboratory experiments. The Pennant sandstones form a part of the Upper Coal Measures. Although the sandstones in the current study area are from Lower and Middle Coal Measures, the two sandstones deposited at approximately the same geological period; they are thus of a similar age and have experienced same burial and tectonic histories, suggesting that the tensile strength of the Pennant sandstones may be used as reasonable estimates of tensile strength of the sandstones in the current study area. If 17 MPa (median of 15-19 MPa) is applied as horizontal boundary tensile stress σ_H in the numerical model, σ_V/σ_H = -1 (critical angle = 45º) represents geological conditions at depth around 700 metres by assuming rock bulk density is 2500 kg/m^3. Taking into account that laboratory experiments generally yield higher tensile strengths than in-situ (field) measurements (Gudmundsson, 2011) and that local stresses are concentrated into relatively stiff materials, the horizontal boundary stress σ_H to form tensile fractures in the sandstone is much smaller than 17 MPa in actual subsurface

conditions. As typical in-situ tensile strengths are 2-4 MPa (Gudmundsson, 2011), σ_V/σ_H = -1 probably represents geological conditions much shallower than 700 metres. In other words, the critical angle easily becomes less than 45 degrees (σ_V/σ_H < -1) with a depth of a few hundred metres in actual geological conditions. Thus, the computation results suggest it would be difficult to form fractures perpendicular to the beddings by horizontal tensile stress when the beds dip at around 45 degrees or larger under most subsurface conditions.

Alderton et al. (2004) report the results of fluid inclusion analyses within quartz veins in anthracite zone of the South Wales coalfield where the current study area lies. They show the pressure and temperature ranges of the quartz precipitation were 180-220 ºC and 60-80 MPa in the anthracite zone. As the physical conditions were estimated from fluid inclusions, the pressure does not represent vertical stress (overburden pressure) but total fluid pressure which is normally less than the vertical stress. They assume the pressure and temperature conditions correspond to a depth of 3,500 to 4,500 metres. Although it is not necessary that all quartz veins in the anthracite zone formed under the same physical conditions, their results imply that the quartz veins in the current study area also formed at the similar depth condition. If we assume the quartz veins formed at a depth of 4,000 metres (median of 3,500-4,500 metres) in the study area, σ_V becomes 98 MPa with rock bulk density of 2500 kg/m^3. As σ_H for tensile fracture formation in the sandstones would be about 5-20 MPa, σ_V/σ_H becomes -5 or less. The corresponding critical angle is about 35 degrees or less. Thus, when we consider the extension fracture formation related with quartz precipitation in the study area, layer-controlled veins could not be formed in the area where beds dip 35 degrees or more.

Bedding planes dip about 60 degrees at site A where the effect of the Variscan Folding is the strongest in outcrops we investigated. Layer-scale extension fractures and veins are common in the sandstones, and they are perpendicular to the bedding at the site as well as the other locations (Figure 6). Although we do not have clear constraints on the open-fractures, the veins probably formed at a depth of a few thousand metres or more (Alderton et al. 2004), implying that at least the veins could not form after the beds dipped 35 degrees or more. It is, thus, suggested that the vein formation predates the Variscan Folding, and that mechanisms other than crustal uplift/exhumation are

required to account for the formation of the extension fracture system associated with veins which has orthogonal patterns at some sandstone layers. Many of these fractures related with quartz precipitation may be formed by high fluid pressure (fluid overpressure caused by gas, water, etc), horizontal tensile stress having acted before folding or combination of them. These hypotheses will be examined in chapter 5 of this thesis.

6.2. Sequence of layer-scale fracture and vein formations and their relation to the basin history

As discussed in section 4.3, extension fractures associated with shale ductile to semi-ductile behaviour are older than mineral veins at least at outcrop G. By combining this field observation with the discussion in section 6.1, extension fractures associated with shale and mineral precipitation must have been formed during basin burial. Ductile behaviour of shale is concordant with the hypothesis.

Other extension fractures not filled with any materials might have been formed at the younger stage, such as crustal exhumation/uplift. In addition, from general considerations, open fractures must be the youngest. This is because if those open fractures existed during the mineral precipitation or shale ductile behaviour, the fractures also must have been filled with the materials. In addition, if the open fractures existed in the geological formation, subsequent fracture systems could not be formed effectively because the most strain must have been accounted by displacement of the existing open fracture systems which are the weakest or most compliant parts in the formation.

7. Conclusions

The field studies and numerical modelling reveal relative-age relationships between layer-scale extension fractures, layer-scale veins and the Variscan Folding at the western part of South Wales coalfield. The results suggest that at least the vein formation predate the Variscan Folding. The Variscan Folding was initiated at approximately same time as maximum burial of the basin, indicating the layer-scale orthogonal extension vein system in the study area formed not during crustal uplift/exhumation but rather during basin burial. Several extension fractures associated with shale are older than the extension veins. Thus, extension fracture systems have the

potential to develop in the early stage of basin history and affect the permeability and fluid transport in deep, subsurface reservoirs although they may behave as barrier of fluid transportation when the fractures are filled with some materials. The main contributions and results of this paper are as follows.

1. Layer-scale fractures and veins in the sandstones and shale which developed in two (orthogonal) or three directions were documented from southern end to northern end at the western parts of the South Wales coalfield. Field observations show relative-age relationship between them: boudinage structures of sandstones and fractures filled with shale in the sandstones are oldest; fractures filled with minerals are second oldest; open fractures (fractures not filled with other materials) are the youngest.
2. Effects of stress rotation were examined by numerical modelling. The results suggest that extension fractures perpendicular to the bedding cannot form when the beds dip 45 degrees or more in most geological conditions, and that at least the layer-scale vein systems formed before the Variscan Folding in the study area.
3. Based on the above two results, layer-scale fractures filled with shale or minerals which could work as barrier of fluid transportation developed during basin burial in the current study area. Development phase of open fractures which could enhance fluid transportation is not well-constrained in this study. However, the open fractures developed after the quartz precipitations whose physical conditions were close to maximum burial of the basin, implying the possibility that the open fractures mostly formed during crustal uplift/exhumation.
4. Minimum compression strain caused by the map-scale folds is calculated as 7%, 21%, 40% in the study area, which increases towards the Variscan Deformation Front (Ritec Fault).

References

Alderton, D.H.M., Oxtoby, N., Brice, H., Grassineau, N., Bevins, R.E., 2004. The link between fluids and rank variation in the South Wales Coalfield: evidence from fluid inclusions and stable isotopes. Geofluids 4, 221-236.

Archer, A.A., 1968. The Upper Carboniferous and later formations of the Gwendraeth Valley and adjoining areas. Special Memoir of the Geological Survey of Great Britain. Her Majesty's Stationery Office, London.

Bai, T., Maerten, L., Gross, M.R., Aydin, A., 2002. Orthogonal cross joints: do they imply a regional stress rotation? Journal of Structural Geology 24, 77-88.

Belayneth, M., Geiger, S., Matthai, S.K., 2006. Numerical simulation of water injection into layered fractured carbonate reservoir analogs. AAPG Bulletin 90, 1473-1493.

Bevins, R.E., White, S.C., Robinson, D., 1996. The South Wales Coalfield: low grade metamorphism in a foreland basin setting? Geological Magazine 133, 739-749.

Calver, M.A., 1969. Westphalian of Britain. Sixieme Congres International de Stratigraphie et de Geologie du Carbonifiere, Compte Rendu 1, 233-254.

Caputo, R., 1995. Evolution of orthogonal sets of coeval extension joints. Terra Nova 7, 479-490.

Cole, J.E., Miliorizos, M., Frodsham, K., Gayer, R.A., Gillespie, P.A., Hartley, A.J., White, S.C., 1991. Variscan structures in the opencast coal sites of the South Wales Coalfield. Proceedings of the Ussher Society 7, 375-379.

Frodsham, K., Gayer, R.A., James, J.E., Pryce, R., 1993. Variscan thrust deformation in the South Wales Coalfield: a case study from Ffos Las opencast coal site. In: Gayer, R.A., Greiling, R.O., Vogel, A.K. (Eds.), Rhenohercynian and Subvariscan Fold Belts. Earth Evolution Series, Vieweg, Braunschweig, 315-348.

Frodsham, K., Gayer, R.A., 1997. Variscan compressional structures within the main productive coal-bearing strata of South Wales. Journal of the Geological Society, London 154, 195-208.

Gayer, R.A., Jones, J., 1989. The Variscan foreland in South Wales. Proceedings of the Ussher Society 7, 177-179.

Gayer, R.A., Pesek, J., 1992. Cannibalisation of Coal Measures in the South Wales Coalfield—significance for foreland basin evolution. Proceedings of the Ussher Society 8, 44-49.

Gayer, R.A., Cole, J., Greiling, R.O., Hecht, C., Jones, J., 1993. Comparative evolution of coal-bearing foreland basins along the Variscan northern margin in Europe. In: Gayer, R.A., Greiling, R.O., Vogel, A.K. (Eds.), Rhenohercynian and Subvariscan Fold Belts. Earth Evolution Series, Vieweg, Braunschweig, 48-82.

George, T.N., 1970. British Regional Geology: South Wales, 3rd edition. Her Majesty's Stationery Office, London.

George, G.T., Kelling, G., 1982. Stratigraphy and sedimentation of Upper Carboniferous sequences in the coalfield of south-west Dyfed. In: Bassett, M.G. (Ed.), Geological Excursions in Dyfed, South-West Wales. National Museum of Wales, Cardiff, 175-202.

George, G.T., 2001. Late Yeadonian (Upper Sandstone Group) incised valley supply and depositional systems in the South Wales peripheral foreland basin: implications for the evolution of the Culm Basin and for the Silesian hydrocarbon plays of onshore and offshore UK. Marine and Petroleum Geology 18, 671-705.

Griffith, A.A., 1924. Theory of rupture. In: Biezeno, C.B., Burgers, J.B. (Eds.), Proceedings of the First International Congress on Applied Mechanics. Delft, Waltman, 55-63.

Gudmundsson, A., 2011. Rock Fractures in Geological Processes. Cambridge University Press, New York.

Hancock, P.L., Dunne, W.M., Tringham, M.E., 1983. Variscan deformation in southwest Wales. In: Hancock, P.L. (Ed.), The Variscan Fold Belt in the British Isles. Adam Hilger, Bristol, 47-73.

Hartley, A.J., Warr, L.N., 1990. Upper Carboniferous foreland basin evolution in SW Britain. Proceedings of the Ussher Society, 7, 212-216.

Hartley, A.J., 1993. Silesian sedimentation in South-West Britain: sedimentary responses to the developing Variscan Orogeny. In: Gayer, R.A., Greiling, R.O., Vogel, A.K. (Eds.), Rhenohercynian and Subvariscan Fold Belts. Earth Evolution Series, Vieweg, Braunschweig, 159-196.

Hathaway, T.M., Gayer, R.A., 1996. Thrust-related permeability in the South Wales Coalfield. Geological Society, London, Special Publications 109, 121-132.

Jones, J.A., 1989. The influence of contemporaneous tectonic activity on Westphalian sedimentation in the South Wales Coalfield. In: Arthurton, R.S., Gutteridge, P., &

Nolan, S.C. (Eds.), The role of tectonics in Devonian and Carboniferous sedimentation in the British Isles. Occasional Publication of the Yorkshire Geological Society 6, 243-253.

Jones, J.A., 1991. A mountain front model for the Variscan deformation of the South Wales coalfield. Journal of the Geological Society, London, 148, 881-892.

Kelling, G., 1988. Silesian sedimentation and tectonics in the South Wales Basin: a brief review. In: Besly, B., Kelling, G. (Eds.), Sedimentation in a Synorogenic Basin Complex: The Upper Carboniferous of Northwest Europe. Blackie, Glasgow, 38-42.

Leveridge, B.E., Hartley, A.J., 2006. The Variscan Orogeny: the development and deformation of Devonian/Carboniferous basins in SW England and South Wales. In: Brenchley, P.J., Rawson, P.F. (Eds.), The geology of England and Wales. Geological Society of London, London, 225-255.

Owen, T.R., 1953. The structure of the Neath disturbance between Bryniau Gleision and Glynneath, South Wales. Quarterly Journal of the Geological Society, London 109, 333-365.

Price, N.J., 1963. The Influence of Geological Factors on the Strength of Coal Measure Rocks. Geological Magazine 100, 428-443.

Roberts, J.C., 1965. Quartz microfracturing in the North Crop of the South Wales coalfield. Geological Magazine, 102, 59-73.

Simon, J.L., Seron, F.J., Casas, A.M., 1988. Stress deflection and fracture development in a multidirectional extension regime: mathematical and experimental approach with field example. Annales Tectonicae 2, 21-32.

Trotter, F.M., 1947. The Structure of the Coal Measures in the Pontardawe-Ammanford area. South Wales. Quarterly Journal of the Geological Society, London 103, 89-133.

Wennberg, O.P., Azizzadeh, M., Aqrawi, A.A.M., Blanc, E., Brockbank, P., Lyslo, K.B., Pickard, N., Salem, L.D., Svana, T., 2007. The Khaviz Anticline: an outcrop analogue to giant fractured Asmari Formation reservoirs in SW Iran. Geological Society, London, Special Publications 270, 23-42.

Woodland, A.W., Evans, W.B., 1964. The geology of the South Wales coalfield, part IV. The country around Pontypridd and Maesteg, 3rd edition. Memoirs of the Geological Survey of Great Britain, Her Majesty's Stationery Office, London.

Chapter 5: Paper 2

Manuscript in preparation

Title: Fluid overpressure estimation from quartz vein aspect ratio in the South Wales coalfield

Authors: Tetsuzo Fukunari and Agust Gudmundsson

Total number of manuscript pages: 30

Statement of my role for the paper 2:

- Collection of structural data
- Analytical calculations with initial support from co-author
- Writing the manuscript and illustrating the figures

Fluid overpressure estimation from quartz vein aspect ratio in the South Wales coalfield

Tetsuzo Fukunari[1,2,*], Agust Gudmundsson[1]

[1]Department of Earth Sciences, Royal Holloway University of London, Egham, Surrey TW20 0EX, UK

[2]Japan Oil, Gas and National Corporation (JOGMEC), Toranomon Twin Building, 2-10-1 Tranomon, Minato-ku, Tokyo 105-0001, JAPN

* email: fukunari-tetsuzo@jogmec.go.jp

Abstract

In order to estimate the fluid overpressure (driving pressure) at the time of vein formation in sandstone layers in the South Wales (UK) coalfield, the aspect (length/thickness) ratios of 502 quartz veins were measured. The veins are estimated to have precipitated at temperatures of 130-220ºC. The results show that the average fluid overpressure at the time of vein formation was about 35 MPa as maximum value. The in-situ tensile strength of sedimentary rocks, including sandstone layers, is generally less than about 10 MPa (we estimate the maximum theoretical tensile strength as 13 MPa in this study) and equal to the excess fluid pressure in the fluid source at its time of rupture and fracture formation. The estimated overpressure is thus much higher than the excess pressure. We relate the high overpressure to two factors: (1) buoyancy and (2) stress concentration in the sandstone layers. Buoyancy relates to the difference in density between the host rock and the fluid (here geothermal water) and increases with increasing dip dimension of the fracture (height of fracture above its fluid source). Stress concentration in the sandstone layers contributes to increasing the difference σ_d between the principal stresses ($\sigma_d = \sigma_1 - \sigma_3$) in the layers. The results suggest that the overpressure was much higher (average 48 MPa) for veins striking NNE-SSW than the overpressure (average 28 MPa) for veins striking WNW-ESE, a difference we attribute

largely to difference in stress concentration. The overpressure results are somewhat higher than those estimated for veins in carbonate rocks (limestone layers) in the Bristol Channel, which we attribute partly to different mechanical properties of limestone and sandstone.

Keywords: fluid overpressure, quartz vein, aspect ratio, fracture formation, South Wales coalfield

1. Introduction

Fracture that development in several directions, such as happens during the formation of orthogonal extension fractures, normally form interconnected networks of comparatively high permeability. Such networks are of great importance in permeability and fluid transport in subsurface reservoirs. Several mechanisms are proposed for the development of such fracture networks, including the following: (1) local stress rotation or flip due to formation of the first set of fractures (Simon et al., 1988; Caputo, 1995; Bai et al., 2002); (2) regional principal stress rotation (Hancock et al., 1987; Eyal, 1996); and (3) post-tectonic strain relaxation of visco-elastic materials (Rives and Petit, 1990; Rives et al., 1994). Regardless of these proposed mechanisms, relationships between the fracture-network formation and the associated geological events and processes are unclear in many sedimentary basins. This is because the mechanism of fracture-network formation may be different for different geological settings and mechanical rock properties, even if the resulting networks may look similar.

The South Wales coalfield is one of foreland basins developed during the Variscan Orogeny (e.g. Kelling, 1988; Gayer and Jones, 1989; Hartley and Warr, 1990; Gayer et al., 1993; Rippon et al., 1997; Burgess and Gayer, 2000; Leveridge and Hartley, 2006). Chapter 4 of this thesis provides detailed data on the patterns of layer-scale fracture-networks in the sandstone layers of the alternating sand-shale pile in the South Wales coalfield. It suggests that the fracture-network was originally developed during the basin subsidence. However, it is not clear which main mechanism contributed the fracture-network formation during the basin subsidence.

The present paper extends and complements the work of chapter 4 and provides new field results and analytical calculations on the layer-scale quartz veins in the sandstones with a view to estimate fluid overpressure at the time of vein formation. The

quartz veins developed in the same directions, that is, have the same strikes, and are of the same fracture mode (mode I) as the layer-scale fractures. Although the open fractures most likely changed their shape slightly subsequent to their initiation, such as the fracture aperture and length, depending on the confining pressure, tectonic stresses, and the later propagation of the fractures, the mineral veins have essentially kept their original shape and preserved the physical conditions at the time of vein formation.

Here we apply same methodology as Philipp (2008, 2012) and Philipp et al. (2013) who calculated the fluid overpressure during the formation of calcite veins from their aspect (length/thickness) ratios at Kilve in the Bristol Channel in Southwest England. Although there have been many studies on the South Wales coalfield, focusing on sedimentology (e.g. Kelling, 1974; George and Kelling, 1982; Wright, 1987; Jones, 1989; Hartley, 1993), deformation (e.g. Cole et al., 1991; Jones, 1991; Frodsham et al., 1993; Hathaway and Gayer, 1994; Hathaway and Gayer, 1996; Frodsham and Gayer, 1997) and metamorphism (e.g. White, 1991; Alderton and Bevins, 1996; Bevins et al., 1996; Gayer et al., 1998), fluid overpressure associated with the formation of the quartz veins has not been studied before in this area.

This paper has two principal aims. First, to present field structural data and observations of the quartz veins, and discusses the timing of the vein formation in association with the layer-scale fracture formation. Second, to use the vein aspect ratios measured in the field, together with basic fracture mechanics, to calculate the associated fluid overpressure during vein formation. In addition, we also discuss the stress conditions which may have contributed to generate the fluid overpressure and the associated mechanism for the development of mineral-filled extension fractures.

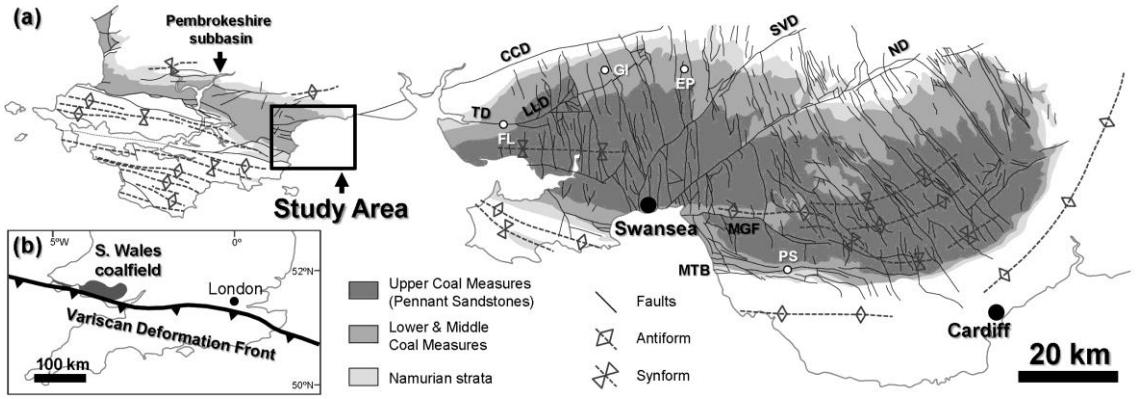

Figure 1 **(a)** Geological map of Silesian sediments in South Wales (Hancock et al., 1983; Hartley 1993). The study area is delineated by a box. Opencast coal sites: FL, Ffos Las; GI, Gilfach Iago; EP, East Pit; PS, Park Slip. Key structures: CCD, Carreg Cennen Disturbance; TD, Trimsaran Disturbance; LLD, Llanon Disturbance; SVD, Swansea Valley Disturbance; ND, Neath Disturbance; MGF, Moel Gilau Fault; MTB, Margam Thrust Belt. **(b)** Inset box shows a relationship between the South Wales coalfield and the Variscan orogeny.

2. Geological setting in the South Wales coalfield

2.1. Sediments and structures in the South Wales coalfield

The present-day South Wales coalfield forms a northward verging syncline with east-west-trending axis (Figure 1). The basin was mostly filled with the Westphalian to Lower Stephanian Coal Measures, which is rimmed by narrow exposures of the Namurian strata. The Namurian sediments are the oldest siliciclastic deposits in the basin and generally overlie the regional unconformity on the Dinantian Carbonates (e.g. Wright, 1987; Leveridge and Hartley, 2006). They are shale-dominant sequences in offshore to shoreface with some fluvio-deltaic channels (e.g. George and Kelling, 1982; Hartley, 1993), which are upwardly transferred into lower to upper coastal plain deposits of the Lower and Middle Coal Measures (Westphalian A to lower Westphalian C). The Lower and Middle Measures are also shale-dominant sequences. Productive coals are mostly contained in these units (e.g. Jones, 1989; Hartley, 1993). Palaeocurrents of the fluvial sandstone bodies in the sediments do not show consistent trend across the basin while terrestrial braided fluvial cannels in the Upper Coal Measures (upper Westphalian C to Westphalian D) indicate dominant flow towards the north (Bluck and Kelling, 1963; Kelling, 1974). This sedimentological evidence most likely reflects basinward progression of the Variscan orogenic belt from the south-

southwest. The Upper Measures are sandstone-dominant sequences, interpreted as deposits in alluvial braided plains. The sandy succession is also referred to as Pennant sandstones.

The coalfield was developed as foreland basin during the northward progression of the Variscan orogenic belt (e.g. Gayer and Jones, 1989; Gayer et al., 1993; Burgess and Gayer, 2000). As a result of the propagation of the compression stress from the orogenic zone, map-scale and outcrop-scale compression-generated structures, such as thrusts and folds, are common throughout the basin (e.g. Cole et al., 1991; Jones, 1991; Frodsham et al., 1993; Hathaway and Gayer, 1996; Frodsham and Gayer, 1997). The structures generally trend E-W to WNW-ESE, that is, in directions subparallel to the Variscan orogenic belt. Timing of the major compression in the current basin area is interpreted as late Westphalian D (nearly end of the sedimentation) at the earliest based on the field studies (e.g. Cole et al., 1991; Jones, 1991). Bevins et al. (1996) also suggest the major folding was induced slightly earlier than the event during which the temperature reached its maximum, based on the interpretation of layers of equal volatile matter.

2.2. Layer-scale fractures in the western part of the South Wales coalfield

Layer-scale fractures are common in the sandstones in the western part of the basin (Chapter 4 of this thesis). Most fractures are extension fractures with apertures that range in size from one millimetre to a few centimetres. Some hybrid or mixed-mode (extension + shear) fractures are also observed. At different localities, the fractures strike in two or three main directions (Figure 2a). In the networks where the fractures strike in two main directions, the fractures are mostly orthogonal: one of the fracture sets is parallel to the direction of the Variscan orogenic compression and the other is parallel to the regional fold axis. The fracture pattern becomes somewhat more complex towards the Variscan orogen, where the fractures parallel to the fold axis strike in two non-orthogonal directions, possibly as conjugate mixed-mode or hybrid (extension + shear) fractures.

Fractures striking WNW-ESE (parallel to the fold axis) become arrested at contacts with fractures striking NNE-SSW (parallel to the Variscan compression) in several outcrops. This suggests that the fracture propagation in WNW-ESE direction is

mostly younger and became arrested at the older and thus pre-existing NNE-SSW striking fractures. It is also observed that both NNE-SSW and WNW-ESE striking fractures become arrested on contact with other fracture sets (with different strikes) where these occur in the same outcrops. Based on these field observations, chapter 4 of this thesis suggests that the two fracture sets, the NNE-SSW and the WNW-ESE striking, were formed at a similar time (the WNW-striking being generally somewhat older, however).

The layer-scale fractures are perpendicular to the bedding across the study area, even where the beds are strongly folded. The perpendicular attitude suggests the fracture formation predates or coincides with that of the folding. Chapter 4 provides results of numerical modelling which show stress rotation cannot account for the fracture formation perpendicular to the beds after the Variscan folding in the study area. By considering that the Variscan folding was initiated just before the maximum burial of the basin, it is interpreted that the layer-scale fracture network was formed during the basin burial in this area.

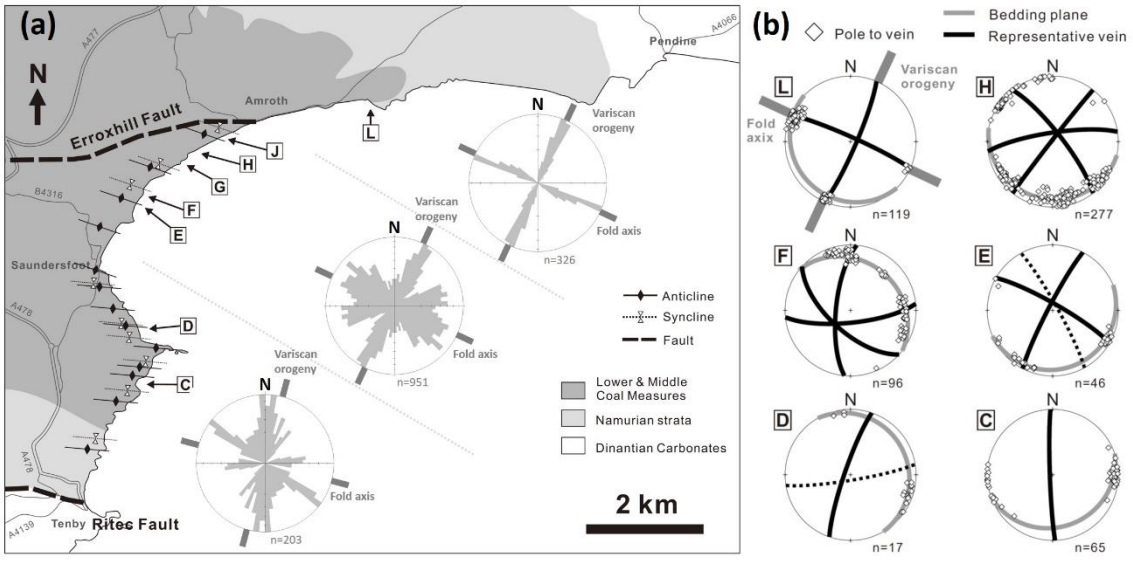

Figure 2 **(a)** Outcrop locations and typical quartz vein patterns in the study area. Alphabets on the map indicate outcrops where vein aspect ratios were measured. Same letter as chapter 4 is used at the same locality. Area-normalised rose diagrams show quartz veins at three areas, indicating fractures parallel to the Variscan orogenic compression are most dominant throughout the study area while fractures parallel to the fold axis become sub-parallel and developed in two or more directions towards the south. Number of vein data is denoted at the bottom of rose diagram. **(b)** Fracture

pattern of the quartz veins at main outcrops where vein aspect ratios were measured. Pole to vein is denoted by white marker with diamond shape. Representative plane of the veins is shown by black great circle. Average bedding at the outcrop is indicated by grey great circle. Number of vein data at each outcrop is also denoted at the lower right of stereonet.

3. Mineral veins in the study area

The geological formations exposed in this area are the Namurian siliciclastic sediments and the Lower and Middle Coal Measures. These formations are composed of shale-dominant marine deposits. Thickness of interbedded sandstones ranges from a centimetre to a few metre in these units. Only one carbonate layer is recognised in the area, namely at outcrop D (Figure 2a). This layer is a very distinctive lithology because the high sedimentation rate of foreland basins normally does not allow colonization of carbonate-bearing creatures. The carbonate is known as Amroth Freshwater Limestone, which contains abundant non-marine bivalve (George and Kelling, 1982). It is interpreted that the limestone deposited in a lake during a specific period of relatively low sedimentation rate. Layer-scale fractures and veins developed in the sandstones and limestone throughout the study area (Figure 3).

3.1. Field observations and structural data of the veins

Mineral veins are common together with layer-scale fractures in the sandstones and the limestone (Figure 3a). The veins developed in the same main strike directions and show the same fracture mode as the layer-scale fractures. In the entire study area, the veins are generally perpendicular to beds (Figure 6 of chapter 4) and thus likely to be formed during the basin burial.

The quartz veins in the sandstones become arrested at the contacts between sandstones and shales (Figure 3c). No mineral vein penetrating shale was recognised in the field although fractures without mineral precipitation were common in the shale. This suggests shale was not consolidated – was still very compliant or soft – during the mineral-vein formation, and that the ductile behaviour prevented brittle extension-fracture development within the shale at the time of vein formation. Many layer-scale extension fractures without quartz also become arrested at contact with shale. However, some of the latter penetrate shale layers (Figure 3d), implying the quartz precipitated in

fractures that developed at relatively earlier stage of the sedimentation in which shale was not consolidated and behaved as ductile material while brittle fractures developed in the sandstones.

Figure 2(b) shows structural data of quartz veins at outcrops where vein aspect ratios were studied. In the studied outcrops, the pattern of veins is similar to that of layer-scale fractures. Because outcrops are strongly deformed in the southern area and exposures of veins suitable to measure vein aspect ratio are limited, only 20 vein aspect ratios were studied in the southern area (outcrop C and D).

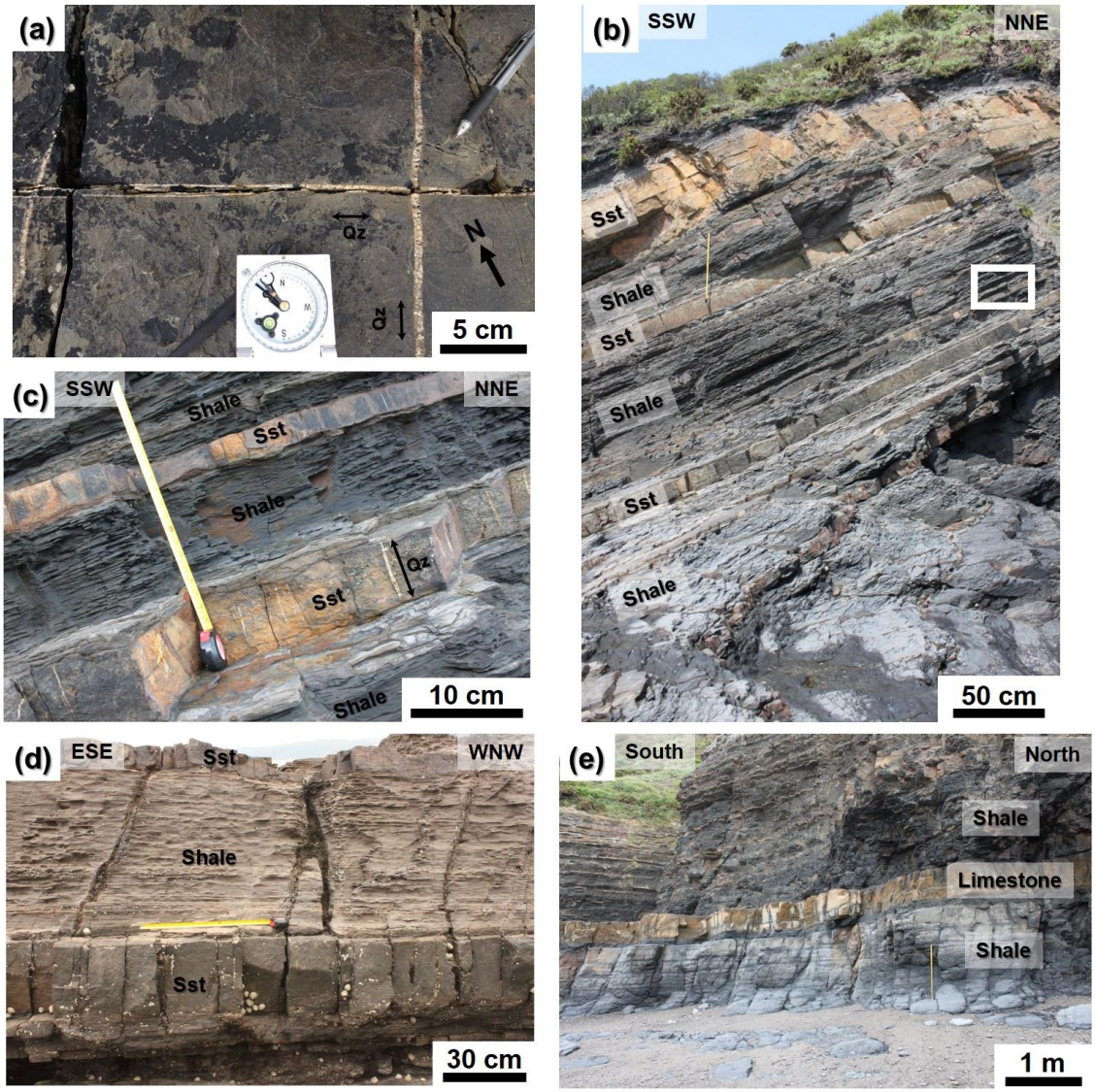

Figure 3 Field photographs of layer-scale fractures and quartz veins **(a)** Quartz veins developed in two orthogonal directions in the sandstone layer at outcrop L. **(b)** Overview of outcrop G. Shale-

dominant alternating sand-shale layers are common in the field. **(c)** Close up of box with white line on (b) Quartz veins developed only in sandstone layers. **(d)** Layer-scale fractures in the sandstones at outcrop G, which mostly become arrested at contact with shale. Several fractures penetrate shale, which have curved or bent fracture plane, showing semi-ductile behaviour of the shale during the fracture formation. **(e)** Overview of the fresh water limestone at outcrop J, which is surrounded thick shales.

3.2. Microstructure and petrography of the veins

The veins in the sandstones consist of quartz with very small amount of mica particles (Figure 4a, b, c). The quartz in the veins is mostly elongated perpendicular to the vein walls. The elongated shape of minerals is formed as a result of crack-seal growth of veins, in which continuous cycle of crack opening and mineral precipitation causes the mineral to grow parallel to the crack opening direction. The result is elongated minerals whose long axes are perpendicular to the vein walls (e.g. Passchier and Trouw, 1996). In general, Fluid inclusions in the elongated quartz minerals are arranged parallel to the vein walls, also indicating crack-seal growth of the quartz in relation to the fracture opening (Figure 4d). The microstructures associated with crack-seal growth suggest simultaneous cyclic processes of the fracture opening and mineral precipitation during the vein formation, indicating that the mineral veins preserve the physical information at the time of extension fracture opening.

In contrast to common quartz precipitation along the fractures in the sandstones, mineral veins in the limestone (the Amroth Freshwater Limestone) are mainly composed of calcite (Figure 4e, f). This is so despite the fact that no calcite mineral was recognised within the veins in the sandstones. The clear difference of mineral assembly of veins between the sandstones and limestone indicates the associated pore-fluids were isolated in each layer and that they were not connected beyond the thick surrounding shale during the vein formation.

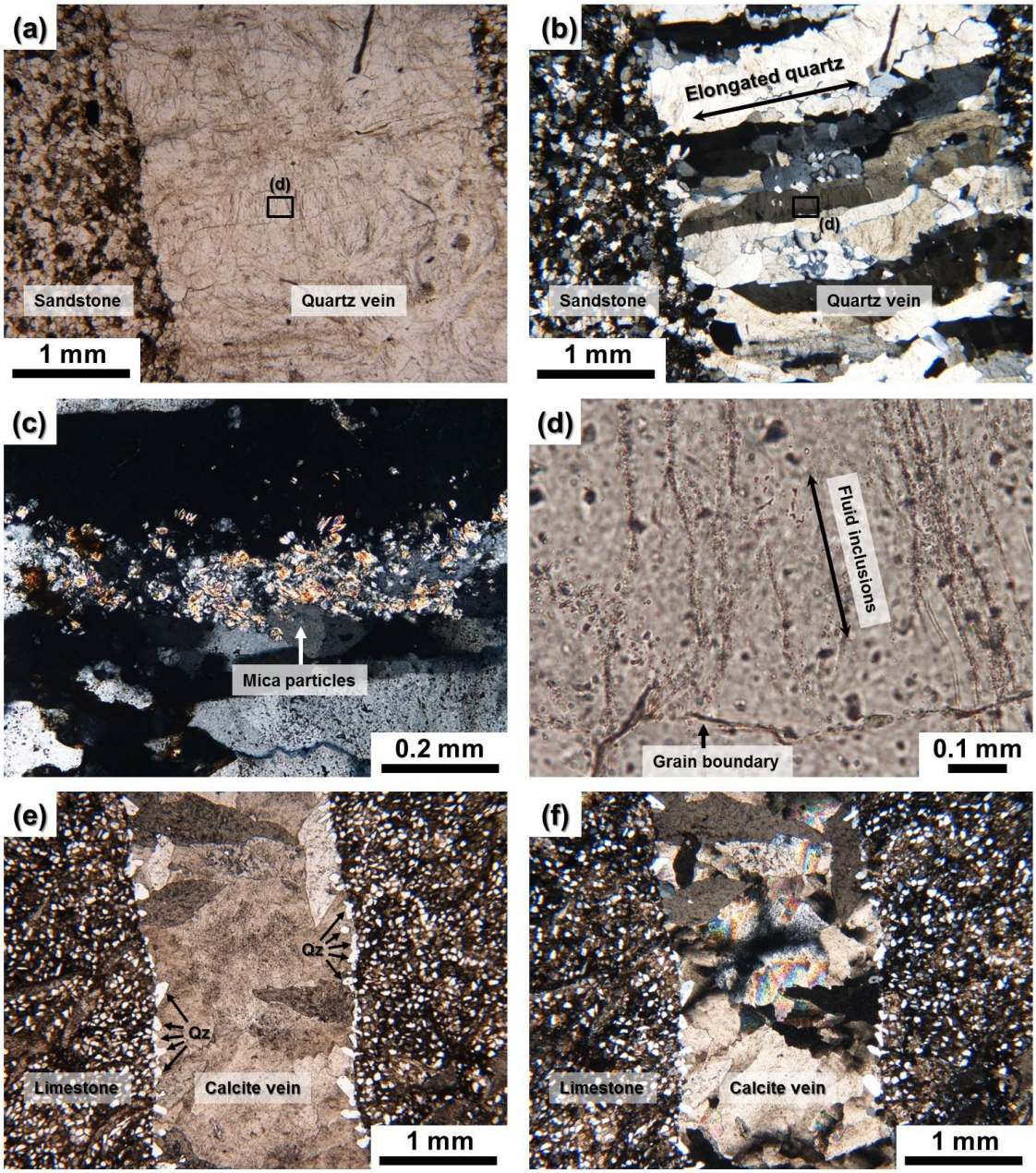

Figure 4 Microphotographs of mineral veins in the sandstones and limestone. **(a)** Quartz vein in the sandstone under plane-polarized light. **(b)** Crossed-polarized light of (a), showing elongated quartz in the direction perpendicular to the vein wall. **(c)** Mica grains which are locally observed in the quartz veins. **(d)** Close up of (a), illustrating fluid inclusions arranged parallel to the vein wall. **(e)** Calcite vein in the limestone under plane-polarized light. The specimen was taken at outcrop D. Small particles with white colour in the host rocks are quartz grains deposited as siliciclastic sediments. In the vein, quartz precipitated only at the area close to the vein wall and the other parts are filled with carbonate minerals. **(f)** Crossed-polarized light of (a).

4. Fluid overpressure

Fluid overpressure is the driving pressure available to rupture the rock and open fractures. Fluid overpressure is defined as the total fluid pressure in the fracture minus minimum principle compressive stress acting on the fracture walls. We constrain the possible overpressure by using vein aspect ratios to estimate a mechanism of the fracture network formation in the South Wales coalfield.

The fluid overpressure of an extension fracture extending from one free surface to another free surface can be calculated using a through-the-thickness crack model (Gudmundsson, 2011). In the study area, the sandstone layers hosting the quartz veins are interbedded by layers of shale that, at the time of vein formation, behaved as ductile. In many cases, during the vein formation, the contacts between the shale and the sandstone layers are thus likely to have be mechanically weak and subject to opening in a manner of Cook-Gordon delamination (Gudmundsson, 2011). For the present purpose, it is thus not an unreasonable assumption to regard the contacts as behaving as free surfaces and model the mineral veins accordingly. The fluid overpressure P_o during the quartz vein formation can then be estimated crudely from the following equation (e.g. Sneddon and Lowengrub, 1969; Gudmundsson, 2011; Philipp, 2012; Philipp et al., 2013):

$$P_o = \frac{\Delta u E}{2L(1-\nu^2)} \tag{1}$$

where E is Young's modulus and ν is Poisson's ration of the host sandstones, and L is the dimension (here the strike dimension or length) of the vein. Δu/L is vein thickness over strike dimension (Figure 5a, b), which is the reciprocal of the vein aspect ratio. Since we model the veins as a mode I through-the-thickness crack, the dip dimension of the vein is effectively infinite and the strike dimension must be used in the calculations. This follows because it is always the smaller of the (strike and dip) dimensions that controls the extension-fracture aperture – and referred to as the controlling dimension (Gudmundsson, 2011; Philipp et al., 2013).

The equation (1) was original derived from isotropic, homogeneous, linear-elastic theory with an assumption that the associated extension fractures have penny shape or flat ellipsoidal body (e.g. Green and Sneddon, 1950; Gudmundsson, 2011). Equation (1) is simplified version of the original equation for through-the-thickness(layer)-crack in which one dimension along major axis of the flat ellipsoid (dip dimension R in Figure 5a) is negligible by assuming the major axis is sufficiently longer than minor axis (strike dimension L in Figure 5a). Because of these logical background, accuracy of the calculation results become less in the following cases: Dip dimension R of the crack is not sufficiently longer than strike dimension L although it cannot be investigate for the through-the-thickness-crack; rock behaviour was not elastic at the time of extension fracture opening; rock was not isotropic and/or homogeneous at the time of extension fracture opening. In order to avoid the second and third cases, mineral veins with unstable shapes which may have been affected by pressure shadow caused by previously developed structures, rock heterogeneity, rock anisotropy or non-linear-elastic deformation were not measured in the field as much as possible.

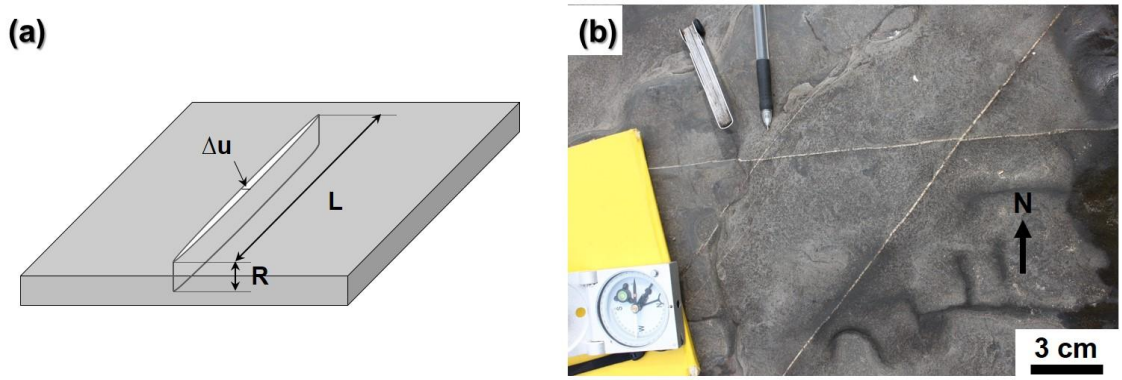

Figure 5 **(a)** Schematic illustration of mineral vein in the study area. Δu is maximum thickness of the vein. R is dip dimension cutting through the layer. L is strike dimension. **(b)** Plane view of quartz veins on a sandstone layer at outcrop H. Maximum thickness Δu and strike dimension L were measured in the field.

4.1. Aspect ratios of the quartz veins

The aspect (length/thickness) ratios of 502 quartz veins, all extension fractures, were measured at 8 outcrops (Figure 2b). Measurement of strike dimension or length requires exposure of both lateral ends of the veins on the bedding. Because continuous outcrops

are relatively rare in the southern area, where impact of the Variscan ogogeny was more intense, only limited number of veins were studied at outcrops C and D. Accordingly, aspect ratios were mostly measured in the central to northern areas (outcrops E, F, G, H, J and L). However, no significant difference of the measured values was recognised between the northern, central and southern areas.

Vein aspect ratios measured in the field show different values depending on mechanical properties of the host-rock sandstones or the development (strike) directions of the veins. Figures 6a and b show scatter plots of strike dimension L versus vein thickness Δu in two different sandstone layers at outcrop H (sandstone A is Layer #25 and sandstone B is Layer #24 in Appendix of this thesis). They indicate clear difference in the average vein aspect ratios between the two sandstone layers. The results of Price (1963) indicate that both the tensile strengths and the stiffnesses (Young's moduli) of the Coal Measure sandstones changes depending on the amount of clay contents and porosity in the sandstones based on laboratory measurements. The difference of aspect ratios at the same outcrop where the sandstones must have experienced approximately the same deformation history during the vein formation is most likely due to the variation of mechanical properties, particularly the stiffnesses most likely caused by volume difference of porosity and clay contents, of the host sandstone layers.

Figure 6c, d also show variation in aspect ratios of veins depending on their strike direction, in the same sandstone layer. Veins striking NNE-SSW commonly have smaller aspect ratios than veins striking WNW-ESE in this layer, and generally in the study area. No anisotropic arrangement of quartz grains was recognised under microscope within the sandstones which are composed of rather isotropic rounded grains in same layers. It is, thus, highly unlikely that horizontal anisotropy of the mechanical properties of individual host-rock sandstone layers caused the variation in the aspect ratios, implying the variation reflects the difference in magnitude of the fluid overpressure in relation with minimum principal compressive stress, σ_3, perpendicular to the veins of different orientation during their formation.

Although vein aspect ratios vary between sandstone layers, partly because of the variation in the mechanical properties (especially Young's modulus) between the layers (Figure 6a, b), the representative aspect-ratio values along the two directions (NNE-SSW and WNW-ESE) could be estimated by combining all data from the different

sandstone layers. This we do because it is extremely difficult to compare the mechanical properties of the different layers accurately, and the associated detailed laboratory works would be beyond the scope of this paper. We measured the vein aspect ratios in 13 sandstone layers. We regard the mean aspect ratio of veins from this number of sandstone layers as representative values for veins with the two main strike directions. Because of this approach, data ranges of vein aspect ratios are moderately wide for each data sets shown in Figure 7. However, the data sets show clear different trend of data variation depending on the vein orientation (Figure 7), indicating analytical approaches from these data sets must reflect difference of fluid overpressures in the vein orientations.

The veins with measured aspect ratios were divided into three date sets in this paper: (1) veins parallel to the Variscan orogenic compression (NNE-SSW striking, with dip-direction azimuths mainly 100-130º and 280-310º); (2) veins striking parallel to subparallel to the regional fold axis (WNW-ESE striking, with the dip-direction azimuths mainly 170-240º and 350-060º); (3) all veins including (1) and (2) (Figure 7). Because the vein aspect ratios show crude lognormal distributions, the geometric mean rather than the arithmetic mean is used as representative values, since it is common for lognormal distributions to represent the data variation distributing lognormally (Swan and Sandilands, 1995). The geometric mean of entire data set is 338. The geometric means of veins striking NNE-SSW and WNW-ESE are 246 and 421, respectively. By assuming that the parent populations of vein aspect ratios have lognormal distribution in the study area, 99% confidence intervals of true geometric means of the vein aspect ratios were calculated for whole veins, veins striking NNE-SSW and veins striking WNW-ESE. The ranges are 314-363 for all veins, 221-274 for veins striking NNE-SSW, and 386-481 for veins striking WNW-ESE.

The 99% confidence limit for lognormal distribution was calculated by following equations:

$$Upper\ confidence\ limit = exp\left(A + B \times \sqrt{C/D}\right) \quad (2)$$

$$Lower\ confidence\ limit = exp\left(A - B \times \sqrt{C/D}\right) \quad (3)$$

where A is mean value of logarithm natural of vein aspect ratio ln(L/Δu); B is confidence coefficient T which is approximately 2.6 in the current cases; C is sample variance of logarithm natural of vein aspect ratio ln(L/Δu); D is sample number.

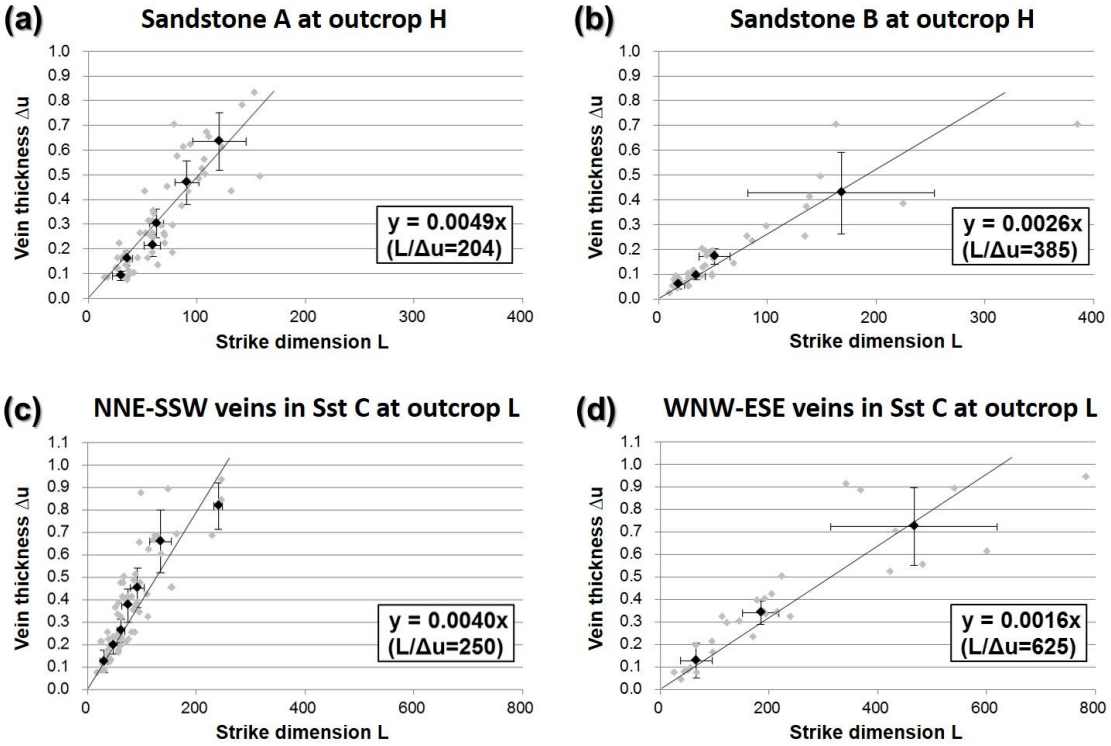

Figure 6 Scatter plots of strike dimension L versus vein thickness Δu, showing difference of vein aspect ratios between the sandstones. Data measured in the field are denoted by grey marker. Black marker indicates average of each 10 data. Error bar shows one standard deviation of the 10 data. Because linear regression in scatter plot is strongly affected by irregular value, the regression line is drawn by the averaged data. **(a)** Vein aspect ratios in sandstone A at outcrop H. **(b)** Vein aspect ratios in sandstone B at outcrop H. **(c)** Aspect ratios of NNE-SSW striking veins in sandstone C at outcrop L. **(d)** Aspect ratios of WNW-ESE veins in sandstone C at outcrop L.

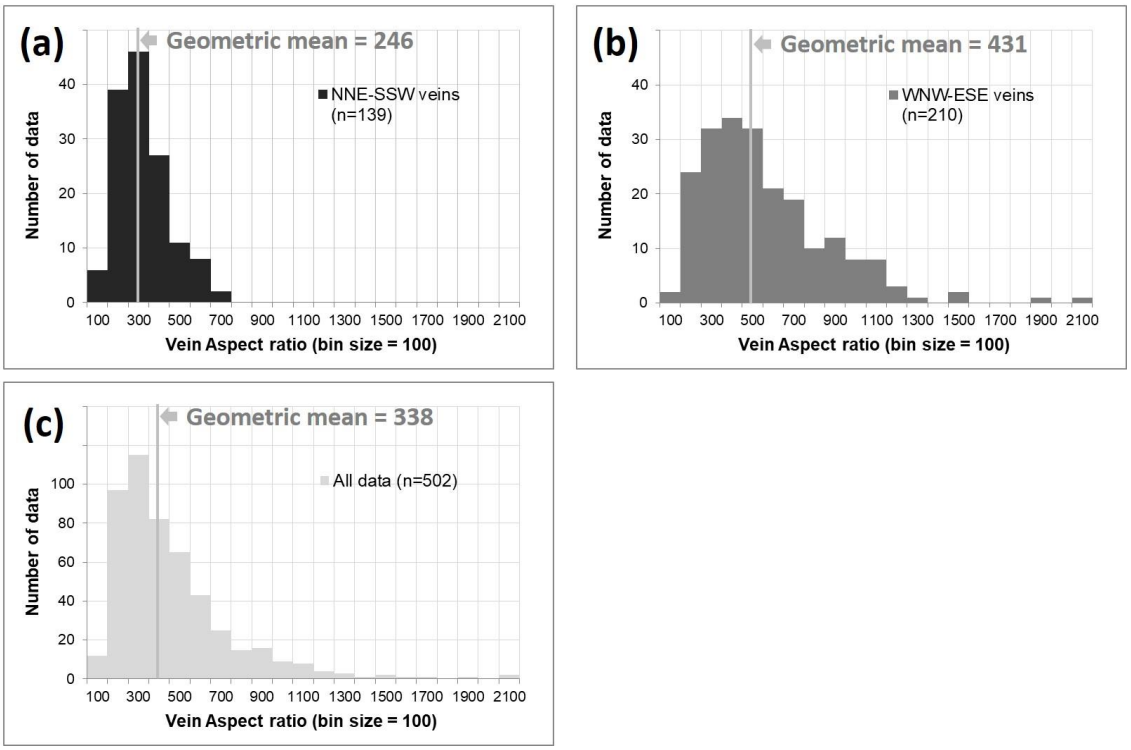

Figure 7 Histogram of vein aspect ratios (length/thickness) showing lognormal distribution. The bin size is 100. The data are sub-divided into three: **(a)** veins striking NNE-SSW; **(b)** veins striking WNW-ESE; **(c)** all data including (a) and (b). Each data set shows lognormal distribution. Geometric means for veins striking NNE-SSW and WNW-ESE are 246 and 431 respectively. Geometric mean for all data is 338.

4.2. Possibility of variation of vein aspect ratios during the vein growth

Based on the microstructures in Figure 4, the current vein shapes (thickness and length) were formed as a result of consecutive cycles of crack-seal growth of the veins. The aspect ratios measured in the field thus do not represent one fracture opening event but rather many. Strictly, the original vein aspect ratio at the time of the initial fracture opening should be used in Eq. (1) to calculate fluid overpressure. However, the linear trends of scatter plots in Figure 6 show the aspect ratio did not change largely during the vein growth and similar values can be obtained from both small and large veins in a same sandstone layer. This is in agreement with earlier results that suggest that many most veins grow as self-similar structures (Gudmundsson, 2011; Philipp, 2012). It follows that the vein aspect ratio normally does not change much during its growth in a given layer so that the aspect ratios measured from current vein shapes (the final aspect

ratios) are can be used to calculate fluid overpressure at the time of fracture opening, as we do in this paper.

4.3. Mechanical properties of the sandstones

Mechanical properties of the Pennant Sandstones in the South Wales coalfield were studied by Price (1958, 1960, 1963). The Pennant Sandstones are from the Upper Coal Measures and thus of different from the present sandstones. However, the sandstones in the study area and the Pennant Sandstones were deposited at a similar time and were subject to the same burial and tectonic histories, implying the mechanical properties of Pennant Sandstones can be used to estimate the mechanical properties of rocks in the study area.

The laboratory tensile strength of the Pennant Sandstone is 15-19 MPa and Young's modulus about 50 GPa (Price, 1958). Since laboratory measurements generally yield values that are 1.5-5 times greater than the in-situ values (Gudmundsson, 2011), the in-situ Young's modulus E and tensile strength T_o of the sandstones are estimated at 10-33 GPa and 3-13 MPa, respectively, at the time of fracture formation. The median values (E = 22 GPa, T_o = 8 MPa) are used as representative. These are reasonable values. In particular, a tensile strength of 8 MPa is in the upper range of in-site tensile strengths as measured through hydraulic fracturing at various depths in the crust (Gudmundsson, 2011).

Although Poisson's ratio of rocks typically ranges from 0.20 to 0.30 (e.g. Bell, 2000), it has no major impact on the calculation result compared with the other parameters. Constant value of 0.25 is thus used for the Poisson's ratio.

4.4. Fluid overpressure at the fracture opening

Using the above average values for elastic parameters and vein aspect ratios, Eq. (1) yields fluid overpressure of 34.7 MPa (99% confidence interval: 32.3-37.4 MPa) for the whole data set, 47.7 MPa (99% confidence interval: 42.8-53.1 MPa) for veins striking NNE-SSW, and 27.9 MPa (99% confidence interval: 24.4-30.4 MPa) for veins striking WNW-ESE. By considering possible variations in the in-situ Young's modulus, the maximum ranges of 99% confidence intervals for the parent populations could range as

widely as 14.7-56.1 MPa for whole dataset, 19.5-79.6 MPa for vein striking NNE-SSW and 11.1-45.6 MPa for veins striking WNW-ESE.

The calculation results are primarily controlled by the assumption of Young's modulus E of the sandstone layers in the current study. Chapter 4 of this thesis implies that the vein formation occurred during basin burial, suggesting that mechanical properties at the time of fracture opening were different from laboratory results obtained from current day rock exposures. Although it would be extremely difficult to predict palaeo mechanical properties, the value must be smaller than the present-day values since they received all the diagenesis in the basin history and must be the maximum values. 10-20 GPa might be more realistic value for the calculation. However, we do not have any direct information to estimate them, we use the calculation results as maximum calculated fluid overpressure. Since Young's modulus is proportional to the fluid overpressure (equation 1), relative difference of fluid overpressure between veins striking NNE-SSW and veins striking WNW-ESE is independent to the Young's modulus. Thus, the results indicate fluid overpressure for veins striking NNE-SSW was about 70 percent larger than that of veins striking WNW-ESE.

The calculation results are also affected by vein aspect ratio because they are inversely proportional to the vein aspect ratio as shown in equation (1). However, as long as we discuss the mean value of vein aspect ratios of parent population with sufficient number of sample measured in the field, the range of the variability caused by source of vein aspect ratios is minimal. In the current study case, the impact to the calculation results is 10-20 percent of the mean value as shown above. We consider the source variability of vein aspect ratios is relatively minor effect compared with the difficulty of prediction of Young's modulus.

5. Discussion

5.1. Driving stress and fracture formation in the South Wales coalfield

Philipp (2012) estimates fluid overpressure of calcite veins in alternating limestone-shale layers of the Jurassic Lias Formation at Kilve in the Bristol Channel. The paper concludes the main driving stress which raised the fluid overpressure was buoyancy caused by density difference between the rocks and fluid (Figure 8a). For significant buoyancy effect on driving pressure, the hydrofracture must propagate through

considerable vertical distance from its source and remain connected to that source. Major faults are interpreted as the main fluid pass from the fluid source in the model. Water sills are assumed as the fluid source (Philipp, 2008, 2012; Philipp et al., 2013).

In the South Wales coalfield, the Dinantian Carbonates underlie the Namurian strata (Figure 2a, 8b). However, no carbonate mineral was recognised within the veins in the sandstones at all outcrops in this study (Figure 4a, b, c). The veins consist of quartz with minor amount of mica particles. If the fluid source existed in the Dinantian Carbonates and the source had been connected to sandstone layers, carbonate minerals should have precipitated within the veins. The lack of carbonate minerals in the sandstones, thus, suggests fluids in the sandstones in the Namurian and the Lower & Middle Coal Measures were not connected to pore-fluid in the Dinantian Carbonates during the vein formation and that the possible fluid source existed at a depth shallower than the bottom of Namurian strata.

The closest sandstone to the Dinantian Carbonates in the outcrops we studied is at outcrop B (Figure 2a). Because no significant folding and thrusting were observed in the northern side of Erroxhill Fault and the bed forms monocline which dips at about 9 degrees in the area (figure 4 of chapter 4 of this thesis), depth difference between outcrop B and the top of Dinantian Carbonates can be calculated as 450-550 metres. Subsequently, maximum estimation of buoyancy effect (same as the case that possible fluid source existed at the bottom of Namurian) is calculated as 6.6-8.1 MPa at outcrop B by assuming density difference between the rocks and fluid was 1500 kg/m^3. This is an example at outcrop B but the buoyancy effect is considerably lower than calculated fluid overpressures, suggesting buoyancy effect, while important, was not the only contribution to the driving pressure (fluid overpressure) during fracture (vein) formation in the sandstones in the South Wales coalfield.

Also, the different mineral assembly in the veins between the sandstones and Amroth Freshwater Limestone (Figure 4) suggests that pore-fluid in those layers which were surrounded by very low permeability (effectively impermeable) shale have not been interconnected during the vein formation. Mineral assemblies in the quartz veins (quartz + mica particles) in the sandstones and calcite veins (calcite + quartz grains) in Amroth Freshwater Limestone can be explained by the mineral components of the host rocks, namely the sandstones consist of quartz and clay minerals and the limestone

consists of carbonates and quartz particles (Figure 4). This suggests the possibility that mineral sources of the veins were the host rocks themselves, and additionally support that the fluid within the stiff layers were essentially isolated in the shale-dominant sedimentary units and that contribution of buoyancy effects on fluid overpressure were comparatively small during the vein formation in this basin as calculated at outcrop L.

Possible factors contributing to fluid overpressure P_o in mineral veins and other fluid-driven fractures are identified in the following equation (Gudmundsson, 2011; Phillip 2012; Philipp et al., 2013)

$$P_o = P_e + (\rho_r - \rho_f)gh + \sigma_d \quad (4)$$

where P_e is excess pressure in the fluid source at the time of fracture initiation, ρ_r is the density of the host rock, ρ_f is the density of the fluid, g is the acceleration due to gravity, h is the height of the fracture (where the aspect ratio is measured) above its source (or the fracture dip dimension), and σ_d is differential stress (the difference between the vertical principal stress and the minimum horizontal principal stress) in the host rocks. The equation is assumed the model shown in Figure 8a. In the case there is no impact of supply of highly pressured fluid from deeper fluid source, the second term must be negligible. In addition, the third tem assumes that there is no permeability in rock matrix and no fluid interaction between fluid within fractures and fluid in matrix porosity. Fluid compressibility is also neglected in the third term. In the current study area, because no visible matrix porosity under the microscope (Figure 4), we assume no matrix permeability. We also assume no fluid compressibility in this case.

Excess pressure P_e was same as tensile strength T_o at the time of fracture opening. Differential stress σ_d ranged 0 to $4T_o$. This is because stress conditions of $\sigma_d > 4T_o$ theoretically form not extension fractures but either hybrid or shear fractures (e.g. Griffith, 1924; Hancock, 1985; Gudmundsson 2011). Thus, the sum of the first and third terms of equation (4) should be $5T_o$ as maximum. The estimated in-situ tensile strength T_o of the host sandstones is 3-13 MPa, suggesting some parts of the calculated overpressure is slightly over $5T_o$, and that both local stress field in the sandstones and buoyancy effects might have contributed on the rise of fluid overpressure though the buoyancy effect probably had been relatively small compared with the study results in

Jurassic Lias Formation at Kilve in the Bristol Channel (Philipp 2012). This is because pore-fluid was unlikely connected between the sandstones or limestone at the time of vein formation as discussed above (mineral composition is different each other), and it would not be reasonable to consider significant contribution by water sill from deeper depth.

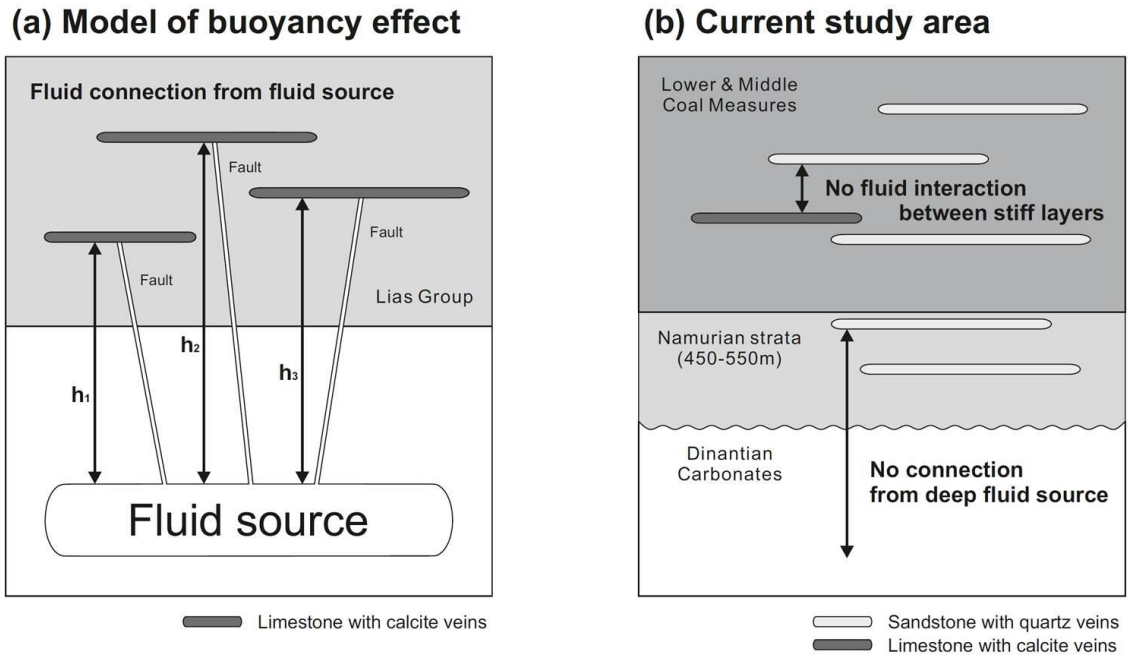

Figure 8 **(a)** Model of buoyancy effect in Lias Formation at Kilve. The fluid overpressures caused by buoyancy effect in the figure are $(\rho_r - \rho_f)gh_1$, $(\rho_r - \rho_f)gh_2$ and $(\rho_r - \rho_f)gh_3$ from the left limestone to the right. ρ_r, ρ_f, g and h are rock density, fluid density, gravity acceleration and depth difference between the limestone and fluid source, respectively. **(b)** Situation of the current study area. Clear difference of mineral assembly within the veins between the sandstones and limestone suggests there was little fluid connection between the layers beyond surrounding thick shale. In addition, carbonate minerals are absent in the veins in the sandstones, also implying limited fluid connection from the Dinantian Carbonates to the sandstones.

5.2. Physical conditions during the vein formation in the South Wales coalfield

Alderton and Bevins (1996) estimate P-T (pressure-temperature) conditions of fluid inclusions in quartz which grew in the cavities of siderite nodules associated with low volatile (bituminous) coals in the Lower and Middle Coal Measures. Their results suggest that the quartz formed at 130-160ºC and 40-55 MPa (total fluid pressure). The paper states the cavities are also filled with carbonates and sulphides and that the

sequence of mineral precipitation is, first carbonates, second sulphides and last quartz. Alderton et al. (2004) also imply the quartz precipitated at a later stage of basin development based on the associated fluid inclusions and stable isotope data of quartz and carbonate minerals in fracture fillings and the siderite nodules. We, therefore, use the P-T conditions of Alderton and Bevins (1996) as first physical conditions of quartz precipitation during the basin burial. It is denoted by [A] in Figure 9. Alderton et al. (2004) also provided P-T (pressure-temperature) conditions of fluid inclusions in quartz associated with anthracite coals which is thermally more matured coal than bituminous coals. Because coal rank in the current study area is categorised as anthracite zone, the results of Alderton et al. (2004) is additionally used to estimate P-T conditions of the study area. The results show physical conditions of quartz precipitation along fractures was at 180-220ºC and 60-80 MPa, which represents later stage of the sedimentation in the study area. The P-T conditions is denoted by [B] in Figure 9.

White (1991) provides vertical and lateral distributions of the volatile matter values across the basin. Bevins et al. (1996) add results of studies of illite crystallinity and vitrinite reflectance, and concludes that maximum achieving temperature in anthracite zone was 200-250 ºC. Coal rank in the Pembrokeshire sub-basin (current study area) is categorised into anthracite (Robinson et al., 1980; Waters and Davies, 2006). The range of 200-250 ºC is, therefore, used as maximum achieving temperature in the study area, which is denoted by [C] in Figure 9.

P-T path of the basin burial and exhumation is roughly illustrated with clockwise rotation by using [A] [B] and [C] as control points (Figure 9). Clockwise rotation of P-T path is generally justified in sedimentary basins because pressure immediately changes with depth while temperature is controlled by thermal conduction and convection, which requires some geological time to achieve the steady-state. High sedimentation rate (130-250 m Ma^{-1}) in the foreland basin (Kelling, 1988; Burgess and Gayer, 2000) supports time lag between pressure and temperature changes and clockwise rotation of the P-T path.

Because the main Variscan compression was initiated just after the maximum burial of the basin (Cole et al., 1991; Jones, 1991; Bevins et al., 1996), intersection between [C] and projected P-T paths from [A] and [B] roughly indicate P-T conditions for the initiation of main Variscan compression.

The layer-scale vein formation predates or coincides with that of the regional folding in the study area (chapter 4 of this thesis). In consequence, layer-scale fractures filled with quartz focused on this paper most likely developed in the physical conditions ranging from [A] to [B] in Figure 9 (from first physical conditions of quartz precipitation to initiation of compression structures). The P-T range of 130-220ºC and 40-80 MPa correspond approximately to depth of 2,500 to 4,500 metres based on pressure model of Alderton et al. (2004). Note that pressure used here is not overburden pressure or fluid overpressure but total fluid pressure estimated by fluid inclusion microthermometry (Alderton and Bevins, 1996; Alderton et al., 2004).

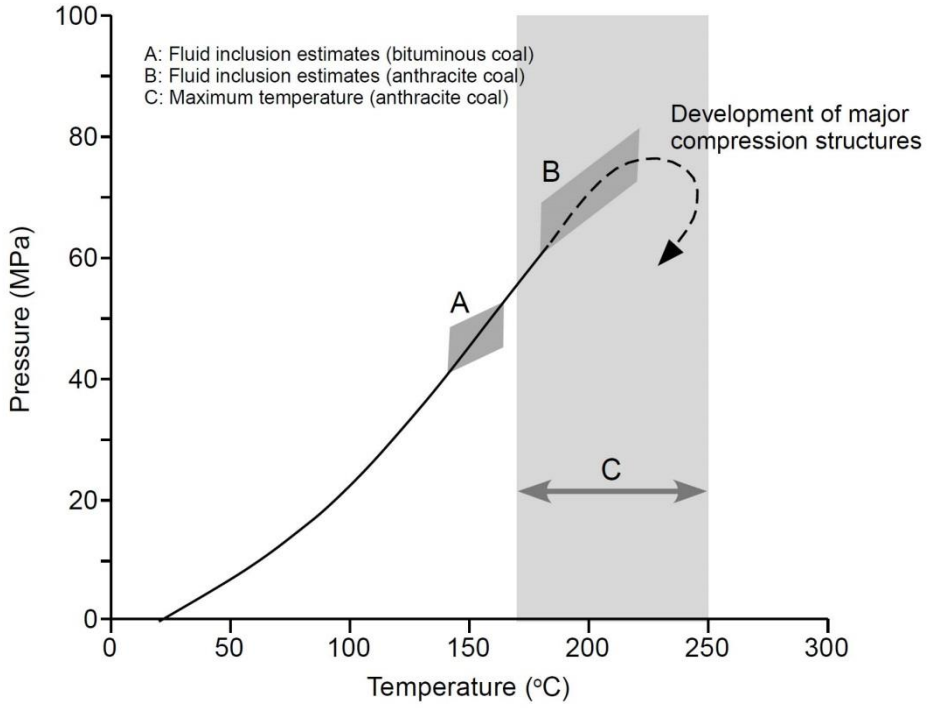

Figure 9 Possible P-T (pressure-temperature) path in the South Wales coalfield. [A] is P-T conditions at the time of quartz precipitation in siderite nodules which are associated with low volatile (bituminous) coals (Alderton and Bevins, 1996). [B] is P-T conditions at the time of quartz precipitation in anthracite zone (Alderton et al. 2004). [C] is maximum achieving temperature in anthracite zone (White, 1991; Bevins et al., 1996). Note that the ordinate axis is not overburden pressure but pore-fluid pressure (total fluid pressure).

5.3. Implications from the calculated overpressure

The current study results show fluid overpressure at the time of vein formation is about 35 MPa as maximum value (the absolute value is not essential since estimation of Young's modulus of the rock is highly uncertain) and that the overpressure for veins striking NNE-SSW was approximately 70 percent higher than that for veins striking WNW-ESE. Chapter 4 of this thesis implies the veins developed during not crustal uplift/exhumation but basin burial. That means the regional maximum compressive stress was in the direction of NNE-SSW because of the Variscan Orogeny which formed the current foreland basin. The difference of horizontal regional stresses between NNE-SSW direction and WNW-ESE direction may have caused general difference of the overpressure in the two direction.

Based on the above discussion, differential stress σ_d or local stress field in the sandstones are more important than buoyancy effect for the vein formation. The buoyancy effect associated with geothermal fluid from deeper depth, which is proposed by other researchers, is not main mechanism of the extension fracture formation in the current study area. Possible mechanism of the overpressure or tensile stress generation for the extension fractures is examined in chapter 6 of this thesis.

Overprinting relationship between veins striking NNE-SSW and WNW-ESE is not clear even under microscope. One group initiated earlier in several thin sections but the other group partly formed earlier in the other thin section. The timing of their development seems to be approximately same in geological time-scale.

There are some variation of vein aspect ratios even in the same sandstone and same vein set. Several fractures commonly show thin thickness of the veins, resulting in the very small fluid overpressure. Those variations were probably caused by difference of sequence of vein formations. Since the sandstones and limestone were surrounded by impermeable shale, once new space was generated by fracturing of rocks, fluid pressure must have dropped immediately that could form thin veins with very high vein aspect ratio. As mentioned in section 4.1, variations between different sandstones were most likely controlled by mechanical properties of the sandstones associated with the amount of clay contents and porosity.

6. Conclusions

The main results of the field and microscope studies of the extension fractures filled with minerals, as well as the associated analytical calculations, are summarised as follows:

1. Fluid overpressure (or driving pressure) at the time of vein formation in the sandstones as estimated from the measured aspect (length/thickness or aperture) ratios of 502 quartz veins in sandstone layers of the Coal Measures of the Bristol Channel, SW England.
2. The results indicate an average fluid overpressure (driving pressure) of about 35 MPa. This is the maximum value estimation since we referred to rock mechanical properties of present-day exposures. The value is somewhat higher than previous fluid-overpressure estimates for veins in carbonate rocks (limestone layer) in the Bristol Channel.
3. Fluid overpressure was mainly generated by stress difference σ_d at the time of vein formation. Buoyancy effect must have been the secondary factor.
4. Analytical calculations show that the estimated overpressures depend on vein orientation. The average estimated overpressure is 48 MPa for veins striking NNE-SSW (parallel to the Variscan orogeny) but only 28 MPa for veins striking WNW-ESE (perpendicular to the orogeny). The absolute values are not essential but the relative difference between the two groups indicate considerable variation of fluid overpressure at the time of vein formations associated with vein orientation.
5. Physical conditions of fluid at the time of the extension fracture formation and mineral precipitation were roughly at total fluid pressure of about 40 -80 MPa (overpressure of about 35 MPa, as maximum), and temperature of 130-220 degrees, which correspond to depth of 2,500 to 4,500 metres.

References

Alderton, D.H.M., Bevins, R.E., 1996. P-T in the South Wales Coalfield: evidence for coexisting hydrocarbon and aqueous fluid inclusions. Journal of the Geological Society , London 153, 265-275.

Alderton, D.H.M., Oxtoby, N., Brice, H., Grassineau, N., Bevins, R.E., 2004. The link between fluids and rank variation in the South Wales Coalfield: evidence from fluid inclusions and stable isotopes. Geofluids 4, 221-236.

Bai, T., Maerten, L., Gross, M.R., Aydin, A., 2002. Orthogonal cross joints: do they imply a regional stress rotation? Journal of Structural Geology 24, 77-88.

Bell, F.G., 2000. Engineering Properties of Rocks, 4th edition. Oxford, Blackwell.

Bevins, R.E., White, S.C., Robinson, D., 1996. The South Wales Coalfield: low grade metamorphism in a foreland basin setting? Geological Magazine 133, 739-749.

Bluck, B.J., Kelling, G., 1963. Channels from the Upper Carboniferous Coal Measures of South Wales. Sedimentology 2, 29-53.

Burgess, P.M., Gayer, R.A., 2000. Late Carboniferous tectonic subsidence in South Wales: implications for Variscan basin evolution and tectonic history in SW Britain. Journal of the Geological Society, London 157, 93-104.

Caputo, R., 1995. Evolution of orthogonal sets of coeval extension joints. Terra Nova 7, 479-490.

Cole, J.E., Miliorizos, M., Frodsham, K., Gayer, R.A., Gillespie, P.A., Hartley, A.J., White, S.C., 1991. Variscan structures in the opencast coal sites of the South Wales Coalfield. Proceedings of the Ussher Society 7, 375-379.

Eyal, Y., 1996. Stress field fluctuations along the Dead Sea Rift since the middle Miocene. Tectonics 15, 157-170.

Frodsham, K., Gayer, R.A., James, J.E., Pryce, R., 1993. Variscan thrust deformation in the South Wales Coalfield: a case study from Ffos Las opencast coal site. In: Gayer, R.A., Greiling, R.O., Vogel, A.K. (Eds.), Rhenohercynian and Subvariscan Fold Belts. Earth Evolution Series, Vieweg, Braunschweig, 315-348.

Frodsham, K., Gayer, R.A., 1997. Variscan compressional structures within the main productive coal-bearing strata of South Wales. Journal of the Geological Society, London 154, 195-208.

Fukunari, T., Gudmundsson, A., 2016. Chapter 2 of this thesis. Paper in preparation.

Gayer, R.A., Jones, J., 1989. The Variscan foreland in South Wales. Proceedings of the Ussher Society 7, 177-179.

Gayer, R.A., Cole, J., Greiling, R.O., Hecht, C., Jones, J., 1993. Comparative evolution of coal-bearing foreland basins along the Variscan northern margin in Europe. In: Gayer, R.A., Greiling, R.O., Vogel, A.K. (Eds.), Rhenohercynian and Subvariscan Fold Belts. Earth Evolution Series, Vieweg, Braunschweig, 48-82.

Gayer, R.A., Garven, G., Rickard, D., 1998. Fluid migration and coal-rank development in foreland basins. Geology 26, 679-682

George, G.T., Kelling, G., 1982. Stratigraphy and sedimentation of Upper Carboniferous sequences in the coalfield of south-west Dyfed. In: Bassett, M.G. (Ed.), Geological Excursions in Dyfed, South-West Wales. National Museum of Wales, Cardiff, 175-202.

Green, A.E., Sneddon, I.N., 1950. The distribution of stress in the neighbourhood of a flat elliptical crack in an elastic body. Proceedings of the Cambridge Philosophical Society, 46, 159-163.

Griffith, A.A., 1924. Theory of rupture. In: Biezeno, C.B., Burgers, J.B. (Eds.), Proceedings of the First International Congress on Applied Mechanics. Delft, Waltman, 55-63.

Gudmundsson, A., 1999. Fluid overpressure and stress drop in fault zones. Geophysical Research Letters 26, 115-118.

Gudmundsson, A., 2000. Fracture dimensions, displacements and fluid transport. Journal of Structural Geology 22, 1221-1231.

Gudmundsson, A., 2011. Rock Fractures in Geological Processes. Cambridge University Press, New York.

Hancock, P.L., Dunne, W.M., Tringham, M.E., 1983. Variscan deformation in southwest Wales. In: Hancock, P.L. (Ed.), The Variscan Fold Belt in the British Isles. Adam Hilger, Bristol, 47-73.

Hancock, P.L., 1985. Brittle microtectonics: principles and practice. Journal of Structural Geology 7, 437-457.

Hancock, P.L., Al-Kadhi, A., Barka, A.A., Bevan, T.G., 1987. Aspects of analyzing brittle structures. Annales Tectonicae 1, 5-19.

Hartley, A.J., Warr, L.N., 1990. Upper Carboniferous foreland basin evolution in SW Britain. Proceedings of the Ussher Society 7, 212-216.

Hartley, A.J., 1993. Silesian sedimentation in South-West Britain: sedimentary responses to the developing Variscan Orogeny. In: Gayer, R.A., Greiling, R.O., Vogel, A.K. (Eds.), Rhenohercynian and Subvariscan Fold Belts. Earth Evolution Series, Vieweg, Braunschweig, 159-196.

Hathaway, T.M., Gayer, R.A., 1994. Variations in the style of thrust faulting in the South Wales Coalfield and mechanisms of thrust development. Proceedings of the Ussher Society 8, 279-284.

Hathaway, T.M., Gayer, R.A., 1996. Thrust-related permeability in the South Wales Coalfield. Geological Society, London, Special Publications 109, 121-132.

Jones, J.A., 1989. The influence of contemporaneous tectonic activity on Westphalian sedimentation in the South Wales Coalfield. In: Arthurton, R.S., Gutteridge, P., & Nolan, S.C. (Eds.), The role of tectonics in Devonian and Carboniferous sedimentation in the British Isles. Occasional Publication of the Yorkshire Geological Society 6, 243-253.

Jones, J.A., 1991. A mountain front model for the Variscan deformation of the South Wales coalfield. Journal of the Geological Society, London, 148, 881-892.

Kelling, G., 1974. Upper Carboniferous sedimentation in South Wales. In: Owen, T.R. (Ed.), The Upper Palaeozoic and post-Palaeozoic rocks of Wales. University of Wales Press, Cardiff, 185-224.

Kelling, G., 1988. Silesian sedimentation and tectonics in the South Wales Basin: a brief review. In: Besly, B., Kelling, G. (Eds.), Sedimentation in a Synorogenic Basin Complex: The Upper Carboniferous of Northwest Europe. Blackie, Glasgow, 38-42.

Leveridge, B.E., Hartley, A.J., 2006. The Variscan Orogeny: the development and deformation of Devonian/Carboniferous basins in SW England and South Wales. In: Brenchley, P.J., Rawson, P.F. (Eds.), The geology of England and Wales. Geological Society of London, London, 225-255.

Passchier, C.W., Trouw, R.A.J., 1996. Microtectonics. Springer-Verlag, Berlin.

Philipp,S.L., 2008.Geometry and formation of gypsum veins in mud-stones at Watchet, Somerset, SW-England. Geological Magazine, 145, 831–844. doi: 10.1017/S001675 6808005451

Philipp, S.L., 2012. Fluid overpressure estimated from the aspect ratios of mineral veins. Tectonophysics 581, 35-47.

Philipp, S.L., Afsar, F., Gudmundsson, A., 2013. Effects of mechanical layering on the emplacement of hydrofractures and fluid transport in reservoirs. Frontiers in Earth Science 1:4., doi: 10.3389/feart.2013.00004

Price, N.J., 1958. A study of rock properties in conditions of triaxial stress. In: Walton, W.H. (Ed.), Proceedings of a Conference on the mechanical properties of non-metallic brittle materials. Butterworth, London, 106-122.

Price, N.J., 1960. The compressive strength of coal measure rocks. Colliery Engineering 37, 283-292.

Price, N.J., 1963. The influence of geological factors on the strength of Coal Measure Rocks. Geological Magazine 100, 428-443.

Rippon, J.H., Gayer, R.A., Miliorizos, M., 1997. Variscan structures in the Kent Coalfield, southeast England and their regional significance. Geological Magazine 134, 855-867.

Rives, T., Petit, J.P., 1990. Experimental study of jointing during cylindrical and non-cylindrical folding. In: Rossmanith, H.P. (Ed.), Proceedings of the International Conference on the Mechanics of Jointed and Faulted Rock. Balkema, Rotterdam, 205-211.

Rives, T., Rawnsley, K.D., Petit, J.P., 1994. Analogue simulation of natural orthogonal joint set formation in brittle varnish. Journal of Structural Geology 16, 419-429.

Robinson, D., Nicholls, R.A., Thomas, L.J., 1980. Clay mineral evidence for low-grade Caledonian and Variscan metamorphism in south-western Dyfed, South Wales. Mineralogical Magazine 43, 857-863.

Simon, J.L., Seron, F.J., Casas, A.M., 1988. Stress deflection and fracture development in a multidirectional extension regime: mathematical and experimental approach with field example. Annales Tectonicae 2, 21-32.

Sneddon, I.N., Lowengrub, M., 1969. Crack problems in the classical theory of elasticity. Wiley, New York.

Swan, A.R.H., Sandilands, M., 1995. Introduction to Geological Data Analysis. Blackwell Science, Oxford.

Waters, C.N., Davies, S.J., 2006. Carboniferous: extensional basins, advancing deltas and coal swamps. In: Brenchley, P.J., Rawson, P.F. (Eds.), The Geology of England and Wales. Geological Society of London, London, 173-223.

White, S.C., 1991. Palaeo-geothermal profiling across the South Wales Coalfield. Proceedings of the Ussher Society 7, 368-374.

Wright, V.P., 1987. The evolution of the early Carboniferous limestone province in southwest Britain. Geological Magazine 124, 477-480.

Chapter 6: Paper 3

Manuscript published as a conference paper in IPTC 2016 (International Petroleum Technology Conference)

Title: Analytical calculation for mode I fracture formation in mechanical layers: Effects of mechanical properties, stress fields, pore-pressure and layer thickness

Authors: Tetsuzo Fukunari and Agust Gudmundsson

Total number of manuscript pages: 18

Statement of my role for the paper 3:

- Analytical calculations
- Writing the manuscript and illustrating the figures

Analytical calculation for mode I fracture formation in mechanical layers: Effects of mechanical properties, stress fields, pore-pressure and layer thickness

Tetsuzo Fukunari[1,2,*], Agust Gudmundsson[1]

[1]Department of Earth Sciences, Royal Holloway University of London, Egham, Surrey TW20 0EX, UK

[2]Japan Oil, Gas and Metals National Corporation (JOGMEC), Toranomon Twin Building, 2-10-1 Tranomon, Minato-ku, Tokyo 105-0001, JAPN

* email: fukunari-tetsuzo@jogmec.go.jp

Abstract

The aim of this paper is to provide analytical solutions of stress fields in mechanical layers which consist of stiff and soft or compliant layers. The paper examines possible geological conditions of mode I (extension) fracture development on the basis of the analytical calculations with various layer thicknesses, Young's moduli, Poisson's ratios, external stress fields and pore-fluid pressure. Linear elastic model with two different mechanical layers is assumed for the calculations. Fluid-driven fractures, hydrofractures, are discussed in detail elsewhere and are not considered here. Layer-parallel stresses in the model caused by external stresses and pore-fluid pressure are mathematically calculated for both stiff and soft layers. Relative Young's modulus and relative thickness between the two types of layers are applied to simplify the associated equations. Poisson's ratio ν is assumed to be same between the two. This is because the possible variation of Poisson's ratio between rocks is much smaller than those of the other parameters. The calculated ratio of minimum to maximum principal stresses within each layer is used to estimate fracture type which can develop under various geological conditions. The results indicate extension fracture preferably develop in stiff layer. Stress conditions in the model are primarily controlled by relationship among

external horizontal stress σ_{XX}, vertical stress σ_{ZZ} and pore-fluid pressure P_f: no extension fracture forms when $\sigma_{XX} > P_f + \nu(\sigma_{ZZ} - P_f)/(1 - \nu)$; extension fractures can form only in stiff layers in soft-layer-dominant system when $P_f + \nu(\sigma_{ZZ} - P_f)/(1 - \nu) > \sigma_{XX} > P_f$; extension fractures form in stiff layers in both stiff-layer-dominant and soft-layer-dominant systems when $P_f > \sigma_{XX} > 4P_f/3 - \sigma_{ZZ}/3$; extension fracture can form in both stiff and soft layers in soft-layer-dominant formation with small relative Young's modulus when $4P_f/3 - \sigma_{ZZ}/3 > \sigma_{XX}$. Only shear fractures can form in soft layers, except the rare geological condition of $4P_f/3 - \sigma_{ZZ}/3 > \sigma_{XX}$ with very small relative Young's modulus. The results of analytical calculations provide potential criterion to estimate when and where layer-scale extension fracture network develops in relation with geological history. One implication of the results is that extension fracture formation is not necessarily related to regional tensile stress field but ratio among horizontal stress, vertical stress and pore-fluid pressure. This implies that extension fracture network can form in mechanical layers not only during crustal uplift/exhumation but also during basin-burial in which horizontal stress, vertical stress and pore-fluid pressure are increasing.

Keywords: extension fracture formation, mechanical layers, analytical calculation, basin subsidence, South Wales coalfield

1. Introduction

Fracture network has great impact on, and sometimes likely control, permeability and fluid transport in subsurface reservoirs. It is, therefore, of importance to understand how such fracture network develops in relation with geological history to estimate where high permeable reservoirs exist in the ground.

The focus of this paper is on mode I (extension) fracture formation in mechanical layers. Mode I fractures (joints and veins) in layered rocks are often documented in outcrops in sedimentary basins (e.g. Price, 1966; Narr and Suppe, 1991; Gross and Engelder 1995; Phillips 2012). Although the developments of such extension fractures require effective tensile stress field, measured horizontal stresses in the ground are generally compressive (McGarr and Gray, 1978; McGarr, 1982). It may suggest that most extension fractures develop only in shallow part of the basin. However, fluid-

driven extension fractures (hydrofractures) can form at any depth. Many researchers also proposed possible mechanisms to explain orthogonal network formation of extension fractures: local stress rotation or flip due to formation of the first set of fractures (Simon et al., 1988; Caputo, 1995; Bai et al., 2002); regional principal stress rotation (Hancock et al., 1987; Eyal, 1996); and post-tectonic strain relaxation of visco-elastic materials (Rives and Petit, 1990; Rives et al., 1994). The given mechanisms require regional tensile stress in two horizontal directions, although normally not at the same time, and the developments of extension fracture networks are associated with uplift or exhumation of geological formations.

One of the questions here is whether those open mode fractures and their networks form only at the shallow depth in relation with crustal uplift/exhumation, if they can also develop during basin-burial in which both horizontal and vertical compressive stresses are increasing. It must be critical when we estimate open mode fracture network in subsurface reservoirs. Some laboratory experiments and field observations suggest flaws, inclusions or pores in rock can induce local tensile stress under external compression (Borg and Maxwell, 1956; Gramberg, 1965; Gallagher et al., 1974; Tapponnier and Brace, 1976; Eidelman and Reeches, 1992; Reeches 1998) but such local tensile stress does not account for extension fracture formation in basin-scale. Bourne (2003) provides analytical solution of stress field in three dimensional layered rock which is idealized as bounded, planar, isotropic, homogeneous, linear-elastic system under compressive stress field. One of scenarios in the Bourne model suggests tensile stress can be induced under compressive stress field. However, there are several parameters in the Bourne model and it is slightly unclear what geological conditions control extension fracture formation. Effect of pore-fluid pressure is also not taken into account. This paper, therefore, proposes simplified/modified version of Bourne model (Bourne, 2003) to investigate main parameters controlling extension fracture formation in the ground and examine the possibility of open mode fracture formation in mechanical layers during basin-burial. The model is based on linear-elastic theory. Some parameters which do not have impact on calculation results are ignored to make the associated equations simpler. Extension-formation through hydrofractures is not considered in this paper, because it is considered in detail elsewhere (Gudmundsson, 2011; Philipp et al., 2013). The results suggest relationship among external vertical and

horizontal stresses and pore-fluid pressure primarily controls extension fracture formation and that relative Young's modulus and relative thickness between stiff and soft layers secondarily affect it. We provide possible geological conditions of external stress field, pore-pressure and other parameters for extension fracture formation. They are not necessarily related with regional tensile stress field and seem to be applicable for increasing phase of vertical stress (during basin-burial) once rocks are consolidated.

2. Basic idea for tensile stress generation in mechanical layers under compressive stress field

In this paper, the associated rocks are assumed as continuous (bounded), isotropic, homogeneous and linear-elastic media. The rocks are composed of only two materials: stiff and soft or compliant layers. This assumption is to simplify the associated equations. Actually, rocks (sandstone, limestone, shale, etc.) have some variation of mechanical properties even in a same rock type. However, range of the variation in a same rock type is commonly much smaller than the range between different rock types. It is, therefore, reasonable to apply only two mechanical properties which represent stiff and soft rocks in mechanical layers such as sand-shale or limestone-shale layers to understand the phenomenon which induced complex stress field in the mechanical layers.

Figure 1 shows two representative cases of strain and stress conditions within the soft and stiff layers when external vertical stress σ_{ZZ} is applied on the mechanical layers. In Figure 1(a), lateral strain is fixed. Therefore, no lateral strain is induced when vertical stress is applied. Instead of lateral elongation of the rock, compressive stresses are generated depending on Poisson's ratios of the soft and stiff layers. In contrast, if lateral strain is not fixed (free), the layered rock is elongated laterally depending on Young's moduli and Poisson's ratios of the stiff and soft layers (Figure 1b). In this case, lateral stresses are also generated due to the difference of mechanical properties between the two layers. The stresses become tensile in stiff layer and compressive in soft layer. This is because soft layers are elongated more largely due to low Young's modulus and they drag adjacent stiff layers where smaller lateral strain is generated due to higher Young's modulus. On the other hand, soft layers are compressed by stiff layers which prevent the soft layers from being elongated. This basic concept is

simplified model of bounded case with vertical loading of Bourne (2003) and suggests that vertical stress applied on mechanical layers can induce tensile stresses in relatively stiff layers if external compressive stress in horizontal direction is sufficiently small.

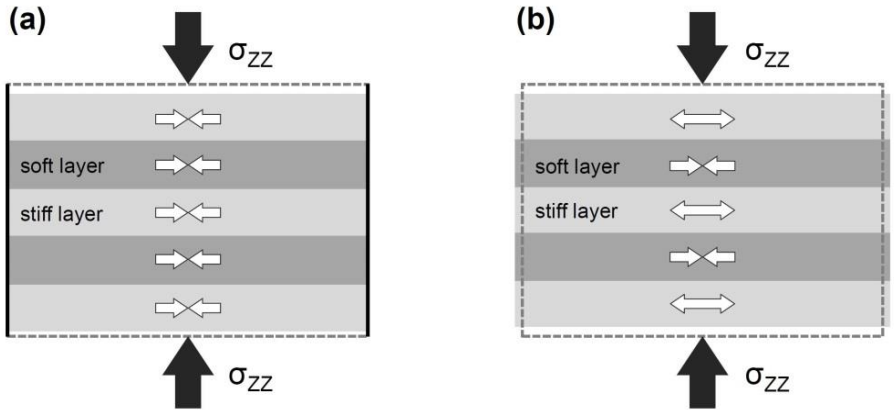

Figure 1 Layer-parallel stresses caused by external vertical stress σ_{ZZ} (overburden pressure) in mechanical layers. External stress is shown by black allow and internal stress in each layer generated by the external stress is shown by white allow. **(a)** Lateral strain of the layered rock is fixed. Compressive stresses are generated in mechanical layers. The intensity of generated stress depends on Poisson's ratio in each layer. **(b)** Lateral strain of the rock is free. Compressive stresses are generated in soft layers and tensile stresses are generated in stiff layers.

3. Analytical solutions for layer-parallel stresses induced by external vertical, horizontal stresses and pore-fluid pressure

In subsurface, lateral strain of rocks must be controlled by both vertical and horizontal stresses. Pore-fluid pressure also affects the stress field. In this section, lateral stresses in the stiff and soft layers of the model which are induced by external vertical stress (overburden pressure), external horizontal stress and pore-fluid pressure are analytically calculated. The equation is simplified version of Bourne (2003) but the results provide simpler relationship between input parameters and stress field in the mechanical layers and better understanding of control factors to develop extension fractures in subsurface mechanical layers.

3.1. Model geometry

Simple three-layer model is assumed to calculate layer-parallel stresses in mechanical layers caused by external stresses and pore-fluid pressure (Figure 2). In the model, Young's moduli and Poisson's ratios are set to be E_a and ν_a for the stiff layer and E_b and ν_b for the soft layers. Thicknesses are set to be Th_{b1}, Th_a and Th_{b2} from upper to lower layers in Figure 2. Applied stresses from outside the model are σ_{XX} and σ_{YY} in horizontal directions and σ_{ZZ} in vertical direction. Induced horizontal stress is shown by $\sigma_{a,xx}$ or $\sigma_{a,yy}$ in stiff layer and $\sigma_{b,xx}$ or $\sigma_{b,yy}$ in soft layer. Three-layer model is assumed for simplification but the number of layers essentially has no impact on calculation results but ratio of total thickness or volume between the stiff and soft layers affects the result as long as continuous (no slip along the layer boundaries) medium with only two different materials are assumed.

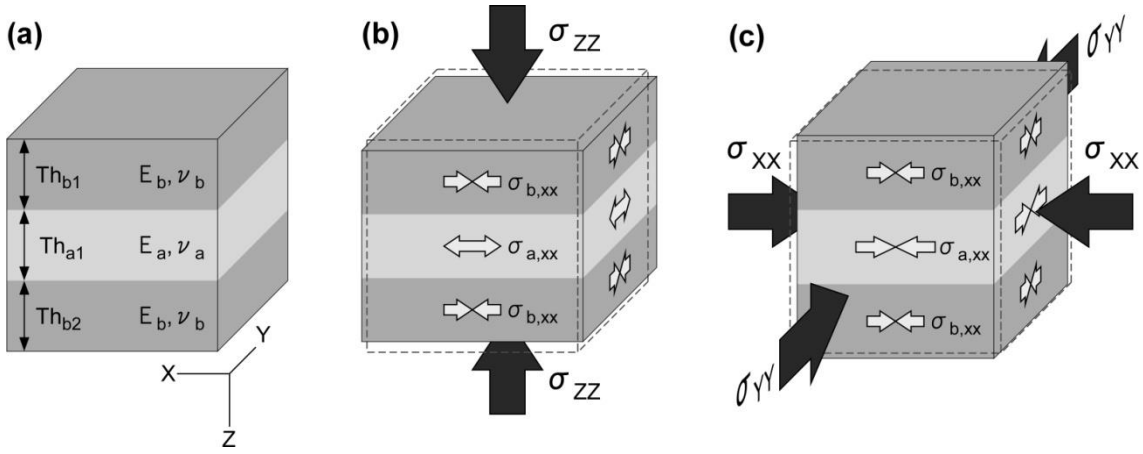

Figure 2 Schematic illustrations of the three-layer model. External stresses applied on the rock are shown by black allows and internal stresses generated by the external stresses are shown by white allows. Darker layers represent soft layers and the other is stiff layer. **(a)** Original condition of layered rock. **(b)** Internal stresses caused by external vertical stress σ_{ZZ}. **(c)** Internal stresses caused by external horizontal stresses σ_{XX} and σ_{YY}.

3.2. Layer-parallel stresses caused by external vertical stress

With the above model settings, lateral strain in the layered rock caused by external vertical stress σ_{ZZ} is shown by following formula. Because the rock is assumed as continuous medium, the lateral strains of stiff and soft layers are same:

$$\varepsilon_{xx} = \frac{\sigma_{a,xx} - \nu_a(\sigma_{a,yy} + \sigma_{ZZ})}{E_a} = \frac{\sigma_{b,xx} - \nu_b(\sigma_{b,yy} + \sigma_{ZZ})}{E_b} \qquad (1)$$

Force balance is as follow when vertical stress σ_{ZZ} is applied:

$$\sum Th_{ai}\sigma_{a,xx} + \sum Th_{bi}\sigma_{b,xx} = 0 \qquad (2)$$

where *i* is layer number. As described above, the number of layers is not essential but total thicknesses or volumes of stiff and soft layers have impact on the calculation results. The form of equation (2), therefore, allows it to solve the problems with four or more layer model

Relative Young's modulus E_r and relative total thickness Th_r are assigned to reduce the parameters in equation (1) and (2). In addition, Poisson's ration is assumed to be same between stiff and soft layers. This is because the variation of Poisson's ratio for rocks is much smaller than that of Young's modulus. Although Young's modulus commonly ranges from 1 to 100 GPa, Poisson's ratio for rocks has normally a very narrow range, commonly between 0.2 and 0.3 (Bell 2000; Gudmundsson 2011). It is, therefore, assumed that Poisson's ratio has smaller impact on calculation results in this paper. In addition, the associated equations become effectively simpler by assuming the same Poisson's ratio between the two rock types.

$$E_r = \frac{E_a}{E_b} \qquad (3)$$

$$Th_r = \frac{\sum Th_{ai}}{\sum Th_{bi}} \qquad (4)$$

$$\nu = \nu_a = \nu_b \qquad (5)$$

Induced horizontal stresses in x-direction and y-direction are same because the model is isotropic:

$$\sigma_{a,xx} = \sigma_{a,yy} \qquad (6)$$

$$\sigma_{b,xx} = \sigma_{b,yy} \qquad (7)$$

By substituting equation (3)-(7) into the formula (1) and (2), layer-parallel stresses $\sigma_{a,xx}$ in the stiff layer and $\sigma_{b,xx}$ in the soft layers induced by external vertical stress σ_{ZZ} are obtained as follows:

$$\sigma_{a,xx} = \frac{\nu(1-E_r)}{(1-\nu)(1+E_r Th_r)}\sigma_{ZZ} \qquad (8)$$

$$\sigma_{b,xx} = -\frac{\nu Th_r(1-E_r)}{(1-\nu)(1+E_r Th_r)}\sigma_{ZZ} \qquad (9)$$

3.3. Layer-parallel stresses caused by external horizontal stress

Layer-parallel stresses caused by external horizontal stresses σ_{XX} and σ_{YY} are calculated in the same manner as that of above section. Lateral strains caused by external horizontal stresses in x- and y-directions are as follows:

$$\varepsilon_{xx} = \frac{\sigma_{a,xx}-\nu_a\sigma_{a,yy}}{E_a} = \frac{\sigma_{b,xx}-\nu_b\sigma_{b,yy}}{E_b} \qquad (10)$$

$$\varepsilon_{yy} = \frac{\sigma_{a,yy}-\nu_a\sigma_{a,xx}}{E_a} = \frac{\sigma_{b,yy}-\nu_b\sigma_{b,xx}}{E_b} \qquad (11)$$

Force balance is given by following equations:

$$\sum Th_{ai}\sigma_{a,xx} + \sum Th_{bi}\sigma_{b,xx} = (\sum Th_{ai} + \sum Th_{bi})\sigma_{XX} \qquad (12)$$

$$\sum Th_{ai}\sigma_{a,yy} + \sum Th_{bi}\sigma_{b,yy} = (\sum Th_{ai} + \sum Th_{bi})\sigma_{YY} \qquad (13)$$

By substituting equation (3)-(5) into the formula (10)-(13), layer-parallel stresses $\sigma_{a,xx}$ in the stiff layer and $\sigma_{b,xx}$ in the soft layers induced by external horizontal stress σ_{XX} and σ_{YY} are obtained as follows. The forms of calculated results are same between x-direction and y-direction. Results in x-direction are shown here:

$$\sigma_{a,xx} = \frac{Er(Th_r+1)}{(1+E_r Th_r)}\sigma_{XX} \qquad (14)$$

$$\sigma_{b,xx} = \frac{Th_r+1}{(1+E_r Th_r)}\sigma_{XX} \qquad (15)$$

3.4. Effective layer parallel stresses under three dimensional compressive stress field

Because forms of equations are same in x- and y-directions, only x-direction is focused in the following equations. Equation (8) and (14) are combined and terms for pore-fluid pressure P_f are added. The result indicates layer-parallel effective stress in x-direction in the stiff layer caused by external vertical and horizontal stresses and pore-fluid pressure. Layer parallel effective stress in soft layers is also shown (the apostrophe being added for effective stress).

$$\sigma'_{a,xx} = \frac{\nu(1-E_r)}{(1-\nu)(1+E_r Th_r)}(\sigma_{ZZ} - Pf) + \frac{Er(Th_r+1)}{(1+E_r Th_r)}(\sigma_{XX} - Pf) \qquad (16)$$

$$\sigma'_{b,xx} = -\frac{\nu Th_r(1-E_r)}{(1-\nu)(1+E_r Th_r)}(\sigma_{ZZ} - Pf) + \frac{Th_r+1}{(1+E_r Th_r)}(\sigma_{XX} - Pf) \qquad (17)$$

4. Relationship among external stresses, pore-fluid pressure and extension fracture formation

4.1. Stress conditions for extension fracture formation

Relationships between the induced horizontal stress $\sigma'_{a,xx}$ and $\sigma'_{b,xx}$ (equation (16) and (17)) and effective external vertical stress ($\sigma_{ZZ} - P_f$) represent two-dimensional effective stress fields in stiff and soft layers. Based on Griffith criterion for fracture initiation (Griffith, 1924), following conditions are required at the time of extension fracture formation:

$$(\sigma_{ZZ} - P_f) - \sigma'_{a,xx} < 4T_a \qquad (18)$$

$$(\sigma_{ZZ} - P_f) - \sigma'_{b,xx} < 4T_b \qquad (19)$$

where T_a and T_b are tensile strengths for stiff layer and soft layers, respectively. At the time of extension fracture formation, $\sigma'_{a,xx}$ is $-T_a$ in stiff layer and $\sigma'_{b,xx}$ is $-T_b$ in soft layer, meaning that effective external vertical stress must be less than $3T_a$ for stiff layer and $3T_b$ for soft layer at that time. Thus, the following stress conditions are required at the time of extension fracture formation:

$$\sigma'_{a,xx}/(\sigma_{ZZ} - P_f) < -1/3 \qquad (20)$$

$$\sigma'_{b,xx}/(\sigma_{ZZ} - P_f) < -1/3 \qquad (21)$$

Relationship between Mohr circle and Griffith failure envelop also provides stress conditions for hybrid or mixed mode (extension + shear) fracture formation. When tangent point between Mohr circle and Griffith failure envelop is at the point of shear strength (horiztontal stress is zero), the diameter of Mohr circle should be $4\sqrt{2}$T with the circle centre of (2T, 0). Therefore, mixed mode fracture formation requires diameter of Mohr circle smaller than $4\sqrt{2}$T:

$$-1/3 < \sigma'_{a,xx}/(\sigma_{ZZ} - P_f) < 3 - 2\sqrt{2} \qquad (22)$$

$$-1/3 < \sigma'_{b,xx}/(\sigma_{ZZ} - P_f) < 3 - 2\sqrt{2} \qquad (23)$$

Subsequently, if the effective stress conditions are as follows, only shear fractures can form in the layers:

$$3 - 2\sqrt{2} < \sigma'_{a,xx}/(\sigma_{ZZ} - P_f) \qquad (24)$$

$$3 - 2\sqrt{2} < \sigma'_{b,xx}/(\sigma_{ZZ} - P_f) \qquad (25)$$

4.2. Relationship among σ_{ZZ}, σ_{XX}, P_f and extension fracture formation

4.2.1. Case of external horizontal stress equal to pore-fluid pressure

Some combination of σ_{ZZ}, σ_{XX} and P_f make equation (16) and (17) simpler. If external horizontal stress σ_{XX} is same as pore-fluid pressure P_f, the second terms of equation (16) and (17) are deleted as follows:

$$\sigma'_{a,xx} = \frac{\nu(1-E_r)}{(1-\nu)(1+E_r Th_r)}(\sigma_{ZZ} - Pf) \qquad (26)$$

$$\sigma'_{b,xx} = -\frac{\nu Th_r(1-E_r)}{(1-\nu)(1+E_r Th_r)}(\sigma_{ZZ} - Pf) \qquad (27)$$

Figure 3 shows relationship between stress conditions and relative thickness Th_r with various relative Young's modulus E_r and Poisson's ratio ν in the stiff and soft layers in the case of equation (26) and (27). In equation (26) which is for stress condition in stiff layer, E_r and ν exist in both numerator and denominator, suggesting that the two parameters are not effective compared with relative thickness Th_r which exists only in denominator. In fact, when $Th_r < 1$ (soft layer dominant case), $\sigma'_{a,xx}/(\sigma_{ZZ} - P_f)$ becomes smaller than $-1/3$ with most combinations of ν and E_r (Figure 3a). This indicates extension fracture can form when soft layer is dominant. Only in the case that difference of Young's modulus between the still and soft layers is very small (E_r is equal or smaller than 2), $\sigma'_{a,xx}/(\sigma_{ZZ} - P_f)$ becomes larger than $-1/3$ and only shear or hybrid fractures can form. On the other hand, if $Th_r > 1$ (stiff layer dominant case), $\sigma'_{a,xx}/(\sigma_{ZZ} - P_f)$ becomes larger than $-1/3$ with most combinations of ν and E_r, suggesting no extension fracture can form when stiff layer is dominant.

Stress $\sigma'_{b,xx}/(\sigma_{ZZ} - P_f)$ becomes larger than $3 - 2\sqrt{2}$ in soft layer with any relative Young's modulus and Poisson's ratio and only shear fractures can form in soft layer when $\sigma_{XX} = P_f$ (Figure 3b).

As summary, under the condition of $\sigma_{XX} = P_f$, extension fractures can form only in stiff layer with relative Young's modulus > 2 when soft layer is dominant in the system (Figure 3a). No extension fracture forms in the case that stiff layer is dominant. Extension fracture also cannot form and only shear fractures develop in soft layer in any conditions (Figure 3b).

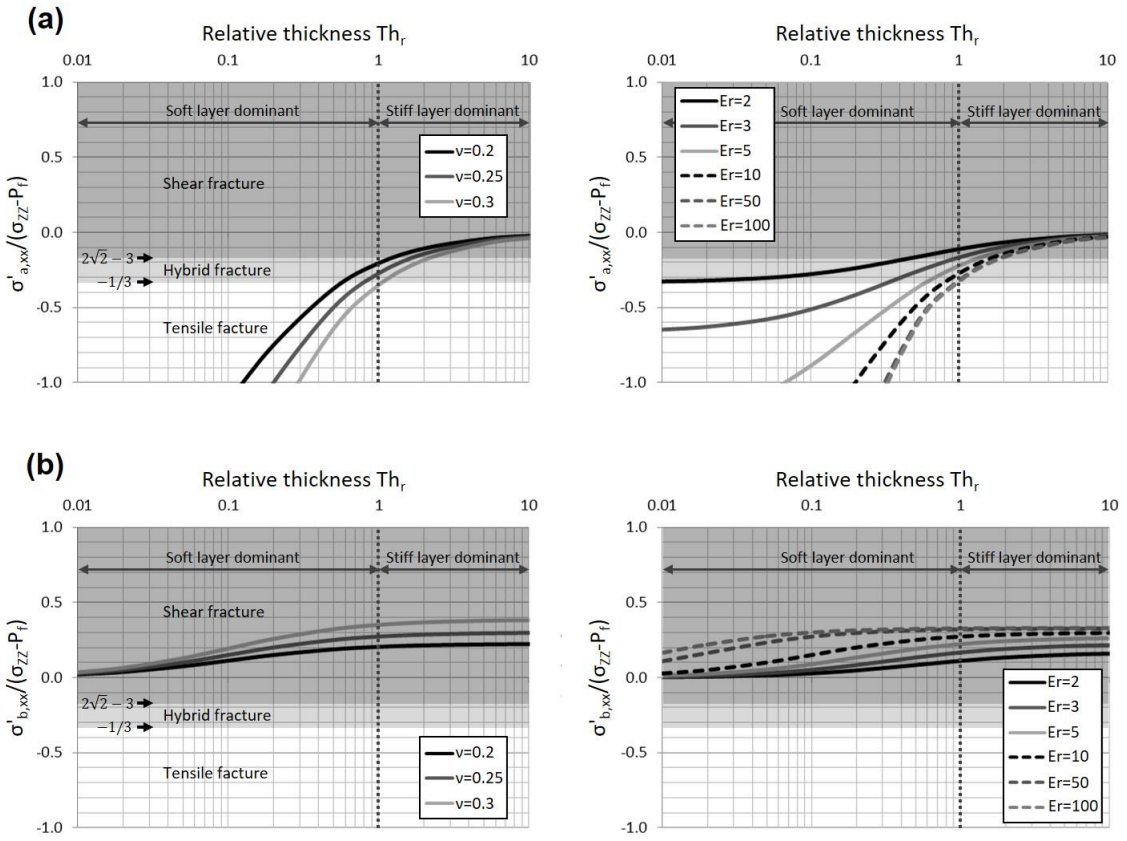

Figure 3 Relationship between effective stress conditions (ordinate axis) and relative thickness (abscissa axis) when $\sigma_{XX} = P_f$. **(a)** Relationship between $\sigma'_{a,xx}/(\sigma_{ZZ} - P_f)$ and Th_r in stiff layer. Relative Young's modulus E_r is 10 and Poisson's ratio ν is changed in the left graph. Poisson's ratio ν is 0.25 and relative Young's modulus E_r is changed in the right graph. **(b)** Relationship between $\sigma'_{b,xx}/(\sigma_{ZZ} - P_f)$ and Th_r in soft layer. E_r is 10 and ν is changed in the left graph. ν is 0.25 and E_r is changed in the right graph.

Figure 4 shows examples of other stress conditions. It illustrates that when σ_{XX} is larger than P_f, extension fractures can form with smaller Th_r and larger E_r. This is one of the remarkable results of these calculations, which indicates extension fracture can form in stiff layer even in the case that effective external horizontal stress is compressive with some geological conditions (e.g. $P_f = 0.4\sigma_{ZZ}$, $\sigma_{XX} = 0.5\sigma_{ZZ}$, Thr < 0.2 and Er > 10). Figure 4 also shows that if σ_{XX} is smaller than P_f (effective external horiztontal stress is negative), extension fracture can form more easily even in stiff layer dominant case.

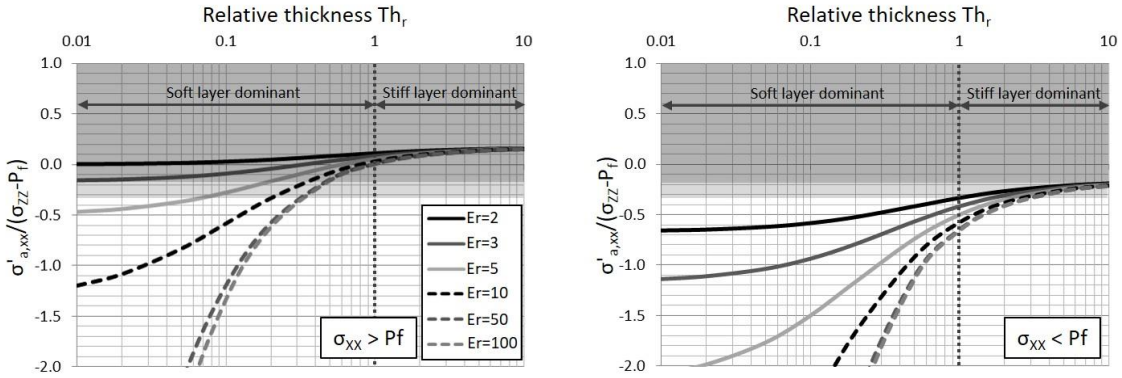

Figure 4 Relationship between effective stress conditions (ordinate axis) and relative thickness (abscissa axis) in stiff layer when $\sigma_{XX} > P_f$ ($P_f = 0.4\sigma_{ZZ}$ and $\sigma_{XX} = 0.5\sigma_{ZZ}$ in left graph) and $\sigma_{XX} < P_f$ ($P_f = 0.4\sigma_{ZZ}$ and $\sigma_{XX} = 0.3\sigma_{ZZ}$ in right graph). Poisson's ratio ν is fixed as 0.25 because of small impact on the current calculations. Relative Young's modulus E_r is changed from 2 to 100 in both graphs.

4.2.2. Case of no extension fracture formation

When relationship among σ_{ZZ}, σ_{XX} and P_f satisfies the following condition, lateral strain becomes nil ($\varepsilon_{xx} = 0$) and other simpler forms of equation (16) and (17) are obtained:

$$(\sigma_{XX} - P_f) = \frac{\nu}{1-\nu}(\sigma_{ZZ} - P_f) \qquad (28)$$

In this case, both equation (16) and (17) become following form and only compressive stress is induced in layer-parallel direction in both stiff and soft layers because effective external vertical stress (overburden pressure) is positive in any case in the ground:

$$\sigma'_{a,xx} = \sigma'_{b,xx} = \frac{\nu}{1-\nu}(\sigma_{ZZ} - P_f) \qquad (29)$$

4.2.3. Case of extension fractures formation in soft layer

Possible combination of σ_{ZZ}, σ_{XX} and P_f for extension fracture formation in soft layer is also estimated from equation (17). Smaller E_r and smaller Th_r are suitable for extension fracture formation in soft layer. Therefore, as an extreme case, minimum values of E_r and Th_r ($E_r = 1$ and $Th_r = 0$) are considered in the equation (17). It is same as only soft layer exists. In that case, the equation (17) becomes $\sigma'_{b,xx} = \sigma_{XX} - P_f$. Stress condition of Equation (21) is required for extension fracture formation. Thus, $(\sigma_{XX} - P_f)/(\sigma_{ZZ} - P_f)$

must be smaller than –1/3 for extension fracture formation in soft layer. As a consequence, if $(\sigma_{XX} - P_f)/(\sigma_{ZZ} - P_f) < -1/3$, and E_r and Th_r are very small, extension fractures may develop even in soft layer although such geological conditions seem to be unrealistic.

4.2.4. Summary of relationship among σ_{ZZ}, σ_{XX}, P_f and extension fracture formation

Relationship between σ_{ZZ}, σ_{XX}, P_f and extension fracture formation is summarized in Figure 5. Pf/σ_{ZZ} is abscissa axis and σ_{XX}/σ_{ZZ} is ordinate axis in the figure. Condition of $(\sigma_{XX} - P_f)/(\sigma_{ZZ} - P_f) < -1/3$ (same as $\sigma_{XX} < 4/3\,P_f - 1/3\,\sigma_{ZZ}$) is required for extension fracture formation in soft layer. In the condition of $4/3\,P_f - 1/3\,\sigma_{ZZ} < \sigma_{XX} < P_f$, extension fractures can develop in stiff layer even in the stiff layer dominant system (right graph of Figure 4). If $P_f < \sigma_{XX}$, (effective external horizontal stress is positive), extension fractures can form in stiff layer only in the stiff layer dominant system (left graph of Figure 4). If relationship between σ_{ZZ}, σ_{XX} and P_f becomes equation (28), which is same as $\sigma_{XX} = P_f + \nu(\sigma_{ZZ} - P_f)/(1 - \nu)$, only compressive stress is induced in both stiff and soft layers in any case. In that case, lateral strain ε_{xx} becomes 0. The limit of stress condition for extension fracture formation is shown as critical condition in Figure 5, which is controlled by Poisson's ratio. As summarized in Figure 5, relationship between external vertical stress σ_{ZZ}, external horizontal stress σ_{XX} and pore-fluid pressure P_f primarily controls extension fracture formation in mechanical layers. Relative Young's modulus E_r and relative thickness Th_r secondarily affect the possibility of extension fracture formation.

One of the main results here is that extension fracture formation in the ground is not always related with external horizontal tensile stress or crustal uplift/exhumation but ratio among external horizontal stress, external vertical stress and pore-fluid pressure. This suggests the possibility that extension fractures form in mechanical layers during basin-burial in which horizontal stress, vertical stress and pore-fluid pressure are increasing.

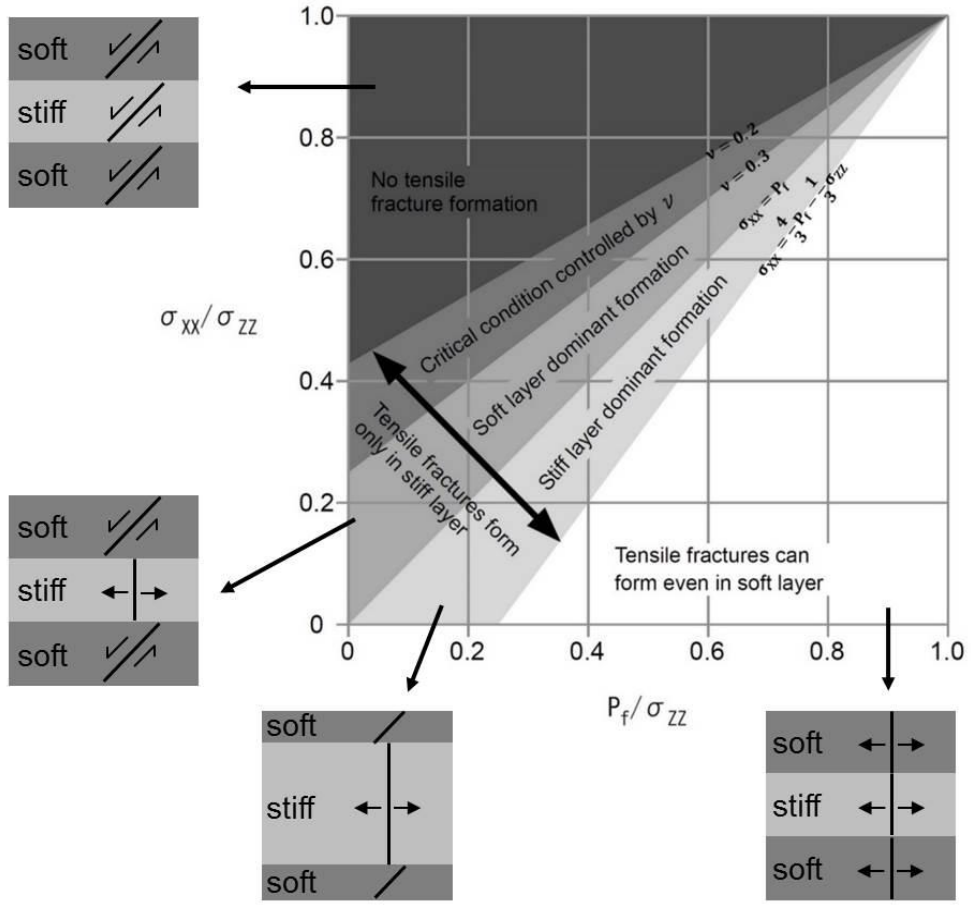

Figure 5 Relationship between σ_{ZZ}, σ_{XX}, P_f and extension fracture formation in alternating stiff-soft layers.

5. Conclusions

Analytical solutions obtained from simple layered model in which rocks are assumed as linear-elastic, continuous (fully bounded), isotropic and homogenous materials provide the following results and implications.

1. Effective tensile stress can be induced in stiff layer which is surrounded by softer layer, depending on external vertical stress, external horizontal stress, pore-fluid pressure and relative Young's modulus and relative total thickness between stiff and soft layers.
2. Relationship between external vertical stress, external horizontal stress and pore-fluid pressure primarily controls development of the extension fractures in mechanical layers.
3. Relative Young's modulus and relative total thickness between stiff and soft layers

secondarily control the possibility of extension fracture formation. Extension fractures develop more easily in stiff layers with soft layer dominant system and larger gap of Young's moduli between the layers.

4. The geological conditions are not necessarily related with external horizontal tensile stress but ratio among horizontal stress, vertical stress and pore-fluid pressure for extension fracture formation. This implies that extension fractures can form in mechanical layers during basin-burial in which horizontal stress, vertical stress and pore-fluid pressure are increasing.

References

Bai, T., Maerten, L., Gross, M.R., Aydin, A., 2002. Orthogonal cross joints: do they imply a regional stress rotation? Journal of Structural Geology 24, 77-88.

Belayneth, M., Geiger, S., Matthai, S.K., 2006. Numerical simulation of water injection into layered fractured carbonate reservoir analogs. AAPG Bulletin 90, 1473-1493.

Bell, F.G., 2000. Engineering Properties of Rocks, 4th edition. Oxford, Blackwell.

Borg, I.Y., Maxwell, J.C., 1956. Interpretation of fabrics of experimentally deformed sands. American Journal of Science 254, 71-74.

Bourne, S.J., 2003. Contrast of elastic properties between rock layers as a mechanism for the initiation and orientation of tensile failure under uniform remote compression, Journal of Geophysical Research, 108 (B8), 2395.

Caputo, R., 1995. Evolution of orthogonal sets of coeval extension joints. Terra Nova 7, 479-490.

Eidelman, A., Reeches, Z., 1992. Fractured pebbles – A new stress indicator. Geology 20, 307-310.

Eyal, Y., 1996. Stress field fluctuations along the Dead Sea Rift since the middle Miocene. Tectonics 15, 157-170.

Gallagher, J.J., Friedman, M., Handin, J., Sowers, G.M., 1974. Experimental studies relating to microfracture in sandstone. Tectonophysics 21, 203-247.

Gramberg, J., 1965. Axial cleavage fracturing, a significant process in mining and geology. Engineering Geology 1, 31-72

Griffith, A.A., 1924. Theory of rupture. In: Biezeno, C.B., Burgers, J.B. (Eds.), Proceedings of the First International Congress on Applied Mechanics. Delft, Waltman, 55-63.

Gross, M.R., Engelder T., 1995. Strain accommodated by brittle failure in adjacent units of the Monterey Formation, U.S.A.: scale effects and evidence for uniform displacement boundary conditions. Journal of Structural Geology 17, 1303-1318.

Gudmundsson, A., 2011. Rock Fractures in Geological Processes. Cambridge University Press, New York.

Hancock, P.L., Al-Kadhi, A., Barka, A.A., Bevan, T.G., 1987. Aspects of analyzing brittle structures. Annales Tectonicae 1, 5-19.

McGarr, A. M., Gay, N.C., 1978. State of stress in the Earth's crust, Annual Review of Eath and Planetary Sciences 6, 401-436.

McGarr, A.M., 1982. Analytical of stress between provinces of constant stress. Journal of Geophysical Research 87, 9279-9288.

Narr, W., Suppe, J.,1991. Joint Spacing in sedimentary rocks. Journal of Structural Geology 13, 1037-1048.

Price, N.J., 1966. Fault and joint development in brittle and semi-brittle rocks. Pergamon Press, Oxford.

Price, N.J., Cosgrove, J.W., 1990. Analysis of geological structures, Cambrige University Press, Cambrige.

Philipp, S.L., 2012. Fluid overpressure estimated from the aspect ratios of mineral veins. Tectonophysics 581, 35-47.

Philipp, S., Afsar, F., Gudmundsson, A., 2013. Effects of mechanical layering on hydrofracture emplacement and fluid transport in reservoirs. Frontiers in Earth Science 1, 1-19.

Reeche, Z., 1998. Tensile fracturing of stiff rock layers under triaxial compressive stress. International Journal of Rock Mechanics and Mining Sciences 35, 4-5.

Rives, T., Petit, J.P., 1990. Experimental study of jointing during cylindrical and non-cylindrical folding. In: Rossmanith, H.P. (Ed.), Proceedings of the International Conference on the Mechanics of Jointed and Faulted Rock. Balkema, Rotterdam, 205-211.

Rives, T., Rawnsley, K.D., Petit, J.P., 1994. Analogue simulation of natural orthogonal joint set formation in brittle varnish. Journal of Structural Geology 16, 419-429.

Simon, J.L., Seron, F.J., Casas, A.M., 1988. Stress deflection and fracture development in a multidirectional extension regime: mathematical and experimental approach with field example. Annales Tectonicae 2, 21-32.

Tapponnier, P., Brace, W.F., 1976. Development of stress-induced micro-cracks in Westerly granite. International Journal of Rock Mechanics and Mining Sciences & Geomechanics Abstract 13, 103-112.

Chapter 7: Discussion and conclusions

7.1. Discussion and summary of results of chapter 4, 5 & 6

Mechanism of extension fracture formation in mechanical layers is focused in this thesis. The main reason of this selection for research subject is that low-resistivity low-contrast pay zones are one of the major exploration and development targets for hydrocarbon reservoirs. The low-resistive low-contrast conditions of the reservoirs are commonly caused by sedimentary layering/lamination (e.g. layering of hydrocarbon-bearing sandstones and shale which contained significant amount of clay-bound-water and capillary-bound-water) thinner than the resolution of wire-line logging. The typical resolution of the logging tools used in the industry is 2 feet. Therefore, better understanding of development mechanism of layer-controlled fractures in centimetre to decimetre scale layered sediments can largely contribute to estimate subsurface fluid transportation of the reservoirs with low-resistivity low-contrast pay zones.

The South Wales coalfield was selected for the study area where layer-controlled extension fractures and veins are commonly developed in two or more directions in shale dominant alternating sand-shale layers. In particular, sandstone layers were focused in this research as they can be main hydrocarbon-bearing zones in low-resistivity low-contrast pay zones.

In chapter 4, based on field observations, relative-age relationship between extension fractures and veins are revealed: boudinage structures of sandstones and fractures filled with shale in the sandstones are oldest; fractures filled with minerals are second oldest; open fractures (fractures not filled with other materials) are the youngest. Results of numerical calculations indicates at least mineral veins must have been formed before the regional folding caused by the Variscan Orogeny, suggesting the extension fractures filled with shale and mineral veins formed during not crustal uplift/exhumation but basin burial. This suggests there would be certain mechanism to form extension fracture systems in association with basin subsidence and show the possibility of existence of extension fracture system in deep, subsurface hydrocarbon reservoir.

In chapter 5, fluid overpressure of the mineral veins were estimated based on analytical calculation, indicating the overpressure during the vein formation was about 35 MPa as maximum value. Because of the difficulty of estimating mechanical

properties at the time of the vein formation, the absolute value must have significant uncertainty. However, relative values calculated by this approach (equation (1) of chapter 5) are not affected by the mechanical property estimation. The relative values implies that overpressure associated with veins striking NNE-SSW was 70 percent larger than that of veins striking WNW-ESE. By considering the timing of vein formation provided from results of chapter 4 (during basin burial), the difference of overpressure probably reflected difference of lateral compressive stress field in which NNE-SSW direction was strongly compressed by the Variscan Orogeny which formed the foreland basin of the South Wales coalfield. Another important result is that difference of mineral composition within veins between sandstone layers and limestone layer, suggesting fluid within the stiff layers were not interconnected through the surrounding shale. This implies the contribution of geothermal fluid which is generally supplied from deeper fluid source was minimal for the vein formation. If the geothermal fluid is the main mechanism for extension fracture formation in deep, subsurface reservoirs, the extension fractures can develop only around the major fault continuing to deeper depth.

By reflecting the results of chapter 4 and 5, mechanism for extension fracture formation in mechanical layers, which is not related with high pressured fluid but related with basin burial were examined in chapter 6. Bourne model is the base of this approach. The analytical solutions indicates extension fractures can develop throughout the stiff layers even in the case that regional horizontal stresses are compressive. It depends on volume ratio of stiff (e.g. sandstone) and soft (e.g. shale) material, relative Young's modulus between the stiff and soft material, ratio of vertical and horizontal stresses and fluid pressure. Increase of vertical stress makes extension fractures in stiff layer easier, implying the proposed mechanism is suitable to form extension fractures during basin burial.

It would be one of the most important results of this thesis that the results show the possibility that layer-controlled extension fractures can develop within thin stiff sandstones of mechanical layers during basin burial. This suggest fluid transportation within the low-resistivity low-contrast pay zones which are recent-day important targets in the oil and gas industry will be controlled by invisible layer-scale fractures in several geological conditions. An erroneous estimation of existence of extension fracture

system may cause erroneous project operation. For instance, if the water flooding and/or gas injection are applied on fractured sandstone layers, the timing of water and/or gas production will be accelerated, resulting shrinkage of oil production. This is critical for economic potential of the project. Thus, the results of this projects can provide new insights and contribute on considering extension fracture formation in the low-resistivity low contrast pay zones.

One of the problems of current approaches is that all analytical and numerical calculations applied in the thesis assume linear-elastic behaviour of the rocks. Rocks are not be pure elastic material in subsurface conditions with a depth of a few thousand metres. In addition, deformation style and the associated mechanical properties of sedimentary rocks are variable depending on diagenesis/consolidation of the sediments, temperature-pressure conditions, fluid pressure and strain-rate of the deformation. Different numerical approaches, such as distinct element method, finite element method with consideration of visco-elastic theory, might be applied for better understanding of real rock behaviours. Relationship between geological history and change of mechanical properties are also essential for this type of numerical/analytical calculations. However, they should be future challenges. In addition, production data associated with low-resistivity low-contrast pay zones should be investigated in future to examine whether the production rate in that zones can be addressed by matrix permeability or fracture permeability, in order to validate the model built in this thesis.

7.2. Conclusions

The field studies and numerical modelling reveal relative-age relationships between layer-scale extension fractures, layer-scale veins and the Variscan Folding at the western part of South Wales coalfield as follows:

1. Layer-scale fractures and veins in the sandstones and shale which developed in two (orthogonal) or three directions were documented from southern end to northern end at the western parts of the South Wales coalfield. Field observations show relative-age relationship between them: fractures filled with shale in the sandstones are oldest; fractures filled with minerals are second oldest; open fractures (fractures not filled with other materials) are the youngest.

2. Effects of stress rotation were examined by numerical modelling. The results suggest that extension fractures perpendicular to the bedding cannot form when the beds dip 45 degrees or more in most geological conditions, and that at least the layer-scale vein systems formed before the Variscan Folding in the study area.
3. Based on the above two results, layer-scale fractures filled with shale or minerals which could work as barrier of fluid transportation developed during basin burial in the current study area. Development phase of open fractures which could enhance fluid transportation is not well-constrained in this study. However, the open fractures developed after the quartz precipitations whose physical conditions were close to maximum burial of the basin, implying the possibility that the open fractures mostly formed during crustal uplift/exhumation.

Fluid overpressure of the mineral veins which formed during basin burial were analytically estimated from the measured aspect (length/thickness). The results indicate followings:

4. Average fluid overpressure (driving pressure) for the vein formation was about 35 MPa as maximum value. Because of the difficulty to estimate mechanical properties at the time of vein formation, the calculated value is not rigid and has some uncertainty.
5. The relative difference of overpressure between veins striking NNE-SSW and veins striking WNW-ESE show considerable variation of fluid overpressure at the time of vein formations associated with vein orientation. Larger fluid overpressure associated with veins striking NNE-SSW is probably related with the compressive stress field caused by the Variscan Orogeny which is concordant with the conclusion 3 above.
6. Mineral compositions of veins in the sandstones and limestone suggests the stiff layers were not interconnected during the vein formation, indicating buoyancy effect by geothermal fluid was minimal in the current study case.

Analytical solutions from simplified version of Bourne model provide the following insights for extension fracture formation in mechanical layers:

7. Effective tensile stress can be induced in stiff layer which is surrounded by softer layer, depending on ratio among external vertical stress, external horizontal stress, and pore-fluid pressure, relative Young's modulus and relative total thickness (or relative volume) between stiff and soft layers.
8. Relationship between external vertical stress, external horizontal stress and pore-fluid pressure primarily controls development of the extension fractures in mechanical layers.
9. Relative Young's modulus and relative total thickness between stiff and soft layers secondarily control the possibility of extension fracture formation. Extension fractures develop more easily in stiff layers with soft layer dominant system and larger gap of Young's moduli between the layers.

The current thesis proposes that extension fracture system can develop even in compressive stress field. It is primarily controlled by ratio among horizontal stress, vertical stress and pore-fluid pressure for extension fracture formation. This implies that extension fractures can form in mechanical layers during basin-burial and can affect permeability and fluid transportation in deep, subsurface reservoirs.

Appendix

Raw data of fractures and veins in individual layers

2,641 layer-scale fractures and 1,608 veins were measured in the field at 13 sites and 36 layers (Figure A.1). Those data are summarized and plotted together in individual sites in the body text. However, raw data for individual layers are not shown. Data from 2 or more layers are combined and plotted together in the body text. Therefore, data measured in each layer are summarized here in detail to provide background information with the body text of the thesis.

Site information, lithology, layer thickness, geometry of bedding are described first. The site name is linked to the body text. Below those descriptions, scan-line information is summarized in a table. Measurement method along scan-line is same as that shown in chapter 3. The measured fractures and veins are grouped into 1 to 4 sets based on their concentration of orientations in stereonet and rose diagram which are illustrated below the table. Range of strike variation for each fracture/vein set is indicated to estimate the associated fracture type (extension, hybrid, and shear). The layer-scale fractures/veins commonly have some amount of apertures/thicknesses, indicating they are extension or hybrid fractures. However, based on Griffith criterion, if range of strike distribution of a fracture set is larger than 45 degrees, some shear fractures must exist in the set unless we assume the fracture/vein set was developed under same orientations of principal stress axes. Therefore, in the case that the range of strike variation in a fracture/vein set is less than 30 degrees, it is assumed that pure extension fractures are relatively common in the set. If the range is 0-45 degrees, it is assumed that both pure extension fractures and hybrid fractures are more common. In the case that a range is larger than 45 degrees, the fracture/vein set includes some amount of shear fractures. If the range is larger than 60 degrees, shear fractures are assumed to be more dominant in the set. Corrected fracture density and mean value of fracture apertures and vein thicknesses are also shown for each set on the rose diagrams.

Fracture and vein densities are calculated following the methodology in chapter 3. Raw fracture/vein densities are simple division of the number of fractures/veins over length of the associated scan-line. Corrected density is the value in which the number of fractures and veins are corrected in the case the associated scan-line traverses purely perpendicular to each fracture/vein plane. If the number of fractures or veins is less than 5 in a scan-line, the density is not calculated since the result probably becomes less-accurate. In the case fracture/vein density can be calculated in two or more scan-lines, scan-line with the largest number of data was used.

Histograms of fracture aperture size and vein thickness for each set are also shown. Since their distributions commonly indicate log-normal or power law, the mean value generally becomes larger than median by reflecting the effect of relatively rare but thicker fracture aperture/vein thickness. In this thesis, mean value is mainly used because simple multiplication of the mean value and correlated fracture density in a same set provides apparent strain caused by the fracture/vein opening associated with the set formation. In the case vein aspect ratio could be measured in the layer, cross-plot of vein length and thickness and histogram for vein aspect ratio are also shown for each vein set.

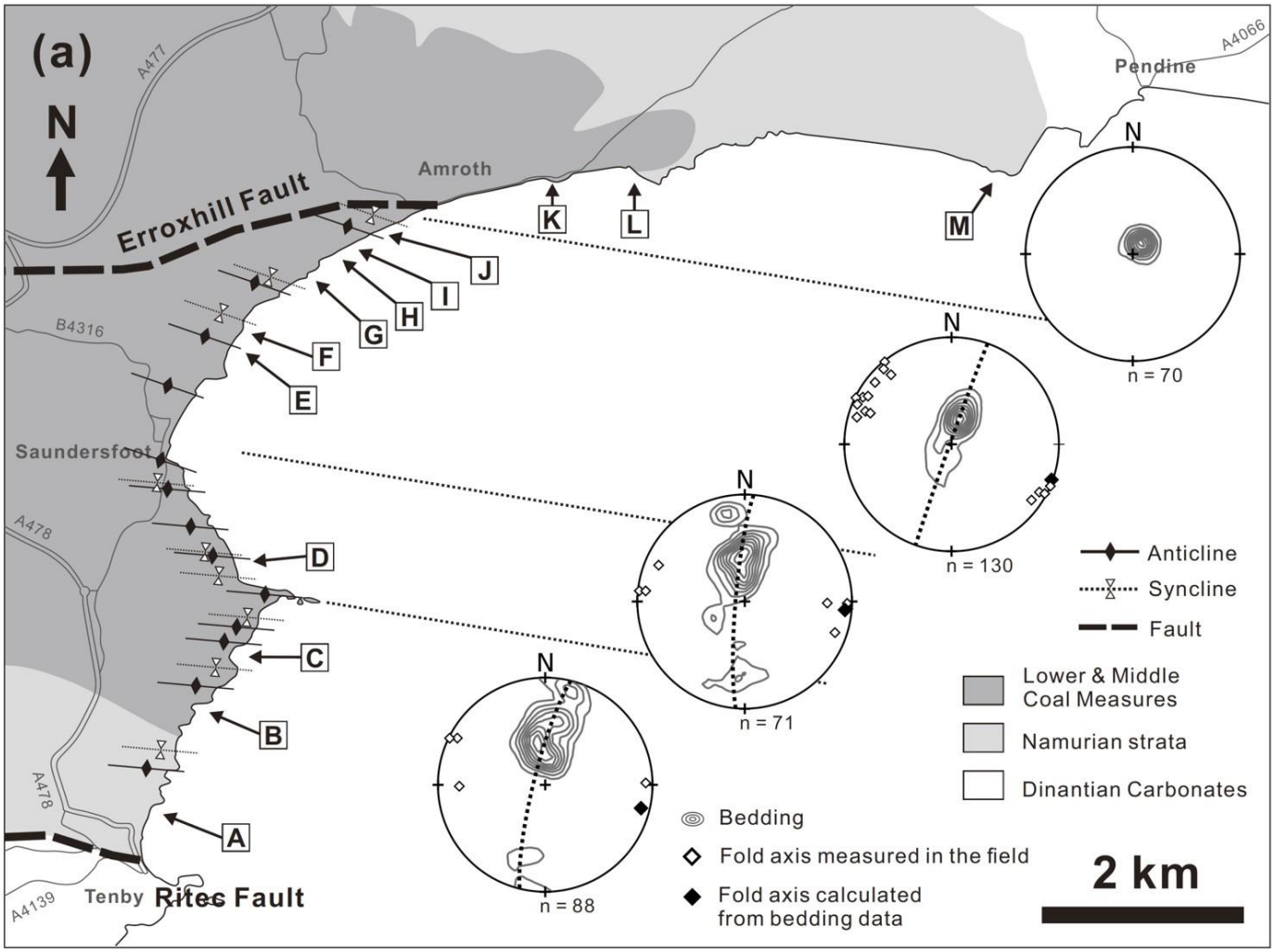

Site	Layer	Lithology	Thickness	Bedding
M	36	sandstone	37cm	199, 11
L	35	sandstone	190cm	226, 15
	34	shale	520cm	240, 20
K	33	sandstone	137cm	219,07
	32	shale	145cm	233,10
J	31	limestone	72cm	295,06
	30	shale	119cm	359,15
I	29	sandstone	13cm	202,25
	28	sandstone	23cm	200,25
	27	sandstone	na	188,13
	26	shale	91cm	195,23
H	25	sandstone	23cm	209,17
	24	sandstone	61cm	196,10
	23	sandstone	18cm	220,37
	22	shale	295cm	186,20
G	21	sandstone	26cm	210,21
	20	sandstone	12cm	202,23
	19	sandstone	4cm	204,23
	18	sandstone	6cm	204,26
	17	shale	11cm	196,29
	16	shale	52cm	204,10
F	15	sandstone	63cm	048,26
E	14	sandstone	19cm	141,13
	13	sandstone	17cm	174,16
	12	sandstone	14cm	084,14
	11	sandstone	11cm	114,14
	10	sandstone	11cm	159,15
	9	sandstone	38cm	133,12
	8	shale	65cm	175,11
D	7	sandstone	36cm	060,13
	6	shale	>1000m	174,23
C	5	sandstone	27cm	150,21
	4	sandstone	47cm	171,27
	3	shale	880m	163,45
B	2	sandstone	27cm	225,11
A	1	sandstone	11cm	182,06

Figure A.1 Geological map of the study area. Table on the right shows relationship between sites and layers. Bedding are shown by dip direction and dip.

Layer #1

Site A (southern limb of close fold)
Lithology Sandstone
Layer thickness 11cm
Bedding 182, 06 (DD: Dip Direction, D: Dip)

scan line	dip direc -tion, dip	length	number of measured data			
			fracture		vein	
			set 1	set 2	set 1	set 2
1	099,06	6.20m	40	0	3	0
2	201,52	3.60m	0	8	0	28
others	-	-	0	0	0	5

Fracture (n=48)

Set 1: NNE-SSW
Range of strikes: 0-30°
Set 2: ESE-WNW
Range of strikes: > 0-60°

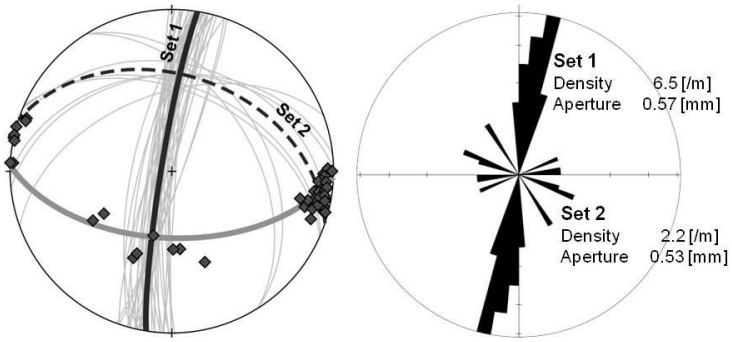

Vein (n=36)

Set 1: NNE-SSW
Range of strikes: 0-30°
Set 2: ESE-WNW
Range of strikes: > 0-60°

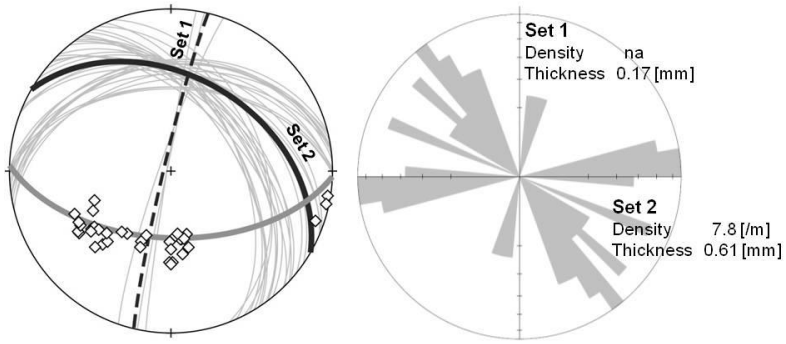

Fracture/vein densities shown on the rose diagrams are corrected fracture/vein density. Aperture/thicknesses are mean value of fracture apertures or vein thicknesses in the set. Those data are also summarized in below.

Note

Fractures mainly strike NNE-SSW (set 1) and ESE-WNW (set 2). Aperture sizes of the two sets are similar but fracture density indicates NNE-SSW is more dominant. Range of the strikes suggests extension fractures are dominant in set 1 and some shear fractures are contained in set 2.

Veins develop with similar geometry as fractures. However, the vein density and thickness suggest ESE-WNW is dominant direction (vein density of set 1 is not calculated but the number of veins are very small along scan-line 1, suggesting their density is much low). Range of the strikes suggests extension fractures are dominant in set 1 and shear fractures are relatively common in set 2.

Although the bedding dips steeply, all fractures and veins are sub-perpendicular to the bed.

Fracture and vein density

Fracture set 1	Raw 6.5 [/m], Corrected 6.5 [/m]	(from 40 data along scan-line 1)
Fracture set 2	Raw 2.2 [/m], Corrected 2.4 [/m]	(from 8 data along scan-line 2)
Vein set 2	Raw 7.8 [/m], Corrected 8.4 [/m]	(from 28 data along scan-line 2)

Fracture aperture size and vein thickness

Fracture set 1	mean = 0.57 [mm], 1σ = 0.71 [mm]
Fracture set 2	mean = 0.53 [mm], 1σ = 0.69 [mm]
Vein set 1	mean = 0.17 [mm], 1σ = 0.06 [mm]
Vein set 2	mean = 0.61 [mm], 1σ = 0.57 [mm]

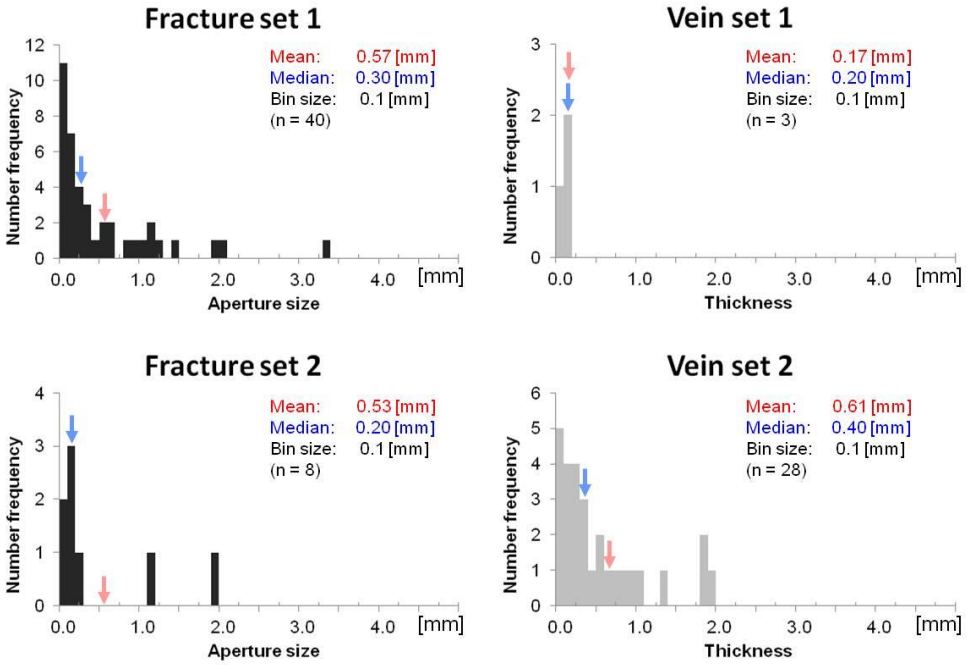

Layer #2

Site	B (southern limb of open fold)
Lithology	Sandstone
Layer thickness	27cm
Bedding	225, 11

scan line	dip direc -tion, dip	length	number of measured data				
			fracture		vein		
			set 1	others	set 1	set 2	set 3
1	305,02	9.38m	27	2	35	1	0
2	215,11	11.89m	1	3	2	6	41

Fracture (n=33)

Set 1: N-S

Range of strikes: 0-45°

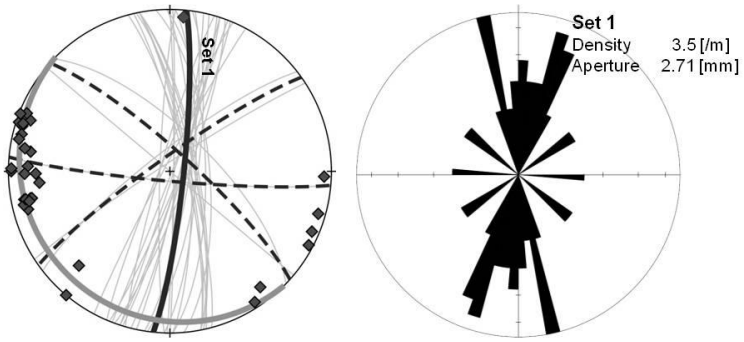

Vein (n=85)

Set 1: NNE-SSW

Range of strikes: > 0-60°

Set 2: E-W

Range of strikes: 0-30°

Set 3: ESE-WNW

Range of strikes: 0-30°

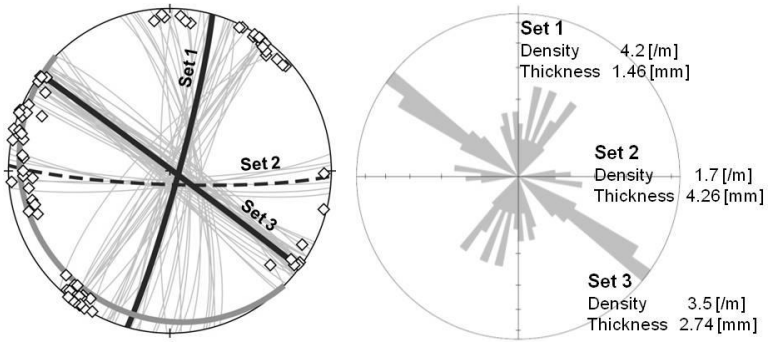

Note

Fractures mainly strike N-S (set 1). 1 or 2 fractures striking NE-SW, E-W and SE-NW are assumed as minor. Range of the strikes suggests both extension fractures and hybrid fractures are contained in the set.

Veins are more common in this layer. The veins strike in similar orientation as fractures but both NNE-SSW (set 1) and ESE-WNW (set 2) are common. Wide distribution of strikes of the NNE-SSW veins may suggest there are some shear fractures in set 1. Small difference of strike orientation of set 2 and set 3, and similar strains caused by vein opening of the sets suggest the possibility that set 2 and 3 are conjugate hybrid fractures.

Most fractures and veins are perpendicular to the bedding.

Fracture and vein density

Fracture set 1	Raw 2.9 [/m], Corrected 3.5 [/m]	(from 27 data of scan-line 1)
Vein set 1	Raw 3.7 [/m], Corrected 4.2 [/m]	(from 35 data of scan-line 1)
Vein set 2	Raw 1.3 [/m], Corrected 1.7 [/m]	(from 6 data of scan-line 2)
Vein set 3	Raw 3.4 [/m], Corrected 3.5 [/m]	(from 41 data of scan-line 2)

Fracture aperture size and vein thickness

Fracture set 1	mean = 2.71 [mm], 1σ = 4.03 [mm]
Vein set 1	mean = 1.46 [mm], 1σ = 1.05 [mm]
Vein set 2	mean = 4.26 [mm], 1σ = 5.53 [mm]
Vein set 3	mean = 2.74 [mm], 1σ = 3.51 [mm]

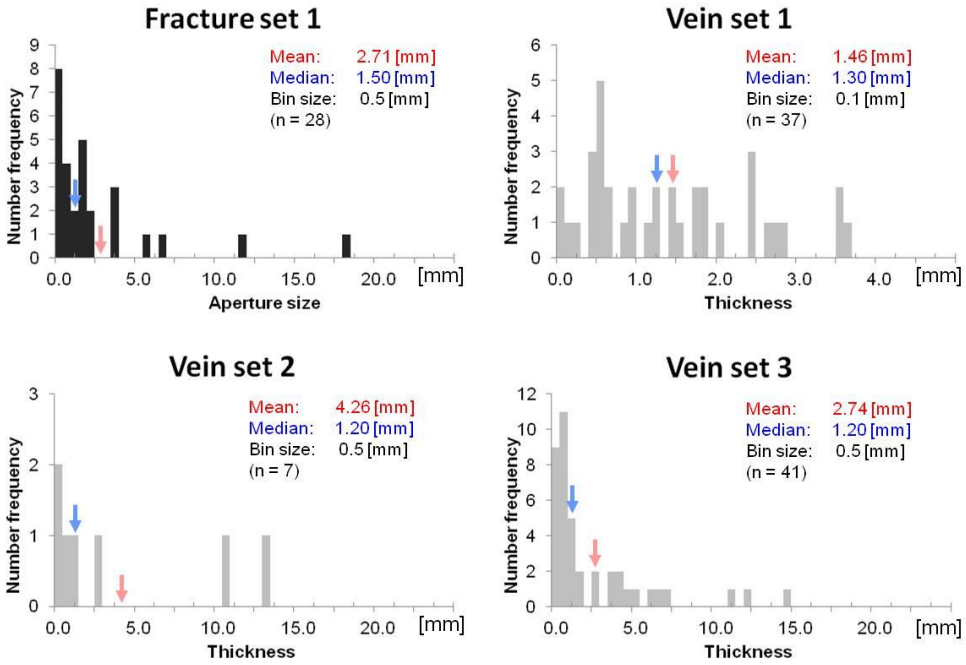

Layer #3

Site	C (southern limb of open fold)
Lithology	Shale
Layer thickness	880cm
Bedding	163, 45

scan line	dip direc -tion, dip	length	number of measured data	
			fracture	
			set 1	set 2
1	305,02	9.38m	24	5
others	-	-	34	5

Fracture (n=68)

Set 1: N-S

Range of strikes: > 0-60°

Set 2: ESE-WNW

Range of strikes: 0-45°

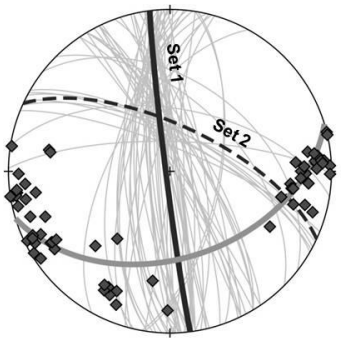

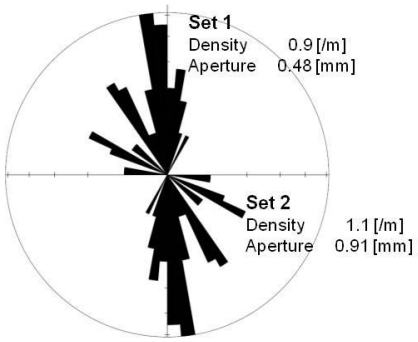

Vein

No vein was found in the layer.

Note

Fractures mainly strike N-S (set 1) and ESE-WNW (set 2) (Because of limited exposure along perpendicular direction to set 2, number of fractures plotted in the stereonet and rose diagram is small. However, fracture density and aperture suggest fractures striking ESE-WNW are also common). Some fractures show wide aperture size in appearance but they are probably not original aperture in the ground because of ductile behaviour of the shale (chapter 3). Range of the strikes suggests fractures striking N-S contain some shear fractures. Non-perpendicular geometry of the fractures to bedding also suggests they are not extension fractures.

Some fractures are not perpendicular to the bedding.

Fracture and vein density

Fracture set 1	Raw 0.8 [/m], Corrected 0.9 [/m]	(from 24 data along scan-line 1)
Fracture set 2*	Raw 0.4 [/m], Corrected 1.1 [/m]	(from 5 data along scan-line 1)

*Fracture set 2 is nearly parallel to scan-line 1 and the correction effect may be too large. In addition, number of measured data is insufficient. Because of these, the corrected fracture density is relatively inaccurate.

Fracture aperture size and vein thickness

Fracture set 1 mean = 0.48 [mm], 1σ = 0.96 [mm]

Fracture set 2 mean = 0.91 [mm], 1σ = 2.05 [mm]

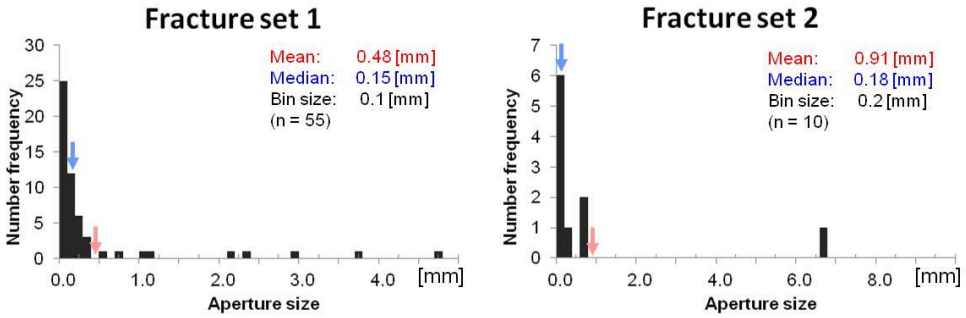

Layer #4

Site	C (southern limb of open fold)
Lithology	Sandstone
Layer thickness	47cm
Bedding	171, 27

scan line	dip direc -tion, dip	length	number of measured data		
			fracture		vein
			set 1	set 2	set 1
1	094,06	10.28m	22	0	32
2	226,15	2.99m	0	5	0
others	-	-	0	5	0

Fracture (n=32)

Set 1: N-S

Range of strikes: 0-60°

Set 2: SE-NW

Range of strikes: 0-30°

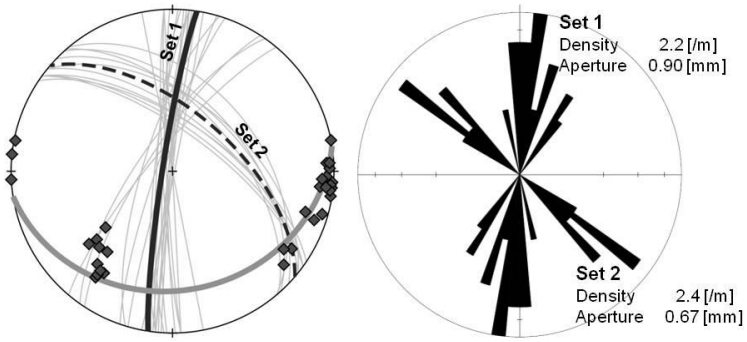

Vein (n=32)

Set 1: N-S

Range of strikes: 0-30°

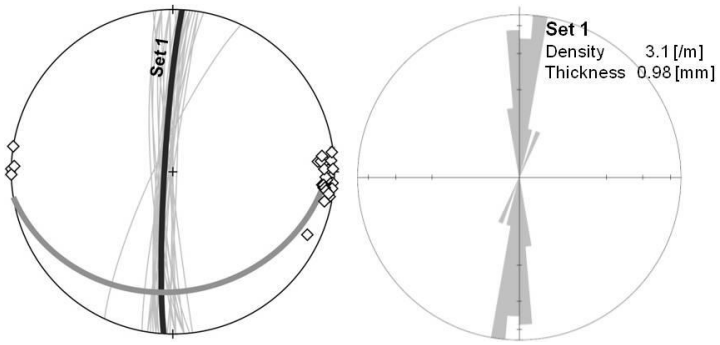

Note

Fractures have similar geometry and concentration as fractures in layer 3 (shale). Range of the strikes suggests set 1 contains some shear fractures. The fractures with similar geometry as those in layer 3 were possibly formed in accordance with fracture development in shale which is dominant lithology based on thickness ratio between the shale and the sandstone.

Veins develop only in N-S direction. The range of strikes suggests they can be dominantly extension fractures.

Some fractures are not perpendicular to the bedding.

<u>Fracture and vein density</u>

Fracture set 1	Raw 2.1 [/m], Corrected 2.2 [/m]	(from 22 data along scan-line 1)
Fracture set 2*	Raw 2.2 [/m], Corrected 2.4 [/m]	(from 5 data along scan-line 2)
Vein set 1	Raw 3.1 [/m], Corrected 3.1 [/m]	(from 32 data along scan-line 1)

*Number of measured data may not be sufficient and the fracture density is relatively inaccurate.

Fracture aperture size and vein thickness

Fracture set 1	mean = 0.90 [mm], 1σ = 1.23 [mm]
Fracture set 2	mean = 0.67 [mm], 1σ = 0.38 [mm]
Vein set 1	mean = 0.98 [mm], 1σ = 1.05 [mm]

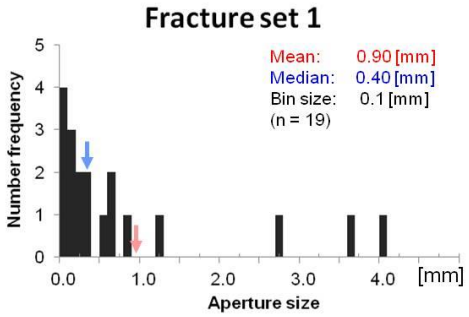

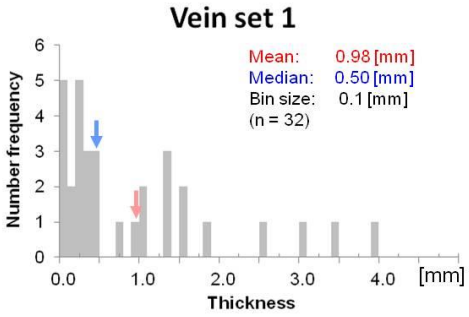

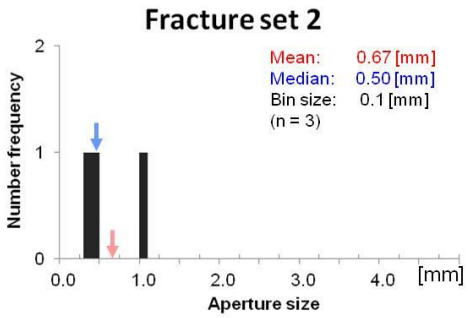

Layer #5

Site	C (southern limb of open fold)
Lithology	Sandstone
Layer thickness	27cm
Bedding	150, 21

scan line	dip direc -tion, dip	length			
			set 1	set 2	set 1
1	079,07	8.59m	28	6	25
others	-	-	0	0	8

Fracture (n=34)

Set 1: N-S

Range of strikes: 0-45°

Set 2: SE-NW

Range of strikes: 0-30°

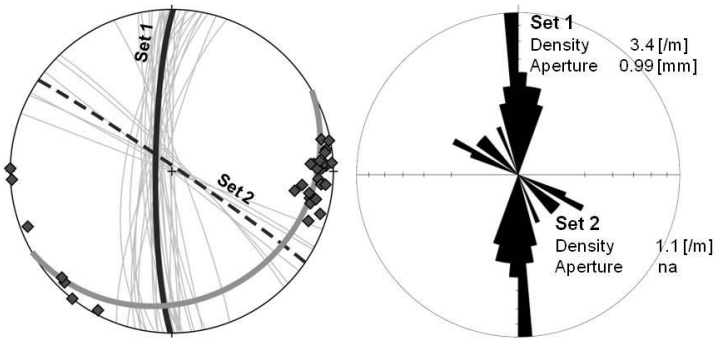

Vein (n=33)

Set 1: N-S

Range of strikes: 0-60°

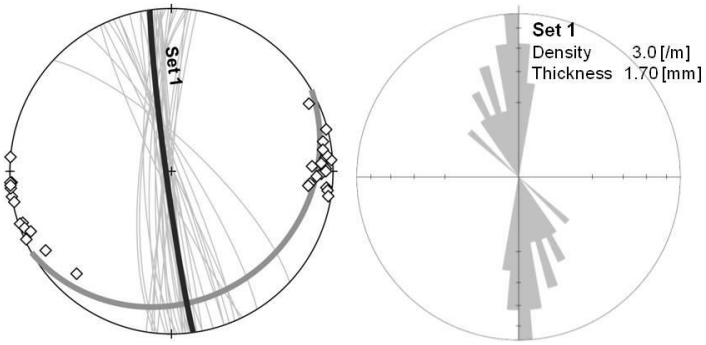

Note

Fractures and veins have similar geometry and concentration as those of layer 4 (sandstone), suggesting the possibility that some fractures were formed together with deformation of much thicker shale. Range of the vein strikes is relatively large in this sandstone.

<u>Fracture and vein density</u>

Fracture set 1	Raw 3.3 [/m], Corrected 3.4 [/m]	(from 28 data along scan-line 1)
Fracture set 2*	Raw 0.8 [/m], Corrected 1.1 [/m]	(from 6 data along scan-line 1)
Vein set 1	Raw 2.9 [/m], Corrected 3.0 [/m]	(from 25 data along scan-line 1)

*Number of measured data may not be sufficient and the fracture density is relatively inaccurate.

Fracture aperture size and vein thickness

Fracture set 1 mean = 0.99 [mm], 1σ = 0.77 [mm]

Vein set 1 mean = 1.70 [mm], 1σ = 1.04 [mm]

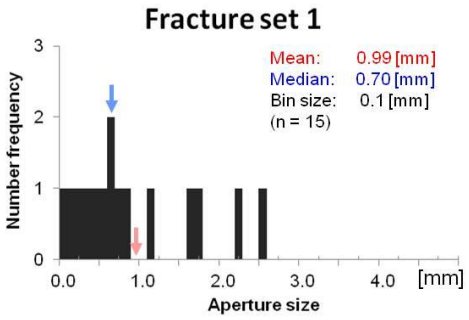

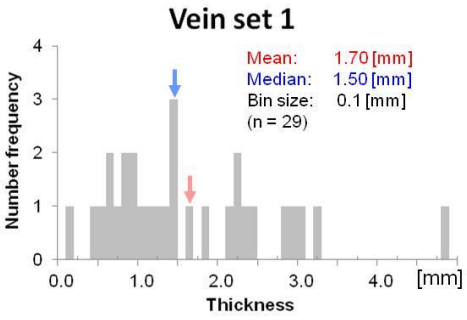

Vein Aspect ratio

Vein set 1 mean = 330, 1σ = 124

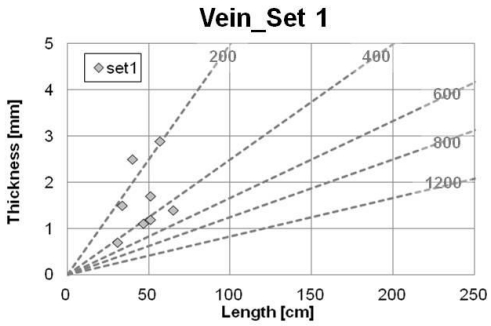

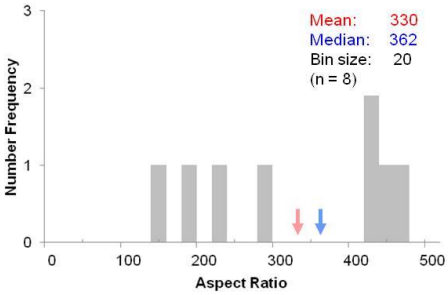

Layer #6

Site	D (southern limb of open fold)
Lithology	Shale
Layer thickness	1,000cm or more
Bedding	174, 23

scan line	dip direc -tion, dip	length	number of measured data	
			fracture	
			set 1	set 2
1	106,08	10.47m	29	2
2	257,03	17.38m	15	22

Fracture (n=68)

Set 1: N-S

Range of strikes: > 0-60°

Set 2: SE-NW

Range of strikes: > 0-60°

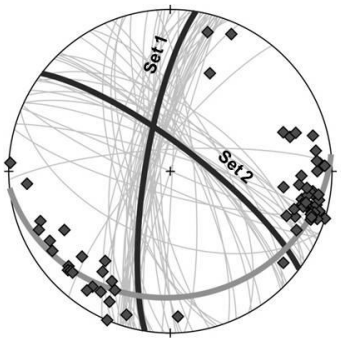

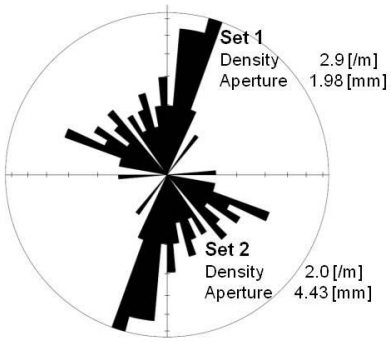

Vein

No vein was found in the layer.

Note

Fracture pattern is more complicated but they mainly strike in the same direction as those in layer 3 (shale at site C). Some fractures show wide aperture size in appearance but they are not original aperture in the ground because of ductile behaviour of the shale (chapter 3). Ranges of strikes of the two sets suggest fractures are more like shear fractures.

Some fractures are not perpendicular to the bedding.

Fracture and vein density

Fracture set 1	Raw 2.8 [/m], Corrected 2.9 [/m]	(from 29 data along scan-line 1)
Fracture set 2	Raw 1.3 [/m], Corrected 2.0 [/m]	(from 22 data along scan-line 2)

Fracture aperture size and vein thickness

Fracture set 1	mean = 1.98 [mm], 1σ = 2.09 [mm]
Fracture set 2	mean = 4.43 [mm], 1σ = 5.24 [mm]

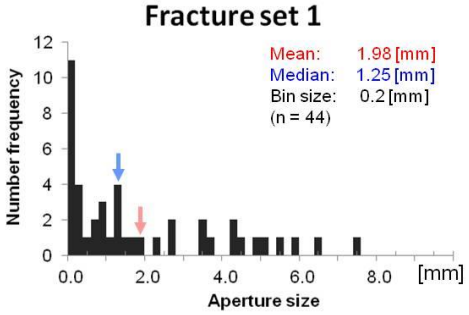

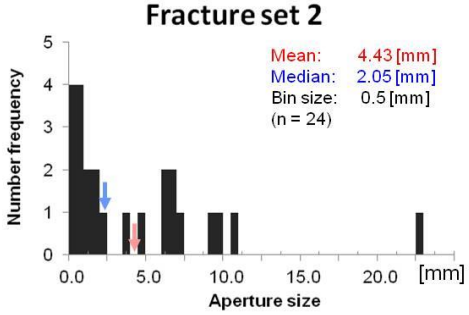

Layer #7

Site	D (close to hinge of open fold)
Lithology	Sandstone
Layer thickness	36cm
Bedding	060, 13

scan line	dip direc -tion, dip	length	number of measured data			
			fracture		vein	
			set 1	set 2	set 1	set 2
1	106,08	10.47m	40	0	11	0
2	257,03	16.35m	0	32	0	3
others	-	-	0	0	3	0

Fracture (n=72)

Set 1: NNE-SSW

Range of strikes: 0-45°

Set 2: E-W

Range of strikes: 0-45°

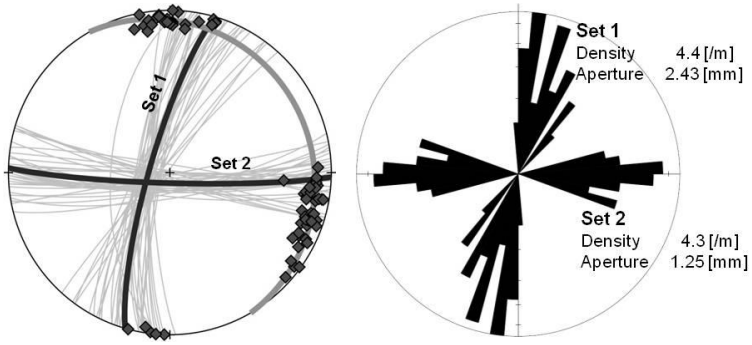

Vein (n=17)

Set 1: NNE-SSW

Range of strikes: 0-45°

Set 2: E-W

Range of strikes: 0-30°

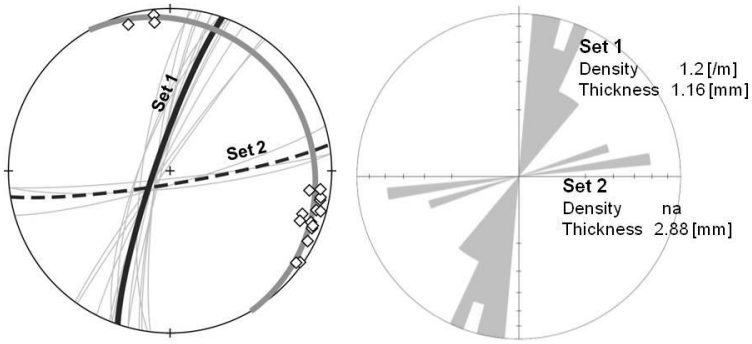

Note

Fractures mainly strike NNE-SSW (set 1) and E-W (set 2). Fracture densities are similar between the two sets but aperture size suggests NNE-SSW fractures were associated with relatively strong deformation. Range of the strikes suggests the possibility that both extension and hybrid fractures are dominant in set 1 and 2.

Veins are relatively rare in this layer. The veins mainly strike NNE-SSW (set 1) and E-W (set 2). Set 1 veins developed in same direction as set 1 of fractures but set 2 has slightly different direction from set 2 fractures. Set 2 veins are thicker than set 1 but the density is very small based on scan-line 2. Range of the strikes suggests they would be extension or hybrid fractures.

Most fractures and veins are perpendicular to the bedding.

Fracture and vein density

Fracture set 1	Raw 4.2 [/m], Corrected 4.4 [/m]	(from 40 data along scan-line 1)
Fracture set 2	Raw 4.2 [/m], Corrected 4.3 [/m]	(from 32 data along scan-line 2)
Vein set 1	Raw 1.2 [/m], Corrected 1.2 [/m]	(from 11 data along scan-line 1)

Fracture aperture size and vein thickness

Fracture set 1	mean = 2.43 [mm], 1σ = 2.40 [mm]
Fracture set 2	mean = 1.25 [mm], 1σ = 1.44 [mm]
Vein set 1	mean = 1.16 [mm], 1σ = 0.88 [mm]
Vein set 2	mean = 2.88 [mm], 1σ = 2.21 [mm]

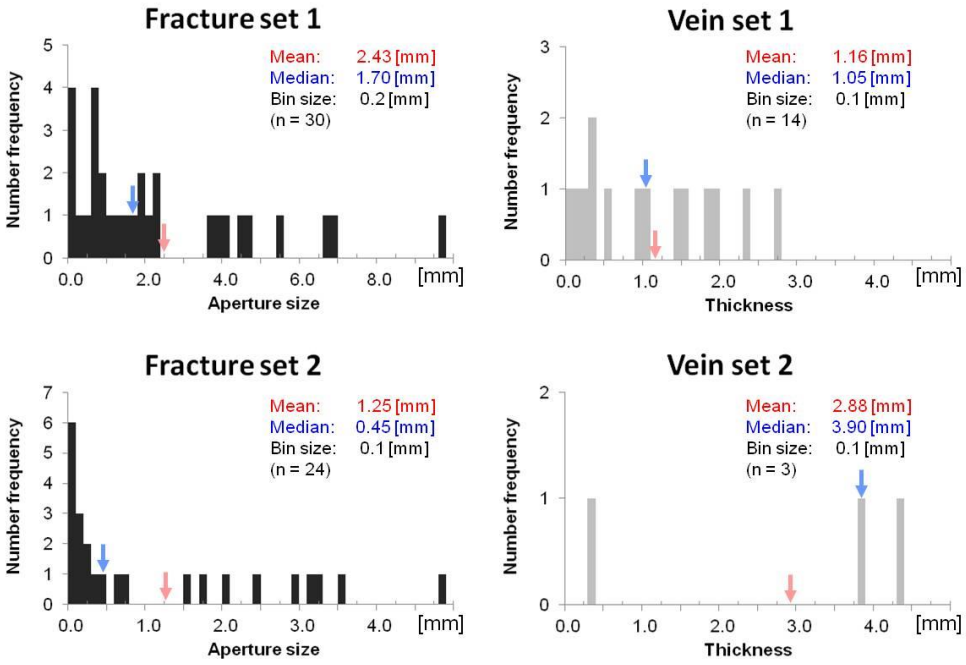

Vein Aspect ratio

Only three vein aspect ratios were measured. Since the three do not show consistent aspect ratio, they were not plotted in graphs. The measured data are as follow.

Vein 1	DD,D = 290,82	length = 55.0 [cm], thickness = 1.90 [mm]	aspect ratio = 289
Vein 2	DD,D = 291,84	length = 39.0 [cm], thickness = 2.80 [mm]	aspect ratio = 139
Vein 3	DD,D = 306,86	length = 94.0 [cm], thickness = 1.60 [mm]	aspect ratio = 588

Layer #8

Site	E (southern limb of gentle fold)
Lithology	Shale
Layer thickness	65cm
Bedding	175, 11

scan line	dip direc -tion, dip	length	number of measured data	
			fracture	
			set 1	set 2
1	084,00	25.05m	52	11

Fracture (n=63)

Set 1: NE-SW

Range of strikes: 0-30°

Set 2: SE-NW

Range of strikes: 0-45°

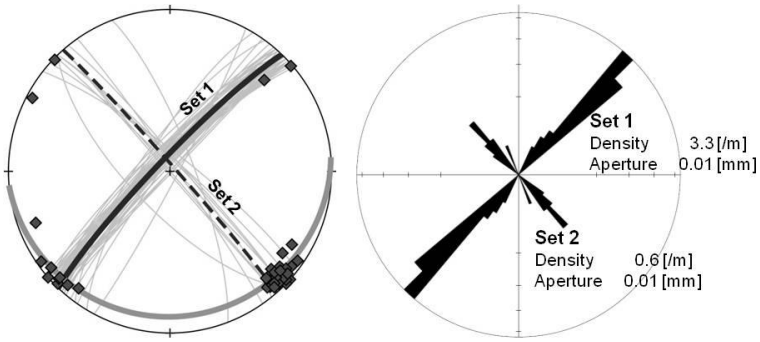

Vein

No vein was found in the layer.

Note

Fractures mainly strike NE-SW (set 1) and SE-NW (set 2). Based on the fracture density, set 1 is much dominant direction. Aperture size of most fractures in this layer is too narrow to measure with feeler gauge and just 0.01 [mm] is assigned as aperture size for most fractures. Fractures in this shale seem to be less ductile with relatively strong geometrical concentration of the fractures.

Some fractures are not perpendicular to bedding but majority are perpendicular.

<u>Fracture and vein density</u>

Fracture set 1	Raw 2.1 [/m], Corrected 3.3 [/m]	(from 52 data along scan-line 1)
Fracture set 2	Raw 0.5 [/m], Corrected 0.6 [/m]	(from 11 data along scan-line 1)

<u>Fracture aperture size and vein thickness</u>

Fracture set 1	mean = 0.01 [mm], 1σ = 0.03 [mm]
Fracture set 2	mean = 0.01 [mm], 1σ = 0.00 [mm]

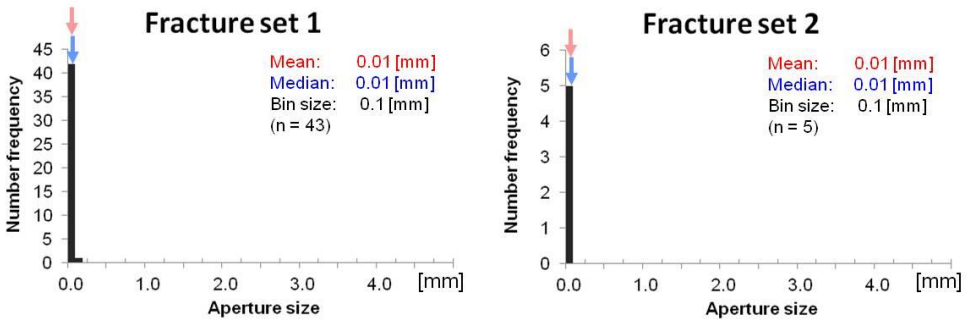

Layer #9

Site	E (close to hinge of gentle fold)
Lithology	Sandstone
Layer thickness	38cm
Bedding	133, 12

scan line	dip direc -tion, dip	length	number of measured data						
			fracture			vein			
			set 1	set 2	others	set 1	set 2	set 3	others
1	123,12	6.56m	5	0	0	19	0	7	0
2	046,01	5.89m	0	7	2	0	17	8	1
3	184,08	4.47m	0	9	6	0	2	6	0
others	-	-	10	0	0	19	5	3	1

Fracture (n=39)

Set 1: NNE-SSW
Range of strikes: 0-30°
Set 2: ESE-WNW
Range of strikes: 0-30°

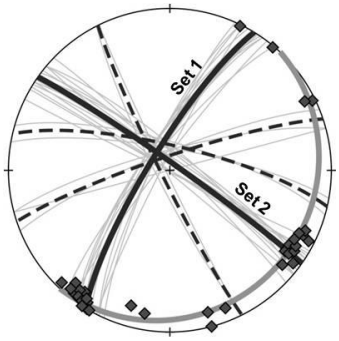

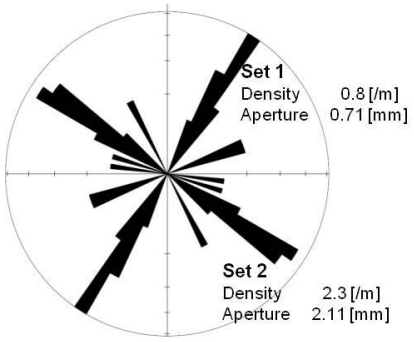

Vein (n=88)

Set 1: NNE-SSW
Range of strikes: 0-30°
Set 2: ESE-WNW
Range of strikes: 0-30°
Set 3: SSE-NNW
Range of strikes: 0-30°

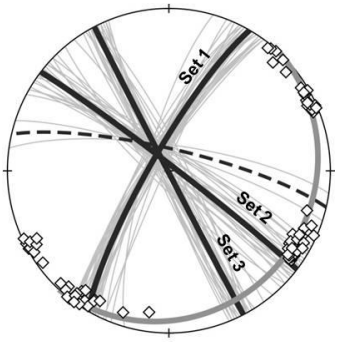

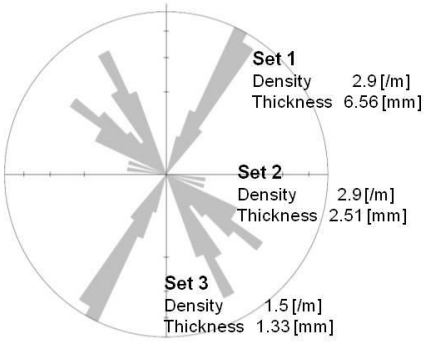

Note

Fractures developed in 4 or 5 directions but three of them are assumed as minor directions. The fractures dominantly strike NNE-SSW (set 1) and ESE-WNW (set 2). Fracture densities and aperture size suggest set 2 fractures were formed associated with relatively strong deformation in this layer. Range of the strikes suggests extension fractures would be common in set 1 and 2.

Veins are more common than fractures in this layer. The veins strikes similar orientation as those of fractures but veins striking SSE-NNE (set 3) were also often observed. Vein density and thickness indicate set 1 caused the largest strain and set 2 caused second associated with the vein opening. Range of the strikes suggests they would be mostly extension fractures.

Most fractures and veins are perpendicular to the bedding.

Fracture and vein density

Fracture set 1	Raw 0.8 [/m], Corrected 0.8 [/m]	(from 5 data along scan-line 1)
Fracture set 2	Raw 2.0 [/m], Corrected 2.3 [/m]	(from 9 data along scan-line 3)
Vein set 1	Raw 2.9 [/m], Corrected 2.9 [/m]	(from 19 data along scan-line 1)
Vein set 2*	Raw 2.9 [/m], Corrected 2.9 [/m]	(from 17 data along scan-line 2)
Vein set 3*	Raw 1.5 [/m], Corrected 1.5 [/m]	(from 8 data along scan-line 2)

*Density of the two sets may be treated as one set of conjugate hybrid or shear fractures.

Fracture aperture size and vein thickness

Fracture set 1	mean = 0.71 [mm], 1σ = 0.89 [mm]
Fracture set 2	mean = 2.11 [mm], 1σ = 1.50 [mm]
Vein set 1	mean = 6.56 [mm], 1σ = 4.28 [mm]
Vein set 2	mean = 2.51 [mm], 1σ = 2.93 [mm]
Vein set 3	mean = 1.33 [mm], 1σ = 1.37 [mm]

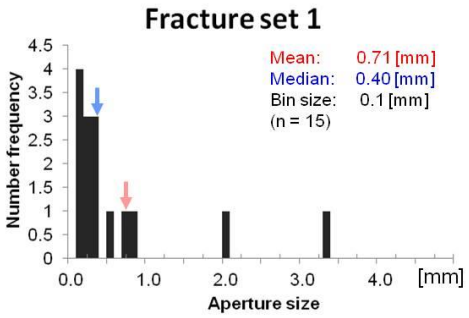

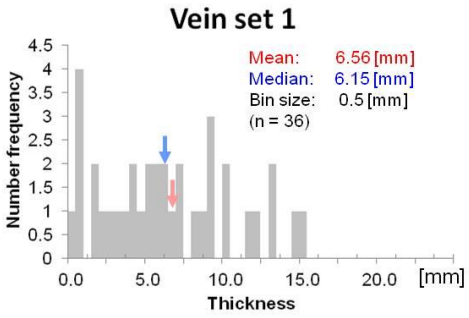

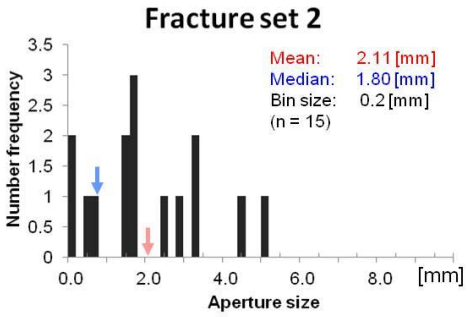

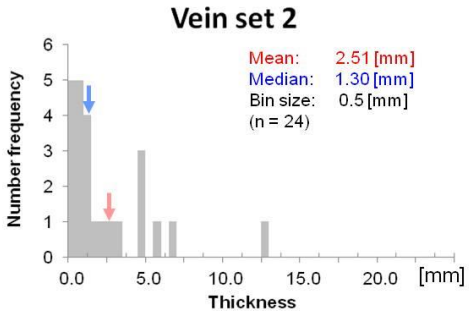

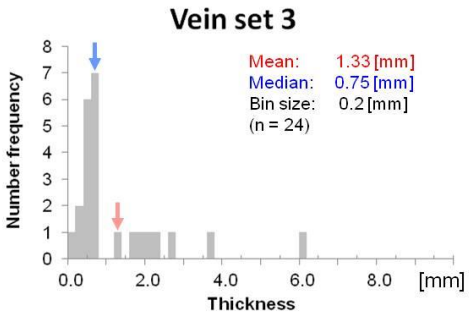

Vein Aspect ratio

Vein set 1	mean = 376, 1σ = 153
Vein set 2	mean = 561, 1σ = 340
Vein set 3	mean = 1142, 1σ = 612

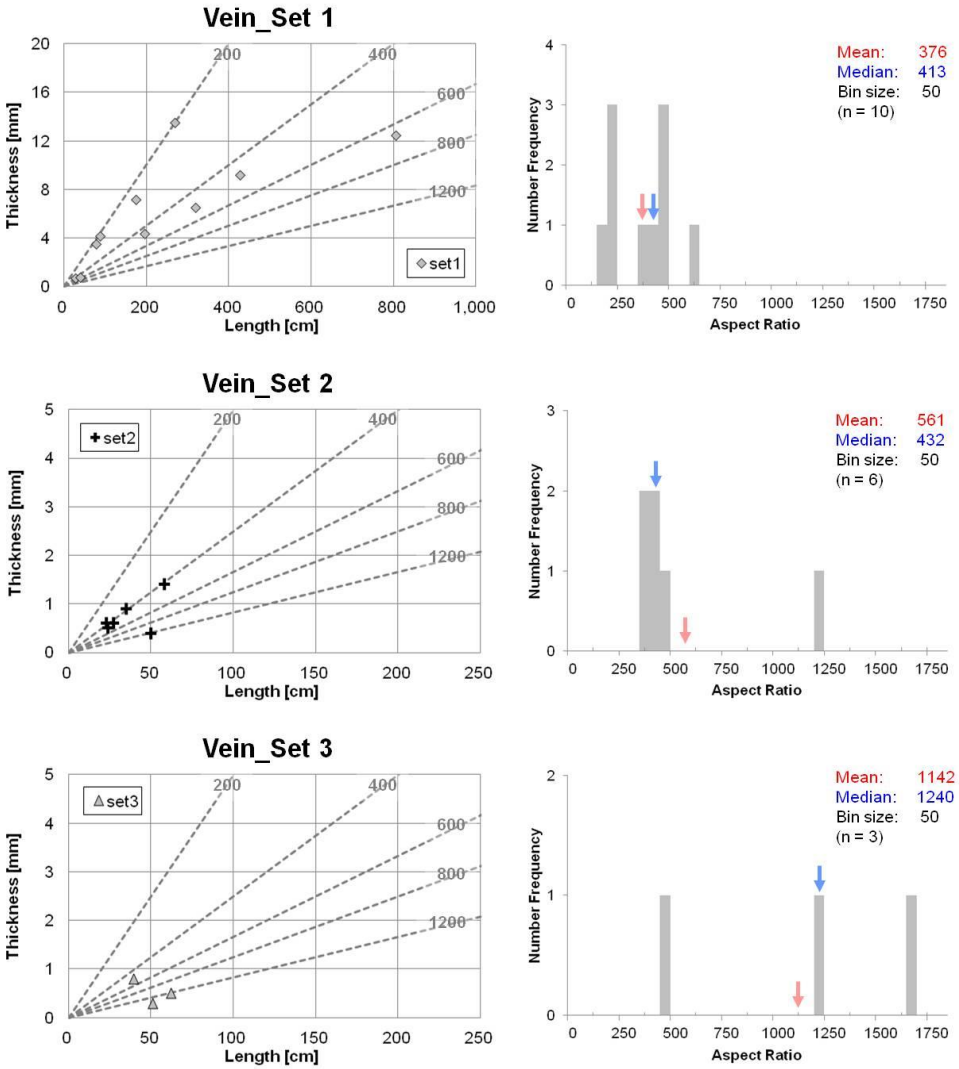

Layer #10

Site	E (close to hinge of gentle fold)
Lithology	Sandstone
Layer thickness	11cm
Bedding	159, 15

scan line	dip direc -tion, dip	length	number of measured data							
			fractures					vein		
			set 1	set 2	set 3	set 4	others	set 1	set 2	others
1	071,01	3.00m	16	5	0	19	0	5	18	1
2	089,05	1.52m	9	5	2	8	1	2	6	0
3	210,09	2.46m	6	0	4	15	0	0	10	0
others	-	-	0	0	0	0	0	0	1	0

Fracture (n=90)

Set 1: N-S
Range of strikes: 0-30°
Set 2: NNE-SSW
Range of strikes: 0-30°
Set 3: E-W
Range of strikes: 0-30°
Set 4: SE-NW
Range of strikes: 0-60°

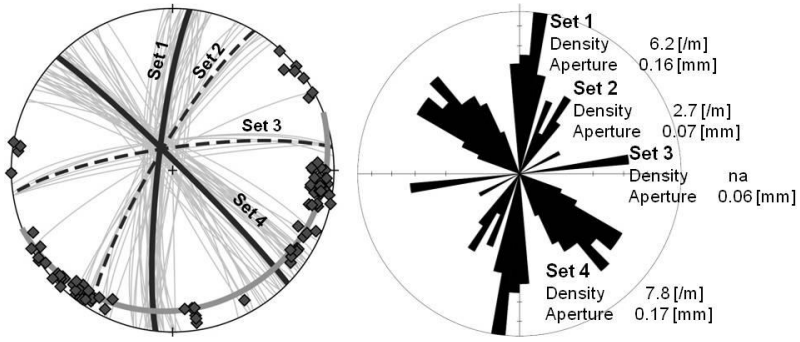

Vein (n=43)

Set 1: NNE-SSW
Range of strikes: 0-30°
Set 2: SE-NW
Range of strikes: 0-60°

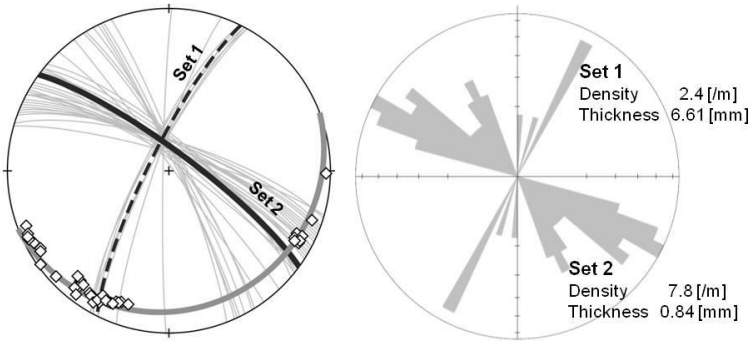

Note

Fractures developed in 4 directions. Fractures striking N-S (set 1) and SE-NW (set 4) are dominant based on fracture density and aperture. The others are relatively minor. Range of strikes of set 4 suggests there are some shear fractures in set 4.

Veins are less common in this layer. The veins strike NNE-SSW (set 1) and SE-NW (set 2). Vein density is high in set 2 but veins are much thicker in set 1. As a result, strain caused by the vein opening of set 1 is larger than that of set 2. Range of strikes of set 2 suggests they contain some shear fractures.

All fractures and veins are sub-perpendicular to the bedding.

Fracture and vein density

Fracture set 1	Raw 5.4 [/m], Corrected 6.2 [/m]	(from 16 data along scan-line 1)
Fracture set 2*	Raw 1.8 [/m], Corrected 2.7 [/m]	(from 5 data along scan-line 1)
Fracture set 4	Raw 6.8 [/m], Corrected 7.8 [/m]	(from 19 data along scan-line 1)
Vein set 1*	Raw 1.7 [/m], Corrected 2.4 [/m]	(from 5 data along scan-line 1)
Vein set 2	Raw 6.3 [/m], Corrected 7.8 [/m]	(from 18 data along scan-line 1)

*Number of measured data may not be sufficient and the fracture density is relatively inaccurate.

Fracture aperture size and vein thickness

Fracture set 1	mean = 0.16 [mm], 1σ = 0.20 [mm]
Fracture set 2	mean = 0.07 [mm], 1σ = 0.08 [mm]
Fracture set 3	mean = 0.06 [mm], 1σ = 0.05 [mm]
Fracture set 4	mean = 0.17 [mm], 1σ = 0.23 [mm]
Vein set 1	mean = 6.61 [mm], 1σ = 3.75 [mm]
Vein set 2	mean = 0.84 [mm], 1σ = 0.83 [mm]

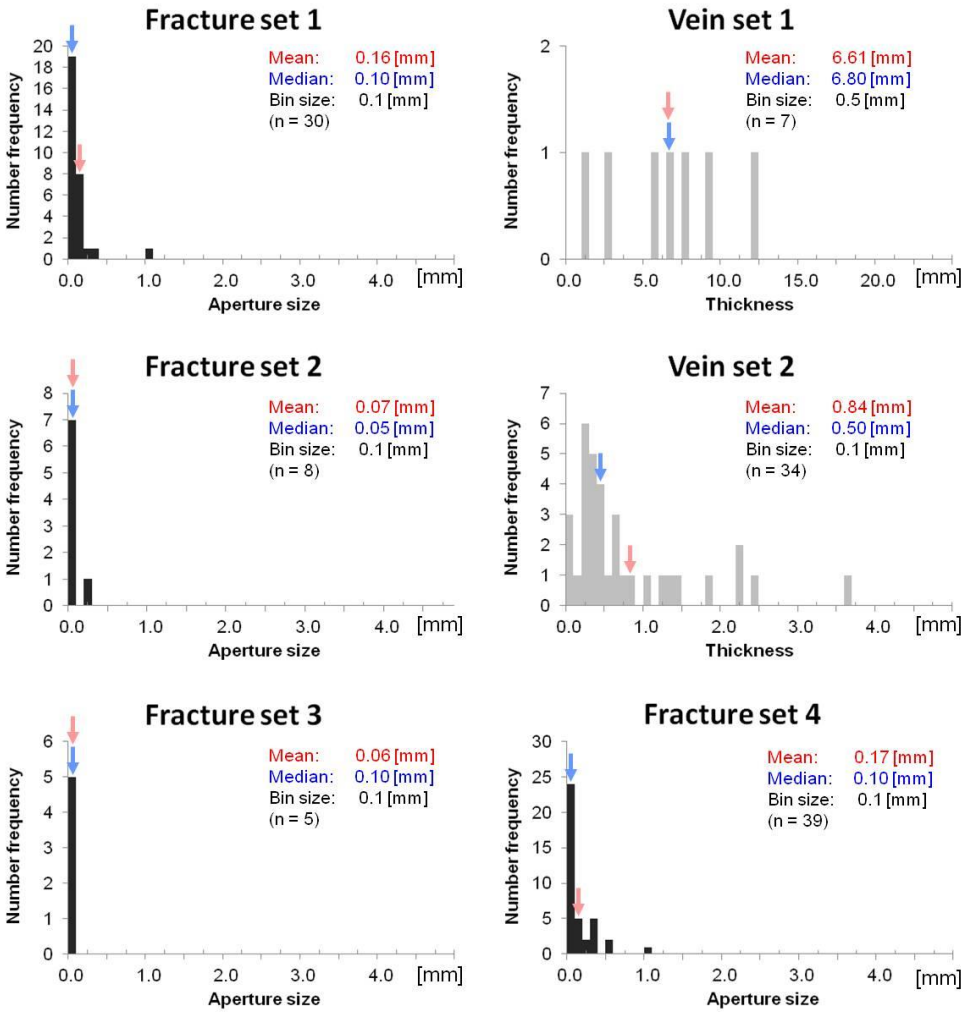

Vein Aspect ratio

Only 1 vein was measured as follow.

Vein 1 DD,D = 023,78 length = 47.0 [cm], thickness = 1.30 [mm] aspect ratio = 362

Layer #11

Site	E (close to hinge of gentle fold)
Lithology	Sandstone
Layer thickness	11cm
Bedding	114, 14

scan line	dip direc -tion, dip	length	number of measured data			
			fracture		vein	
			set 1	set 2	set 1	set 2
1	063,09	5.95m	23	21	5	15
2	124,14	4.07m	44	0	3	0
3	029,01	1.90m	0	6	0	8

Fracture (n=94)

Set 1: NE-SW

Range of strikes: 0-60°

Set 2: SE-NW

Range of strikes: 0-30°

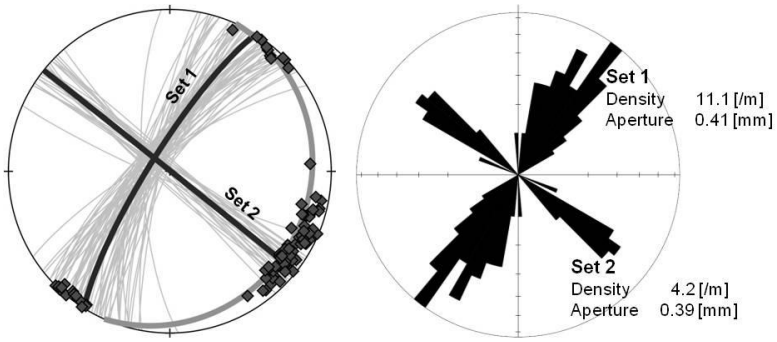

Vein (n=31)

Set 1: NNE-SSW

Range of strikes: 0-30°

Set 2: SE-NW

Range of strikes: 0-30°

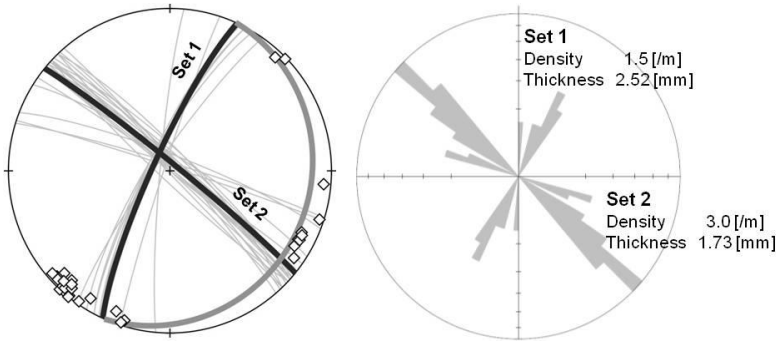

Note

Fractures strike NE-SW (set 1) and SE-NW (set 2). Based on fracture density, set 1 was more dominant direction of fracture formation. Range of strikes of set 1 suggests they contain some shear fractures.

Veins are less common in this layer. The veins strike NNE-SSW (set 1) and SE-NW (set 2). Vein density is high in set 2 but veins are thicker in set 1. There are some veins striking ESE-WNW. Based on geometrical relationship between set 2 and veins striking ESE-WNW, the two groups are possibly conjugate hybrid fractures.

All fractures and veins are sub-perpendicular to the bedding.

<u>Fracture and vein density</u>

Fracture set 1	Raw 10.8 [/m], Corrected 11.1 [/m]	(from 44 data along scan-line 2)
Fracture set 2	Raw 3.8 [/m], Corrected 4.2 [/m]	(from 21 data along scan-line 1)
Vein set 1*	Raw 0.9 [/m], Corrected 1.5 [/m]	(from 5 data along scan-line 1)
Vein set 2	Raw 2.5 [/m], Corrected 3.0 [/m]	(from 15 data along scan-line 1)

*Number of measured data may not be sufficient and the fracture density is relatively inaccurate.

Fracture aperture size and vein thickness

Fracture set 1	mean = 0.41 [mm], 1σ = 0.54 [mm]
Fracture set 2	mean = 0.39 [mm], 1σ = 0.63 [mm]
Vein set 1	mean = 2.52 [mm], 1σ = 3.73 [mm]
Vein set 2	mean = 1.73 [mm], 1σ = 1.20 [mm]

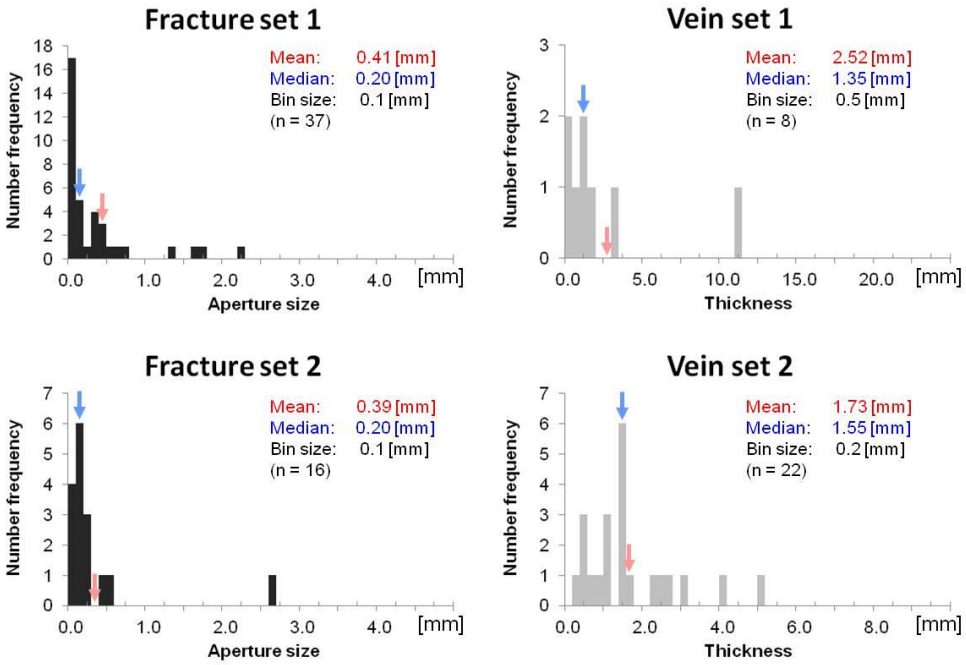

Layer #12

Site E (close to hinge of gentle fold)
Lithology Sandstone
Layer thickness 14cm
Bedding 084, 14

scan line	dip direc -tion, dip	length	number of measured data							
			fracture				vein			
			set 1	set 2	set 3	others	set 1	set 2	set 3	others
1	126,10	8.15m	58	3	0	1	8	2	3	0
2	013,05	7.48m	2	3	18	1	4	1	26	1
others	-	-	0	0	0	0	22	0	6	0

Fracture (n=86)
Set 1: NNE-SSW
Range of strikes: 0-45°
Set 2: ENE-WSW
Range of strikes: 0-30°
Set 3: ESE-WNW
Range of strikes: 0-30°

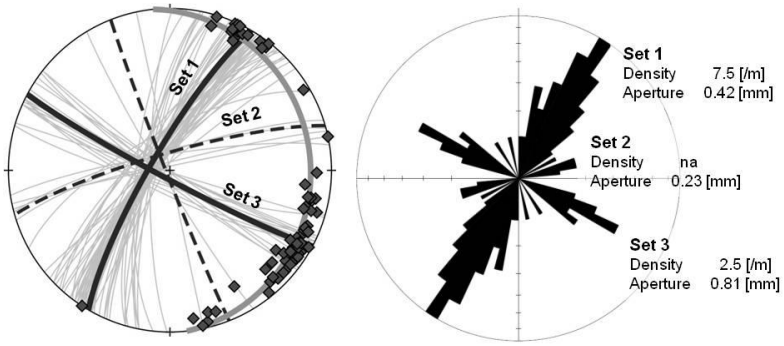

Vein (n=73)
Set 1: NNE-SSW
Range of strikes: 0-30°
Set 2: ENE-WSW
Range of strikes: 0-30°
Set 3: ESE-WNW
Range of strikes: 0-45°

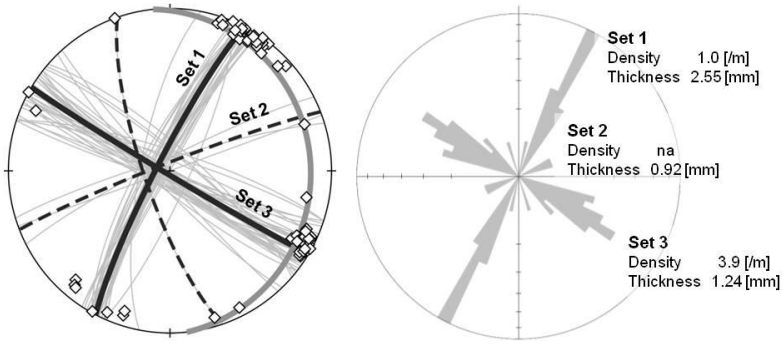

Note

Fractures mainly strike NNE-SSW (set 1) and ESE-WNW (set 3). Fractures striking ENE-WSW (set 2) are relatively rare. Fracture density is higher in set 1 and aperture size is greater in set 3. Strain caused by fracture opening is the largest in set 1. Range of strikes of set 1 suggests some hybrid or shear fractures are contained in set 1.

Veins strike similar orientations as those of fractures. Veins striking NNE-SSW (set 1) and ESE-WNW (set 3) are dominant. In contrast to fractures, vein density is higher in set 3 and vein thickness is greater in set 1. Range of strikes of set 3 suggests there are some hybrid fractures in set 3.

Most fractures and veins are perpendicular to the bedding.

<u>Fracture and vein density</u>

Fracture set 1	Raw 7.3 [/m], Corrected 7.5 [/m]	(from 58 data along scan-line 1)
Fracture set 3	Raw 2.4 [/m], Corrected 2.5 [/m]	(from 18 data along scan-line 2)
Vein set 1*	Raw 1.0 [/m], Corrected 1.0 [/m]	(from 8 data along scan-line 1)
Vein set 3	Raw 3.6 [/m], Corrected 3.9 [/m]	(from 26 data along scan-line 2)

*Number of measured data may not be sufficient and the fracture density is relatively inaccurate.

Fracture aperture size and vein thickness

Fracture set 1	mean = 0.42 [mm], 1σ = 0.42 [mm]
Fracture set 2	mean = 0.23 [mm], 1σ = 0.22 [mm]
Fracture set 3	mean = 0.81 [mm], 1σ = 1.14 [mm]
Vein set 1	mean = 2.55 [mm], 1σ = 2.22 [mm]
Vein set 2	mean = 0.92 [mm], 1σ = 1.20 [mm]
Vein set 3	mean = 1.24 [mm], 1σ = 1.04 [mm]

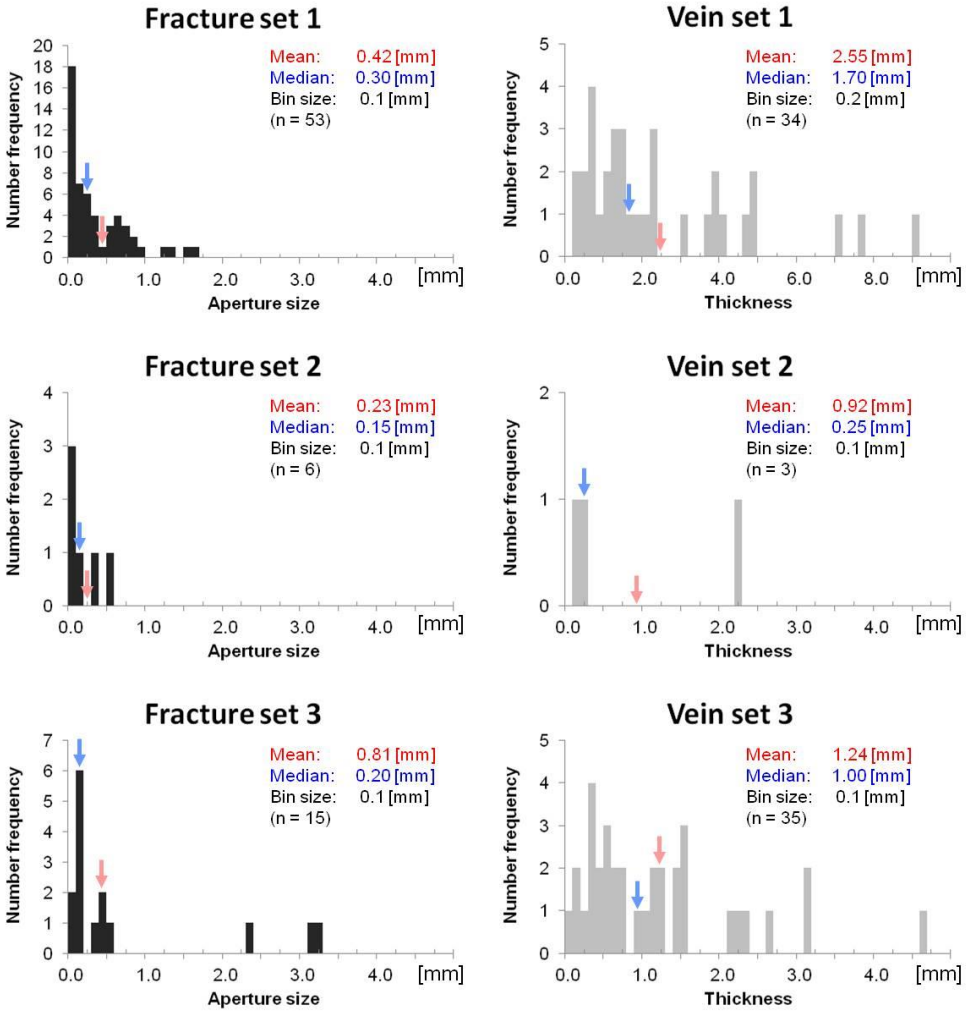

Vein Aspect ratio

Vein set 1 mean = 258, 1σ = 68

Vein set 2 mean = 488, 1σ = 265

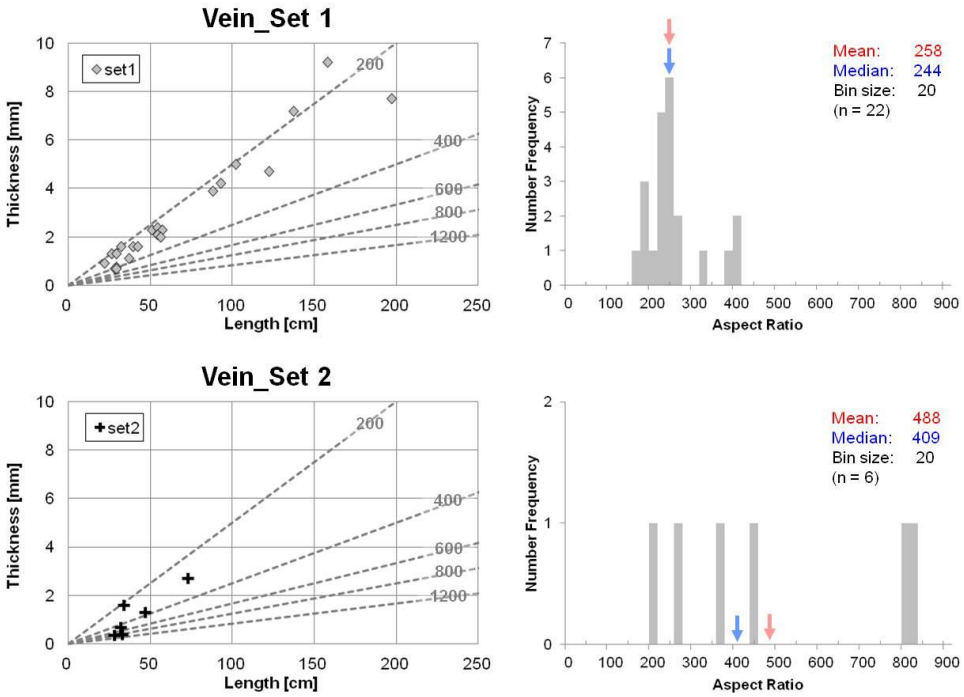

Layer #13

Site	E (close to hinge of gentle fold)
Lithology	Sandstone
Layer thickness	17cm
Bedding	174, 16

scan line	dip direc -tion, dip	length	number of measured data			
			fracture			
			set 1	set 2	set 3	Others
1	097,04	3.35m	64	3	15	0
2	167,16	0.75m	0	5	0	0
3	243,06	0.91m	0	0	4	1
others	-	-	0	5	5	0

Fracture (n=101)

Set 1: NNE-SSW
Range of strikes: 0-30°
Set 2: ENE-WSW
Range of strikes: 0-30°
Set 3: SSE-NNW
Range of strikes: 0-30°

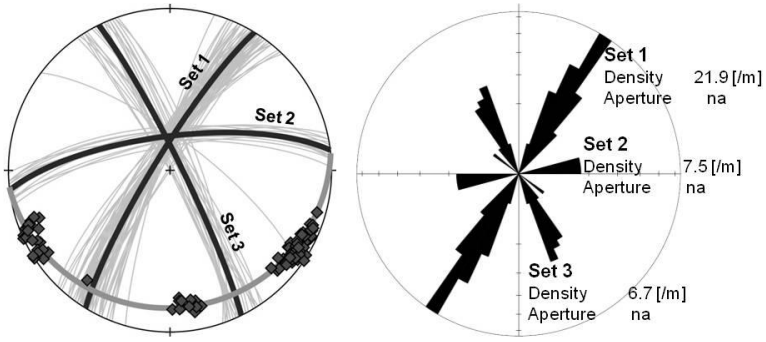

Vein

No vein was found in the layer.

Note

Fractures strike NNE-SSW (set 1), ENE-WNW (set 2), and SSE-NNW (set 3). Fracture aperture size was not measured in this layer. Based on fracture density, set 1 fractures are most dominant, and set 2 and 3 fractures have similar fracture density. Based on the geometrical relationship and similarity of fracture density, set 2 and 3 may be conjugate set of shear fractures.

All fractures are perpendicular to the bedding.

Fracture and vein density

Fracture set 1	Raw 19.7 [/m], Corrected 21.9 [/m]	(from 64 data along scan-line 1)
Fracture set 2*	Raw 7.3 [/m], Corrected 7.5 [/m]	(from 5 data along scan-line 2)
Fracture set 3	Raw 6.7 [/m], Corrected 6.7 [/m]	(from 15 data along scan-line 1)

*Number of measured data may not be sufficient and the fracture density is relatively inaccurate.

Fracture aperture size and vein thickness

Not measured

Layer #14

Site	E (close to hinge of gentle fold)
Lithology	Sandstone
Layer thickness	19cm
Bedding	141, 13

scan line	dip direc -tion, dip	length	number of measured data				
			fracture			vein	
			set 1	set 2	others	set 1	set 2
1	233,00	7.51m	0	62	0	0	10
2	083,07	11.97m	63	2	1	7	0

Fracture (n=128)

Set 1: NNE-SSW

Range of strikes: 0-45°

Set 2: SE-NW

Range of strikes: 0-45°

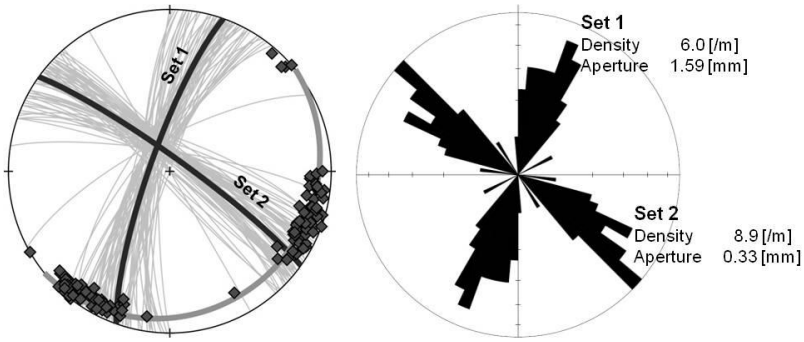

Vein (n=17)

Set 1: NNE-SSW

Range of strikes: 0-30°

Set 2: ESE-WNW

Range of strikes: 0-45°

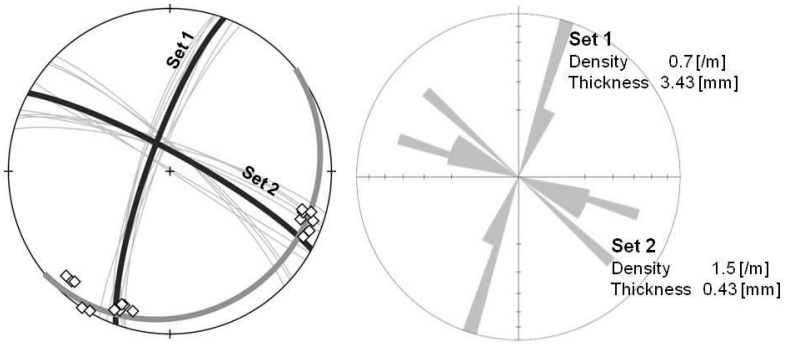

Note

Fractures strike NNE-SSW (set 1) and SE-NW (set 2). Fracture density is relatively high in set 2 but aperture size is much greater in set 1. Ranges of strikes of the two sets suggest they contain some hybrid fractures.

Veins are relatively rare in the layer. They strike same orientations as those of fractures (set 1: NNE-SSW, set 2: ESE-WNW). Vein density is high in set 2 but vein thickness is much greater in set 1. Distribution of strikes of set 2 suggests majority of them are conjugate set of hybrid fractures.

Most fractures and veins are perpendicular to the bedding.

<u>Fracture and vein density</u>

Fracture set 1	Raw 5.3 [/m], Corrected 6.0 [/m]	(from 62 data along scan-line 2)
Fracture set 2	Raw 8.3 [/m], Corrected 8.9 [/m]	(from 63 data along scan-line 1)
Vein set 1	Raw 0.6 [/m], Corrected 0.7 [/m]	(from 10 data along scan-line 2)
Vein set 2*	Raw 1.3 [/m], Corrected 1.5 [/m]	(from 7 data along scan-line 1)

*Number of measured data may not be sufficient and the fracture density is relatively inaccurate.

Fracture aperture size and vein thickness

Fracture set 1	mean = 1.59 [mm], 1σ = 4.37 [mm]
Fracture set 2	mean = 0.33 [mm], 1σ = 0.48 [mm]
Vein set 1	mean = 3.43 [mm], 1σ = 4.41 [mm]
Vein set 2	mean = 0.43 [mm], 1σ = 0.22 [mm]

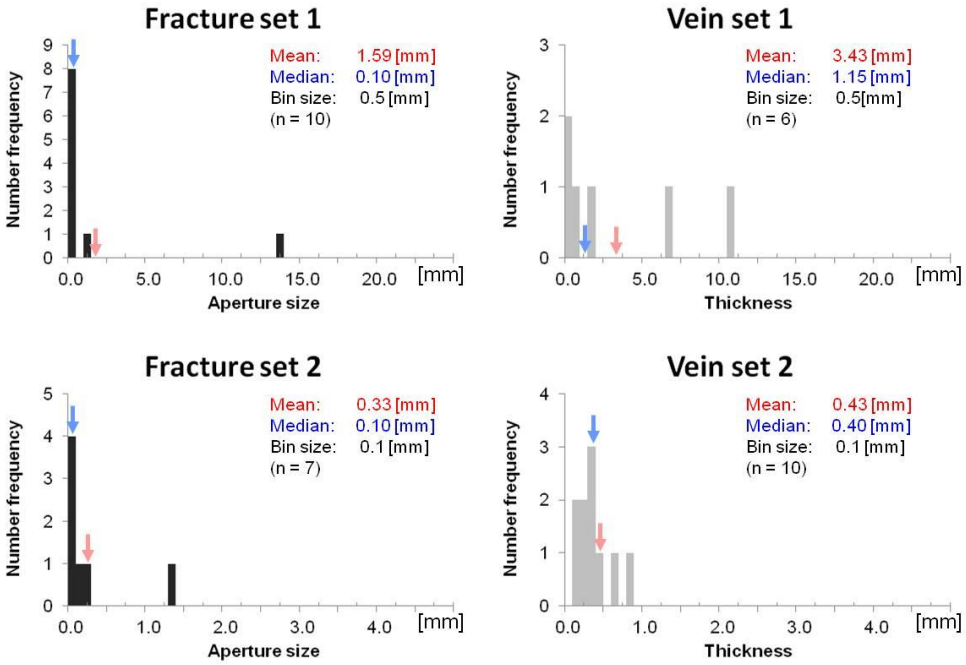

Layer #15

Site	F (northern limb of gentle fold)
Lithology	Sandstone
Layer thickness	63cm
Bedding	048, 26

scan line	dip direc -tion, dip	length	number of measured data			
			fracture	vein		
			set 1	set 1	set 2	set 3
1	125,06	15.77m	4	42	33	1
others	-	-	0	39	62	15

Fracture (n=4)

Set 1: NNE-SSW

Range of strikes: 0-45°

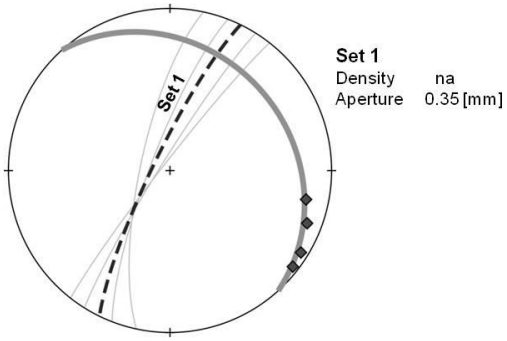

Vein (n=192)

Set 1: N-S

Range of strikes: 0-60°

Set 2: ENE-WSW

Range of strikes: 0-45°

Set 3: SE-NW

Range of strikes: 0-30°

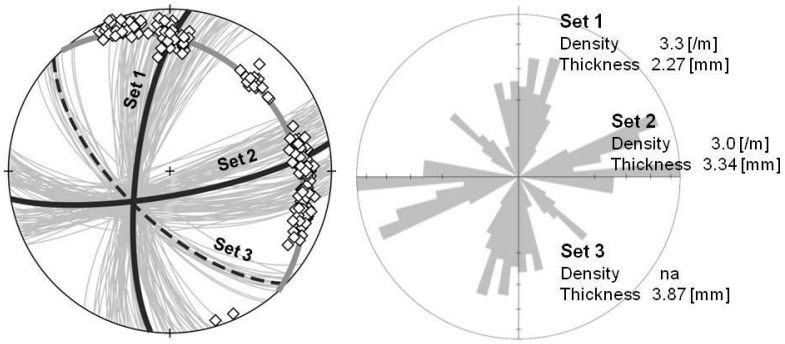

Note

Most fractures are filled with minerals in this layer. Only 4 fractures striking NNE-SSW were measured.

Veins strikes N-S (set 1), ENE-WSW (set 2), and SE-NW (set 3). Because of limited exposure in NE-SW direction, density of set 3 veins could not be estimated. Vein density is similar between the other two sets. Aperture size among the three sets is similar though it is relatively thin in set 1. Because data of set 2 are separated into two orientations, most of set 2 veins are conjugate set of hybrid fractures. Range of strikes of set 1 also suggests there are some shear and hybrid veins in set 1.

Most fracture and veins are perpendicular to the bedding.

<u>Fracture and vein density</u>

Vein set 1	Raw 2.8 [/m], Corrected 3.3 [/m]	(from 42 data along scan-line 2)
Vein set 2	Raw 2.1 [/m], Corrected 3.0 [/m]	(from 33 data along scan-line 2)

Fracture aperture size and vein thickness

Fracture set 1	mean = 0.35 [mm], 1σ = 0.24 [mm]
Vein set 1	mean = 2.27 [mm], 1σ = 3.60 [mm]
Vein set 2	mean = 3.34 [mm], 1σ = 2.92 [mm]
Vein set 3	mean = 3.87 [mm], 1σ = 1.82 [mm]

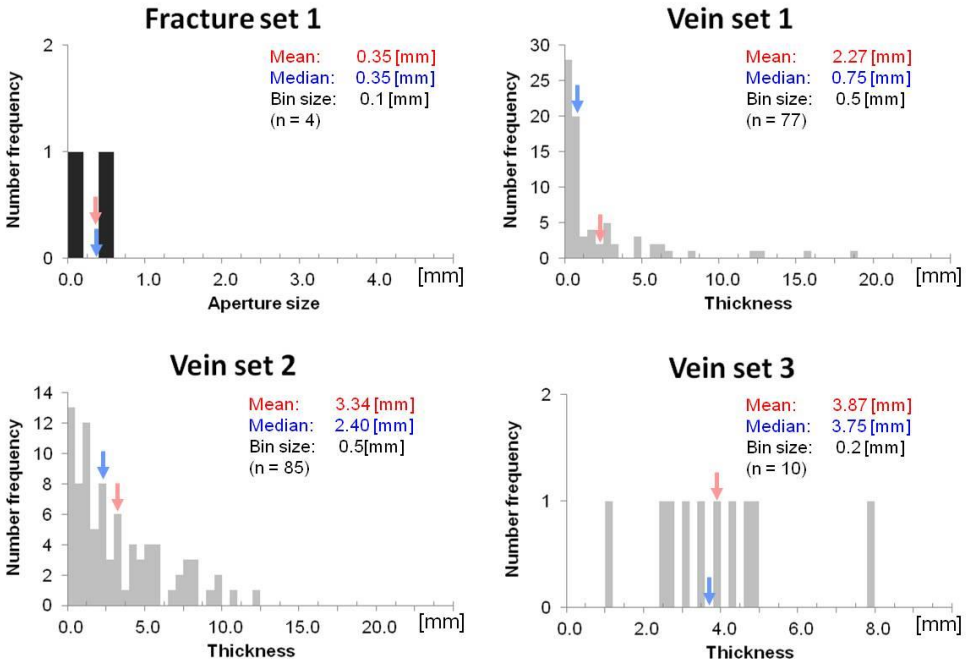

Vein Aspect ratio

Vein set 1	mean = 578, 1σ = 438
Vein set 2	mean = 304, 1σ = 194
Vein set 3	mean = 879, 1σ = 381

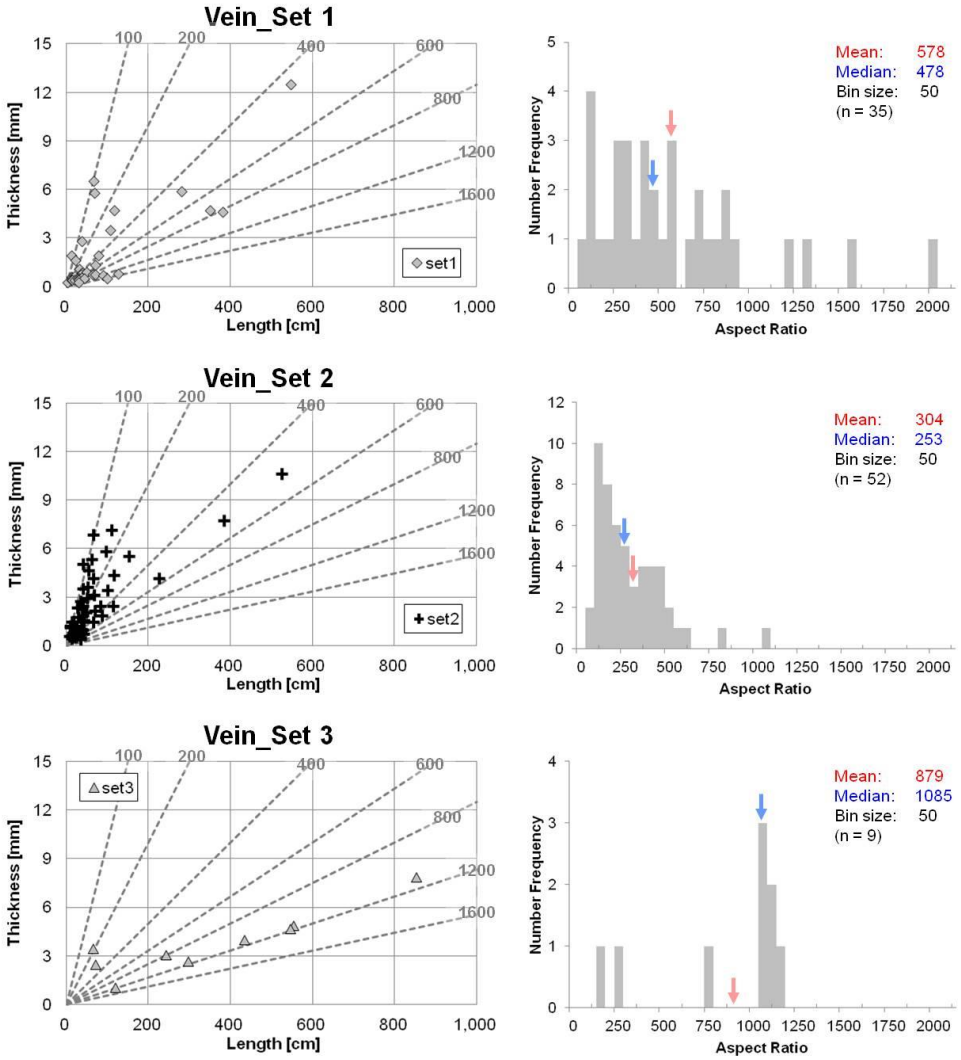

Layer #16

Site	G (southern limb of gentle fold)
Lithology	Shale
Layer thickness	52cm
Bedding	204, 10

scan line	dip direc -tion, dip	length	number of measured data		
			fracture		
			set 1	set 2	others
1	115,00	6.98m	24	0	1
2	205,20	4.94m	0	14	1

Fracture (n=40)

Set 1: NE-SW

Range of strikes: 0-45°

Set 2: ESE-WNW

Range of strikes: 0-30°

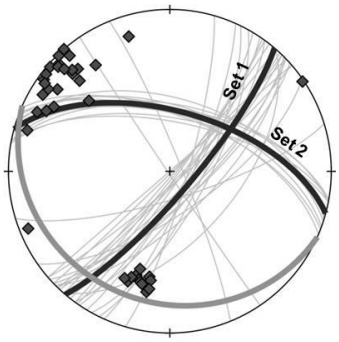

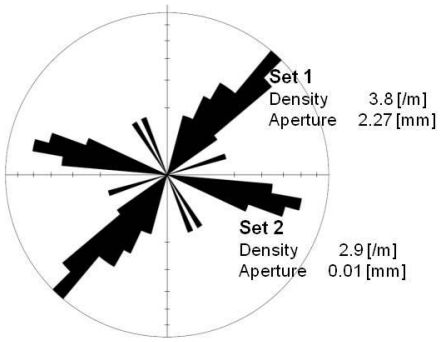

Vein

No vein was found in the layer.

Note

Fractures mainly strike NE-SW (set 1) and ESE-WNW (set 2). There are some fractures striking other directions but they are assumed as minor. Fracture density of set 1 is relatively larger. Aperture size of set 1 is mm-scale but they are not probably original size in the ground because of ductile nature of the fractures (curved fractures) in the shale. Aperture sizes along set 2 fractures are too small to measure by feeler and 0.01 [mm] is assigned.

Most fractures are not perpendicular to the bedding.

Fracture and vein density

Fracture set 1	Raw 3.4 [/m], Corrected 3.8 [/m]	(from 24 data along scan-line 1)
Fracture set 2	Raw 2.8 [/m], Corrected 2.9 [/m]	(from 14 data along scan-line 2)

Fracture aperture size and vein thickness

Fracture set 1	mean = 2.27 [mm], 1σ = 1.90 [mm]
Fracture set 2	mean = 0.01 [mm], 1σ = 0.00 [mm]

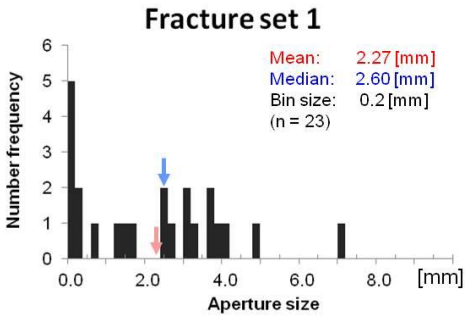

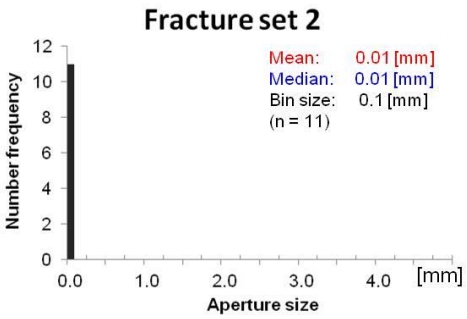

Layer #17

Site	G (southern limb of gentle fold)
Lithology	Shale
Layer thickness	11cm
Bedding	196, 29

scan line	dip direc -tion, dip	length	number of measured data			
			fracture			
			set 1	set 2	set 3	others
1	123,08	2.79m	72	11	0	0
2	177,27	2.87m	16	0	60	1

Fracture (n=160)

Set 1: NE-SW
Range of strikes: 0-45°
Set 2: ENE-WSW
Range of strikes: 0-45°
Set 3: ESE-WNW
Range of strikes: 0-45°

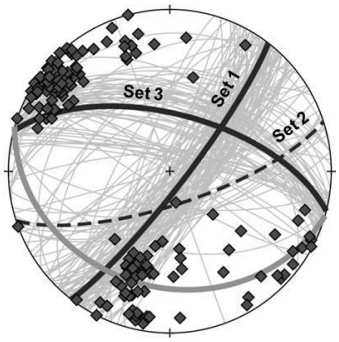

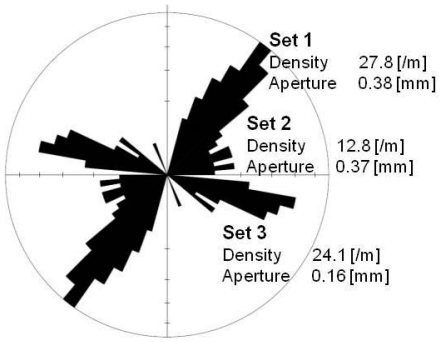

Vein

No vein was found in the layer.

Note

Fractures developed more complicatedly than those of layer 16 (shale) but dominant orientations are same. They mainly strike NE-SW (set 1) and ESE-WNW (set 3) based on the fracture density. Fractures striking ENE-WSW (set 2) are also common.

Most fractures are not perpendicular to the bedding.

Fracture and vein density

Fracture set 1	Raw 25.8 [/m], Corrected 27.8 [/m]	(from 72 data along scan-line 1)
Fracture set 2	Raw 8.7 [/m], Corrected 12.8 [/m]	(from 11 data along scan-line 1)
Fracture set 3	Raw 20.9 [/m], Corrected 24.1 [/m]	(from 60 data along scan-line 2)

Fracture aperture size and vein thickness

Fracture set 1	mean = 0.38 [mm], 1σ = 1.01 [mm]
Fracture set 2	mean = 0.37 [mm], 1σ = 0.53 [mm]
Fracture set 2	mean = 0.16 [mm], 1σ = 0.31 [mm]

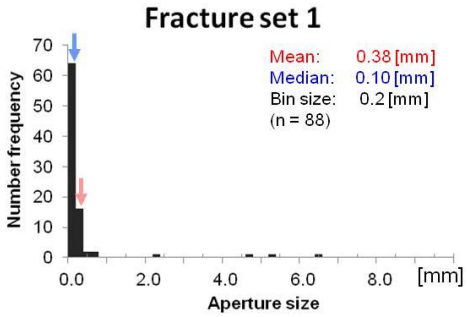

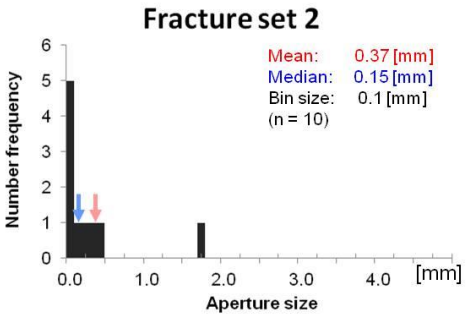

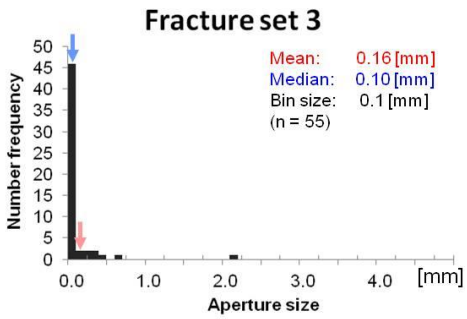

Layer #18

Site	G (southern limb of gentle fold)
Lithology	Sandstone
Layer thickness	6cm
Bedding	204, 26

scan line	dip direc -tion, dip	length	number of measured data		
			fracture		vein
			set 1	set 2	set 1
1	121,03	5.34m	69	0	0
2	185,24	4.94m	0	56	3

Fracture (n=125)

Set 1: N-S

Range of strikes: 0-45°

Set 2: ESE-WNW

Range of strikes: > 0-60°

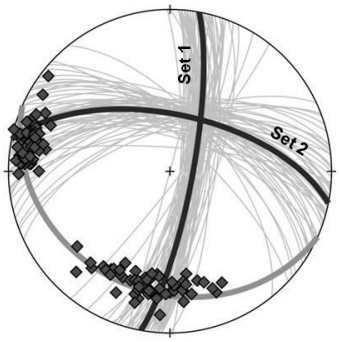

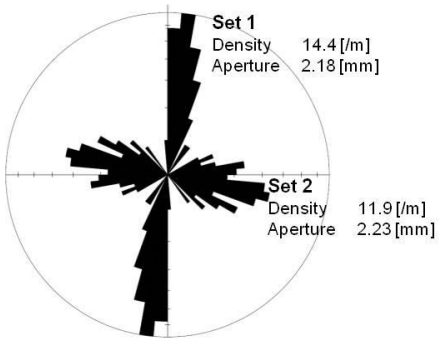

Vein (n=3)

Set 1: ESE-WNW

Range of strikes: 0-45°

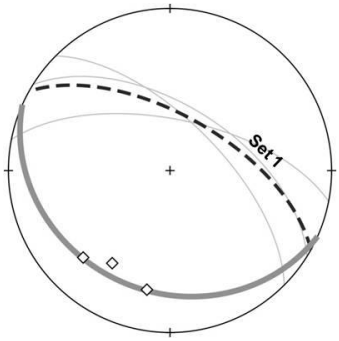

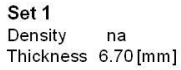

Note

Layer 16-21 were measured in an approximately same outcrop. Layer 18 is slightly far from the others. However, fracture pattern of layer 16-17 (shale) and fracture pattern in layer 18-21 (sandstone) are very similar each other. It would be suitable to investigate the relationship between fracture density and aperture size, and layer thickness among the layer 18-21.

Fractures strike N-S (set 1) and ENE-WNW (set 2). Fracture density and aperture size are similar between the two sets. Ranges of strikes of the sets suggest set 1 fractures are more like extension fractures, and that set 2 contains some shear fractures.

Veins are very rare in the layer. Only 4 veins striking ESE-WNW (set 1) were measured. In this outcrop (layer 18-21), veins are commonly observed only in ESE-WNW direction. In addition, veins become rare in thinner sandstone.

Most fractures and vein are perpendicular to the bedding.

Fracture and vein density

Fracture set 1	Raw 12.9 [/m], Corrected 14.4 [/m]	(from 69 data along scan-line 1)
Fracture set 2	Raw 11.3 [/m], Corrected 11.9 [/m]	(from 56 data along scan-line 2)

Fracture aperture size and vein thickness

Fracture set 1	mean = 2.18 [mm], 1σ = 2.37 [mm]
Fracture set 2	mean = 2.23 [mm], 1σ = 0.33 [mm]
Vein set 1	mean = 6.70 [mm], 1σ = 3.46 [mm]

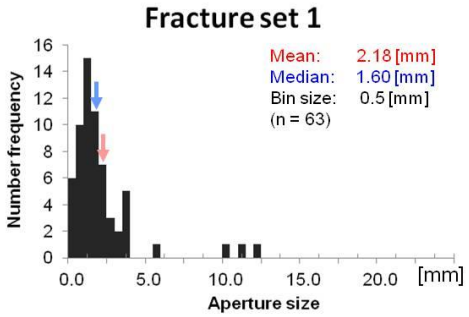

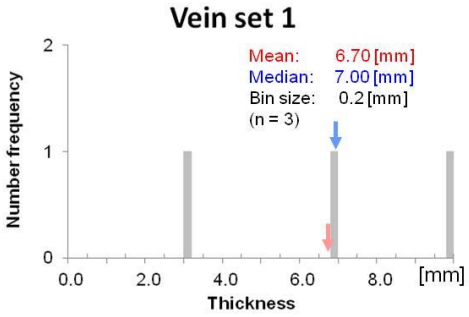

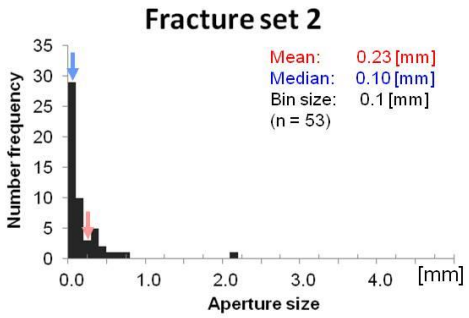

Layer #19

Site	G (southern limb of gentle fold)
Lithology	Sandstone
Layer thickness	4cm
Bedding	204, 23

scan line	dip direc -tion, dip	length	number of measured data		
			fracture		
			set 1	set 2	set 3
1	121,03	3.21m	58	19	2
2	185,22	3.05m	20	2	62

Fracture (n=163)

Set 1: NNE-SSW
Range of strikes: 0-30°
Set 2: NE-SW
Range of strikes: 0-30°
Set 3: ENE-WSW
Range of strikes: > 0-60°

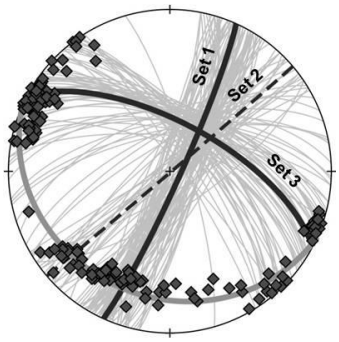

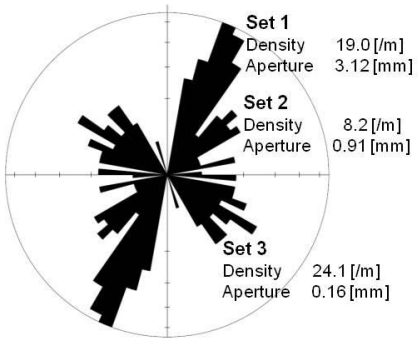

Vein

No vein was found in the layer.

Note

Fractures mainly strike NNE-SSW (set 1) and ENE-WNW (set 3). Fractures striking NE-SW (set 2) were also observed. Fractures in this orientation were not observed in layer 18, 20 and 21. They seemed to be formed in accordance with fracture formation in shale (layer 16 and 17). Relatively thin sandstone (small ratio of thickness between the sandstone and surrounding shale) might be affected by much dominant shale. Fracture density is relatively high in set 3 but aperture size is much greater in set 1. Wide distribution of strikes of set 3 suggests some hybrid and shear fractures are contained in set 3. Most fractures are perpendicular to the bedding, except set 2 which are probably associated with shale deformation.

Fracture and vein density

Fracture set 1	Raw 18.4 [/m], Corrected 19.0 [/m]	(from 58 data along scan-line 1)
Fracture set 2	Raw 7.6 [/m], Corrected 8.2 [/m]	(from 19 data along scan-line 1)
Fracture set 3	Raw 20.3 [/m], Corrected 24.1 [/m]	(from 62 data along scan-line 2)

Fracture aperture size and vein thickness

Fracture set 1	mean = 3.12 [mm], 1σ = 8.65 [mm]
Fracture set 2	mean = 0.91 [mm], 1σ = 2.96 [mm]
Fracture set 3	mean = 0.16 [mm], 1σ = 0.31 [mm]

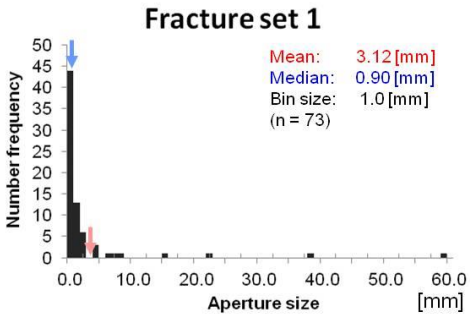

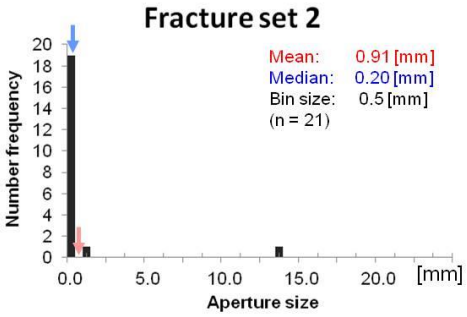

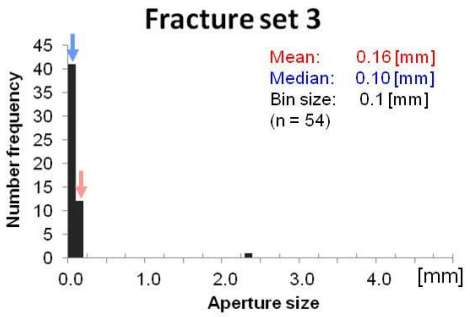

Layer #20

Site	G (southern limb of gentle fold)
Lithology	Sandstone
Layer thickness	12cm
Bedding	202, 23

scan line	dip direc -tion, dip	length	number of measured data			
			fracture		vein	
			set 1	set 2	set 1	others
1	113,00	3.83m	49	3	23	1
2	183,22	1.82m	9	14	59	1
3	195,23	3.06m	8	39	0	0

Fracture (n=115)

Set 1: NNE-SSW

Range of strikes: 0-30°

Set 2: ESE-WNW

Range of strikes: > 0-60°

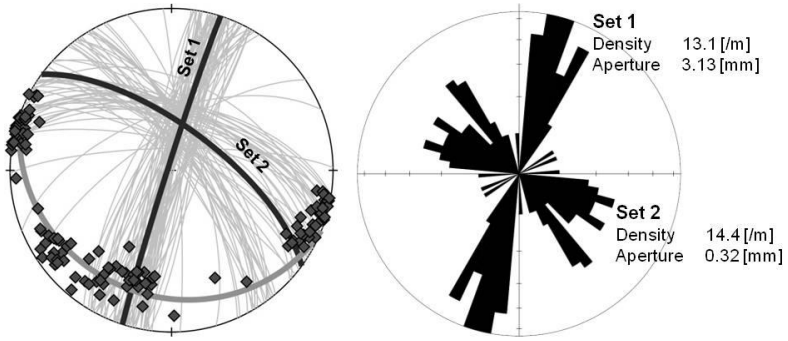

Vein (n=84)

Set 1: ESE-WNW

Range of strikes: > 0-60°

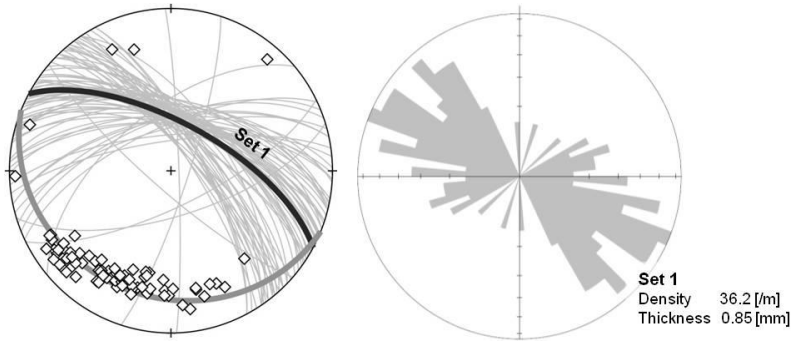

Note

Fractures strike NNE-SSW (set 1) and ENE-WNW (set 2). Fracture density is similar between the two sets but aperture size suggests set 1 was associated with stronger deformation. Ranges of strikes of the sets suggest set 1 fractures are more like extension fractures, and that set 2 contains some hybrid and shear fractures.

Veins mainly strike ESE-WNW (set 1) and the other directions are assumed as minor. Range of the strikes suggests they contain hybrid and shear fractures in set 1.

Most fractures and vein are perpendicular to the bedding.

Fracture and vein density

Fracture set 1	Raw 12.8 [/m], Corrected 13.1 [/m]	(from 49 data along scan-line 1)
Fracture set 2	Raw 12.7 [/m], Corrected 14.4 [/m]	(from 39 data along scan-line 3)
Vein set 1	Raw 32.4 [/m], Corrected 36.2 [/m]	(from 59 data along scan-line 2)

Fracture aperture size and vein thickness

Fracture set 1	mean = 3.13 [mm], 1σ = 4.53 [mm]
Fracture set 2	mean = 0.32 [mm], 1σ = 0.61 [mm]
Vein set 1	mean = 0.85 [mm], 1σ = 1.09 [mm]

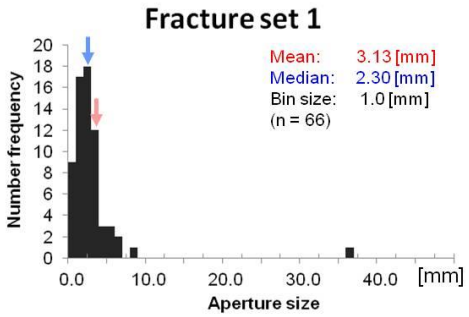

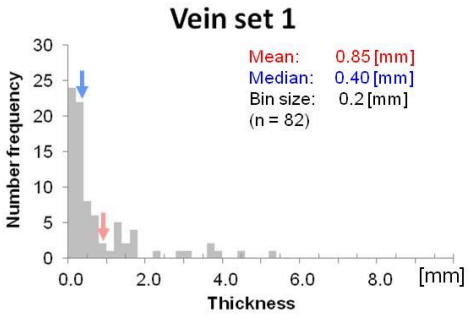

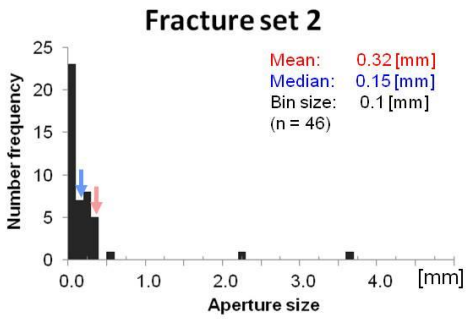

Layer #21

Site	G (southern limb of gentle fold)
Lithology	Sandstone
Layer thickness	26cm
Bedding	210, 21

scan line	dip direc -tion, dip	length	number of measured data		
			fracture		vein
			set 1	set 2	set 1
1	295,02	6.77m	72	0	0
2	206,21	5.17m	4	39	91

Fracture (n=115)

Set 1: NNE-SSW

Range of strikes: 0-30°

Set 2: ESE-WNW

Range of strikes: > 0-60°

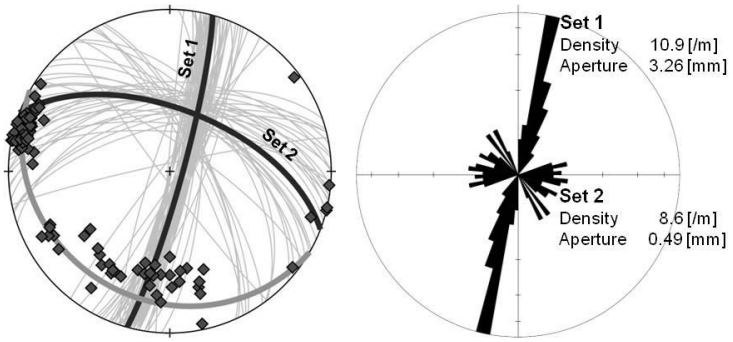

Vein (n=91)

Set 1: ESE-WNW

Range of strikes: > 0-60°

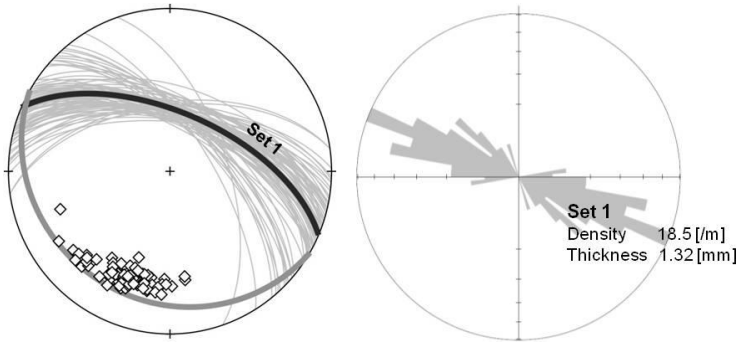

Note

Fractures strike NNE-SSW (set 1) and ENE-WNW (set 2). Fracture density is similar between the two sets but aperture size is much greater in set 1, suggesting set 1 was associated with stronger deformation. Ranges of strikes of the two sets suggest set 1 fractures are more like extension fractures, and that set 2 contains some hybrid and shear fractures.

Veins mainly strike ESE-WNW (set 1) . Range of the strikes suggests they contain hybrid and shear fractures in set 1.

Most fractures and vein are perpendicular to the bedding.

Fracture and vein density

Fracture set 1	Raw 10.6 [/m], Corrected 10.9 [/m]	(from 72 data along scan-line 1)
Fracture set 2	Raw 7.6 [/m], Corrected 8.6 [/m]	(from 39 data along scan-line 3)
Vein set 1	Raw 17.8 [/m], Corrected 18.5 [/m]	(from 91 data along scan-line 2)

Fracture aperture size and vein thickness

Fracture set 1	mean = 3.26 [mm], 1σ = 1.87 [mm]
Fracture set 2	mean = 0.49 [mm], 1σ = 1.01 [mm]
Vein set 1	mean = 1.32 [mm], 1σ = 1.43 [mm]

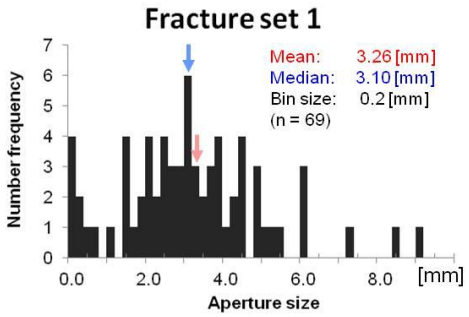

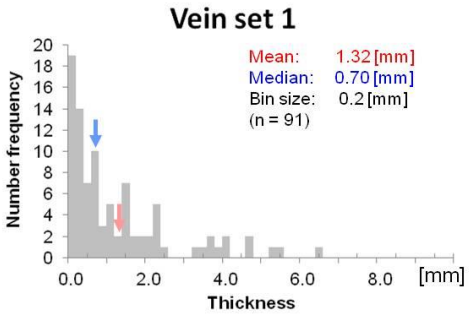

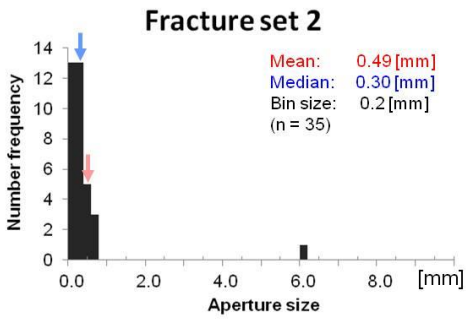

Layer #22

Site	H (southern limb of gentle fold)
Lithology	Shale
Layer thickness	295cm
Bedding	186, 20

scan line	dip direc -tion, dip	length	number of measured data	
			fracture	
			set 1	set 2
1	101,02	57.99m	61	8

Fracture (n=69)

Set 1: N-S

Range of strikes: > 0-60°

Set 2: ENE-WSW

Range of strikes: 0-45°

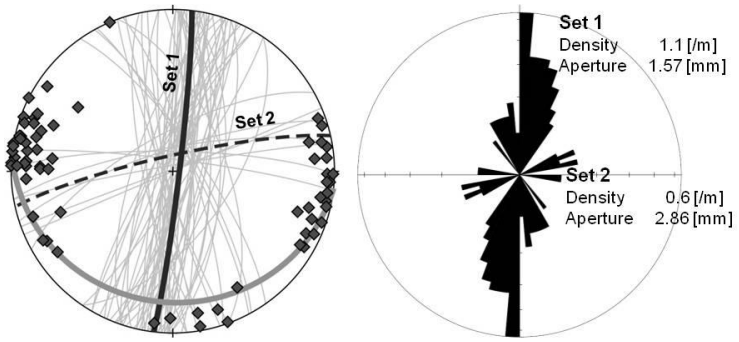

Vein

No vein was found in the layer.

Note

Fractures strike N-S (set 1) and ENE-WSW (set 2). Fracture density is higher in set 1 but aperture is greater in set 2. Strains caused by the fracture openings are similar between the two. Ranges of strikes suggest shear fractures are more dominant in set 1, and that set 2 fractures are more like extension or hybrid fractures. Some fractures are not perpendicular to the bedding.

Fracture and vein density

Fracture set 1	Raw 1.1 [/m], Corrected 1.1 [/m]	(from 61 data along scan-line 1)
Fracture set 2*	Raw 0.2 [/m], Corrected 0.6 [/m]	(from 8 data along scan-line 1)

*Fracture set 2 is nearly parallel to scan-line 1 and the correction effect may be too large. In addition, number of measured data is insufficient. Because of these, the corrected fracture density is relatively inaccurate.

Fracture aperture size and vein thickness

Fracture set 1	mean = 1.57 [mm], 1σ = 1.94 [mm]
Fracture set 2	mean = 2.86 [mm], 1σ = 2.30 [mm]

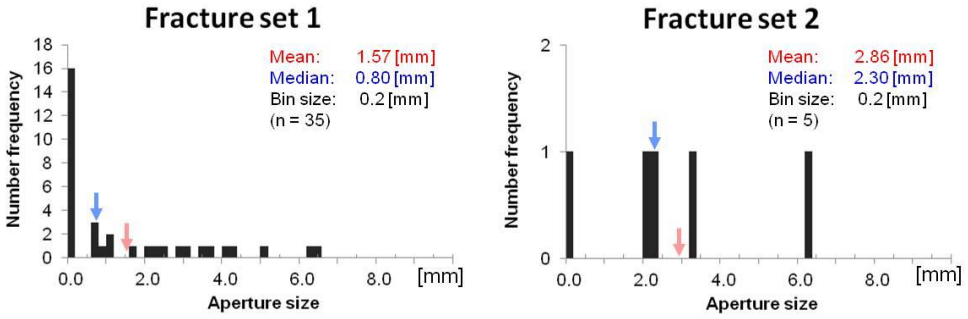

Layer #23

Site	H (southern limb of gentle fold, close to thrust fault)
Lithology	Sandstone
Layer thickness	18cm
Bedding	220, 37

scan line	dip direc -tion, dip	length	number of measured data	
			fracture	
			set 1	set 2
1	302,05	25.05m	34	11

Fracture (n=45)

Set 1: NE-SW

Range of strikes: 0-60°

Set 2: SE-NW

Range of strikes: 0-30°

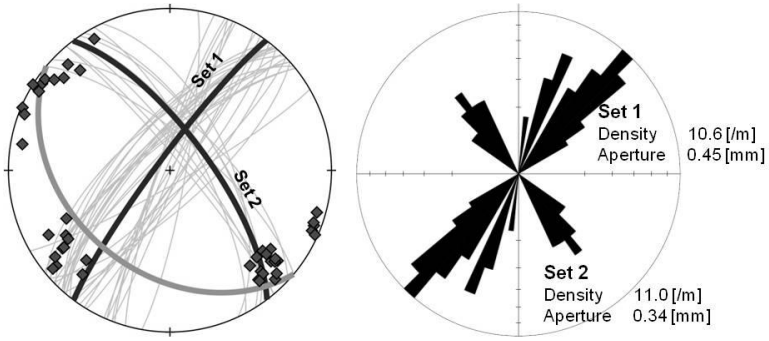

Vein

No vein was found in the layer.

Note

Fractures strike NE-SW (set 1) and SE-NW (set 2). The densities and aperture sizes are similar between the two sets. The outcrop where the fractures measured is close to outcrop-scale thrust which is probably continuous more than 10 meters. Beddings and fracture orientations seem to be relatively variable in this area. Some fractures are not perpendicular to the bedding.

Fracture and vein density

Fracture set 1	Raw 9.9 [/m], Corrected 10.6 [/m]	(from 34 data along scan-line 1)
Fracture set 2	Raw 3.5 [/m], Corrected 11.0 [/m]	(from 11 data along scan-line 1)

*Fracture set 2 is nearly parallel to scan-line 1 and the correction effect may be too large because of this, the corrected fracture density is relatively inaccurate.

Fracture aperture size and vein thickness

Fracture set 1	mean = 0.45 [mm], 1σ = 0.57 [mm]
Fracture set 2	mean = 0.34 [mm], 1σ = 0.35 [mm]

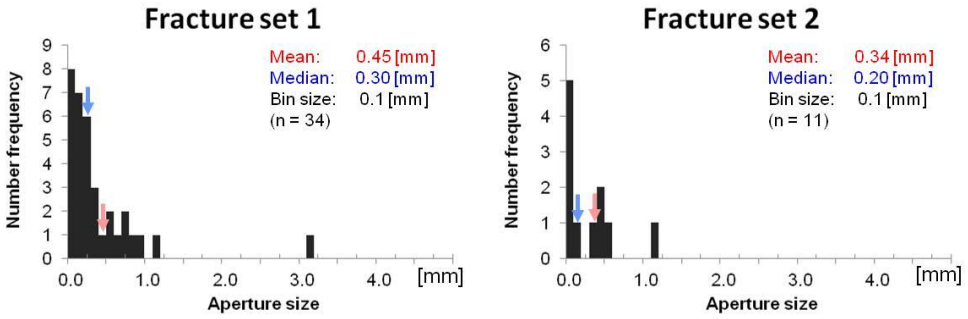

Layer #24

Site	H (southern limb of gentle fold)
Lithology	Sandstone
Layer thickness	61cm
Bedding	196, 10

scan line	dip direc -tion, dip	length	number of measured data			
			fracture		vein	
			set 1	set 2	set 1	set 2
1	152,07	10.24m	0	0	6	66
2	257,05	22.17m	1	45	1	0
others	-	-	0	0	0	59

Fracture (n=46)

Set 1: NNE-SSW

Range of strikes: 0-30°

Set 2: SSE-NNW

Range of strikes: 0-30°

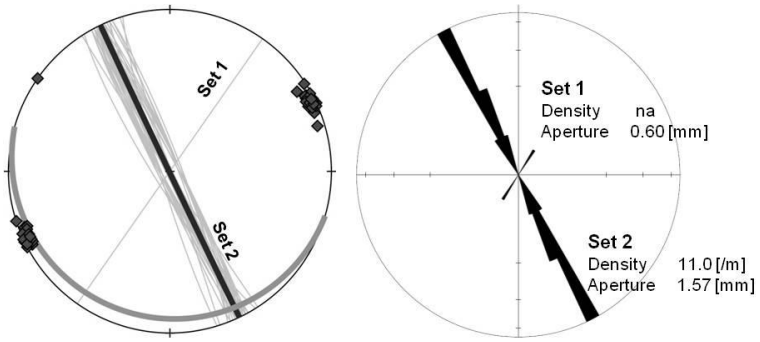

Vein (n=132)

Set 1: NNE-SSW

Range of strikes: 0-30°

Set 2: ENE-WSW

Range of strikes: 0-30°

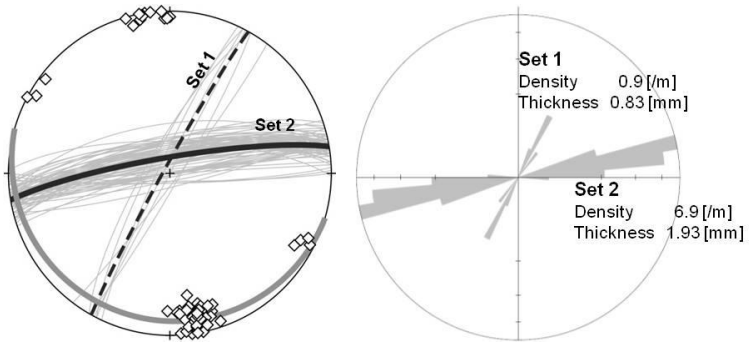

Note

Fractures strike NNE-SSW (set 1) and SSE-NNW (set 2). Set 2 is much dominant direction based on fracture density and aperture size (only 1 fracture was measured in set 1 along two scan-lines, indicating the fracture density must be very low). Dextral displacement was commonly observed along set 2 in the field.

Veins are more common in the layer. The veins strike NNE-SSW and ENE-WNW. Based on fracture density and aperture size, set 1 is relatively minor and most veins concentrate in set 2 direction.

Most fractures and veins are perpendicular to the bedding.

Fracture and vein density

Fracture set 2	Raw 3.5 [/m], Corrected 11.0 [/m]	(from 11 data along scan-line 1)
Vein set 1*	Raw 0.8 [/m], Corrected 0.9 [/m]	(from 6 data along scan-line 1)
Vein set 2	Raw 6.4[/m], Corrected 6.9 [/m]	(from 66 data along scan-line 1)

*Number of measured data may not be sufficient and the fracture density is relatively inaccurate.

Fracture aperture size and vein thickness

Fracture set 2	mean = 1.57 [mm], 1σ = 1.48 [mm]
Vein set 1	mean = 0.83 [mm], 1σ = 1.06 [mm]
Vein set 2	mean = 1.93 [mm], 1σ = 2.38 [mm]

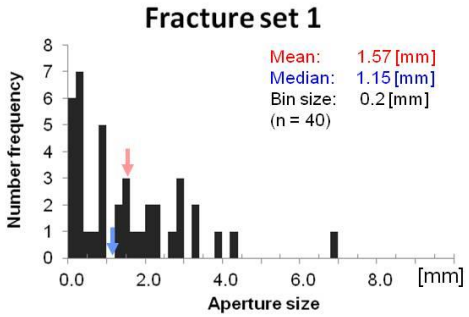

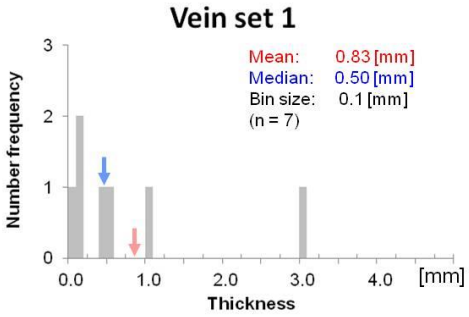

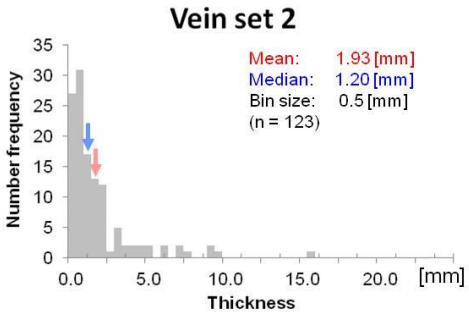

Vein Aspect ratio

Vein set 2	mean = 641, 1σ = 370

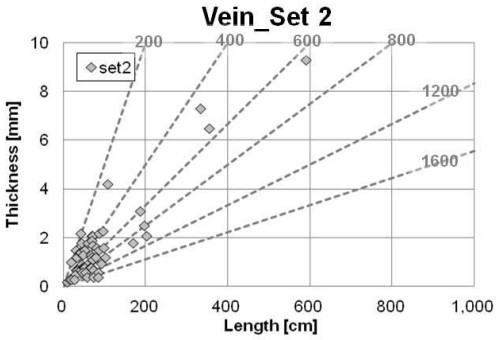

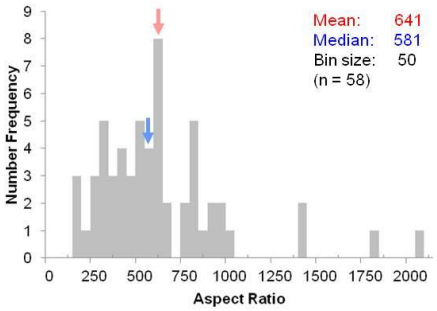

Layer #25

Site	H (southern limb of gentle fold)
Lithology	Sandstone
Layer thickness	23cm
Bedding	209, 17

scan line	dip direc -tion, dip	length	number of measured data					
			fracture			vein		
			set 1	set 2	set 3	set 1	set 2	set 3
1	142,07	5.11m	31	16	0	48	22	0
2	215,17	9.07m	0	0	42	0	0	0
3	215,17	1.39m	0	0	0	0	0	40
others	-	-	0	0	0	0	70	0

Fracture (n=89)

Set 1: NNE-SSW
Range of strikes: 0-30°
Set 2: ENE-WSW
Range of strikes: 0-30°
Set 3: SE-NW
Range of strikes: 0-30°

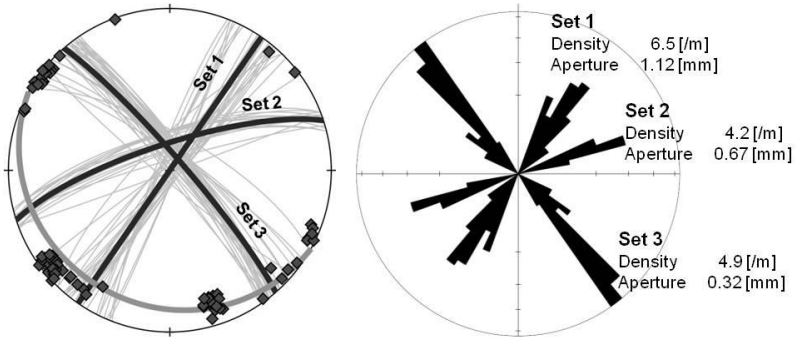

Vein (n=180)

Set 1: NNE-SSW
Range of strikes: 0-30°
Set 2: ENE-WSW
Range of strikes: 0-30°
Set 3: SE-NW
Range of strikes: 0-45°

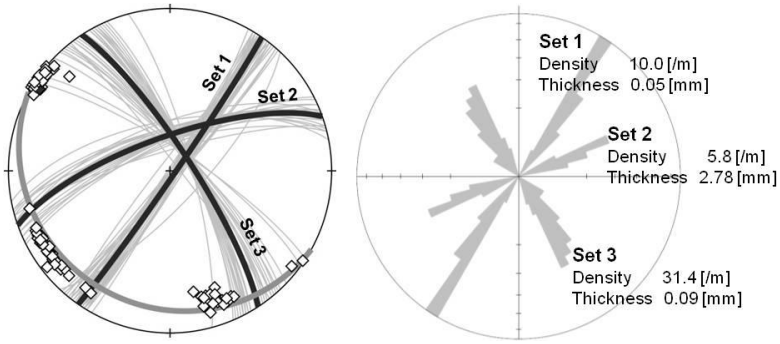

Note

Fractures strike NNE-SSW (set 1), ENE-WSW (set 2), and SE-NW (set 3). Based on fracture density and aperture size, set 1 fractures were associated with stronger deformation. Fracture density of set 2 and 3 are similar.

Veins developed in same orientations as those of fractures. However, only very thin veins formed in set 1 and 3 directions and most of visible veins are in set 2.

Most fractures and veins are perpendicular to the bedding.

Fracture and vein density

Fracture set 1	Raw 6.1 [/m], Corrected 6.5 [/m]	(from 31 data along scan-line 1)
Fracture set 2	Raw 3.9 [/m], Corrected 4.2 [/m]	(from 16 data along scan-line 1)
Fracture set 3	Raw 4.6 [/m], Corrected 4.9 [/m]	(from 42 data along scan-line 2)
Vein set 1	Raw 9.4 [/m], Corrected 10.0 [/m]	(from 48 data along scan-line 1)
Vein set 2	Raw 5.4 [/m], Corrected 5.8 [/m]	(from 22 data along scan-line 1)
Vein set 3	Raw 28.8 [/m], Corrected 31.4 [/m]	(from 40 data along scan-line 3)

Fracture aperture size and vein thickness

Fracture set 1	mean = 1.12 [mm], 1σ = 2.39 [mm]
Fracture set 2	mean = 0.67 [mm], 1σ = 0.92 [mm]
Fracture set 3	mean = 0.32 [mm], 1σ = 0.51 [mm]
Vein set 1	mean = 0.05 [mm], 1σ = 0.03 [mm]
Vein set 2	mean = 2.78 [mm], 1σ = 2.00 [mm]
Vein set 3	mean = 0.09 [mm], 1σ = 0.04 [mm]

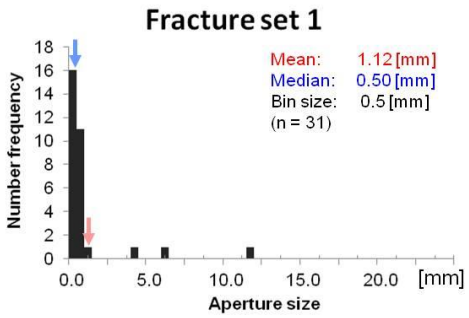

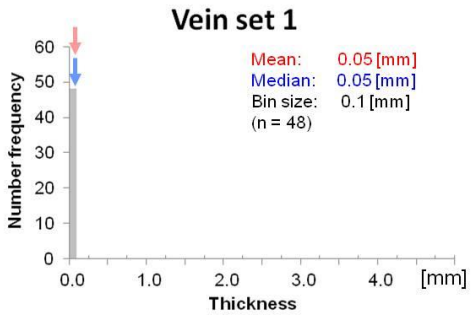

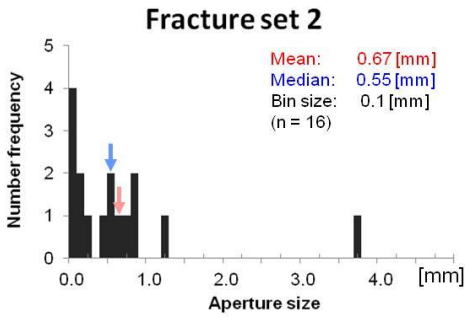

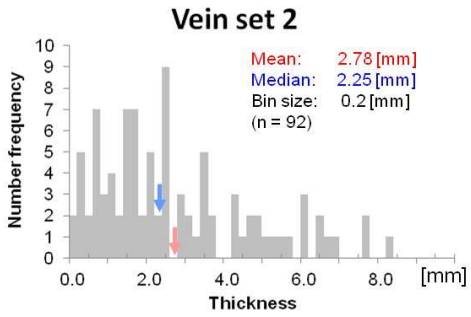

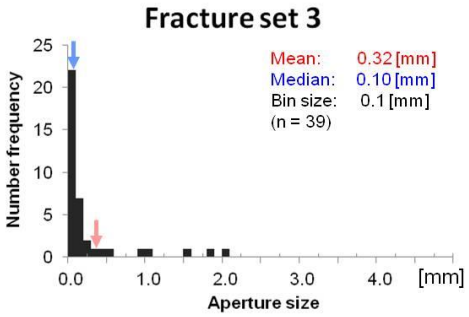

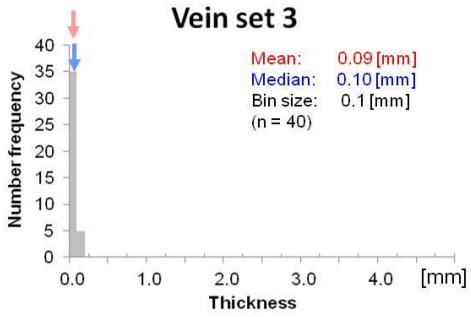

Vein Aspect ratio

Vein set 1	mean = 271, 1σ = 137

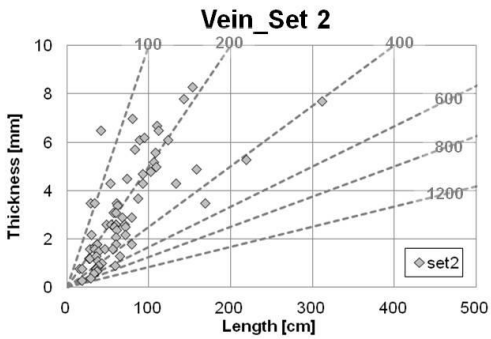

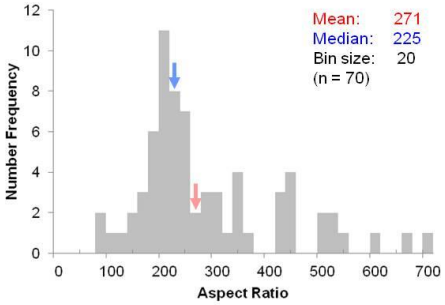

Layer #26

Site	I (southern limb of gentle fold)
Lithology	Shale
Layer thickness	91cm
Bedding	195, 23

scan line	dip direc -tion, dip	length	number of measured data	
			fracture	
			set 1	set 2
1	190,23	2.40m	0	22
2	121,06	29.72m	52	0
others	-	-	0	4

Fracture (n=78)

Set 1: NNE-SSW

Range of strikes: 0-60°

Set 2: SSE-NNW

Range of strikes: 0-45°

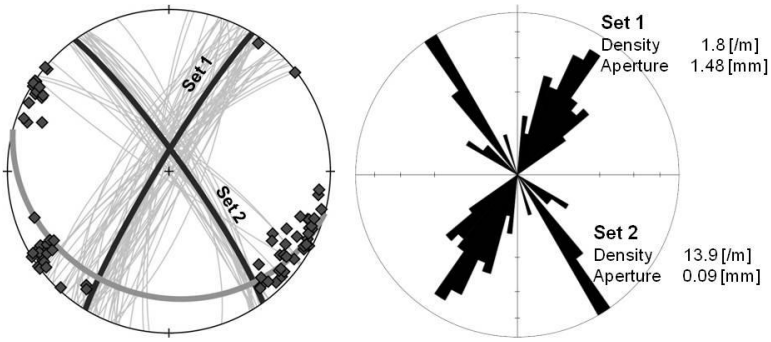

Vein

No vein was found in the layer.

Note

Fractures strike NNE-SSW (set 1) and SSE-NNW (set 2). Fracture density is much higher in set 2 and aperture is greater in set 1. This shale layer surrounds layer 28 and 29 (sandstones). Set 2 fractures cut this shale layer and the sandstones together though the other fractures commonly arrested at layer boundaries. This may suggest set 2 are relatively young as they formed after consolidation level became similar between shale and sandstones.

Fracture and vein density

Fracture set 1	Raw 1.7 [/m], Corrected 1.8 [/m]	(from 52 data along scan-line 2)
Fracture set 2	Raw 9.2 [/m], Corrected 13.9 [/m]	(from 22 data along scan-line 1)

Fracture aperture size and vein thickness

Fracture set 1	mean = 1.48 [mm], 1σ = 1.77 [mm]
Fracture set 2	mean = 0.09 [mm], 1σ = 0.12 [mm]

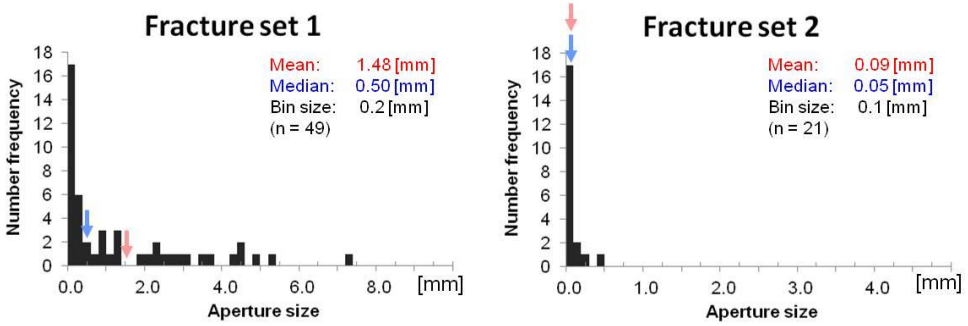

Layer #27

Site	I (southern limb of gentle fold)
Lithology	Sandstone
Layer thickness	Not measured
Bedding	188, 13

scan line	dip direc -tion, dip	length	number of measured data		
			vein		
			set 1	set 2	set 3
others	-	-	47	21	29

Fracture

Fractures exist in the layer but only veins were measured. This is mainly in order to obtain vein aspect ratio.

Vein (n=97)

Set 1: NE-SW
Range of strikes: 0-45°
Set 2: E-W
Range of strikes: 0-30°
Set 3: SE-NW
Range of strikes: 0-30°

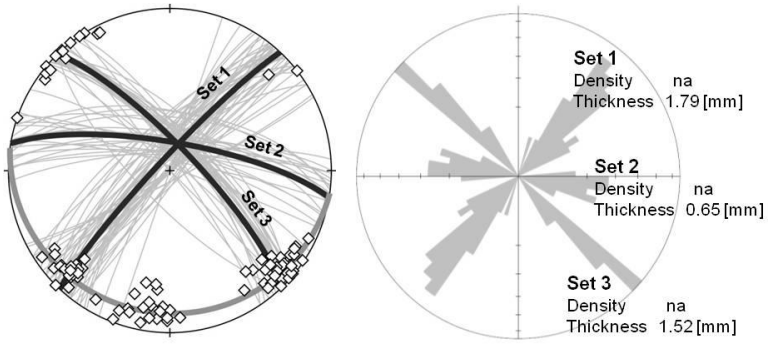

Note

Only veins were measured in this layer to collect data of vein aspect ratio.

Fracture aperture size and vein thickness

Vein set 1	mean = 1.79 [mm], 1σ = 1.67 [mm]
Vein set 2	mean = 0.65 [mm], 1σ = 0.33 [mm]
Vein set 3	mean = 1.52 [mm], 1σ = 1.08 [mm]

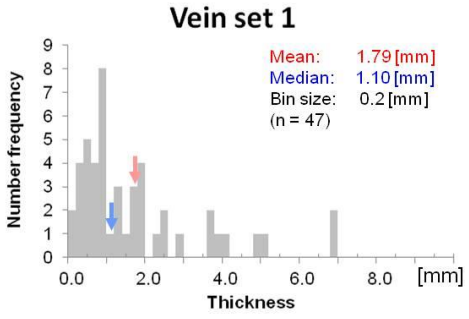

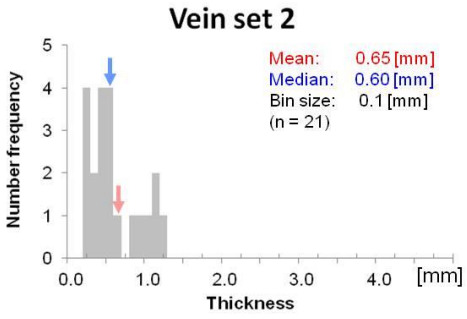

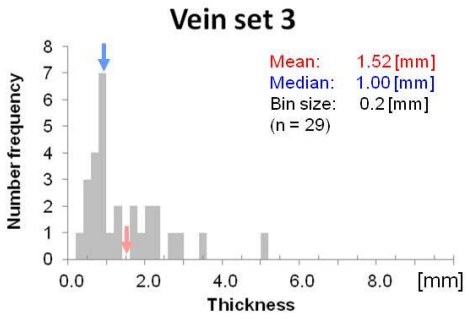

Vein Aspect ratio

Vein set 1	mean = 380, 1σ = 193
Vein set 2	mean = 306, 1σ = 143
Vein set 3	mean = 469, 1σ = 181

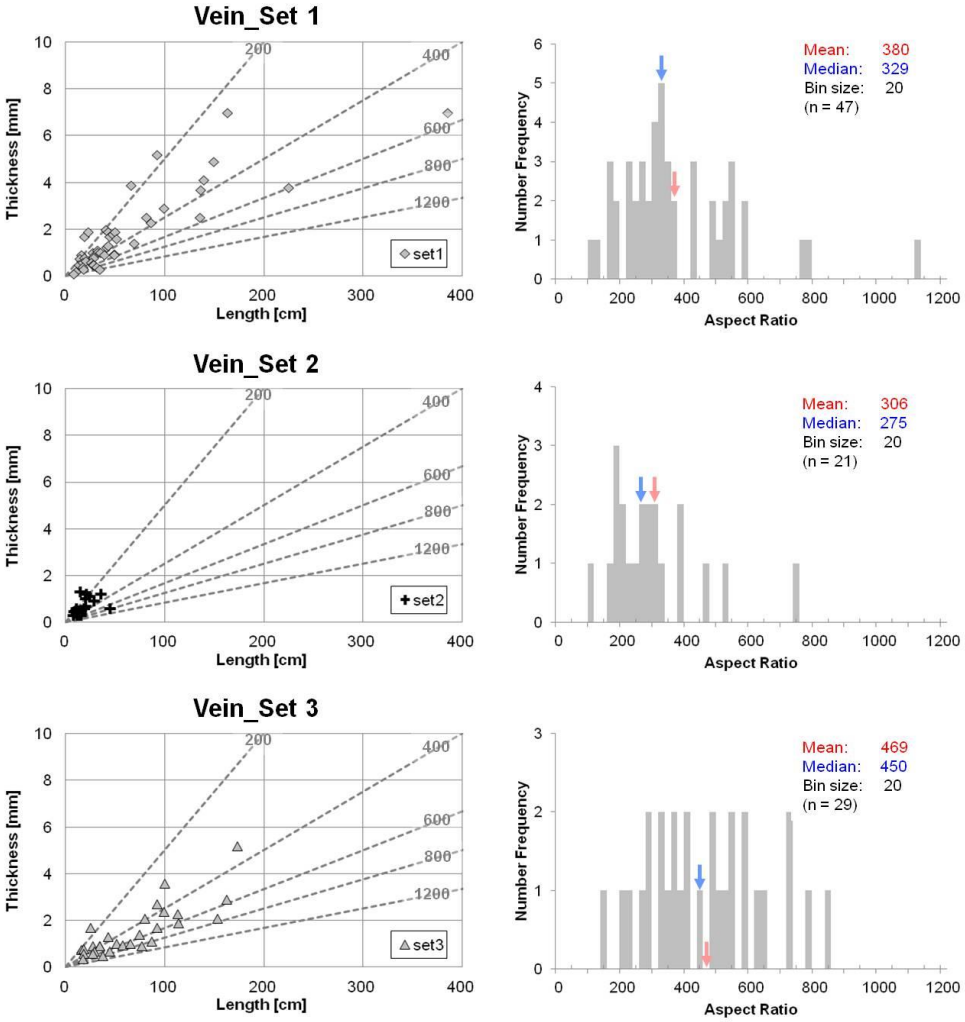

Layer #28

Site I (southern limb of gentle fold)
Lithology Sandstone
Layer thickness 23cm
Bedding 200, 25

scan line	dip direc -tion, dip	length	number of measured data					
			fracture			vein		
			set 1	set 2	set 3	set 1	set 2	others
1	118,03	2.42m	39	0	0	19	0	0
2	206,25	6.21m	0	29	20	0	7	1

Fracture (n=88)
Set 1: NNE-SSW
Range of strikes: 0-30°
Set 2: ESE-WNW
Range of strikes: 0-45°
Set 3: SE-NW
Range of strikes: 0-30°

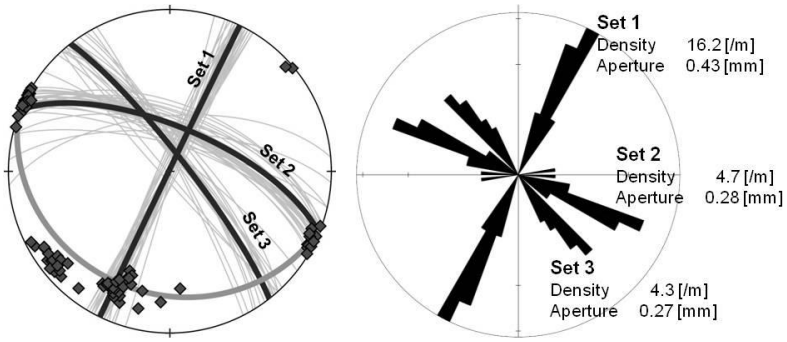

Vein (n=27)
Set 1: NNE-SSW
Range of strikes: 0-30°
Set 2: ESE-WNW
Range of strikes: 0-45°

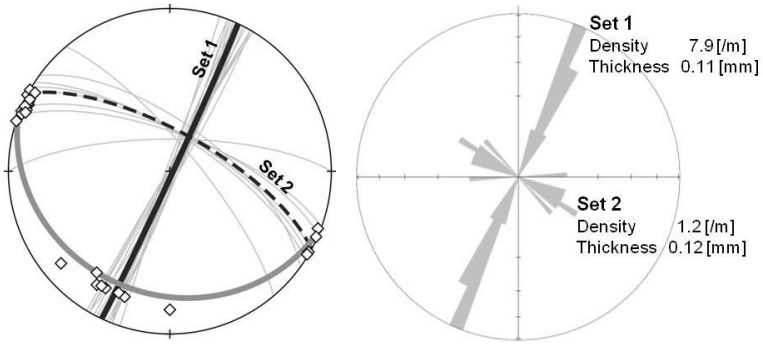

Note

Fractures strike NNE-SSW (set 1), ESE-WNW (set 2), and SE-NW (set 3). Fracture density is much higher in set 1 and the aperture size is relatively large. Set 2 and 3 have similar fracture density and aperture size. Set 3 fractures cut shale (layer 26) and sandstones (layer 28 and 29) together, suggesting set 3 is young after shale was well consolidated as well as sandstones. Because of this field observation, set 2 and 3 cannot be conjugate fractures. Ranges of strikes of the sets suggest they would be either extension or hybrid fractures.

Veins are less common in the layer and the thicknesses of them are very thin. The veins strike similar orientations as those of fractures (NNE-SSW: set 1, ESE-WNW: set 2). Vein density is higher in set 1.

Most fractures and veins are perpendicular to the bedding, except for fracture set 2.

Fracture and vein density

Fracture set 1	Raw 16.1 [/m], Corrected 16.2 [/m]	(from 39 data along scan-line 1)
Fracture set 2	Raw 4.7 [/m], Corrected 4.7 [/m]	(from 29 data along scan-line 2)
Fracture set 3	Raw 3.6 [/m], Corrected 4.3 [/m]	(from 20 data along scan-line 2)
Vein set 1	Raw 7.9 [/m], Corrected 7.9 [/m]	(from 19 data along scan-line 1)
Vein set 2*	Raw 1.1 [/m], Corrected 1.2 [/m]	(from 7 data along scan-line 2)

*Number of measured data may not be sufficient and the fracture density is relatively inaccurate.

Fracture aperture size and vein thickness

Fracture set 1	mean = 0.43 [mm], 1σ = 0.57 [mm]
Fracture set 2	mean = 0.28 [mm], 1σ = 0.28 [mm]
Fracture set 3	mean = 0.27 [mm], 1σ = 0.35 [mm]
Vein set 1	mean = 0.11 [mm], 1σ = 0.04 [mm]
Vein set 2	mean = 0.12 [mm], 1σ = 0.06 [mm]

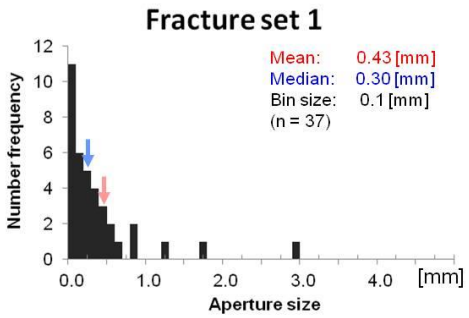

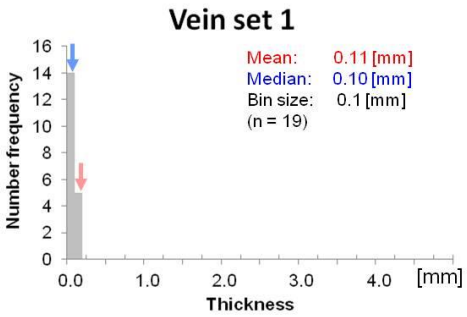

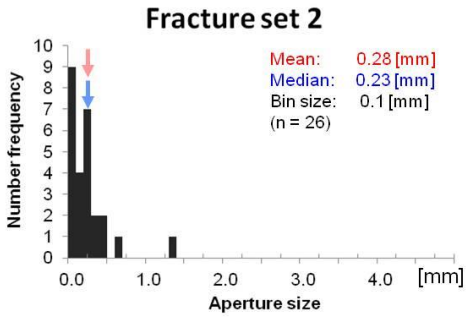

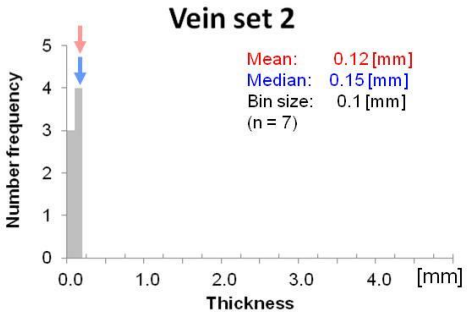

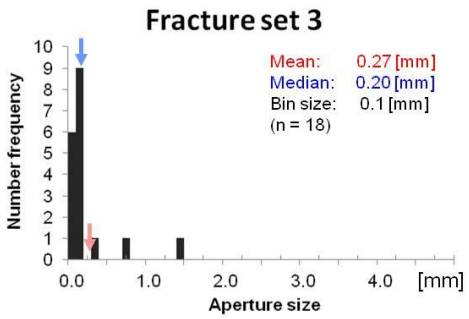

Layer #29

Site I (southern limb of gentle fold)
Lithology Sandstone
Layer thickness 13cm
Bedding 202, 25

scan line	dip direc -tion, dip	length	number of measured data			
			fracture			vein
			set 1	set 2	set 3	set 1
1	116,22	2.20m	65	0	0	0
2	205,25	5.29m	0	37	24	1

Fracture (n=126)

Set 1: NNE-SSW
Range of strikes: 0-30°
Set 2: ESE-WNW
Range of strikes: 0-30°
Set 3: SE-NW
Range of strikes: 0-30°

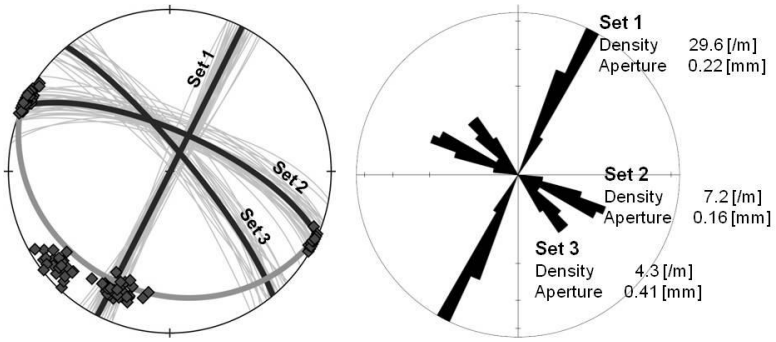

Vein (n=1)

Only one thin vein was found along ESE-WNW direction.

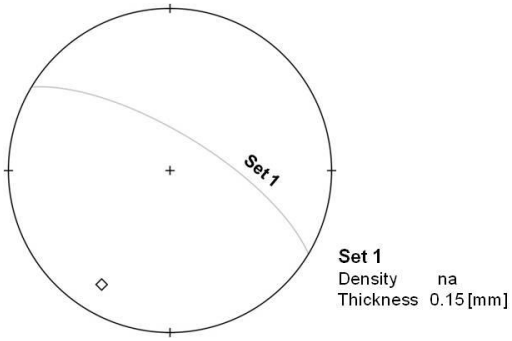

Note

Fracture pattern is same as that of layer 28. Fracture density is much higher in set 1. Set 2 fractures cut across layer 26, 28, and 29. Veins are difficult to find in the field probably because of their thin thickness. Only 1 vein was measured. Veins seem to become rare in thinner sandstone. Most fractures are perpendicular to the bedding, except for fracture set 2 (young fracture).

Fracture and vein density

Fracture set 1	Raw 29.5 [/m], Corrected 29.6 [/m]	(from 65 data along scan-line 1)
Fracture set 2	Raw 7.1 [/m], Corrected 7.2 [/m]	(from 37 data along scan-line 2)
Fracture set 3	Raw 3.6 [/m], Corrected 4.3 [/m]	(from 24 data along scan-line 2)

Fracture aperture size and vein thickness

Fracture set 1 mean = 0.22 [mm], 1σ = 0.51 [mm]
Fracture set 2 mean = 0.16 [mm], 1σ = 0.16 [mm]
Fracture set 3 mean = 0.41 [mm], 1σ = 0.69 [mm]

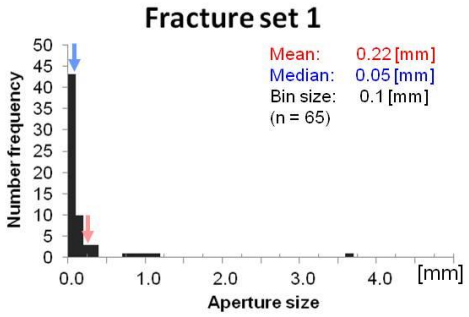

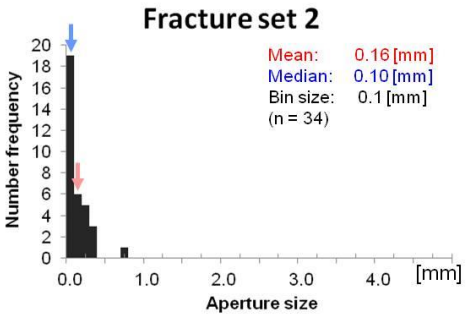

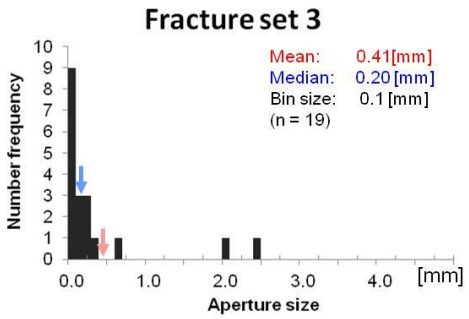

Layer #30

Site	J (close to hinge of gentle fold)
Lithology	Shale ~ Shaly limestone
Layer thickness	119cm
Bedding	359, 12

scan line	dip direc -tion, dip	length	number of measured data	
			fracture	
			set 1	set 2
1	069,05	23.10m	0	46
2	082,02	29.10m	35	2
others	-	-	2	0

Fracture (n=85)

Set 1: NNE-SSW

Range of strikes: 0-45°

Set 2: SE-NW

Range of strikes: 0-45°

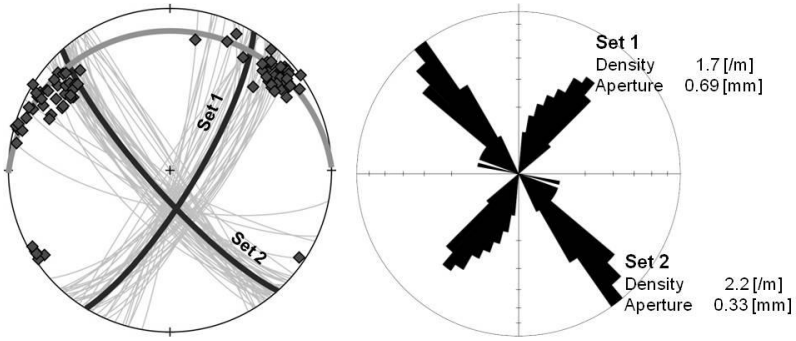

Vein

No vein was found in the layer.

Note

Fractures strike NNE-SSW and SE-NW. Fracture density is slightly high in set 2 and aperture is greater in set. This layer emplaced just below layer 31 (limestone). The lithology is not pure shale but more like shaly limestone. The fracture planes are relatively flat with less ductility. Ranges of strikes of the two sets suggests they would be either extension or hybrid fractures. Most fractures are perpendicular to the bed.

<u>Fracture and vein density</u>

Fracture set 1	Raw 1.2 [/m], Corrected 1.7 [/m]	(from 35 data along scan-line 2)
Fracture set 2	Raw 2.0 [/m], Corrected 2.2 [/m]	(from 46 data along scan-line 1)

<u>Fracture aperture size and vein thickness</u>

Fracture set 1	mean = 0.69 [mm], 1σ = 0.62 [mm]
Fracture set 2	mean = 0.33 [mm], 1σ = 0.45 [mm]

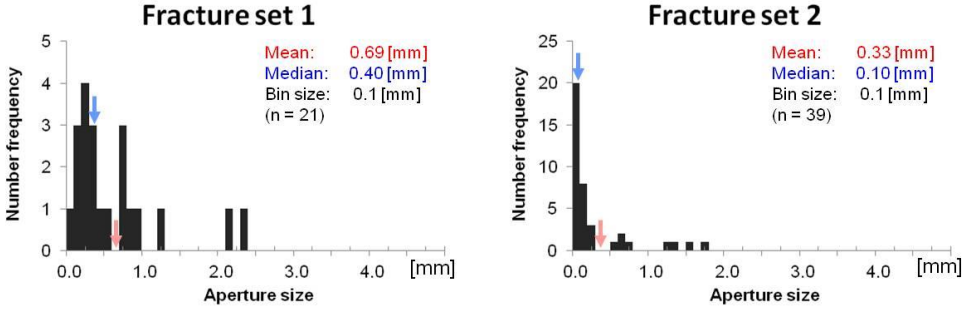

Layer #31

Site	J (close to hinge of gentle fold)
Lithology	Limestone
Layer thickness	72cm
Bedding	295, 06

scan line	dip direc -tion, dip	length	number of measured data			
			fracture			vein
			set 1	set 2	set 3	set 1
1	021,00	12.68m	0	32	22	0
2	277,06	7.60m	51	7	5	22

Fracture (n=117)

Set 1: NNE-SSW
Range of strikes: 0-30°
Set 2: E-W
Range of strikes: 0-30°
Set 3: ESE-WNW
Range of strikes: 0-45°

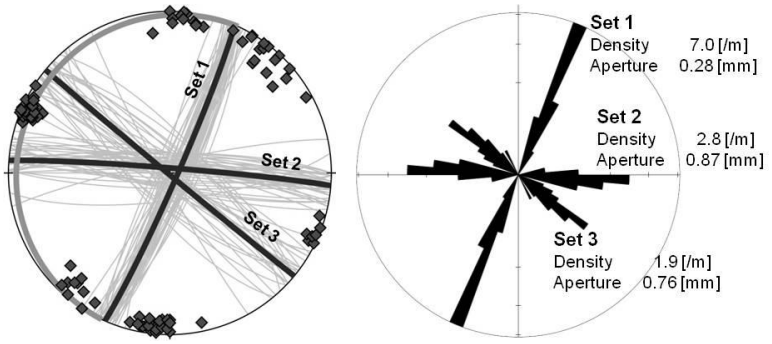

Vein (n=20)

Set 1: NNE-SSW
Range of strikes: 0-30°

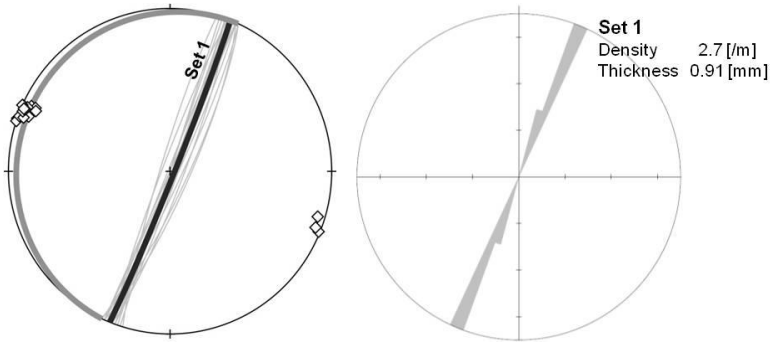

Note

Fractures strike NNE-SSW (set 1), E-N (set 2), and ESE-WNW (set 3). Fracture density is high in set 1 and aperture size is greater in set 2 and 3. In the field, set 2 and 3 seem conjugate set of hybrid fractures based on their similarities (without vein, length, aperture, etc). Range of the strikes of set 1 suggests they are dominantly extension fractures.

Veins are less common in the layer. The veins are composed of calcite and siderite in this limestone layer although veins mainly consist of quartz in sandstone layers (chapter 5). The veins strike only NNE-SSW. Range of the strikes suggests they are dominantly extension fractures.

Most fractures and veins are perpendicular to the bed.

Fracture and vein density

Fracture set 1	Raw 6.7 [/m], Corrected 7.0 [/m]	(from 51 data along scan-line 2)
Fracture set 2	Raw 2.7 [/m], Corrected 2.8 [/m]	(from 32 data along scan-line 1)
Fracture set 3	Raw 1.8 [/m], Corrected 1.9 [/m]	(from 22 data along scan-line 1)
Vein set 1	Raw 2.6 [/m], Corrected 2.7 [/m]	(from 22 data along scan-line 2)

Fracture aperture size and vein thickness

Fracture set 1	mean = 0.28 [mm], 1σ = 0.55 [mm]
Fracture set 2	mean = 0.87 [mm], 1σ = 0.79 [mm]
Fracture set 3	mean = 0.76 [mm], 1σ = 0.64 [mm]
Vein set 1	mean = 0.91 [mm], 1σ = 0.77 [mm]

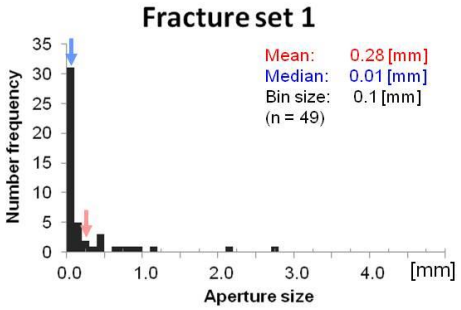

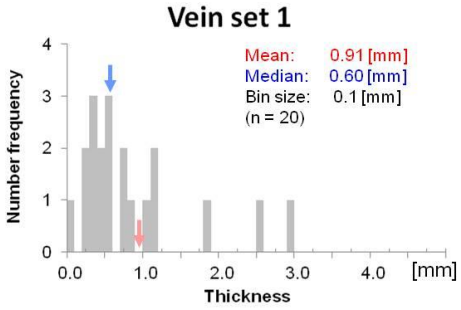

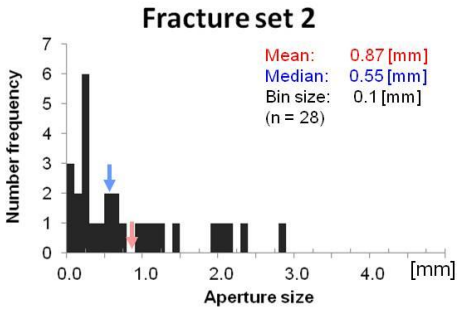

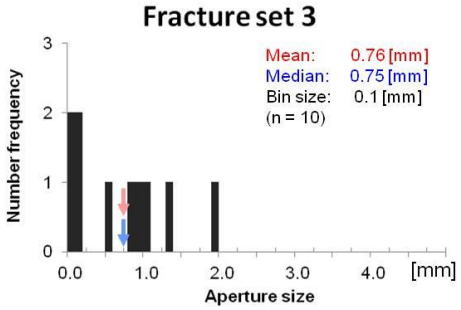

Layer #32

Site	K (gentle monocline dipping to south)
Lithology	Shale
Layer thickness	145cm
Bedding	233, 10

scan line	dip direc -tion, dip	length	number of measured data			
			fracture			
			set 1	set 2	set 3	others
1	277,07	16.53m	28	9	13	0
2	212,09	6.98m	1	7	9	1

Fracture (n=68)

Set 1: NNE-SSW
Range of strikes: 0-30°
Set 2: ENE-WSW
Range of strikes: 0-30°
Set 3: SE-NW
Range of strikes: 0-30°

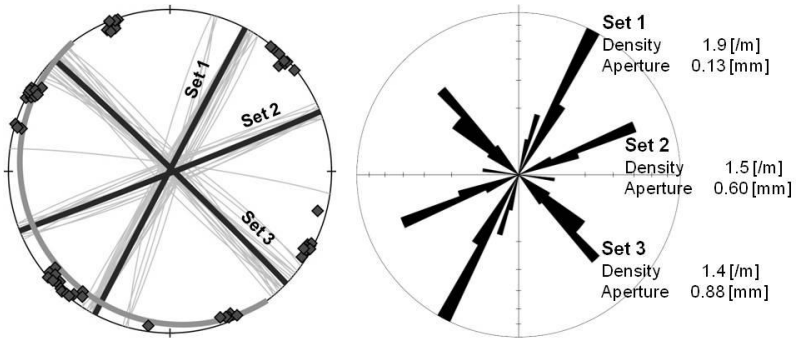

Vein

No vein was found in the layer.

Note

Fractures strike NNE-SSW (set 1), ENE-WSW (set 2), and SE-NW (set 3). Fracture densities are similar among the three sets. Aperture size is thicker in set 3 and thinner in set 1. Ranges of the strikes suggest that they are mostly extension fractures. The fracture planes are flat with less ductility in the shale layer. Most fractures are perpendicular to the bed.

Fracture and vein density

Fracture set 1	Raw 1.7 [/m], Corrected 1.9 [/m]	(from 28 data along scan-line 1)
Fracture set 2*	Raw 0.7 [/m], Corrected 1.5 [/m]	(from 9 data along scan-line 1)
Fracture set 3	Raw 0.8 [/m], Corrected 1.4 [/m]	(from 13 data along scan-line 1)

*Number of measured data may not be sufficient and the fracture density is relatively inaccurate.

Fracture aperture size and vein thickness

Fracture set 1 mean = 0.13 [mm], 1σ = 0.33 [mm]
Fracture set 2 mean = 0.60 [mm], 1σ = 0.71 [mm]
Fracture set 3 mean = 0.88 [mm], 1σ = 1.13 [mm]

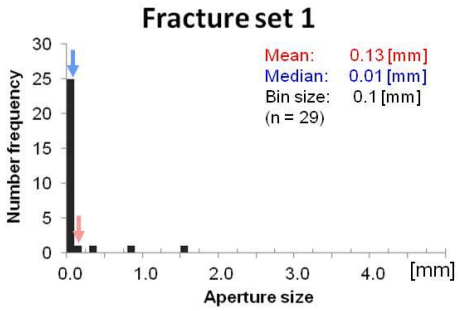

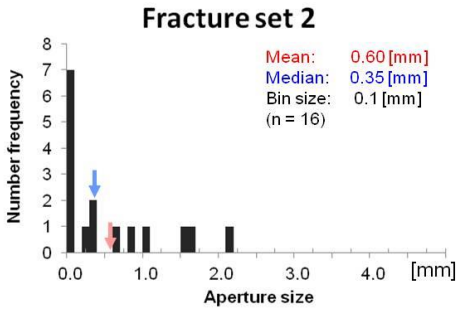

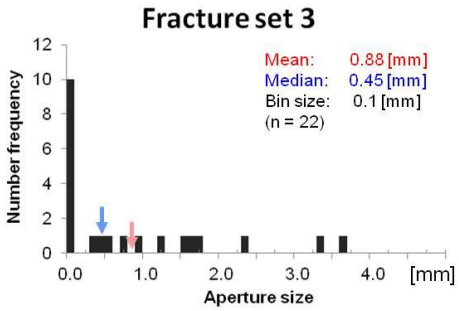

Layer #33

Site	K (gentle monocline dipping to south)
Lithology	Sandstone
Layer thickness	137cm
Bedding	219, 07

scan line	dip direc -tion, dip	length	number of measured data					
			fracture				vein	
			set 1	set 2	set 3	other	set 1	set 2
1	295,02	36.99m	13	6	2	0	57	0
2	206,07	33.15m	0	4	17	2	0	28

Fracture (n=44)

Set 1: NNE-SSW
Range of strikes: 0-45°
Set 2: ENE-WSW
Range of strikes: 0-30°
Set 3: SE-NW
Range of strikes: 0-30°

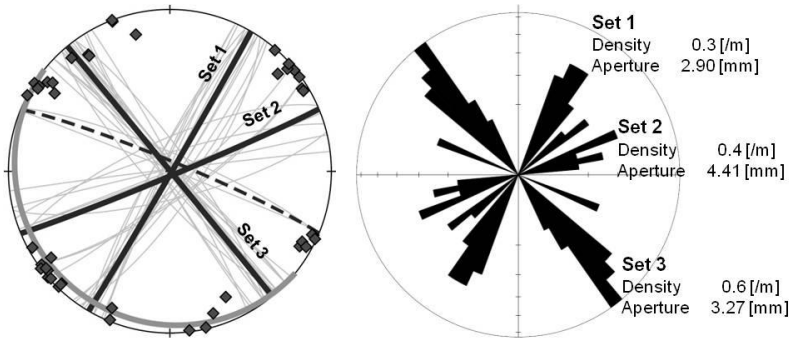

Vein (n=85)

Set 1: NNE-SSW
Range of strikes: 0-30°
Set 2: ESE-WNW
Range of strikes: 0-30°

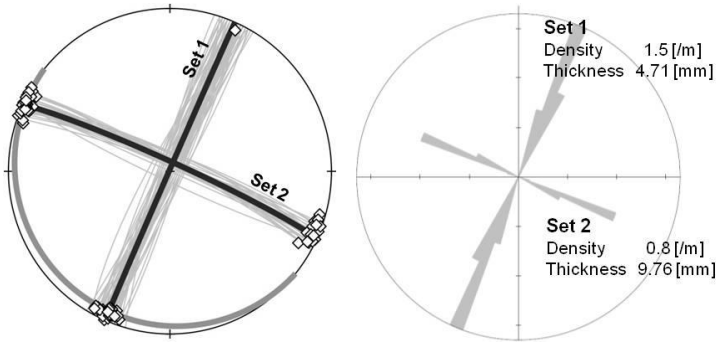

Note

Fractures mainly strikes NNE-SSW (set 1), ENE-WSW (set 2), and SE-NW (set 3). Fracture density and aperture size are similar among the three. Close orientation of set 1 and 2 may suggest that they are conjugate hybrid fractures.

Veins are relatively common in the layer. The veins strike NNE-SSW and ESE-WNW. Vein density is higher in set 1 but thickness is larger in set 2. Because of the situations, strains associated with the vein openings are similar between the two. Ranges of the strikes of the two sets suggest they are mostly extension fractures.

Most fractures and veins are perpendicular to the bedding.

Fracture and vein density

Fracture set 1	Raw 0.3 [/m], Corrected 0.3 [/m]	(from 13 data along scan-line 1)
Fracture set 2*	Raw 0.3 [/m], Corrected 0.4 [/m]	(from 6 data along scan-line 1)
Fracture set 3	Raw 0.5 [/m], Corrected 0.6 [/m]	(from 17 data along scan-line 2)
Vein set 1	Raw 1.5 [/m], Corrected 1.5 [/m]	(from 57 data along scan-line 1)
Vein set 2	Raw 0.8 [/m], Corrected 0.8 [/m]	(from 28 data along scan-line 2)

*Number of measured data may not be sufficient and the fracture density is relatively inaccurate.

Fracture aperture size and vein thickness

Fracture set 1	mean = 2.90 [mm], 1σ = 1.26 [mm]
Fracture set 2	mean = 4.41 [mm], 1σ = 2.79 [mm]
Fracture set 3	mean = 3.27 [mm], 1σ = 2.48 [mm]
Vein set 1	mean = 4.71 [mm], 1σ = 6.25 [mm]
Vein set 2	mean = 9.76 [mm], 1σ = 10.18 [mm]

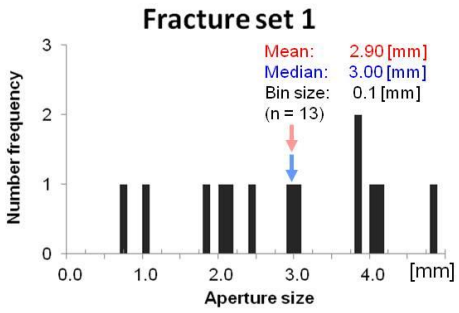

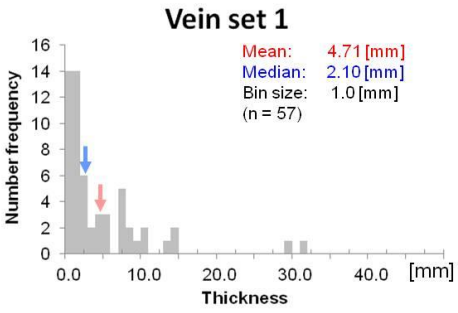

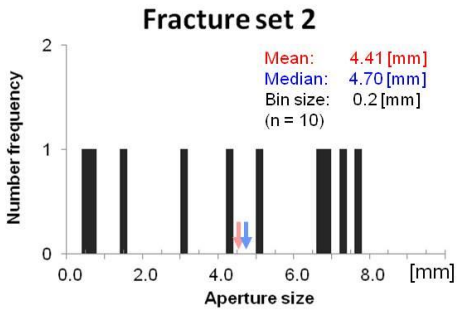

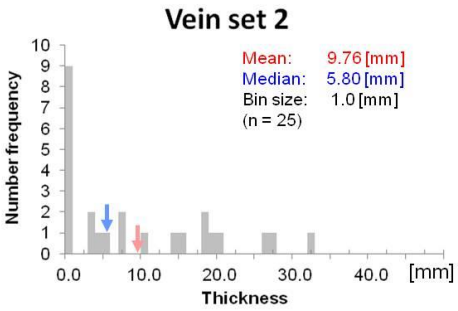

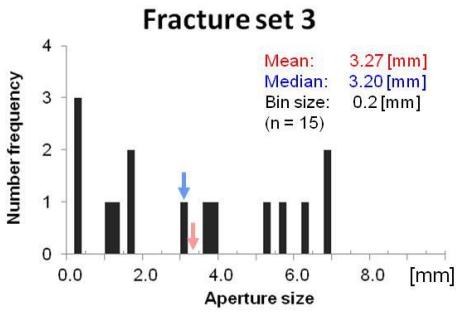

Layer #34

Site L (gentle monocline dipping to south)
Lithology Shale
Layer thickness 520cm
Bedding 240, 20

scan line	dip direc -tion, dip	length	number of measured data	
			fracture	
			set 1	set 2
1	303,10	14.78m	35	0
others	-	-	0	8

Fracture (n=43)

Set 1: NNE-SSW
Range of strikes: 0-45°
Set 2: SE-NW
Range of strikes: 0-45°

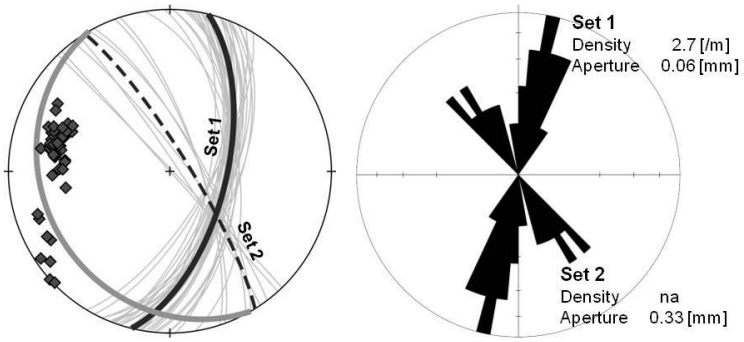

Vein

No vein was found in the layer.

Note

Fractures strike NNE-SSW (set 1) and SE-NW (set 2). Because of limited exposure of the shale along NE-SW direction, set 2 fractures were not measured along a scan-line. Range of the strikes is less than 45 degrees, suggesting the possibility that they are hybrid or extension fractures. The fracture planes are relatively flat with less ductility in the shale layer. Most fractures are not perpendicular to the bedding.

Fracture and vein density

Fracture set 1 Raw 2.4 [/m], Corrected 2.7 [/m] (from 35 data along scan-line 1)

Fracture aperture size and vein thickness

Fracture set 1 mean = 0.06 [mm], 1σ = 0.19 [mm]
Fracture set 2 mean = 0.33 [mm], 1σ = 0.27 [mm]

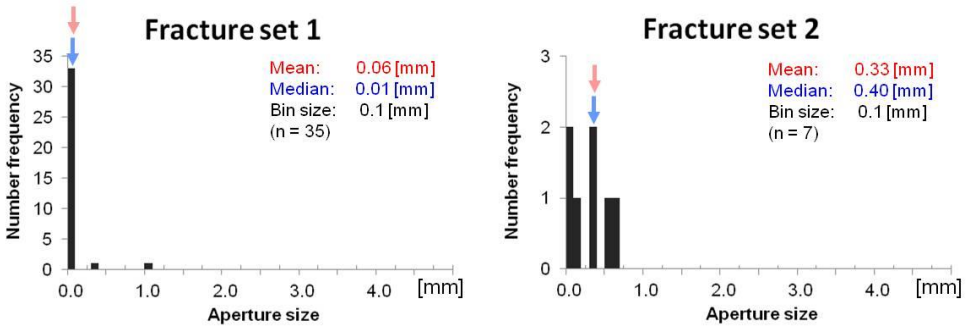

Layer #35

Site	L (gentle monocline dipping to south)
Lithology	Sandstone
Layer thickness	190cm
Bedding	226, 15

scan line	dip direc -tion, dip	length	number of measured data			
			fracture		vein	
			set 1	set 2	set 1	set 2
1	304,03	19.78m	34	0	36	0
2	204,14	57.37m	0	14	0	28
others	-	-	0	0	78	41

Fracture (n=48)

Set 1: NNE-SSW

Range of strikes: 0-30°

Set 2: ESE-WNW

Range of strikes: 0-45°

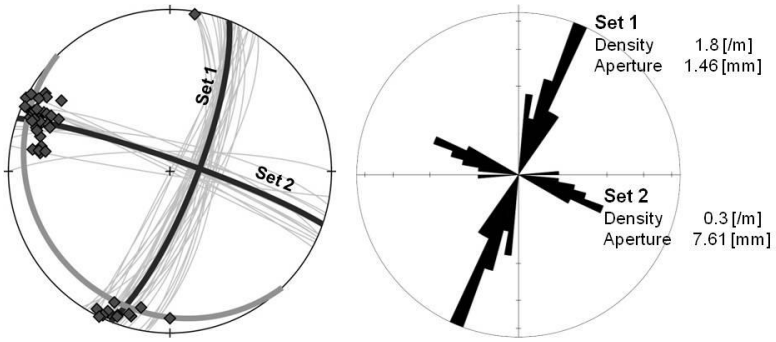

Vein (n=183)

Set 1: NNE-SSW

Range of strikes: 0-30°

Set 2: ESE-WNW

Range of strikes: 0-30°

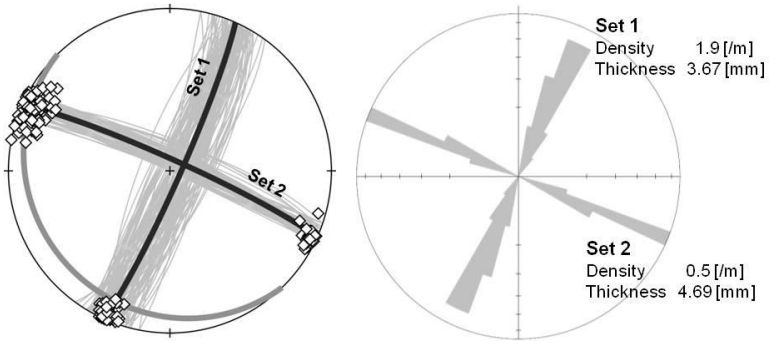

Note

Fractures strike NNE-SSW (set 1) and ESE (set 2). Aperture size of set 2 is much larger than that of set 1 but fracture density is greater in set 1. Because of these conditions, strains caused by both fracture sets are similar. Ranges of the strikes of the two sets suggest they are mostly either extension or hybrid fractures.

Veins are more common in the layer. The veins strike same orientations as those of fractures. Aperture size of set 2 is larger and density of set 1 is greater. However, strain caused by set 1 vein opening is three times larger than that of set 2. Ranges of the strikes of the two sets suggest they are mostly extension fractures.

Fractures and veins are sub-perpendicular to the bed but majority of them are not exactly perpendicular.

<u>Fracture and vein density</u>

Fracture set 1	Raw 1.7 [/m], Corrected 1.8 [/m]	(from 34 data along scan-line 1)
Fracture set 2	Raw 0.2 [/m], Corrected 0.3 [/m]	(from 14 data along scan-line 2)
Vein set 1	Raw 1.8 [/m], Corrected 1.9 [/m]	(from 36 data along scan-line 1)
Vein set 2	Raw 0.5 [/m], Corrected 0.5 [/m]	(from 28 data along scan-line 2)

Fracture aperture size and vein thickness

Fracture set 1	mean = 1.46 [mm], 1σ = 1.92 [mm]
Fracture set 2	mean = 7.61 [mm], 1σ = 9.80 [mm]
Vein set 1	mean = 3.67 [mm], 1σ = 3.50 [mm]
Vein set 2	mean = 4.69 [mm], 1σ = 3.32 [mm]

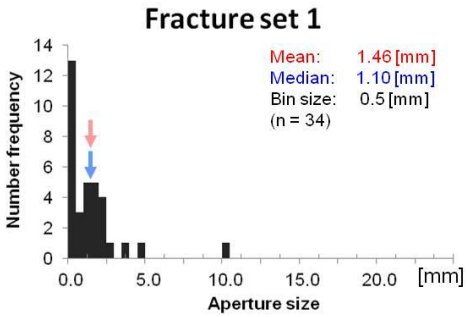

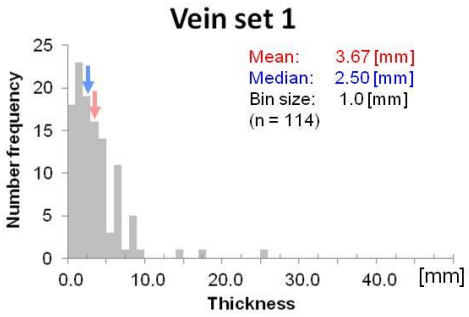

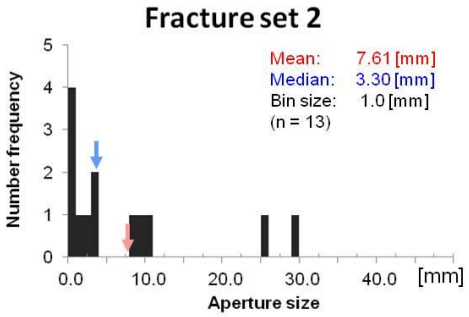

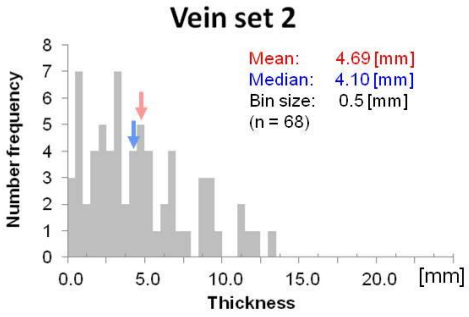

Vein Aspect ratio

Vein set 1	mean = 251, 1σ = 121
Vein set 2	mean = 587, 1σ = 258

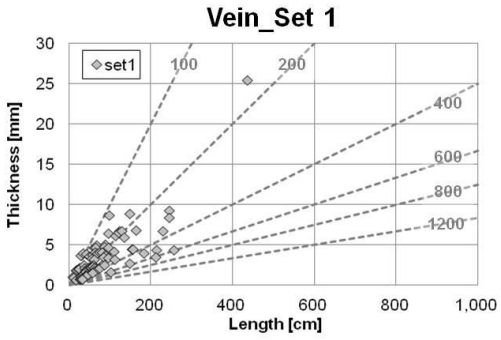

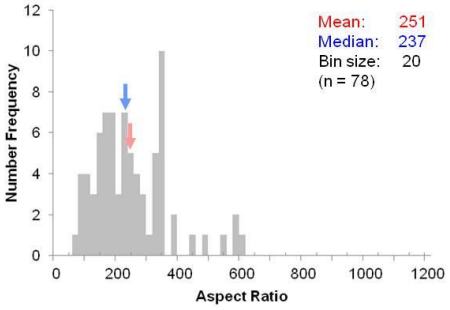

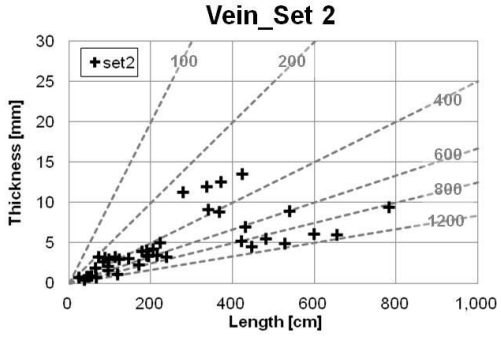

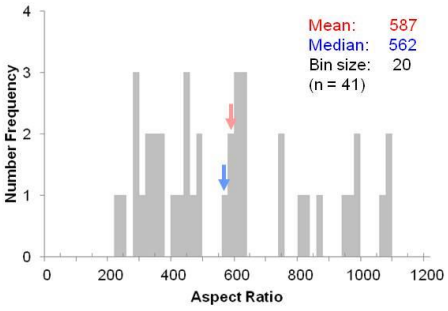

Layer #36

Site	M (gentle monocline dipping to south)
Lithology	Sandstone (Quartzite)
Layer thickness	37cm
Bedding	199, 11

scan line	dip direc -tion, dip	length	number of measured data		
			fracture	vein	
			set 1	set 1	set 2
1	115,01	9.62m	17	25	0
2	204,11	9.42m	0	0	33

Fracture (n=17)

Set 1: NNE-SSW

Range of strikes: 0-30°

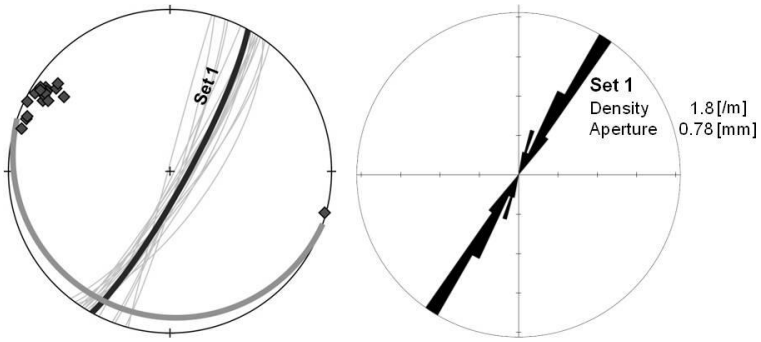

Vein (n=58)

Set 1: NNE-SSW

Range of strikes: 0-45°

Set 2: ESE-WNW

Range of strikes: 0-30°

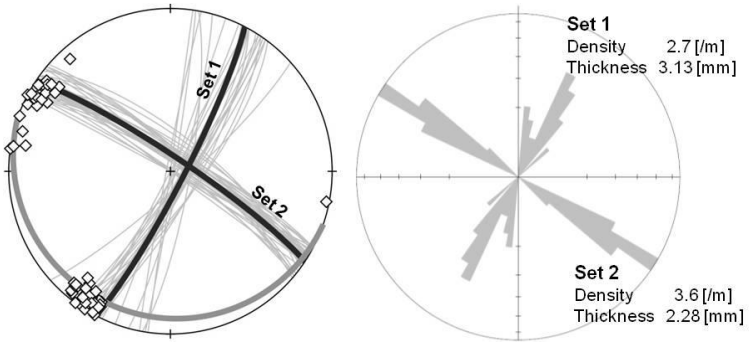

Note

Fractures strike only NNE-SSW (set 1). Range of the strikes suggests they are mostly extension fractures.

Veins are relatively common in the layer. The veins strikes NNE-SSW (set 1) and ESE-WNW (set 2). The vein density and thickness are similar between the two sets. Ranges of the strikes of the two sets suggest they are mostly either extension or hybrid fractures.

Most fractures and veins are perpendicular to bed.

<u>Fracture and vein density</u>

Fracture set 1	Raw 1.8 [/m], Corrected 1.8 [/m]	(from 17 data along scan-line 1)
Vein set 1	Raw 2.6 [/m], Corrected 2.7 [/m]	(from 25 data along scan-line 1)
Vein set 2	Raw 3.5 [/m], Corrected 3.6 [/m]	(from 33 data along scan-line 2)

Fracture aperture size and vein thickness

Fracture set 1	mean = 0.78 [mm], 1σ = 0.95 [mm]
Vein set 1	mean = 3.13 [mm], 1σ = 3.82 [mm]
Vein set 2	mean = 2.28 [mm], 1σ = 1.81 [mm]

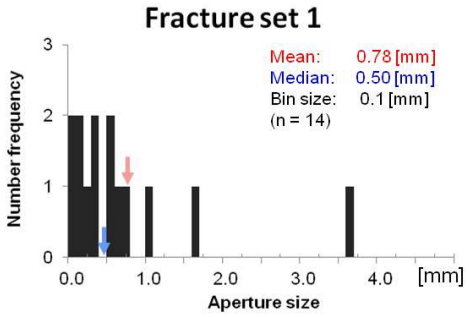

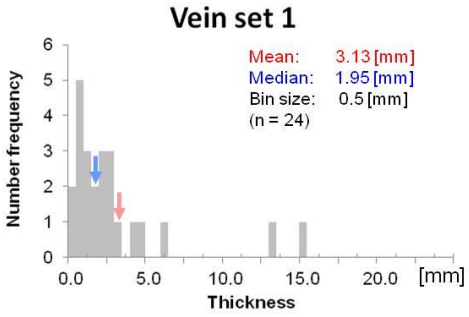

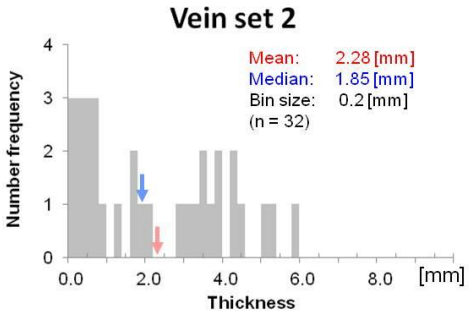

Relationship between fracture density / fracture space and layer thickness of the 36 layers

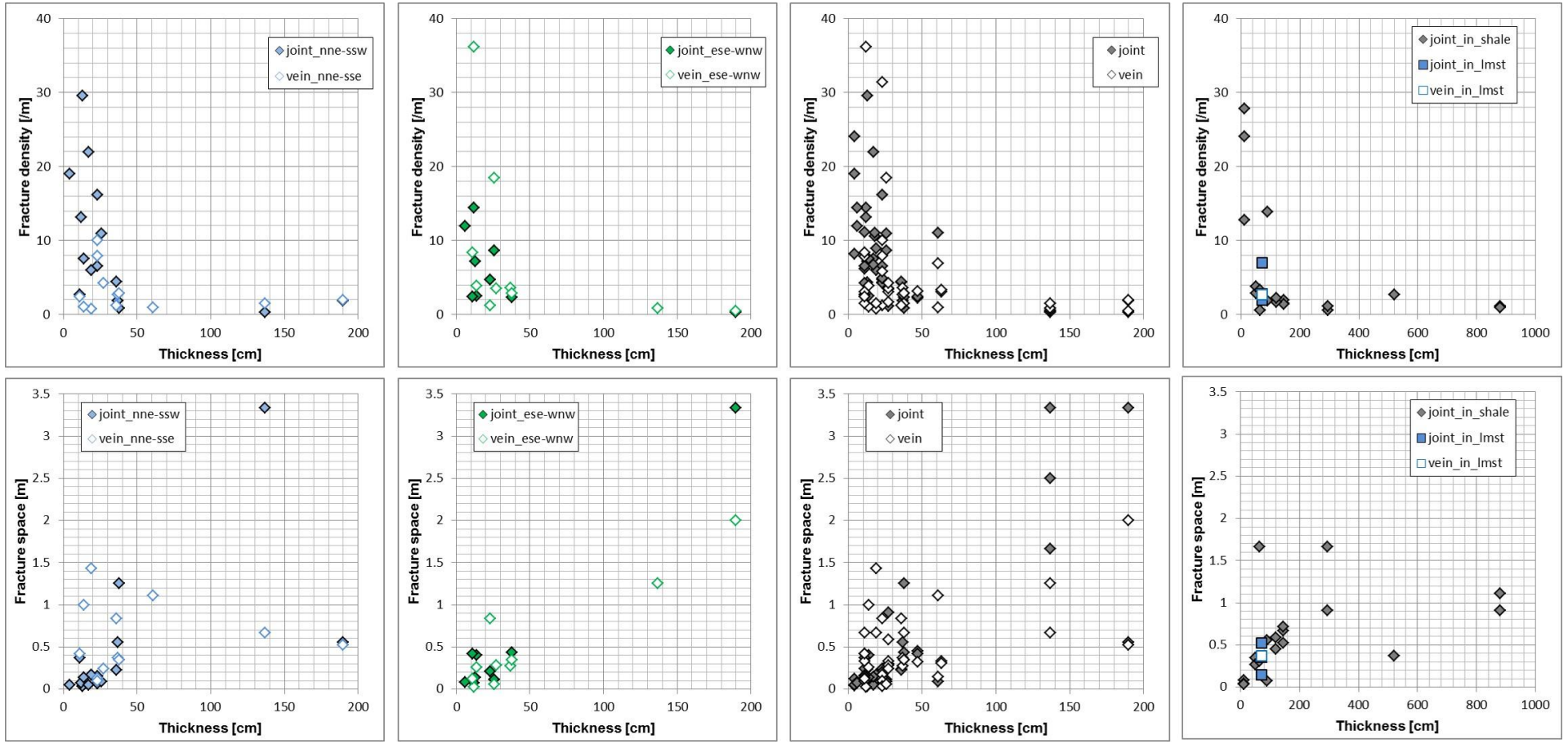

Fracture density is corrected value shown on above pages. Inverse number was used for fracture space here.

Relationship between mean aperture size / strain and layer thickness of the 36 layers

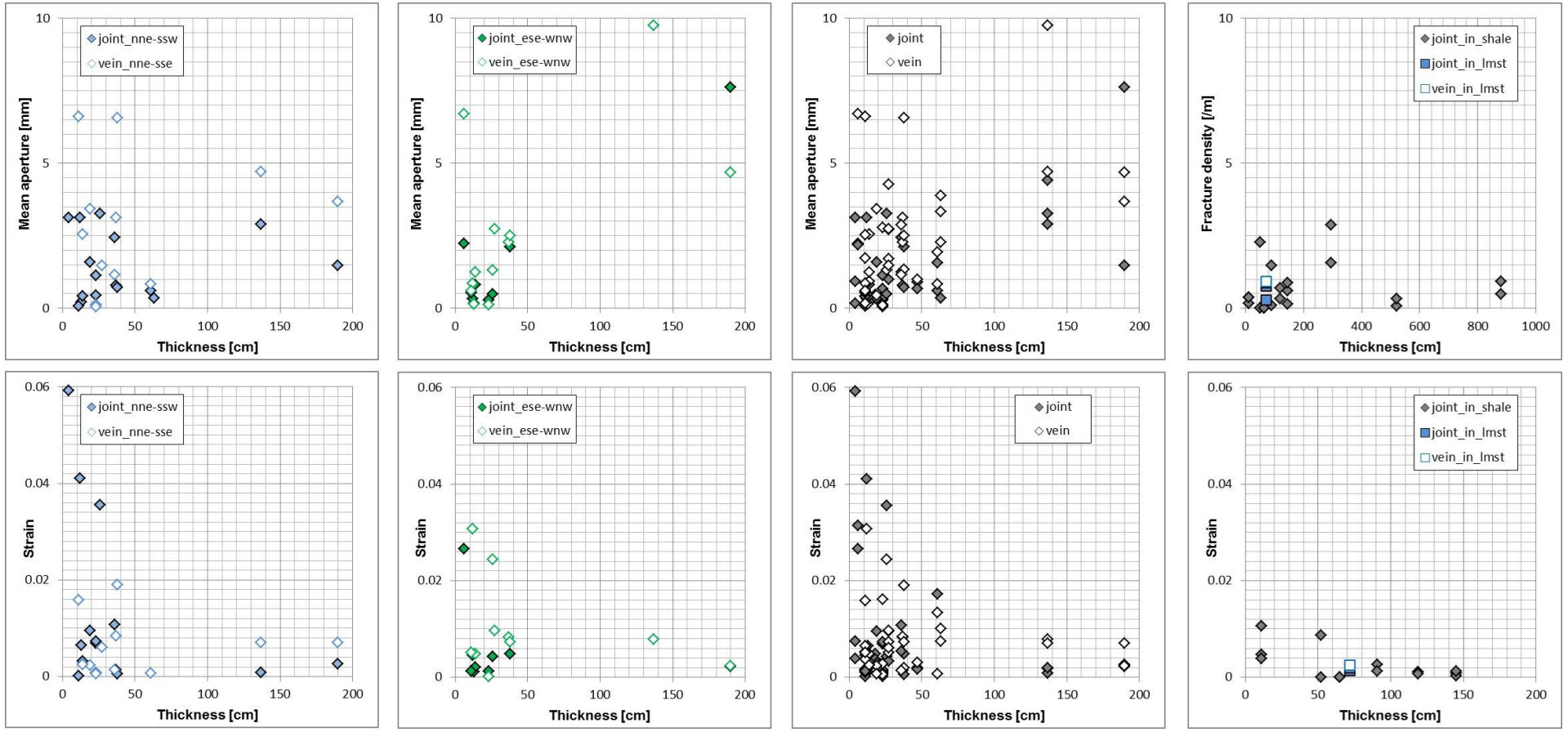

Mean aperture size for each layer is shown on above pages. Stain is multiplication of corrected fracture density and mean aperture size for each set.